NASA Contractor Report 4582- Vol-1

F/A-18 Forebody Vortex Control
Volume 1—Static Tests

Brian R. Kramer, Carlos J. Suárez, Gerald N. Malcolm, and Bert F. Ayers

Eidetics International, Inc.
3415 Lomita Blvd.
Torrance, CA 90505

Prepared for
Ames Research Center
CONTRACT NAS2-13383
March 1994

NASA
National Aeronautics and
Space Administration

Ames Research Center
Moffett Field, California 94035-1000

TABLE OF CONTENTS

Table of Contents
(continued)

LIST OF FIGURES

NOMENCLATURE

A_j	blowing jet exit area, ft^2
A_S	blowing slot exit area, ft^2
α, AOA	angle of attack, degrees
β	sideslip angle, degrees
b	wing span, 2.245 ft
C_A	axial force coefficient (body axis)
C_l	rolling moment coefficient (body axis)
C_m	pitching moment coefficient (body axis)
C_N	normal force coefficient (body axis)
C_n	yawing moment coefficient (body axis)
C_Y	side force coefficient (body axis)
C_μ	blowing coefficient, $\frac{\dot{m}_j V_j}{q\ S}$
c	mean aerodynamic chord, 0.691 ft
c_{ref}	moment reference center, 0.25c
δ	vertical nose strake deflection (+, trailing edge left)
δr	rudder deflection (+, trailing edge left)
F.S.	fuselage station, inches on full-scale aircraft
L	model length, 3.36 ft
M	Mach number
MFR	mass flow ratio, $\frac{\dot{m}_j}{\dot{m}_{ref}}$
$\dot{m}$	mass flow rate, lbm / sec
$\dot{m}_j$	mass flow rate of the jet, $\rho_j A_j V_j$
$\dot{m}_{ref}$	freestream mass flow rate, $\rho S V$
Φ	azimuth angle (from the windward meridian), degrees
q, Q	free-stream dynamic pressure, lbf / ft^2
ρ_j	air density at blowing jet exit, slugs / ft^3
ρ	freestream air density, slugs / ft^3
Rn	Reynolds number
S	reference wing area , 1.44 ft^2
t^*	convective time = t V / L
V	free-stream velocity, ft / sec
V_j	blowing jet exit velocity, ft / sec
V_S	blowing slot exit velocity, ft / sec
x	distance from tip of nose (model fuselage station), inches

SUMMARY

Forebody vortex control (FVC) techniques have been evaluated on a 6%-scale F/A-18 model in the NASA Ames 7 x 10-ft wind tunnel. Both static and rotary-balance experiments were conducted. Results of the static experiments are reported in this volume (1) and rotary-balance results are in Volume 2. Techniques included jet and slot blowing, rotatable miniaturized tip strakes and a unique tip-mounted vertical strake (rhino horn). Forces and moments and surface static pressures at three fuselage stations were measured. Dynamic pressure transducers were used to measure time-delay responses of the surface pressures on the fuselage, LEX and wing with initiation and decay of jet and slot blowing on the forebody. Angles of attack ranged from 0 to 60° with zero and 10° sideslip. Reynolds numbers ranged from 0.387 to 0.636 x 10^6 based on wing mean aerodynamic chord. Comparisons are made to other F/A-18 sub-scale and full-scale wind tunnel and flight measurements. In general, all of the FVC techniques are effective above 30° AOA. Jet blowing with nozzles in the straight aft direction was not effective, but canting the nozzles inboard up to 60° provided significant yawing moments with little interaction on either rolling or pitching moments. The best jet configuration is located at fuselage station 82.2 (full-scale in inches) and 150° azimuth from windward meridian with a 60° inboard cant angle. Blowing with a jet on the right side produces a positive yawing moment and vice-versa. Momentum blowing coefficients of 0.002 provide yawing moments in excess of that provided by fully deflected rudders at zero angle of attack. Effectiveness was not significantly diminished by sideslip up to 10° and was relatively invariant with Reynolds number. Slot blowing with the direction of the slot jet tangential to the surface of the forebody and blowing towards the leeward side was most effective with the slot at the maximum half-breadth of the forebody starting at F.S. 69.8 and ending at F.S. 85.8. Blowing at very low rates produces a yawing moment opposite in direction to the blowing slot (right slot blowing produces a negative yawing moment), but at higher rates, the behavior is very similar to jet nozzles with right side blowing producing positive yawing moments. Time lag measurements revealed that the response of the airframe flow field to initiation of either jet or slot blowing on the forebody is about three convective time units, i.e., the time required for the free stream air to travel three lengths of the fuselage. Both single and dual rotatable tip strakes were evaluated. Both provide levels of yawing moment comparable to blowing and are effective at zero and 10° sideslip. The pivotable vertical tip strake also is effective at zero and 10° sideslip and provides yaw control power comparable to the rotatable strakes. Pressure distributions measured on the forebody and LEX showed clearly the effects of the various FVC techniques on the model surface and correlated well with the measured forces and moments. Comparisons of baseline F/A-18 (without FVC) pressure data with other sub-scale and full-scale wind tunnel and flight data showed that the forebody pressures at F.S. 142 were very similar despite large differences in Reynolds numbers. The most notable differences at the lower Reynolds numbers is earlier separation on the sides of the forebody and a lack of a distinct suction peak produced by the primary vortex on the leeward side of the forebody. The suction peaks on the sides of the forebodies prior to separation were nearly identical for all experiments. Comparison of FVC results to full-scale wind tunnel data was limited to one example with blowing slots at 50° AOA. The yawing moment level for comparable blowing levels (mass flow ratio) was significantly higher for full-scale.

1.0 INTRODUCTION

In order to provide for increased agility of existing and future fighter aircraft at high angles of attack, including the ability to roll robustly about the velocity vector, advanced aerodynamic control techniques are the focus of research in government laboratories as well as in industry. One of the techniques that is receiving significant attention and research resources is the technology of forebody vortex control.

The principal reason for the high interest in forebody vortex control technology is that it offers a realistic potential solution to high-angle-of-attack aerodynamic control deficiencies in the region where the vertical tail and conventional rudder become relatively ineffective. Unfortunately, this ineffectiveness often occurs in the angle of attack range for maximum lift and in the post stall regime where it is desirable to perform velocity vector rolls. An illustration of this degradation and the potential advantage of forebody vortex control is shown in Fig. 1. Without rudder power, other means are needed to impart the required yawing moment and coordinated rolling moment to produce a robust roll about the velocity vector. One means is with thrust vectoring, but it is expensive, heavy and, obviously, depends on having adequate engine thrust available.

An alternative, or perhaps complementary method, is through the controlled manipulation of the forebody vortices, either by some mechanical system which activates a strake or surface on the forebody, or by pneumatic means where the vortices are influenced by blowing with jets or slots on the forebody surface at the appropriate location. Control of the vortices provides the means for controlling the local side force on the forebody and the resulting yawing (and sometimes rolling) moments of the entire airframe.

The technology of forebody vortex control (FVC) was originated in the late 1970's and early 1980's and has been actively pursued by many researchers since, as evidenced by the examples of published work in Refs. 1 - 32. References 1 and 2 provide a summary of the technology from its inception until 1991. References 3-31 show the many and varied research investigations that have aggressively advanced our knowledge of this technical area. Reference 32 is an updated review of most of the published FVC research results from 1991 to early 1993. There are many research programs still in progress, with some focused on demonstrating the utility of forebody vortex control for specific aircraft, such as this report which documents forebody vortex control research performed on an F/A-18 model.

Experiments have been conducted under an SBIR Phase II contract with NASA Ames Research Center to evaluate several forebody vortex control techniques, including mechanical and pneumatic, for the F/A-18 fighter configuration. The experiments consisted of both static and rotary-balance tests in the Ames 7 x 10-ft low speed wind tunnel. The results of the static and rotary-balance experiments are reviewed individually in Volumes 1 and 2, respectively. Each of the two volumes stands alone, with some of the same introductory and background material provided in both volumes. Where required, reference is made from one volume to the other.

In addition to the present experiments focused specifically on F/A-18 forebody vortex control, there have also been numerous other experiments on the baseline F/A-18 that are very useful for comparison to the baseline configuration data of the present experiments. A very thorough data base has been documented in Ref. 33 by Erickson et al with a 6%-scale model. These experiments acquired forces and moments, surface pressures, and extensive flow visualization. Reference 34 by Banks also investigates the baseline F/A-18 with a 16%-scale model with heavy emphasis on surface oil flow studies.

The full-scale wind tunnel results reported in Refs. 8 and 18 show baseline F/A-18 data as well as forebody vortex control data. There are also flight data (Refs. 35-37) obtained at NASA Ames-Dryden Flight Research Facility on an F/A-18 (HARV) documenting surface and off-surface flow visualization and surface pressures. Some of these data are used in Volume 1 to compare to the static data from the present tests. Comparisons are also made to previous baseline F/A-18 rotary-balance data reported in Ref. 38, which were obtained in the NASA Langley Spin Tunnel.

1.1 FOREBODY VORTEX CONTROL TECHNIQUES

1.1.1 Pneumatic - Blowing Jets and Slots

The pneumatic techniques that have been investigated in the references and in the Phase I studies for the F/A-18 consist mostly of blowing jets that are tangential to the forebody surface or slots that are located near the forebody maximum half-breadth and blow tangential to the surface towards the leeward side. Both techniques are designed to alter the forebody vortices by controlling the behavior of flow separation and the strength of the vortices.

Early experiments investigated blowing circular jets that were either pointed straight aft or straight forward (Refs. 4-7, 9-11). Later experiments, specifically those conducted on the X-29A configuration (Refs. 12 and 13), discovered that canting the jets inboard up to 60° from the centerline of the forebody and slotting the jets provided a significantly higher forebody side force and yawing moment for the same blowing rate. With this background of experimental data, the present experiments included the investigation of forebody jets at several longitudinal and radial locations and with many different cant angles.

Blowing slots with the flow directed tangential to the forebody surface towards the leeward side were also included in the present tests. The slots were located at the same radial locations as for previous full-scale F/A-18 experiments in the Ames 80 x120-ft wind tunnel. The length of the slot was varied to determine the minimum length required to achieve the goals for producing yawing moments at high AOA.

A detailed description of the placement of jets and slots on the model for the present tests is presented later in the discussion of the model.

1.1.2 Mechanical - Rotatable Tip Strakes, Vertical Nose Strake

The alternative to pneumatic systems is to influence the vortices by physically altering the surface of the forebody with a movable strake of some type. An extensive data base exists for deflectable or retractable strakes on generic configurations (Refs. 3-7). A major research effort has been underway at NASA-Langley for several years and, most recently, full-scale wind tunnel tests were conducted in the Ames 80 x 120-ft wind tunnel to investigate large hinged conformal strakes on the F/A-18 forebody. A brief review of this work is discussed in Ref. 8.

The mechanical concept that has been the focus of the work in both the Phase I water tunnel tests and the present wind tunnel tests for the F/A-18 utilizes miniaturized strakes that are fixed at the tip and are rotated around the forebody longitudinal axis. The incentive for the rotating tip strakes is to reduce the size of the physical surfaces required to influence the vortices sufficiently that strakes could realistically be considered for practical application in a production aircraft. The rotatable miniaturized strakes are described briefly in the review of the Phase I water tunnel experiments and in more detail in the discussion of the present wind tunnel tests.

The pivotable vertical nose strake is a small single strake mounted on the leeward meridian line of the forebody near the forebody tip that pivots about an axis perpendicular to the surface of the forebody, similar to a highly-miniaturized all-movable vertical tail or rudder mounted on the nose tip. This is an alternative means of manipulating the vortices with a very small surface without having to rotate the model tip, but instead rotate (pivot) only the strake.

2.0 OBJECTIVES OF EXPERIMENTS

The objective of the work reviewed in the two volumes of this report was to investigate a variety of FVC techniques in the NASA-Ames 7 x 10-ft wind tunnel specifically for the F/A-18, including mechanical devices and pneumatic schemes. The preceding Phase I studies were conducted in the Eidetics International Flow Visualization Water Tunnel and are reviewed in detail in Refs. 17, 21, and 29. Results from the water tunnel tests included both flow visualization and simultaneously measured yawing moments in response to the various techniques for manipulating the forebody vortices.

Blowing was investigated with 1) nozzles that were tangential to the forebody leeside surface, blowing aft and forward at various longitudinal and circumferential locations on the forebody and 2) longitudinal slots that were located near the maximum half-breadth of the forebody at various locations and with various lengths with the blowing sheet directed towards the leeside, creating a "Coanda" effect to enhance flow attachment. In addition, miniature forebody tip strakes, single and dual, that could be rotated to various radial angles around the longitudinal axis of the model were also investigated. The principle of the strakes was based on the well-known phenomena that the forebody vortices and resulting forebody surface pressure distribution is highly sensitive to minute geometry changes near the tip of slender forebodies at medium to high angles of attack. The tip strakes are designed to take advantage of this sensitivity in a controlled manner.

Figure 2 shows a sketch of the F/A-18 forebody model representing some of the techniques explored in the water tunnel. The model, consisting of only the front portion, was 6% scale and the jets and slots were placed in the model as shown. The nose tip strakes were mounted on a rotatable tip section and could be remotely rotated by hand during the water tunnel tests. The pivotal strake (the rhino-horn) was pivoted manually and set to different angles.

An example of the effect of manipulating the forebody vortices is shown in Fig. 3, where the orientation of the left and right vortices changes with blowing from a slot on either side of the forebody. This forced asymmetry creates a local forebody side force producing a substantial yawing moment.

All methods, pneumatic and mechanical, were found to be effective in generating controlled asymmetric vortices on the forebody and significant resulting yawing moments. All of the methods influence the forebody flow field, the vortices and resulting moments by controlling flow separation on the surface of the forebody and vortex strength. Controlling separation results in controlling the strength and location of the resulting vortices. Maximizing the effectiveness of any of these methods will require an optimization study to select the proper location and to understand the dependency of the forebody forces on such parameters as blowing rate and direction and, for rotating tip strakes, the proper size, location, and configuration, i.e., single or dual, including spacing.

The results of the Phase I work showed clearly the potential merit of several techniques, and the Phase II work was proposed to investigate these techniques further with wind tunnel tests. The proposed wind tunnel tests were divided into two specific investigations. The first was to perform static tests, and the second was to perform rotary-balance tests to evaluate the effectiveness in the presence of a velocity-vector roll motion, which is primarily what FVC will be used for in real flight. The static experiments were performed in the NASA Ames 7 x 10-ft wind tunnel in the fall of 1992, and were followed by rotary-balance tests in late 1992 and early 1993. The results of the static tests are reported in Volume 1 and the rotary-balance results are presented in Volume 2.

3.0 STATIC WIND TUNNEL EXPERIMENTS

The focus of the static wind tunnel experiments was to investigate, within practical time limits, as many forebody vortex control techniques as possible based in part on the Phase I water tunnel tests and in part on the success of wind tunnel experiments on other configurations. There was also an additional objective to acquire sufficient data to compare with results from full-scale experiments on an F/A-18 model in the Ames 80 x 120-ft wind tunnel, some of which are reported in Refs. 8 and 18. Following the presentation of the results from the present experiments, some comparisons are made with the full-scale results and an evaluation of the Reynolds number effects. The specifics of the experiments in the Ames 7 x 10-ft tunnel are now reviewed.

4.0 MODEL AND MODEL INSTRUMENTATION

4.1 MODEL DESIGN AND CONSTRUCTION

The model for these experiments is a new 6%-scale model designed and built by Eidetics International. The model exterior lines were determined by borrowing the Navy/McAir 6%-scale force and moment steel model to make a pattern and permanent mold. From this mold, a fiberglass shell with an accurate external shape was fabricated. The forebody part of the mold was then also used to make several forebody (nose portion only) model pieces.

The model structural design was required to accommodate the loads of both the static test and the rotary-balance tests. The fiberglass shell of the model attaches to a structure that consists of base plates, six aluminum bulkheads and stringers. The structural center of the model is a stainless steel balance block with mounting tabs for the wing and the base plates. The wings have a steel core to carry the aerodynamic loads, and the airfoil shape is built up with wood and fiberglass around the structural center. The leading and trailing-edge flaps and ailerons were all deflectable; however, the test was conducted with the leading edge flaps only in the maneuver position (34°) and the trailing-edge flaps undeflected. The ailerons were tested in the plus and minus 10° positions to estimate roll control power. The vertical tails have an aluminum core and rudders that can be deflected plus and minus 30°. The horizontal tails were fixed at 0° for the entire test. Photographs in Fig. 4 show the model structure, components, and the assembled model with and without the top cover.

4.2 REMOVABLE FOREBODIES

The nose section of the model was removable so that different forebody vortex control devices could be studied by replacing the nose section. The baseline configuration was an unmodified nose cone that is identified as the "clean nose." There were five blowing jet positions (Fig. 5a), three of which were at 135° azimuth from the windward meridian, at three fuselage stations (Noses 1, 2, 3). The middle position (x = 0.93 inches model scale) corresponded to the furthest aft fuselage station that was tested in the 1992 test of the F/A-18 in the 80x120 Foot Wind Tunnel at NASA Ames (Refs. 8 and 18). The furthest aft position (x = 1.30 inches) corresponds to 0.5 equivalent nose diameters aft of the nose tip. At this fuselage station, in addition to the jet at 135°, there were jets at 150° and 120° (Noses 4 and 5). All of the nozzles, except the furthest forward, had the ability to rotate to any desired angle in order to try to duplicate the success of Guyton (see Ref. 12).

In addition to the jet blowing noses, there was a slot blowing nose. The slotted nose was a challenge to build at this scale. The slot width was held to a reasonably constant width with small metal shims between each of the four segments (A,B,C and D) (Fig. 5b). Unlike the full scale aircraft, size constraints made it impossible to have separate supply pressure lines to each slot segment. Instead, the interior of the nose was made into two plenums, one for the left side and one for the right, that supplied all of the segments. The slot size tested was 0.006 inches wide with a length of 2.58 inches beginning 0.56 inches from the nose tip. This was the slot configuration that showed the highest effectiveness in the 1992 test of the F/A-18 in the 80x120 Foot Wind Tunnel at NASA Ames (Refs. 8 and 18). Different slot lengths were tested by taping over portions of the slot.

In addition to the pneumatic control systems, several mechanical, miniaturized strake configurations were tested. The first type of control scheme was the rotating nose tip strake. The strakes were implemented as a single strake or as dual strakes (fixed-pair rotating together) on the very front of the nose cone, as shown in Fig. 5c. Two strake sizes were tested; the one depicted in Fig. 5c is the small strake and the one referred to as large strake in section 7.4.1.1 has the same length but twice the width. The strakes rotate about the axis of the radome, driven by a 12 Volt electric motor turning at 1 rpm. The position of the strakes is measured by a potentiometer geared to the motor shaft.

An additional nose piece with a miniature vertical nose strake is shown in Fig. 5d. Although similar in shape to the rotating nose tip strakes, the vertical nose tip strake is mounted on the leeward meridian line of the forebody and pivots about an axis perpendicular to the surface of forebody.

4.3 MODEL INSTRUMENTATION

The detailed design of the model was significantly influenced by the placement of instrumentation and sensors. The model has a very high density of instrumentation, including a multi-port electronic scanning pressure module, pressure ports and tubing, unsteady pressure transducers, pneumatic control valves, plenum pressure transducers and thermocouples, dc motor and potentiometer for the rotating tip strakes, etc. in addition to the basic 6-component force and moment balance (Fig. 6a). The model volume is quite small, and the challenge of placing all of the planned instrumentation in the model was significant.

The aerodynamic forces acting on the model were measured using a 1.5 inch Task Mark IIE six component internal strain gage balance. These force measurements were used to calculate the standard body and stability axis coefficients.

A System 8400 (by Pressure Systems, Inc.) electronically scanned pressure acquisition system was used to control a 64 port (ESP-64) module in the model. The model was designed for a 48 port module, but the 64 port was the only one available and the additional size did not cause any problems. Figure 6b shows the location of the 48 static pressure taps on the model. The three fuselage stations (F.S. 142, 253, and 357 full scale) that were used corresponded to locations used for the 80X120 test and the F/A-18 HARV experiments.

In addition to the static pressure measurements, time-dependent pressure measurements were made as well. It was desired to measure the time lag from the initiation of a forebody vortex control device to the time when a new steady state flow field, and hence a yawing moment, was established. In order to eliminate the pneumatic lag time associated with the tube length to normal pressure transducers, Endevco surface mounted dynamic pressure sensors were installed on the model as shown in Fig. 6c.

The pneumatic forebody vortex control system consisted of a pair (right and left) of two-position valves to turn the flow on and off remotely, and a pair of large diameter plenums with a total pressure probe and transducer, and a thermocouple. These measurements were used to determine the isentropic flow conditions at the jet or slot exit. Based on previous experience at NASA, a flow calibration was performed on both the jet and slot configurations. Using a highly accurate (0.1 gram) Toledo scale and a regulated air supply tank, the true mass change was used to calibrate both an Omega volumetric flow meter and the model's plenum (which used isentropic assumptions). The flow meter was found to be in good agreement (3 percent) with the measured change in mass, but the isentropic equations for the plenum required significant correction in the form of a "discharge coefficient" (on the order of 0.70). The correlation between the plenum pressures, blowing momentum coefficient C_μ and blowing mass flow ratio MFR are shown for the blowing jets and slots in Table 1 at the end of the text. Operation of the mechanical systems required replacing the pneumatic control components in the forward fuselage section with the strake drive motor and potentiometer.

5.0 EXPERIMENTAL SETUP

5.1 WIND TUNNEL DESCRIPTION

The Ames 7 x 10-ft wind tunnel is a closed-throat, single return atmospheric tunnel with about 10% air exchange accomplished by a ventilating tower. The tunnel is powered by a single 8-blade, 8.5m (28 ft) diameter fan driven by a 1600 HP synchronous motor located in the nacelle in the return passage.

5.2 MODEL SUPPORT SYSTEM AND INSTALLATION

The model was sting mounted on a dog-leg and turntable system as shown in Fig. 7. The model was mounted on the sting at a 90° roll angle (wings vertical) and the model was pitched in the horizontal direction with the floor mounted turntable. Sideslip angles were introduced by inserting angled wedges between the sting base and the vertical strut.

5.3 TEST CONDITIONS

The test was run at a dynamic pressure of 27 psf (approximately 150 ft/sec) and a Reynolds number of 0.92×10^6 per foot. A few runs were made at dynamic pressures of 10 psf ($V=90$ ft/sec and $R_N=0.56 \times 10^6$ per foot) and 20 psf ($V=131$ ft/sec and $R_N=0.8 \times 10^6$ per foot) to explore Reynolds number differences. The angle of attack was varied from 0° to 60°, and the sideslip angle at 0° or -10°.

6.0 DATA ACQUISITION AND REDUCTION SYSTEM

The data acquisition and reduction for this phase of the test was provided by NASA Ames. The Standard Wind Tunnel Balance Program (SWTS) was used for everything except the acquisition and reduction of the pressure tap data. The pressure data were collected by a Pressure Systems 8400 and then passed to SWTS.

7.0 RESULTS AND DISCUSSION

The data presented in this report and primarily in the form of the longitudinal and lateral-directional force and moment coefficients (six in all) plotted against angle of attack. In addition to force and moment coefficients, selected pressure data will be presented and discussed. Most of the data are at a Reynolds number of 0.636 based on wing mean aerodynamic chord with a few examples at Rn = 0.553 and 0.387 x 10^6. Unless otherwise noted, the data presented is at Rn = 0.636 x 10^6. Time lag effects are discussed as well as comparisons to other sub-scale and full-scale wind tunnel and flight data.

7.1 BASELINE CONFIGURATION

The baseline configuration consisted of the complete aircraft with all control surfaces set to zero except the leading edge flap which was tested in the maneuver position of δ_f = -34° (leading edge down). Because there was not a mechanism for accurately scaling the mass flow through the inlet at all conditions, a fairing was used to provide a smoother flow field around the inlet than if it were left partially blocked with a large spillage wake. The missile racks were in place on the wing tips, but no missiles were modeled.

7.1.1 Force and Moment Coefficients

The pressure supply line that delivered the air for the pneumatic control systems was a pliable plastic (Tygon) tube that caused very little interference crossing the metric boundary when it was not pressurized. Figure 8 shows the effect of pressurizing the blowing tube to the maximum available supply pressure (~125 psia). The only effect from the stiffened lines appears to be a 0.02 change in axial force in the negative direction (pushing the model forward as expected). Figure 9 shows that fairing the inlets causes a decrease in drag and a slight decrease in nose down pitching moment due to the decrease in drag at the inlets. The lateral-directional components are essentially unchanged due to the fairing. Although SWTS is unable to take out flow angularity in its' calculations, an "inverted" run was conducted and is shown compared to upright in Fig. 10. The side force and rolling moment coefficients look as though the upright case is really at a negative sideslip or possibly a roll angle. An adjustment to fix this was not available.

Figure 11 shows a comparison of data from Ref. 38 documenting a 1/10 scale F-18 configuration in the Langley Spin Tunnel and the current test at NASA Ames. Because the Spin Tunnel uses a top entry mount, the interference effects for this model are quite different. This is most evident in the axial direction where the correlation is rather poor. Comparison of the data for the other axes all look reasonably good.

The rudder control effectiveness was documented as a function of angle of attack and is shown in Fig. 12. With the rudder deflected 30° the yawing moment coefficient is a constant 0.035 up to α = 20°. Between 20° and 60° AOA the effectiveness falls off nearly linearly to zero with angle of attack as the vertical tails become hidden in the separated wake of the wing. Because the F/A-18's vertical tails are canted outboard, there is also an effect in rolling moment. The aileron effectiveness for a ±10° deflection is shown in Fig. 13. The rolling moment coefficient generated by the ailerons is about 0.02 at low angles of attack but falls off slightly above 20° AOA. There is still a ΔC_l = 0.01 at 60° AOA.

The effect of sideslip on the baseline, clean nose, configuration was never tested. However, Fig. 14 shows the effect of sideslip on Nose 4 with the jets canted inboard 60° and compares that to the clean nose baseline. The difference between the non-yawed runs is apparent at high angles of attack. The tubes that extend from the nose for the canted jet nozzles act like very small strakes and cause a difference in the shed vortex wake which affects the lateral-directional forces and moments. Comparing the differences between the β = 0° and β = -10° data shows that $C_{n\beta}$ is stable (positive) below 30° AOA and becomes unstable above that. Data available from Ref. 38, shown in Fig. 15, show the same type of trend occurring at a little over 20° AOA. Likewise, $C_{Y\beta}$ and $C_{l\beta}$ agree fairly well with the data in Ref. 38, and are both stable at all angles of attack.

The effect of Reynolds number was investigated within the stress level limits of the model. For this study, dynamic pressures of 27, 20, and 10 psf were used. This corresponded to Reynolds numbers of 0.92 x 10^6, 0.80 x 10^6 and 0.56 x 10^6 per foot or 0.636 x 10^6, 0.553 x 10^6 and 0.387 x 10^6 based on wing mean aerodynamic chord. Figure 16 shows that there are only small differences due to Reynolds number. It should be noted that the lack of repeatability at 55° AOA was due to buffeting that caused the model to bounce in the plane of it's gravity vector. The repeatability could probably have been improved by averaging the data over an extended time period, but this was not done.

7.1.2 Pressure Distributions

Pressure distributions were obtained on the forebody and LEX at the fuselage stations shown in Fig. 6. These stations were chosen to match some of the locations of pressure taps in the full-scale F/A-18 model tested in the Ames 80 x 120-Ft Wind Tunnel (Fig. 17 and Refs. 8 and 18) and in the flight test F/A-18 HARV. The baseline forebody and LEX pressures are shown in Fig. 18 for angles of attack from 30° to 60°. The forebody pressures (at F.S. 142) are seen to be very symmetric about the geometric plane of symmetry throughout the angle of attack range, which is consistent with the side force and yawing moment measurements that show nearly zero values for the same angle of attack range. The forebody cross section at this fuselage station is slightly elliptic with the major axis in the vertical direction. The peak suction at all angles of attack is in the vicinity of a radial angle of 70° to 80° from the windward stagnation line. The Reynolds number based on the width of the forebody cross section at this point (2.1 inches at 6% scale) is 0.161 x 10^6 which means that the flow is most likely laminar in character. There is no surface grit to artificially trip the boundary layer. The pressure distributions indicate that the location for primary separation is near a radial angle of approximately 120° to 130°. There is no evidence of a strong suction peak on the leeward side due to the primary vortex flow reattachment, as is often seen in flows at higher Reynolds numbers.

Pressure distributions on the LEX (F.S. 253 and 357) are also shown in Fig. 18. One of the pressure ports at F.S. 253 failed during the test, so for convenience in plotting, this point is duplicated from the same port on the opposite LEX, assuming the flow is symmetric. Thus, dashed lines are shown connecting to that point. The assumption of symmetric flow is well supported as can be seen by the plots for the forebody and the rearward fuselage station for the LEX. At F.S. 253, the maximum suction from the LEX vortices occurs at an angle of attack between 40° and 45°. The suction decreases substantially at 55° and 60°, reflecting the fact that the LEX vortices have burst ahead of that fuselage station.

The magnitude of the suction at F.S. 357 is significantly less than further forward, as expected. The maximum suction is at an angle of attack of 30°. This is consistent with the known behavior of the LEX vortex burst location moving forward with angle of attack. The burst location has already moved slightly forward of this fuselage station at an angle of attack between 30° and 35°. In fact, results from flow visualization studies for sub-scale and full-scale F/A-18 configurations in Fig. 19 (Ref. 33) show that the LEX burst location is at F.S. 253 at an angle of attack of 42° and at F.S. 357 at an angle of attack of 32°.

7.2 JET BLOWING

7.2.1 Force and Moment Coefficients

The addition of small jet nozzles to the forebody produce a change in the lateral directional characteristics of the F/A-18 primarily at angles of attack above 40° because the nozzles act like small strakes. Figure 20 shows the effect of nozzles, with no blowing, pointed straight aft at the various fuselage stations and azimuth angles (Noses 1-5). It is interesting to note that Nose 2, the nose that matches the Ames Full-Scale Test jet location, is the only one that is significantly different from other "nozzle on" configurations. Nose 2 may have a jet location that is just in front of the local separation region and is therefore able to influence the local flow. Figure 21 shows the effect of nozzles, with no blowing, at different inboard cant angles on Nose 4. Changing the cant angle seems to have a small influence on rolling moment that was not seen with the straight aft nozzles.

7.2.1.1 Jet Blowing Straight Aft

The influence of blowing rate coefficient (C_μ) was tested with the nozzles facing straight aft at all of the fuselage stations. Figure 22 shows the furthest forward nozzle position, Nose 1. The change of yawing moment with blowing rate is not very large ($\Delta C_n < 0.02$), and in fact a yawing moment is produced in the direction away from the side with the blowing jet (positive moment from left side blowing), and is not much more than the variation in the baseline repeatability at 60° AOA. This is the same direction noted by Lemay (see Ref. 11). This indicates that blowing is causing the flow to separate sooner than it would naturally. This is the same effect that was seen in the full scale test. When blowing was done on the left side, the moment produced was insensitive to blowing rate. Blowing on the right showed some difference with blowing rate, but no well behaved trends.

Noses 2 through 4 (Figs. 23 to 25) show similar trends, with the yawing moment increment tending to be small and in the direction away from the side with the blowing jet. Nose 5 was interesting (Fig. 26) because it showed the opposite sign at angles of attack below about 50°, but above 50° the signs reversed. It appears that at 50° the flow wants to separate at the location of the nozzles. Therefore, at angles less than 50°, blowing disrupts the flow that would normally continue up around the forebody. However, at higher angles, the flow is separating below the nozzle, so blowing helps to create a favorable pressure gradient and the flow stays attached longer.

7.2.1.2 Jet Blowing at 60° Inboard

Angling the jet blowing nozzles inboard has been shown to greatly increase their effectiveness (see Guyton - Ref. 12). Nose 2 (Fig. 27) shows yaw control effect at angles of attack as low as 35°. At this forward fuselage station it is possible to get yawing moments of about 0.03 that sustain to 60° AOA with extremely low blowing coefficients (0.0004). As the blowing rate was increased, the maximum yawing moment (0.04) was obtained at 55° AOA, but at lower angles of attack, the jet was over-blowing and was in fact producing a smaller effect than the lower blowing rate. This is consistent with what was observed with Nose 5 when blowing straight aft.

Nose 3 showed a similar trend of over-blowing on the right side (Fig. 28), but not on the left side and produced increasing increments of yawing moment as the blowing rate was increased (for angles of attack above 40°). At angles less than 40°, there is evidence of a very small amount of over-blowing.

The yawing moment increments from Nose 5 (Fig. 29) were rather insignificant with the nozzles turned inboard. Nose 4 provided the best behaved trends with increase blowing rate. With Nose 4 (Fig. 30), yawing moment coefficients of ±0.05 were observed at 50° AOA. This moment is 40% larger than that provided by maximum rudder deflection at zero angle of attack. A more detailed study of blowing rate was conducted and is shown for the left nozzle in Fig. 31. Here it is apparent that, with this jet configuration, blowing harder than $C\mu = 0.0015$ can provide increased yaw power only at angles of attack above 55° and can cause over-blowing at angles below 50°.

It should be noted that while these jet configurations did provide sizable yawing moments, there were also substantial nose-down pitching moments associated with them ($\Delta Cm \approx 0.2$). If these two moments can be decoupled, there may be an opportunity to enhance high angle of attack pitch agility as well as yaw control.

7.2.1.3 Jet Blowing at Variable Angles

The optimum jet blowing configuration that was tested was Nose 4 with the nozzles canted inboard 60°. However, several other cant angles were examined and are shown in Fig. 32 for a constant $C\mu$ of 0.0023. Both 30° and 60° cant angles were much better than straight aft blowing. The 45° cant angle looked well behaved on the left side but showed a strange reversal on the right side at angles of attack below 50°. Studies currently underway at Eidetics on an F-16 model indicated that even larger cant angles (>60°) may produce larger control power increments. To follow up on this, additional static runs were conducted during the rotary balance test and are presented in Fig. 33 for a constant 51° AOA. The x-axis for these plots is $C\mu$, the blowing rate coefficient.

It is evident, when looking at the yawing moment plot, that the angle of the nozzle has a dramatic influence not only on the jet's effectiveness, but on it's entire character. The trend with higher blowing rate for 60° cant angle is for increasing effectiveness up to a plateau. The 90° cant angle is similar to the 60° case up to a $C\mu$ of 0.001 and then it becomes less effective with higher blowing rates. The 120° cant angle case is quite different. The yawing moment starts out with the same sign as the others (blowing on left gives negative yawing moment), but quickly changes direction and reaches a plateau of about 0.04 of the opposite sign. When the nozzle is rotated to 150°, the yawing moment starts with the opposite sign (blowing on left gives positive yawing moment), and then, in a manner similar to the 120° case, changes sign at a $C\mu$ of 0.0015 and reaches a maximum Cn of 0.04 (blowing on left gives negative yawing moment).

Figure 34 is included for completeness and shows Nose 2 with a jet cant angle of 30°. It is able to generate a good sized yawing moment (0.04) only at high angles and only with right side blowing (the left side was ineffective).

7.2.1.4 Jet Blowing at Sideslip

Due to time constraints, only one jet blowing configuration was tested in sideslip and at various Reynolds numbers. Nose 4 with the nozzles canted inboard 60° was judged to be the best jet blowing configuration because of both the high level of yawing moment it produced and its' behavior with increasing blowing rate coefficient. It was therefore the configuration used for the additional runs. Figure 35 shows the effect of -10° of sideslip on blowing effectiveness. In this orientation, the windward (left) side is able to produce very large yawing moments beginning at an angle of attack of 35°. On the leeward (right) side, the jets are not very effective until an AOA of about 50°. Even at sideslip, the jets are able to produce yawing moment coefficient increments up to 0.05 in either direction.

7.2.1.5 Jet Blowing at Different Reynolds Numbers

Figure 36 shows jet blowing on the left side for a Reynolds number of 0.8×10^6 per foot or 0.553×10^6 based on c (q = 20 psf). Likewise, Fig. 37 shows a Reynolds number of 0.56×10^6 per foot or 0.387×10^6 based on c (q = 10 psf). It is apparent that the jets still provide large yawing moments (>0.04) for low blowing rate coefficients. There has been some debate on which parameter should be used to non-dimensionalize the blowing rate so that the yawing moment coefficient will best correlate across various Mach numbers, Reynolds numbers and model scales. Figure 38 shows cross plots of ΔC_n verses $C\mu$, Mass Flow Ratio (MFR), and velocity ratio. Table 1, following the text, shows the correlation between C_μ and MFR at q = 27 psf. The idea is that if one of these parameters does a perfect job of correlating across the three Reynolds numbers, then the curves will collapse into a single curve. For the blowing jets, it appears that $C\mu$ does a good job of collapsing almost all of the points to a single curve. Mass Flow Ratio also does a good job with most of the data, except the highest blowing rates for the case at q = 27 psf. The velocity ratio does not do a good job of correlating the yawing moment when the jet becomes choked, because, by definition, the velocity will not change above that point.

7.2.2 Pressure Distributions

In addition to measuring pressures on the baseline configuration without active vortex control, pressure data were also obtained during the various vortex control investigations. The response of the surface pressures to blowing jets are documented in the next few data figures. First, in order to assess the effects of the protruding jets for Nose 4 (with the jets at 60° inboard as discussed in the previous section) on the flow field without blowing, an angle of attack sweep was run and the data were compared to the results with the baseline (clean) forebody. The pressure distributions for the forebody with the jets in place are shown in Fig. 39 for 30° to 60° AOA. The results, when compared to the results from the baseline forebody in Fig. 18, show that the effect of jet nozzles on the pressure distributions is very small. The location of the first row of pressure taps (F.S. 142) is far aft enough of the nozzles that there is no apparent influence on the flow field. These plotted curves represent the new "baseline" data for the investigations with jet blowing.

The effects of jet blowing were seen earlier to produce significant forebody side forces and yawing moments in the direction of the side where the jet is located. Figure 40 shows the pressure distribution for 50° AOA and Fig. 41 for 60° AOA at the three fuselage stations noted. The most pronounced effect can be seen on the forebody at F.S. 142, as expected. The effect of the blowing is to increase the level of the suction on the blowing side compared to that on the opposite side. Reversing the side for blowing at the same mass flow rate provides a mirror image response and reverses the pressure distribution. As a reminder, there is a missing pressure tap on the right side of the LEX at F.S. 253 (y/s' of 0.4). For the non blowing case, the pressure data point from the left side has been artificially repeated in order to connect the pressure data for a clearer representation of the overall pressure distribution. For the non blowing case this is a very reasonable approximation.

For the blowing case, left and right side blowing could be expected to produce approximately equal but opposite effects, as seen on the forebody. In order to help the reader to see more clearly the pattern at F.S. 253, the authors have taken some liberty and plotted a phantom data point (equal and opposite to that from the left side) for the missing pressure port on the right side connected with a dashed line through the measured data. The asymmetry due to blowing can be seen in the forward LEX flow at 50° AOA as well as on the forebody, but it is more subtle. For the LEX station of 253 at 60° AOA, blowing on either side produces a positive pressure increment on both right and left side LEX's. It appears that blowing on the right side has a much larger effect on the left side LEX vortex than on the right side vortex. Blowing on the left side has almost no effect on the left LEX pressure distribution. The aft LEX location has a slight asymmetry, but it is not particularly significant.

7.2.3 Time Lag Effects - Jet Blowing

An investigation was made to determine whether there is a significant time delay from activation of jet blowing to the time when the aircraft experiences a "fully transitioned" change in the yawing moment. The time lag is important not only for the onset of blowing control, but also for the decay time after the jet is turned off. The time lag was measured by looking at the pressure field response on the surface of the model with Endevco dynamic pressure sensors. The location of these transducers are shown in Fig. 6. In addition, the Task balance outputs were recorded in raw counts, but not reduced to forces or coefficients. As a reference point, the time that it takes the flow to traverse the length of the fuselage (convective time) is 22 msec.

Figure 42 shows the jet blowing onset at 50° AOA and a dynamic pressure of 27 psf. When the solenoid valve opens (at 0.065 sec), there is a finite period of time required for the plenum pressure to establish (~45 msec). At about 0.090 sec, Endevco #1 begins to respond. Because of the proximity of Endevco #1 on the forebody to the blowing jet, it is apparent that there is a pneumatic lag from not only the plenum filling but also the tubing length from the plenum to the jet exit. By 0.140 sec, Endevco #1 indicates that the flow is fully established at this point on the body. The other Endevcos shown, as well as those not shown, do not sense any change in the flow field caused by the blowing. This is in agreement with the static pressure data discussed above which also saw most of the effect only on the forebody. Perhaps more conclusive evidence of the time lag period is seen by examining the balance output. Here it is clear that by 0.130 sec the new steady state yawing moment has been established. Therefore, a conservative estimate of the time lag for the onset of control (including large pneumatic lags) would be 65 msec. If the pneumatic lags were removed, the time lag would be on the order of 40 msec or about 2 convective time units. Figure 43 shows similar results at 40° AOA.

Figure 44 shows time lag associated with the decay of jet blowing at 50° AOA and a dynamic pressure of 27 psf. It took 30 msec for the plenum pressure to bleed down to the static pressure. If it were physically possible, it would be desirable to have the shut off valve right at the nozzle exit to eliminate this lag. Even if this lag is included in the total time, the overall lag is only about 80 msec (from 0.500 to 0.580). If the pneumatic lag were eliminated, the control lag would be on the order of 60 msec (3 convective time units). Likewise, Fig. 45 shows similar results at 40° AOA.

7.3 SLOT BLOWING

7.3.1 Force and Moment Coefficients

The slot configuration with all four segments blowing (A,B,C and D) was the most effective in the full scale wind tunnel test (see Refs. 8 and 18). However, it was apparent that for the six percent scale model, the nose plenum was not able to provide uniform flow to each slot segment when all four were open. Because the slot works by entraining the forebody flow and causing it to remain attached for an increased distance around the forebody, it is expected that non-uniform blowing will not create as large a yawing moment increment. With all four segments open, segment C, and to some extent segment A, had less flow than segments B and D. The flow was much more uniform when only two or three segments were used. After the rotary test was completed, an attempt was made to survey the flow from the slot with different blowing rates.

In general, this investigation revealed that the flow did not exit the slot perpendicularly, but instead the velocity vector was inclined forward. The flow appeared to travel upward and not in an outboard direction even at low blowing rates. An analogy to the forward flow from the slots can be drawn to the jet blowing cases at an inboard cant angle of 120° and 150° (both with a large forward component and well as inboard). In the case of the slots, the Coanda effect provides the inboard component, and the nose plenum apparently provides a forward component. As will be discussed below, both of these different blowing schemes cause a yawing moment response that begins with a moment away from the side of the forebody with blowing, and then, with increasing $C\mu$, crosses over so that left side blowing causes a negative yawing moment.

7.3.1.1 Slot Blowing with Four Segments

Figure 46 shows the results of blowing with all four segments. The magnitude of the resulting yawing moment was only 0.01 to 0.02 and at angles of attack above 50° blowing on the right side actually produced a small negative increment in yaw.

7.3.1.2 Slot Blowing with Three Segments

Slot configuration ABC produced much better results than the four segment slot, perhaps due to much more uniform flow. Figure 47 shows that a yawing moment coefficient increment of 0.01 was produced above 30° AOA, and increased to a maximum of 0.05 at 55°.

7.3.1.3 Slot Blowing with Two Segments

The two-slot blowing configuration was examined not only for the effect of length, but also for the effect of the fuselage station where it was initiated. Segment AB was the furthest forward and provide the best comparison with the longer slots because they all begin at the same fuselage station. Figures 48 and 49 show yawing moments for segment AB plotted for various blowing coefficients from 0.0006 to 0.0034. Above 35°, the slot produces more yaw control power than the rudder and reaches a level of 0.05 (which is 40% greater than the rudder at zero degrees AOA). At low blowing rates (0.0006 and 0.0016) the slot produces yawing moments in the direction away from the side of the forebody that is blowing (left blowing creates positive yaw), but as the blowing rate is increased, the forebody boundary layer flow changes from being disturbed to being entrained and the sign changes so that left blowing gives a negative yawing moment as expected.

Segment BC produced well behaved yawing moments (Fig. 50) at angles of attack above 40°, but with a lower magnitude than segment AB for a given blowing coefficient. The trend continued as the slot was moved back to segment CD (Fig. 51) where the increment in yawing moment coefficient was only about 0.02 for a blowing coefficient of 0.0034.

7.3.1.4 Slot Blowing with One Segment

When a single segment of the slot was used, the flow on the right hand slot tended to be pointed forward instead of perpendicular to the slot. This is probably due to the interior shape of the nose plenum. Figure 52 shows the segment A only configuration. Only one blowing rate was tested ($C\mu$ = 0.0017) and both right and left sides produced a negative yawing moment. Segment B only (Fig. 53) behaves in about the same way at a $C\mu$ of 0.0017, but at a lower rate (0.0008), the yawing moment is in the positive direction. Figure 54 shows segment C only, which seems to do nothing on the right side but does provide a 0.03 C_n increment on the left side.

The baselines for the single segment blowing are all rather different. This is probably due to the way that the slot segments were isolated. In order to prevent the tape from being blown off of the closed segments, aluminum tape was used. It appears possible that the thickness of the aluminum tape could have been enough to affect the boundary layer at the nose tip and change the flow characteristics.

7.3.1.5 Slot Blowing at Sideslip

The slot that gave the best observed performance, segment AB, was tested at a sideslip angle of -10°. As Fig. 55 shows, low blowing rates ($C\mu$ = 0.0006) produced reversed yawing moments, but as the blowing rate increased the slots were able to produce large yawing moment increments in either direction. In contrast to the blowing jets case, the slot on the leeward (right) side provided more yaw control at angles of attack of 40° or less than the windward (left) slot.

7.3.1.6 Slot Blowing at Different Tunnel Dynamic Pressures

In the discussion of the blowing jets, it was stated that the blowing coefficient C_μ provided a good correlation of the yawing moment generated by jet blowing at different q conditions (and, consequently, different Reynolds Numbers), and that mass flow ratio MFR was also a good correlation parameter except for the higher values. An assessment of different correlation parameters was also made for the slots. Figure 56 shows the results of three runs at different q conditions where the blowing pressure was chosen for each run to result in the same blowing coefficient. For the runs at q=20 psf and 27 psf, the results are basically the same, indicating a good correlation using C_μ. For the q=10 psf condition, the chosen blowing pressure was in error and the resulting blowing coefficient was too low. This curve is included even though it does not match the others.

To further investigate the correlation of the yawing moments generated at different q conditions, runs were made at three q conditions where the blowing pressures were varied through the available range at each q. (Table 1 following the main text shows a correlation between the plenum blowing pressures, the blowing coefficient C_μ and mass flow ratio MFR at q = 27 psf). Figure 57 shows the results of this correlation study. The best correlation parameter for the slots appears to be MFR. The blowing momentum coefficient C_μ appears to correlate well for the higher q conditions but not for the lower q condition. The ratio of V_{jet}/V is not a good correlation beyond the point where the slots have choked flow since the velocity of the slot jet is constant for all higher pressures. Since the Reynolds number is varied as the tunnel q is varied, it is not known whether the lack of correlation with C_μ and the good correlation with MFR has an inherent Reynolds number effect or not. The only means to sort this out would be to independently change q without changing Reynolds number.

7.3.2 Pressure Distributions

As discussed above, several slot configurations were investigated. The best configuration was SLOT AB. The effects of blowing with this slot configuration are shown in Fig. 58 for 50° AOA and Fig. 59 for 60° AOA for the forebody and two LEX stations with pressure taps. Only the upper surface pressures are shown for the LEX stations. The effects on the pressure distributions for the larger blowing rate (C_μ=0.0035) are very similar to those observed on NOSE 4 jet blowing at C_μ=0.0023 (Fig. 40). For the lower blowing rate (C_μ=0.0007), the response is in the opposite direction, as was shown earlier in the force and moment data. A very low blowing rate on the right results in slightly higher suction on the left rather than the right and a higher suction on the left, which, of course will result in a reversed side force on the forebody. At the higher blowing rate the response to blowing on the right side is significantly increased suction on the right side and decreased suction on the left side. Reversing the blowing side produces a mirror image in the pressure distributions.

The response to forebody slot blowing on the LEX pressure distributions are also shown in Fig. 58. Comparing the response to the jet blowing, it appears that, despite very similar pressure distributions on the forebody for jet and slot blowing, the response at the LEX is somewhat different. For the forward part of the LEX (F.S. 253) it appears that blowing on the left or right sides with slots produces a slightly increased suction on the left LEX. (The response on the right LEX is difficult to discern because of the missing pressure tap.) The aft LEX position (F.S. 357) shows little response to the forebody vortex control. The reasons for the differences on the LEX between jet and slot blowing are not known. It is known from other experiments that there is a very strong coupling between the forebody and LEX vortices and small differences in the forebody vortex pattern can have large effects on the responding LEX vortices.

Perhaps, more to the point for this case at 50° AOA, it is the fact that the LEX vortices are bursting very near the apex of the LEX and the pressure field downstream is going to be determined by a flow field that is subject to all of the variations that occur in the very turbulent flow behind the burst vortex. At 50° AOA, the forebody vortices are well above the fuselage, as well, and there is a lot of space between these vortices and the LEX surface which can lead to a resulting surface pressure distribution that is very sensitive to any non-symmetrical disturbances. The level of the LEX asymmetries is low compared to the forebody asymmetries, which provides some evidence to support the notion that forebody vortex control is primarily a yaw control technique and response in roll to its use is minor.

The variation in the aft LEX pressures is small no matter what blowing scheme is incorporated. This location is quite far aft of the forebody and at 50° AOA there is not much effect to be realized in the forebody/LEX flow interaction.

7.3.3 Time Lag Effects - Slot Blowing

The methodology for the slot blowing time lag measurements was identical to that discussed in section 7.2.3 for jet blowing. The results are also nearly identical. Figures 60 and 61 show the results of the onset of slot blowing for 50° and 40° AOA respectively. In both cases, if the pneumatic lag is retained, the time from when the valve began to open until the flow field has stabilized in it's new orientation is approximately 70 msec (3.5 convective time units).

Figures 62 and 63 examine the decay period after the solenoid valves are closed. Similarly to the blowing jet results, the slots show no significant increase in the time it took for the flow to return to its unperturbed state (~70 msec or 3.5 convective time units).

7.4 ROTATING NOSE-TIP STRAKES

7.4.1 Force and Moment Coefficients

7.4.1.1 Single Strake

Tests were conducted with two strake sizes. The "small" strake is the one shown in Fig. 5c, and the "large" strake has the same length but twice the width. In order to get a preliminary idea of the effectiveness of a single strake to manipulate the forebody vortices, the model was placed at fixed angles of attack and the large strake was rotated through discrete angles up to 360°. Forces, moments and pressures were measured for different strake angles Φ (20° increments), and the yawing moment coefficient at various angles of attack is presented in Fig. 64. The trends with strake angle are similar for the different angles of attack, and in general, the strake becomes more effective as α increases. The rotation of the strake produces a positive yawing moment for Φ's between 0° and 60° and between 180° and 300°. A negative yawing moment is induced between 60° and 180°; between 300° and 360°, a negative yawing moment is produced only at high angles of attack ($\alpha = 55°$ and 60°).

The effect of strake size was evaluated using the same experimental approach, and results are shown in Fig. 65 for the case at 50° angle of attack. The performances of the small and the large strakes are very similar in terms of the magnitude of the yawing moments induced; however, the changes produced by the small strake appear to be better behaved. Data for the small strake show two definite "gradients", i.e. linear changes in yawing moment with strake angle, that could be used for directional control. One gradient is around $\Phi = 0°$ and the other around $\Phi = 180°$. The gradient around $\Phi = 0°$ has a moderate slope, thus the strake has to rotate more than +/- 90° to obtain the maximum control. Moreover, there is a small reversal in the slope between $\Phi = 0°$ and 20°, which might complicate the control system. On the other hand, as clearly seen in Fig. 65, the gradient around $\Phi = 180°$ provides a means to obtain maximum control with minimum strake movement.

The better behavior of the small strake, plus the advantage of having a smaller planform, suggested that additional tests with the small strake should be performed along the $\Phi = 180°$ gradient. Results of angle of attack sweeps for various strake angles are presented in Fig. 66. The rotation of the strake produces negligible changes in normal and axial force and very small changes in pitching moment. The largest effect, as expected, is in side force and yawing moment coefficients. With the strake at $\Phi = 180°$ (leeward meridian), the flow field is similar to the baseline flow. By rotating the strake +/-20° about $\Phi = 180°$ ($160°<\Phi<200°$), positive and negative yawing moments can be obtained. In general, rotating the strake 20° from the leeward meridian towards the right side of the forebody produces a right-vortex-high pattern, with the corresponding negative or "nose-left" yawing moment.

The mechanism that makes the strake so efficient when acting on this area of the forebody is not very clear, and further flow visualization experiments might help to find the reason. The strake is either acting as a "spoiler", and, therefore, when it is rotated to the right produces an early separation on that side with the associated nose-left yawing moment, or is changing the secondary vortex structure and reattachment. The secondary vortices are difficult to visualize at this model scale, so it is difficult to confirm that the latter is the mechanism responsible for the changes in vortex pattern and yawing moment. Rotating the strake to the left side of the forebody has the opposite effect and a positive yawing moment is obtained. The changes in yawing moment are well-behaved and are comparable to, and sometimes larger than, the maximum rudder power shown in Fig. 12. At angles of attack lower than 30°, the single strake is not effective. Changes in rolling moment are erratic but relatively small (Fig. 66).

7.4.1.2 Single Strake at Sideslip

The single strake was also investigated under sideslip conditions, as indicated in Fig. 67. At $\beta = -10°$, the gradient around $\Phi = 180°$ appears to be efficient for manipulating the forebody vortices and changing the nature of the yawing moment on the forebody from destabilizing to stabilizing.

7.4.1.3 Dual Strakes

Dual strakes (a fixed pair of strakes that rotate together) have been evaluated in other investigations to either increase the magnitude of the directional changes or to make those changes more gradual and smoother with rotational position changes. As seen in the previous section, the two gradients that could be used for controlling the aircraft at high angles of attack with a single strake are either too abrupt or too moderate. By using a set of two strakes with the appropriate "dihedral" or separation angle, it might be possible to change the slope of those gradients as desired. Because the cross-over points (the angles at which the yawing moment changes sign) were close to +/-60° for the single strake case, it was decided to start the experiments with the strakes placed at +/-60°, i.e., a strake separation angle $\Delta\Phi = 120°$. A strake angle $\Phi = 0°$ is now defined as the angle at which the strakes are located symmetrically at +/-60° from the windward ray. The effect of rotating large and small dual strakes on the yawing moment coefficient is shown in Fig. 68. Again, there are not noticeable differences between the two strake sizes. In general, the small dual strakes induce a negative yawing moment for Φ = 0° to 180°, and a positive yawing moment between Φ = 180° and 360°.

The strake separation angle ΔΦ can significantly affect the performance of this control configuration. With a separation angle ΔΦ = 150° (Fig. 69) , the rotation of the dual strakes produces a different yawing moment pattern than the ΔΦ = 120° case. Differences are noticeable between Φ = 90° and 270°, where the two configurations induce exactly opposite yawing moments. For strake angles between 0° and 90° and 270° and 360°, the trends are very similar; however, it appears that the 120° case provides a better-behaved and smoother gradient along Φ = 0°. Two more dihedral angles (ΔΦ = 135° and 170°) were evaluated later during the rotary-balance tests. It is appropriate to note that for these later runs, the model support was different than the sting support used in the initial tests. The model was supported on a C-strut mounting system (part of the rotary rig apparatus). This particular set-up provides for fixed angles of attack from 0° to 60° at 3° increments, and, therefore, the test point nearest $\alpha = 50°$ was $\alpha = 51°$.

Before presenting data for the two new angles, a comparison of results obtained with the model mounted on the two different support systems is shown for the ΔΦ = 120° case in Fig. 70. As seen in this graph, the general behavior of the yawing moment curve is very similar for the two model supports; therefore, it is concluded that the differences in angle of attack and in model support do not affect the results significantly and the data for ΔΦ = 135° and 170° can be very useful for understanding and detecting trends in the dual strake behavior. The yawing moment changes produced by the rotation of the ΔΦ = 135° and 170° strakes are presented in Fig. 71. Again, the largest differences are seen for strake rotation angles between 90° and 270°.

If the net effect of the dual strakes is simply the algebraic addition of the effects of each individual single strake at its particular position, then the effect of the dihedral angle could be predicted analytically. A simple prediction exercise was performed after the test, so the results could be compared to the actual wind tunnel data. The first step in the exercise was to take the single strake data from the wind tunnel test (for both the small and large strakes), and get an "idealized" single strake database. In order to do so, the experimental data were smoothed, and all the asymmetries were eliminated. The results are presented in Fig. 72. It is assumed that the "ideal" strake data used for the prediction exercise, which are not significantly different from the real data, will produce results and trends that are easier to interpret and visualize. By simply adding up the yawing moment produced by each strake at various rotation angles, the total yawing moment produced by the combination can be calculated.

Results from this prediction exercise are compared to the experimental cases corresponding to ΔΦ = 135°, 150° and 170° in Fig. 73. The prediction compares fairly well for these cases; therefore, it appears that the general behavior of the dual strake combination at different dihedral angles can be predicted by using this approach. This simple exercise could be useful in future experiments to minimize the test matrix and to focus the test on the configurations that apparently give the best results.

The performance of dual strakes with different dihedral angles, i.e. from $\Delta\Phi = 20°$ to 180° in 10° increments, was predicted and is shown in Fig. 74. For separation angles between 20° and 40°, the dual strakes act as a single strake. The magnitude of the maximum yawing moment produced by these cases is probably over-predicted; since the strakes are so close to each other, the net effect will not be the simple addition of each strake. The shape of the curve is changed for $\Delta\Phi = 50°$. The positive gradient around $\Phi = 180°$ starts deteriorating, and the negative gradient around $\Phi = 0°$ becomes better-behaved but it still has a moderate slope. The gradient around 180° definitely disappears for $\Delta\Phi$ between 70° and 130°. The gradient around $\Phi = 0°$ is still almost linear, with the magnitude of the yawing moment slightly increasing as the dihedral angle is increased (for constant strake angles Φ between -40° (320°) and 40°. For the larger dihedral angles, the slope of the $\Phi = 0°$ gradient starts decreasing, so it appears that a dihedral angle of 120° or 130° might be the optimum configuration. Another linear gradient starts to appear from $\Delta\Phi = 160°$ around $\Phi = 180°$, which has the same negative slope as the gradient around $\Phi = 0°$. A dihedral angle of 180° seems to give the best gradient around $\Phi = 180°$; however, its slope is moderate and large strake rotations are required to reach the maximum yawing moment.

Figure 75 shows a comparison of the various strake angles investigated in the wind tunnel tests, while a comparison of the predictions for the same angles is presented in Fig. 76. In order to get a better visualization of the gradient around $\Phi = 0°$, the scale of the horizontal axis (strake angle) was changed from 0° to 360° to -180° to 180° ($\Phi = 270° = -90°$). Both graphs indicate that the gradient around $\Phi = 0°$ is best for the $\Delta\Phi = 120°$ case. The experimental data clearly show that, despite the larger yawing moment magnitudes induced by the $\Delta\Phi = 150°$ and 170° cases, the $\Delta\Phi = 120°$ configuration has the smoothest gradient. The negative gradient around 180° produced by the large dihedral angles is evident in both graphs, so further tests of dual strakes at $\Delta\Phi = 180°$ might be appropriate in the future.

Additional experiments were conducted for dual strakes with a separation angle $\Delta\Phi = 120°$. In these tests, the strake was fixed at one particular Φ, and an angle of attack sweep was performed (Fig. 77). The small dual strakes do not affect the longitudinal characteristics significantly, even though the changes in normal force and in pitching moment are slightly higher than those produced by rotating the single strake, especially at $\alpha = 55°$. No effect on axial force is observed. The largest changes occur again in the directional characteristics. At $\Phi = 0°$, the flow still presents an asymmetric flow field as in the baseline (no strakes) case. Large changes in side force and yawing moment are induced by rotating the strakes +/-40°; trends are well-behaved, with $\Phi = +/-40°$ producing a larger yawing moment than $\Phi = +/-20°$ throughout the entire angle of attack range, except at $\alpha = 60°$. The effect of the strakes on rolling moment is similar to the single strake case.

7.4.1.4 Dual Strakes at Sideslip

Dual strakes were also investigated under sideslip conditions, and the results indicate that they are equally effective at $\beta = -10°$ (Fig. 78). The yawing moment curve for the sideslip case presents a positive offset, but rotating the strakes to $\Phi = 40°$ from the windward ray is still enough to produce stabilizing yawing moments.

7.4.1.5 Correlation to Water Tunnel Tests

An excellent correlation between this test and a water tunnel test conducted on a similar configuration (Ref. 29) was obtained, and is shown in Fig. 79. In the water tunnel test, flow visualization was performed, and the reference yawing moment produced by the rotation of dual strakes was measured with a one-component balance. The model, despite being the same size (6% F/A-18), was only the forebody section and, therefore, the magnitude of Cnref is referenced directly to the one-component strain gage output located 34.9 inches behind the model nose tip. In the comparison plot, the maximum yawing moments have been normalized to the same level. However, the similarities in the variation of the yawing moments with roll angle produced by the dual strakes in both tests are very clear in Fig. 79, emphasizing once again the usefulness of a water tunnel to predict vortex flow behavior.

7.4.2 Pressure Distributions

The responses of the forebody and LEX surface pressures to various orientations of the nose-tip strakes, both single and dual, are shown in Figs. 80 and 81, respectively. The effect of a single strake at roll positions of 160° and 200° (with the symmetric baseline of 180° where the single strake is on the leeward side) is shown in Fig. 80 on the forebody for angles of attack of 50° and 60°. As expected, based on the force and moment results above, with the strake placed at 160° or 20° clockwise from the leeward side (pilot's view, placing the strake on the right), there is increased suction on the left side of the forebody and less on the right side resulting in a yawing moment to the left. Conversely if the strake is rolled 20° in the opposite direction to 200°, the pressure distributions reverse.

The effect of dual strakes spaced 120° apart is shown in Fig. 81. In this case the strakes are placed symmetrically +/- 60° from the windward stagnation line and then rotated as a pair. Therefore, at zero rotation angle both strakes are on the windward side 120° apart. The pressure distributions for 50° and 60° AOA are shown in Figs. 81a and 81b. Conversely to the data for the single strake, a pilot's view clockwise roll angle, i.e., from 0° to 340° and 320°, produces higher suction on the right side than the left resulting in a yawing moment to the right. The reason is that the strake on the right side has moved from 60° to 40° and 20°, which helps delay flow separation on that side and the strake on the left moves from 60° to 80° and 100° which promotes separation. The combination of the two strakes is, to a degree, additive.

The variation in the pressure distribution from left to right sides is especially significant for 60° AOA. Even though the baseline is not symmetric at 60° AOA (natural forebody vortex asymmetry begins to emerge at about 60°), the clockwise and counter-clockwise rotations produce nearly equal and opposite reactions on the forebody, as verified by the pressure distributions. The asymmetry in the flow field for the baseline symmetric strake configuration is overcome by the rotated strake configuration. One difference between the data for 50° and 60° is that the maximum peak suction (and also the maximum differential between left and right sides) is at 40° and 320° for 50° AOA and at 20° and 340° for 60° AOA. In other words, to achieve the maximum benefit of the rotated strakes requires only 20° of rotation at 60° AOA instead of 40° for 50° AOA.

The effects of dual strake rotation on the LEX pressures for 50° and 60° AOA are also shown in Figs. 81. The effect on the pressures is quite small. The mirror image of left and right strake rotation can be seen, although the pressure changes are very small, at span stations of +/- 0.15. At more outboard stations the differences between + and - rotation are not as well defined. Basically, this relatively small change to the LEX pressures means that at 50° and 60° AOA there is very minor coupling between the forebody flow field and the LEX flow, which means that rotating the strakes provides almost pure yaw input and very little in roll.

7.5 VERTICAL NOSE STRAKE

7.5.1 Force and Moment Coefficients

As discussed earlier, the vertical nose strake (VNS) is a small strake mounted on the leeward side of the forebody near the tip. The VNS pivots about an axis perpendicular to the surface of the forebody. A positive VNS deflection δ is defined as trailing edge left, looking from the top. The vertical nose strake proved very effective in manipulating the forebody vortices in preliminary water tunnel tests.

Even though the largest effects are seen in the directional characteristics, the VNS also modifies the normal force and the pitching moment for angles of attack higher than 50°. As shown in Fig. 82, when pivoted more than 20°, the VNS produces a slight decrease in normal force and an increase in negative pitching moment. No major changes are observed in axial force.

The VNS induces large changes in side force and yawing moment. A positive deflection (trailing edge left) produces a positive yawing moment and vice versa. From flow visualization obtained in the water tunnel, when the vertical nose strake is pivoted trailing edge left, a strong vortex forms at the leading edge of the VNS. This leading edge vortex moves towards the left side of the forebody, and apparently, is increasing the suction on the right side and, at the same time, is pushing the left forebody vortex away from the body surface. This creates a left-vortex-high pattern with the associated positive yawing moment. When the VNS is pivoted trailing edge right, a negative yawing moment is induced, as seen for the δ = -20°, -36° and -50° cases. As for the rotatable strake case, the changes in rolling moment are small, erratic and depend strongly on angle of attack.

7.5.1.2 Vertical Nose Strake at Sideslip

Figure 83 shows the effect of the vertical nose strake on the lateral directional characteristics under sideslip conditions ($\beta = -10°$). A VNS deflection $\delta = 36°$ is capable of producing stabilizing yawing moments at angle of attack greater than 50°.

7.5.2 Pressure Distributions

The effect of the vertical strake configuration is shown in Fig. 84a and 84b for angles of attack of 50° and 60°. The strake is pivoted about a vertical axis +/- 36° to produce left and right yawing moments and the pressure distributions resulting from the deflections are shown. On the forebody (F.S. 142.5) a trailing-edge left deflection (+36°) provides higher suction on the right side of the forebody, and -36° provides a reversed pressure distribution. The effectiveness in terms of variation of the differential pressure distribution about the baseline is greater for 60° AOA than 50° AOA. The effect on the LEX pressure distributions is small at 60° AOA. As was seen earlier with the rotating tip strakes, the flow field on the forebody at 60° AOA is quite sensitive and is easily driven asymmetric by small disturbances on the forebody. The response of the pressure distribution to +/- deflections is in the same direction, rather than opposite directions as seen on the forebody.

7.6 COMPARISON OF DATA TO OTHER TEST RESULTS

One of the objectives of this research program was to compare some of the forebody vortex control results from the present sub-scale tests in Ames 7 x 10-ft wind tunnel with previous full-scale results from the Ames 80 x 120-ft wind tunnel. Since the focus of the present experiments is primarily on forebody vortex control, the emphasis for comparison was initially to be on the resulting yawing and rolling moments with a secondary interest in pitching moment as a result of various FVC techniques. Unfortunately, only limited data from the 80 x 120-ft tunnel were available, so only a few comparisons can be made with FVC. Basically only yawing moment is available for jet and slot blowing for 50° AOA from Ref. 8. There is also a comparison of rudder effectiveness with angle of attack from sub-scale, full-scale and the current F/A-18 aerodynamic model widely used for F/A-18 simulation.

Even though there are little FVC data to compare to, there are other baseline F/A-18 sub-scale wind tunnel data and full-scale flight data available with surface pressure measurements at the identical locations on the forebody and LEX, and some of these data are used for comparison to understand the differences between sub-scale and full-scale Reynolds numbers.

7.6.1 Force and Moment Coefficients

The only yawing moment results available to us to compare with from the full-scale wind tunnel tests in the Ames 80 x 120-ft wind tunnel with and without blowing are those shown in Ref. 18. Figure 85 shows a comparison between the present sub-scale results and Ames full-scale results. Figure 85a shows yawing moment data for the blowing left-side jet case with the nozzle mounted 16 inches from the forebody tip on the full-scale model and blowing straight aft. Data for the comparable configuration from the sub-scale tests are also shown, but at a lower MFR. There were not two comparable runs at identical MRF values. Neither, however, was very robust and do not show good agreement with each other. The observed difference could be due to the difference in the blowing mass flow ratio or it could be a strong function of Reynolds number. There is no means to sort this out with only one comparison to consider.

The blowing slot results that are compared are shown in Fig. 85b. The slot configuration is the one where the slot starts at 11 inches from the forebody tip and extends 16 inches in length on the left side only. The equivalent slot in the sub-scale model is "SLOT AB" discussed previously in Section 7.3. The full-scale (80x120) data are for 30°, 40° and 50° AOA. The present results are at 40° and 50° AOA. The plot is the variation of yawing moment with increasing MFR. The correlation between sub-scale and full-scale data is rather poor. The reversal in the yawing moment direction with increasing MFR is observed in both tests but the magnitude and blowing rate where it reverses is quite different. The full-scale tests show much larger yawing moments and the cross-over is at much lower levels of MFR. The Reynolds number difference based on wing mean aerodynamic chord is 0.63×10^6 for the sub-scale tests and 12.0×10^6 for the full-scale tests.

A comparison of the rudder effectiveness is shown in Fig. 85c. There is fairly good agreement between the sub-scale tests and the F/A-18 aerodynamic model widely used for simulation for the F/A-18. The agreement between full-scale wind tunnel tests and full-scale aerodynamic model is not particularly good, especially above 30° AOA. The increase in rudder effectiveness with increasing angle of attack for the 80 x 120 data is not very consistent with other data and with the expectation of decreased rudder effectiveness with angle of attack with virtually all fighter aircraft.

7.6.2 Pressure Distributions

Pressure data have been obtained on the baseline F/A-18 from other sub scale experiments (Ref. 33), from full-scale tests in the wind tunnel (Refs. 8 and 18), and in flight with the High Attitude Research Vehicle F-18, HARV (Refs. 35-37). The full scale wind tunnel data from NASA Ames 80 x 120-ft wind tunnel are at M=0.15 and the HARV flight data are at a Mach number of 0.26. The subsonic wind tunnel data reported in Ref. 33 were obtained with a different 6% scale model in the Navy's 7 x 10-ft wind tunnel at David Taylor Research Center (DTRC). These tests covered a Mach number range and results showed that there were noticeable Mach number effects on the LEX pressure distributions even at the low Mach numbers of 0.15 to 0.25. Pressure distributions showed that the maximum suction on the LEX tends to be higher for lower Mach numbers, particularly if the Reynolds number is low as it is for sub scale tests. However, there were no Mach number effects on the forebody pressures up to M=0.6.

This section will show some comparisons of the pressure distributions on the forebody and LEX between the present tests, the other 6% model tests by NASA Langley at DTRC and full-scale HARV data at angles of attack of 30°, 40° and 50°. Comparisons will also be made between the present tests and the full-scale wind tunnel tests at Ames, where possible.

A comparison between the present tests, the Langley/DTRC tests and the full-scale flight tests for HARV are shown for angles of attack of 30°, 40° and 50° in Fig. 86. Each set of plots is for the three common fuselage stations of 142, 253 and 357. At 30° AOA, the comparison between the sub-scale wind tunnel experiments and the full-scale flight test results show extremely good agreement. The full-scale data show small suction peaks that probably correspond to the leeside primary and, perhaps, secondary vortices. The Eidetics data do not have sufficient density of pressure orifices to detect these pressures, if present. The Langley/DTRC model had more pressure orifices but it also does not detect the suction peaks experienced by the full-scale model. It is likely that this difference is due to Reynolds number, or possibly the inability of small models to accurately reproduce the full-scale geometry. The LEX pressures at F.S. 253 and 357 are also quite comparable between tests. The higher suction pressures for the Eidetics results compared to the DTRC results could be due to the slightly lower Mach number of the Eidetics tests. The difference of the full-scale data from the sub-scale data could either be due to Reynolds number or scale effects in geometry fidelity. The agreement at the aft LEX station is extremely good.

At 40° AOA, the forebody pressures are in very good agreement with the vortex suction peaks more evident in the full-scale data than in the sub-scale data. The Eidetics results tend to have a slightly higher suction pressure than the other data. The LEX pressure distributions at F.S. 253 show higher suction peaks for the Eidetics data at the lower Mach number than the DTRC data. No data were available for the HARV. The aft LEX station show almost identical data.

At 50° AOA, the forebody pressures are still in quite good agreement with the Eidetics data showing slightly higher suction peaks around the sides of the forebody. The flight test data, and to some extent the DTRC data, show small suction peaks on the leeward side in response to the primary vortices. The LEX pressure distributions are also in good agreement overall. There are some small differences in the pressure levels at F.S. 253.

Comparisons between the sub-scale data of the present tests and the full-scale results from the Ames 80 x 120-ft wind tunnel are shown in Fig. 87 for angles of attack of 30°, 40° and 50°. Comparisons are shown at F.S. 142 on the forebody and at 253 and 357 on the LEX. Both sets of data were acquired at a nominal Mach number of 0.15. The Reynolds number based on wing mean aerodynamic chord were 0.63×10^6 for the sub-scale tests and 12.0×10^6 for the full-scale tests. It should be noted that the full-scale tests were run with the horizontal tail settings set as a function of angle of attack to trim the configuration in pitch, whereas the sub-scale data were acquired with the tails set at zero.

The comparison of results at 30° AOA generally shows good agreement. The maximum suction on the sides of the forebody is nearly identical between the two tests. The full-scale results show a better pressure recovery following separation than the sub-scale results, because of the higher Reynolds number. For the sub-scale tests, based on the shape of the pressure distribution and surface flow visualization from other sub-scale tests (Ref. 33 and 34), there is most likely a laminar separation bubble on the forebody and the surface velocity of the reattached flow from the primary vortex on the leeward surface is relatively low, resulting in low suction (higher pressure) than shown in the full-scale results. The local suction peaks resulting from the primary vortices are evident for the full-scale results and not for the sub-scale. The location of primary separation is also undoubtedly delayed for the full-scale Reynolds number case. The LEX pressures are very similar with the sub-scale data showing only slightly higher suction. The sub-scale data are too sparse to compare the details near the maximum suction peak.

At 40° AOA, the sub-scale results show overall higher suction pressures than the full-scale data. On the forebody the shapes of the pressure distributions are similar, but the recovery pressure on the leeward side is higher for the full-scale than the sub-scale configuration for the same reasons described above. One obvious difference between the data at 30° and 40° AOA is the magnitude of the suction on the LEX at F.S. 357. At 30° the LEX vortex location is aft of both LEX fuselage stations and, therefore, there is significant suction at both stations. At 40° AOA the LEX vortex burst location has moved to a point just aft of F.S. 253 but ahead of F.S. 357. This is verified by the reduced suction pressure at F.S. 357 but nearly unchanged suction pressure at F.S. 253 comparing data for 40° AOA to 30° AOA. The pressure distribution downstream of the LEX vortex burst (F.S. 357 at 40° AOA) is relatively flat, as expected since the vortex is no longer producing high velocities near the surface.

At 50° AOA, the LEX vortex burst has moved to the apex of the LEX, ahead of the two LEX pressure stations. Consequently, the suction levels are significantly reduced compared to the lower angles of attack. The forebody pressures, however, show higher suction levels and the agreement between the sub-scale and full-scale results is quite good. As shown for the lower angles of attack, the sub-scale tests show slightly higher overall suction levels but do not measure a local suction peak associated with the primary vortex. The laminar flow of the sub-scale test results in earlier separation and most likely a laminar bubble on the leeward side, where the full-scale tests have predominantly transitional to turbulent flow. The full-scale data show clearly both the suction peaks for the primary vortex at an azimuth angle of 200° and the secondary vortex at approximately 250° on the forebody left side.

8.0 CONCLUSIONS

In order to select the most promising configurations, for further testing on the rotary balance, a static wind tunnel test was conducted to examine a wide range of forebody vortex control schemes. Blowing jets were tested at three fuselage stations and three azimuth angles. In addition, the jet nozzle cant angle was varied from 0° to 150° inboard. A series of blowing slots was also examined, with varying slot length and initial fuselage station location. Several mass flow rates were tested for each of the pneumatic techniques.

Mechanical methods of controlling the forebody vortices were also used. Both single and dual, rotatable, miniature, nose tip strakes were tested. The size of the strakes and the separation angle between the dual strakes were varied in addition to the strake roll angle (Φ). A single, miniature, vertical nose tip strake was tested at a number of deflection angles (pivoting about it's center axis like a full-flying rudder). The following are the major conclusions of the static test:

1) The baseline pressure data agree well with the Langley/DTRC (sub-scale test) and the HARV (full-scale flight test) test results.

2) The baseline pressure data agree well with the NASA Ames 80x120 Foot Full-Scale F/A-18 wind tunnel test.

3) The baseline force and moment data agree well with Langley Spin Tunnel data (NASA CR-3608)

4) Typically, forebody vortex control techniques are effective above 30° AOA.

5) Jet blowing straight aft is not an effective yawing moment producer. Angling the jets inboard makes them much more effective.

6) Nose 4 (x = 1.30 inches, 150° azimuth) with the nozzles canted inboard 60° was the most effective jet configuration.

7) Jet cant angles of 120° or 150° cause the yawing moment response to increased blowing rate to first go in the direction opposite to the side that is blowing and then cross over and produce a positive yawing moment for right side blowing and negative for left.

8) Sideslip decreases the effectiveness of the leeward jet, and increases the effectiveness of the windward jet. Overall, the jet is still quite effective at 10° of sideslip.

9) The jets were effective at the three Reynolds Numbers tested (0.636×10^6, 0.553×10^6, 0.387×10^6 based on wing mean aerodynamic chord). The yawing moment produced by the jets correlated well with C_μ and MFR.

10) Slot blowing was most effective with the forward two segments tested (Slot AB).

11) The slot acted similarly to the jets (when they were rotated to 120° or 150°) with a yawing moment toward the side opposite of the blowing slot for low blowing rates, which then crosses over with higher blowing rates, and produces a positive yawing moment for right side blowing (and negative for left).

12) Sideslip increased the effectiveness of the leeward slot, and decreased the effectiveness of the windward slot. This is in contrast to the jet. Overall, the slot is still quite effective at 10° of sideslip.

13) The slots were effective at the three Reynolds numbers tested (0.636×10^6, 0.553×10^6, 0.387×10^6). The yawing moment produce by the slots correlated very well with MFR. For the two highest Reynolds numbers, it correlated well with C_μ. It is not known if the low Rn case didn't correlate because of C_μ not being the right parameter, or a true Reynolds number effect.

14) The time lag between the beginning (onset) of jet or slot blowing and the response of the aircraft is about three convective time units. The lag associated with the shut down (decay) of blowing is not measurably different.

15) Dual strakes can be utilized to modulate the changes in directional characteristics. The complexity of the system increases slightly, however, since there is an extra parameter (the strake separation angle $\Delta\Phi$) that appears to be important and needs to be optimized.

16) Both single and dual strakes are efficient under sideslip conditions up to at least 10°.

17) Both the experimental data and a simple prediction exercise, that assumes that the net effect of the dual strake combination is the addition of the effects of each single strake, appear to indicate that dual strakes with a separation angle of 120° could be used very efficiently along the $\Phi = 0°$ gradient. Rotating the strakes +/-40° produces changes in yawing moments comparable to those obtained with a +/-30° rudder deflection, along a gradient that presents almost linear characteristics and no reversals.

18) Very good correlation was also found between this test and previous water tunnel tests performed on a similar configuration (150° dual strakes).

19) The vertical nose strake appears to be a powerful yaw control effector. It worked well at 10° of sideslip, and appears worth further study.

20) The pressure distribution on the forebody clearly confirmed the characteristics of the force measurements, revealing the different flow field asymmetries produced by the different forebody vortex control devices.

21) High Reynolds number testing must be performed to verify the characteristics of these forebody vortex control methods. Work on the X-29 (Ref. 12) indicates that the full-scale results may be better than the sub-scale test results.

9.0 ACKNOWLEDGMENTS

The authors wish to acknowledge the support and encouragement of our technical monitor, Dr. Lewis Schiff and our alternate monitor, Dr. James Ross, who both maintained a high level of interest and active participation in the technical discussions throughout the period of this contract. We would also like to recognize the significant efforts of Mr. Kevin James of Sterling Federal Systems who performed as Test Director for NASA Ames Research Center for both the static and the rotary-balance tests and the NASA support personnel responsible for the operation of the 7 x 10-ft wind tunnel, including the tunnel mechanics, technicians, and programmers. We would particularly like to acknowledge the help of Mr. Art Silva for his conscientious commitment to providing the best instrumentation support possible.

10.0 REFERENCES

1) Malcolm, G. N.,"Forebody Vortex Control," Special Course on Aircraft Dynamics at High Angles of Attack: Experiments and Modeling presented at NASA Langley Research Center April 8-11, 1991 and von Karman Institute, April 22-25, 1991, AGARD Report No. 776, March 1991.

2) Malcolm, G. N., "Forebody Vortex Control," Progress in Aerospace Sciences, Vol. 28, pp. 171-234,1991.

3) Murri, D. G. and Rao, D. M., "Exploratory Studies of Actuated Forebody Strakes for Yaw Control at High Angles of Attack," AIAA Paper 87-2557-CP.

4) Malcolm, G. N., Ng, T. T., Lewis, L. C. and Murri, D. G., "Development of Non-Conventional Control Methods for High Angle of Attack Flight Using Vortex Manipulation," AIAA Paper 89-2192.

5) Malcolm, G. N., Ng, T. T., "Forebody Vortex Manipulation for Aerodynamic Control of Aircraft at High Angles of Attack," SAE Paper 892220.

6) Malcolm, G. N., Ng, T. T., Lewis, L. C. and Murri, D. G., "Development of Non-Conventional Control Methods for High Angle of Attack Flight Using Vortex Manipulation," AGARD CP 465, Paper No. 11, April 1990.

7) Malcolm, G. N. and Ng, T. T., "Aerodynamic Control of Fighter Aircraft by Manipulation of Forebody Vortices," AGARD CP-497, Paper No. 15, November 1991.

8) Lanser, W. R. and Murri, D. G., "Wind Tunnel Measurements on a Full-Scale F/A-18 with Forebody Slot Blowing or Forebody Strakes," AIAA Paper 93-1018.

9) Skow, A. M., Moore, W. A. and Lorincz, D. J.,"Forebody Vortex Blowing - A Novel Concept to Enhance the Departure/Spin Recovery Characteristics of Fighter Aircraft," AGARD CP-262, May 1979.

10) Moore, W. A., Skow, A. M. and Lorincz, D. J., "Control of the Forebody Vortex Orientation by Asymmetric Air Injection - Application to Enhance Departure/Spin Recovery," AIAA Paper 80-0173.

11) LeMay, S. P., Sewall, W. G. and Henderson, J. F., "Forebody Vortex Flow Control on the F-16C Using Tangential Slot and Jet Nozzle Blowing," AIAA Paper 92-0019.

12) Guyton, R. W. and Maerki, G., "X-29 Forebody Jet Blowing," AIAA Paper 92-0017.

13) Cornelius, K. C., Pandit, N., Osborn, R. F., and Guyton, R. W., "An Experimental Study of Pneumatic Vortex Flow Control on High Angle of Attack Forebody Model," AIAA Paper 92-0018.

14) Pellicano, P. and Krumenacker, J. L., "Flight Test Techniques, Simulation and Data Analyses During a High Angle of Attack Vortex Flow Control Flight Test Program," 23rd Symposium of Society of Flight Test Engineers, August 3-7, 1992.

15) Hancock, R. and Fullerton, G., "X-29 Vortex Flow Control Tests," Proceedings of the Thirty Sixth Symposium of the Society of Experimental Test Pilots, pp. 209-219, September, 1992.

16) Rosen, B. S. and Davis, W. H., "Numerical Study of Asymmetric Air Injection to Control High Angle-of-Attack Forebody Vortices on the X-29 Aircraft," AIAA Paper 90-3004-CP.

17) Ng, T. T and Malcolm, G. N., "Aerodynamic Control Using Forebody Blowing and Suction," AIAA Paper 91-0619.

18) Lanser, W. R. and Meyn, L. A., "Forebody Flow Control on a Full-Scale F/A-18 Aircraft," AIAA Paper 92-2674.

19) Ng, T. T., Ong, L., Suarez, C. J. and Malcolm, G. N., "Wing Rock Suppression Using Forebody Vortex Control," AIAA Paper 91-3227.

20) Suarez, C. J., Kramer, B. R., Ayers, B. F. and Malcolm, G. N., "Forebody Vortex Control for Suppressing Wing Rock on a Highly-Swept Wing Configuration," AIAA Paper 92-2716.

21) Ng. T. T., Suarez, C. J. and Malcolm, G. N., "Forebody Vortex Control Using Slot Blowing," AIAA Paper 91-3254.

22) Gee, K. ,Tavella, D. and Schiff, L. B., "Computational Optimization of a Pneumatic Forebody Flow Control Concept," AIAA Paper 91-3249-CP.

23) Gee, K., Rizk, Y. M., Murman, S. M., Lanser, W. R., Meyn, L. A. and Schiff, L. B., "Analysis of a Pneumatic Forebody Flow Control Concept About a Full Aircraft Geometry." AIAA Paper 92-2678-CP

24) Font, G. I., Celik, Z. Z. and Roberts, L., "A Numerical and Experimental Study of Tangential Jet Blowing Applied to Bodies at High Angles of Attack," AIAA Paper 91-3253-CP.

25) Ross, A. J., Jefferies, E. B. and Edwards, G. F. "Control of Forebody Vortices by Suction at the Nose of the RAE High Incidence Research Model," AGARD CP-494, October, 1990.

26) Ross, A. J., Jeffries, E. B. and Edwards, G. F., "Dynamic Tests on Large-Scale High Incidence Research Models (HIRM1) in the DRA 24-Ft Wind Tunnel with Control of Forebody Vortices by Nose Suction," DRA Tech. Report 92067, December, 1992

27) Moskovitz, C. A., Hall, R. M. and DeJarnette, F. R., "New Device for Controlling Asymmetric Flowfields on Forebodies at Large Alpha," AIAA Journal of Aircraft, Vol. 28, No. 7, July 1991.

28) Suarez, C. J., Malcolm, G. N. and Ng, T. T.,"Forebody Vortex Control with Miniature Rotatable Nose-Boom Strakes," AIAA Paper 92-0022.

29) Ng, T. T. and Malcolm, G. N., "Aerodynamic Control Using Forebody Strakes," AIAA Paper 91-0618.

30) Wurtzler, K., "Numerical Analysis of a Chined Forebody with Asymmetric Strakes," AIAA Paper 93-0051.

31) Boalbey, R. E., Ely, W. L. and Robinson, B. A., "A Sensitivity Study for Pneumatic Vortex Control on a Chined Forebody," AIAA Paper 93-0049.

32) Malcolm, G. N., "Forebody Vortex Control - A Progress Review," AIAA Paper 93-3538, AIAA 11th Applied Aerodynamics Conference, Monterey, CA, August 9-11, 1993.

33) Erickson, G. E., Hall, R. M., Banks, D. W., Del Frate, J. H., Schreiner, J. A., Hanley, R. J. and Pulley, C. T., " Experimental Investigation of the F/A-18 Vortex Flows at Subsonic Through Transonic Speeds," AIAA 89-2222.

34) Banks, D. W., "Wind-Tunnel Investigation of the Forebody Aerodynamics of a Vortex-Lift Fighter Configuration at High Angles of Attack," SAE Paper 881419.

35) Fisher, D. F., Del Frate, J. H. and Richwine, D. M., "In-Flight Flow Visualization Characteristics of the NASA F-18 High Alpha Research Vehicle at High Angles of Attack," NASA TM 4193, May 1990.

36) Fisher, D. F., Banks, D. W. and Richwine, D. M., "F-18 High Alpha Research Vehicle Surface Pressures: Initial In-Flight Results and Correlation With Flow Visualization and Wind Tunnel Data," NASA TM 101724, August 1990.

37) Bjarke, L. J., Del Frate, J. H. and Fisher, D. F., "A Summary of the Forebody High-Angle-of-Attack Aerodynamics Research on the F-18 and X-29A Aircraft," SAE Paper 921996.

38) Hulzberg, R., "Low Speed Rotary Aerodynamics of F-18 Configuration for 0° to 90° Angle of Attack - Test Results and Analysis," NASA CR 3608, August 1984.

JET BLOWING

PRESSURE (psia)	Cμ	MFR
20	0.0004	0.000042
30	0.0011	0.000080
40	0.0015	0.000112
50	0.0019	0.000145
60	0.0023	0.000177
70	0.0027	0.000210

SLOT BLOWING (SEGMENT A-B)

PRESSURE (psia)	Cμ	MFR
20	0.0007	0.000072
30	0.0016	0.000116
40	0.0022	0.000166
50	0.0029	0.000217
60	0.0035	0.000264

Table 1 - Blowing coefficient and mass flow ratio for different plenum pressures (q = 27 psf)

Yaw control power - with forebody vortex control.

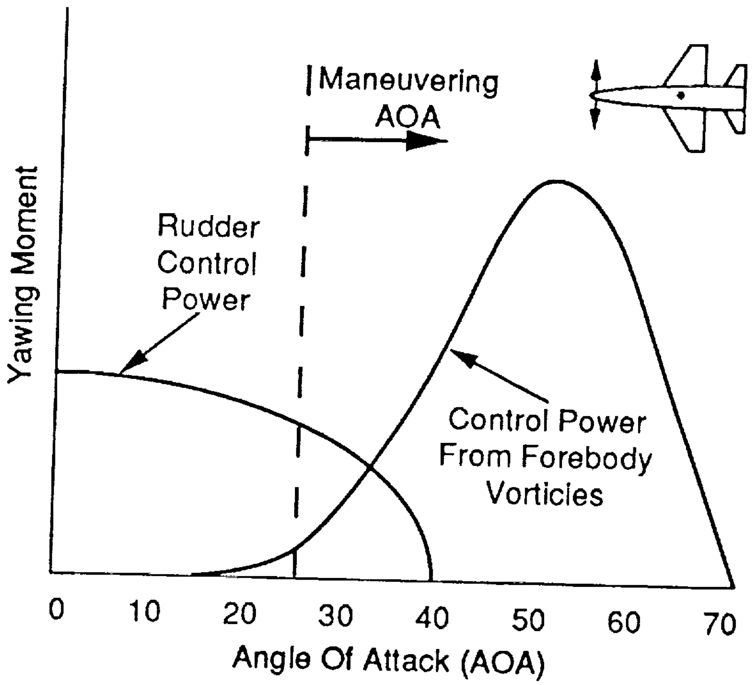

Figure 1 - Yaw control power with conventional control surfaces and with Forebody Vortex Control (FVC)

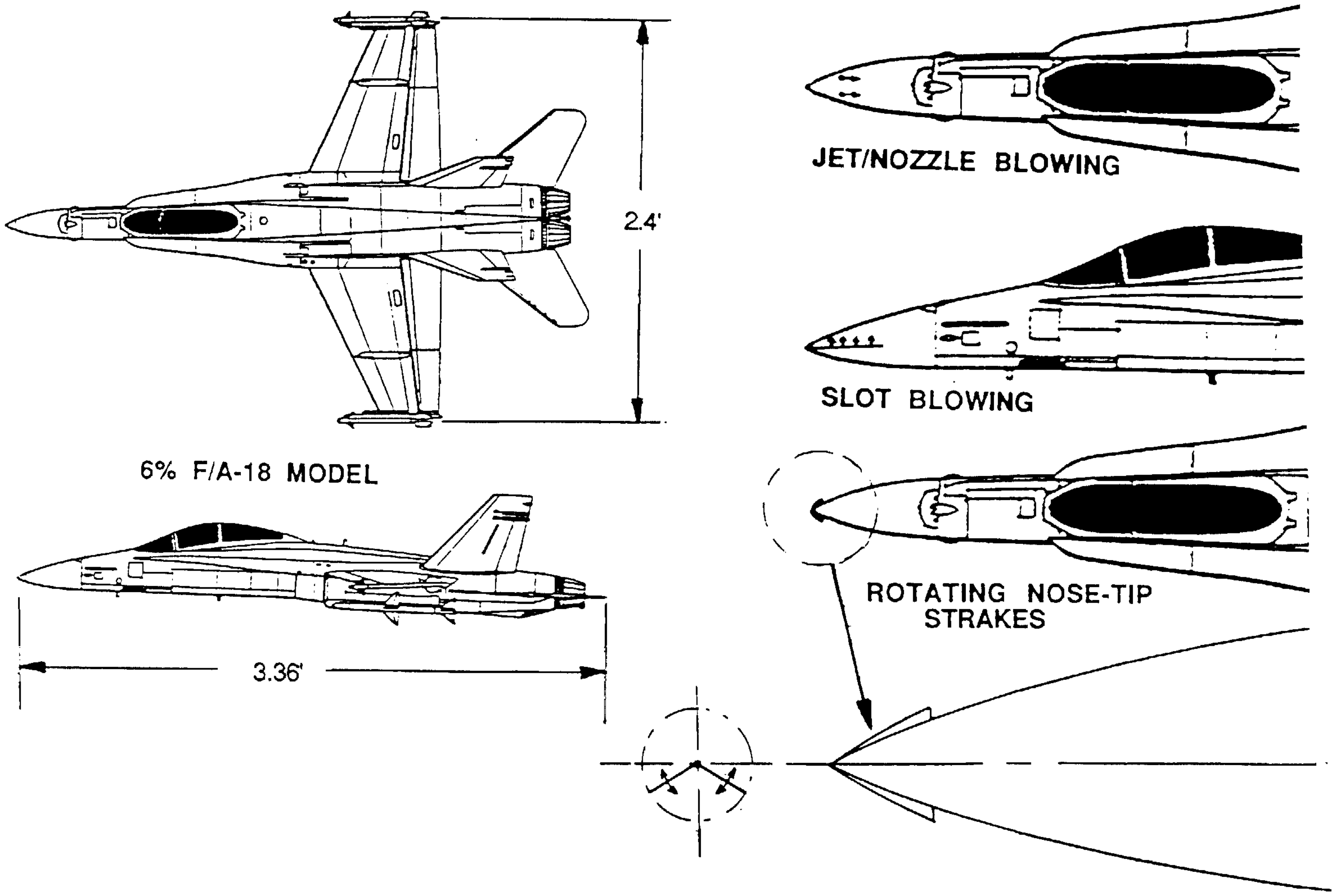

Figure 2 - Water tunnel model with different forebody vortex control techniques

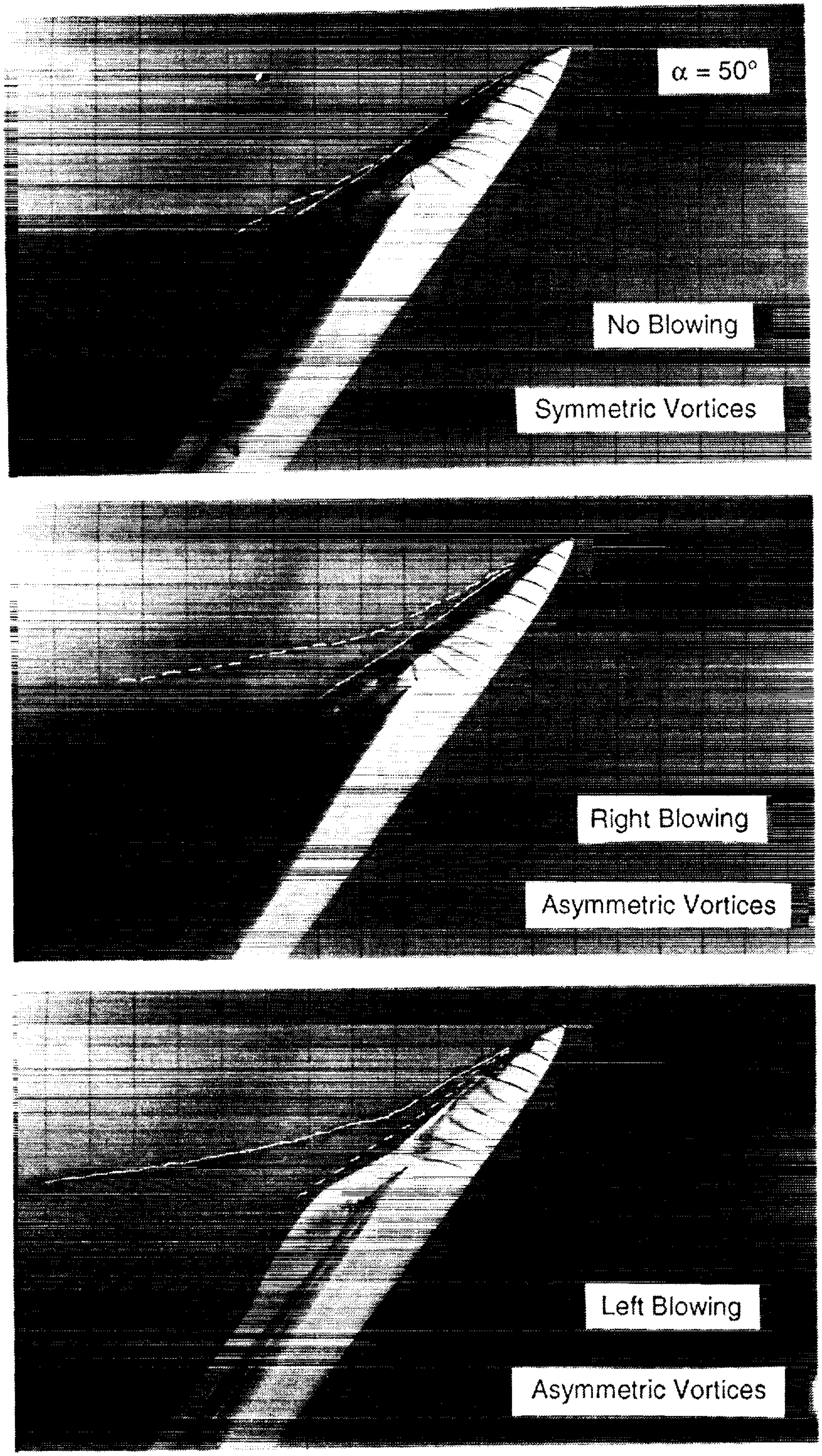

Figure 3 - Effect of slot blowing on the forebody vortices (water tunnel test)

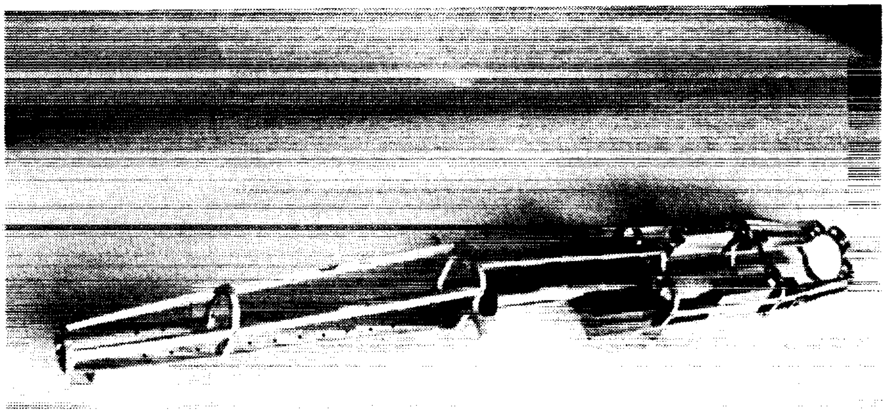

(a) Internal structural frame of model

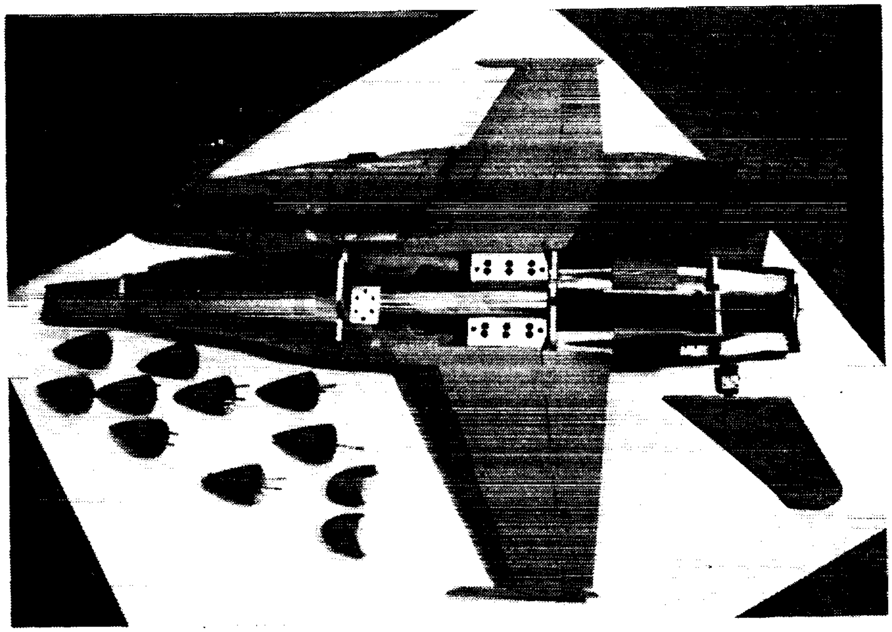

(b) Model with assorted forebody pieces

Figure 4 - Photographs of 6% F/A-18 wind tunnel model

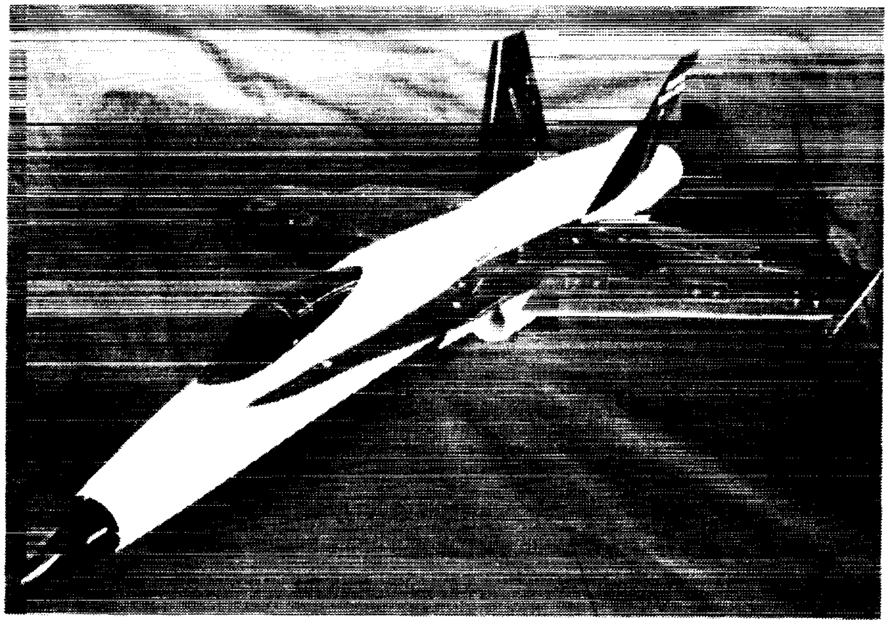

(c) Assembled model

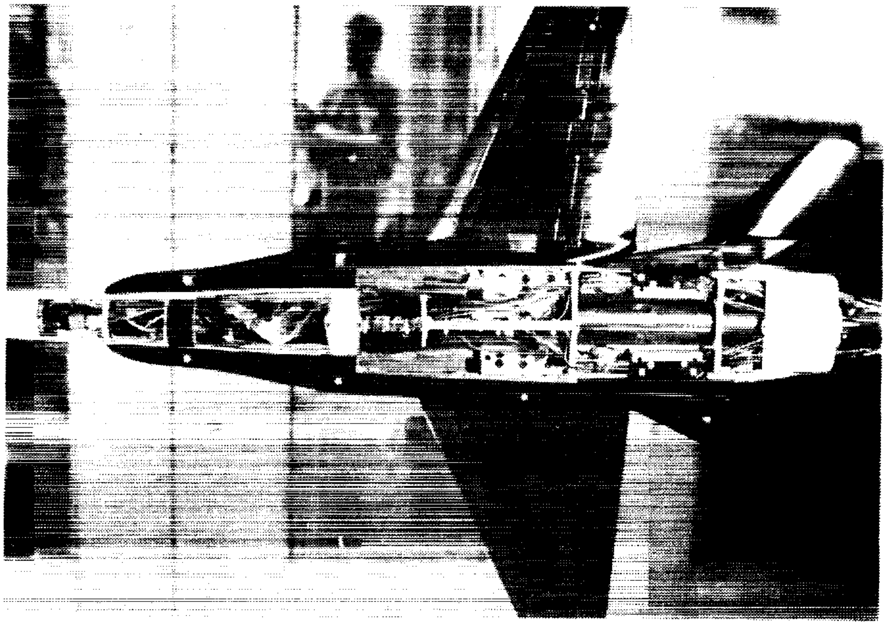

(d) Assembled model with top cover removed

Figure 4 - Concluded

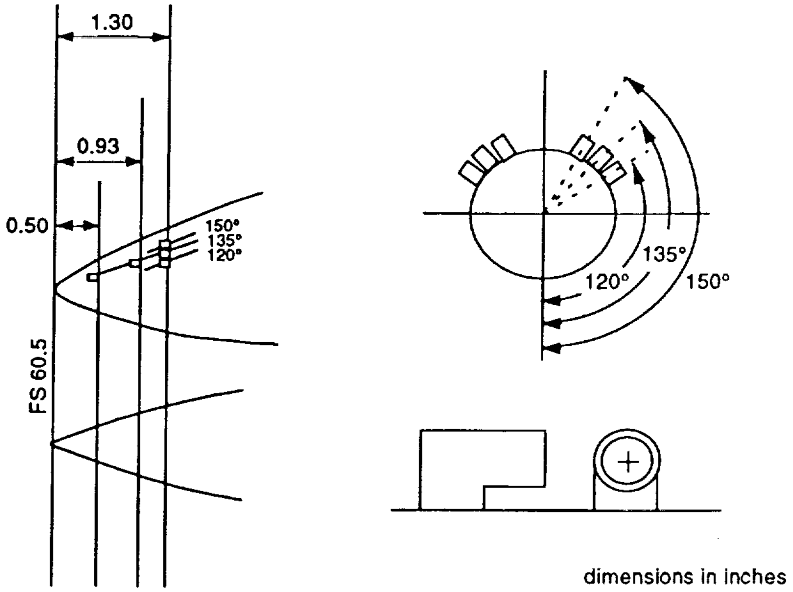
BLOWING JET GEOMETRY AND LOCATION

(a) Jet blowing

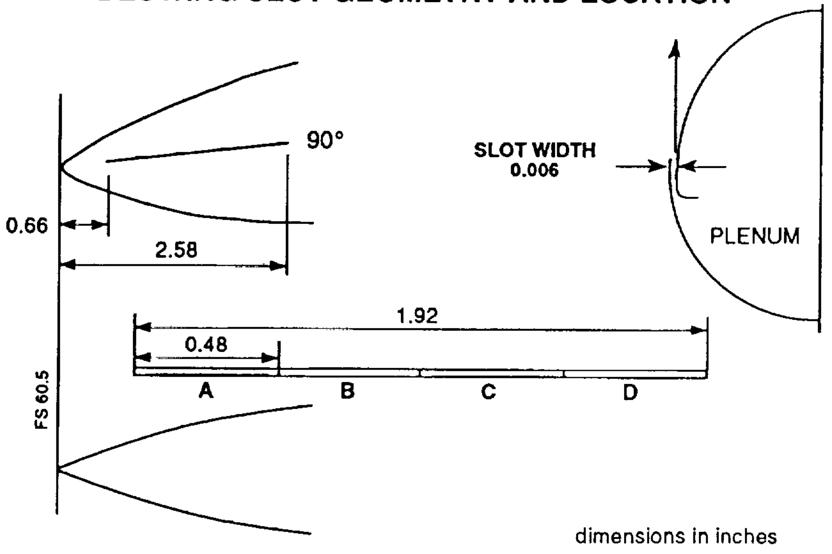
BLOWING SLOT GEOMETRY AND LOCATION

(b) Slot blowing

Figure 5 - Forebody vortex control techniques investigated in the wind tunnel test

STRAKE GEOMETRY AND LOCATION

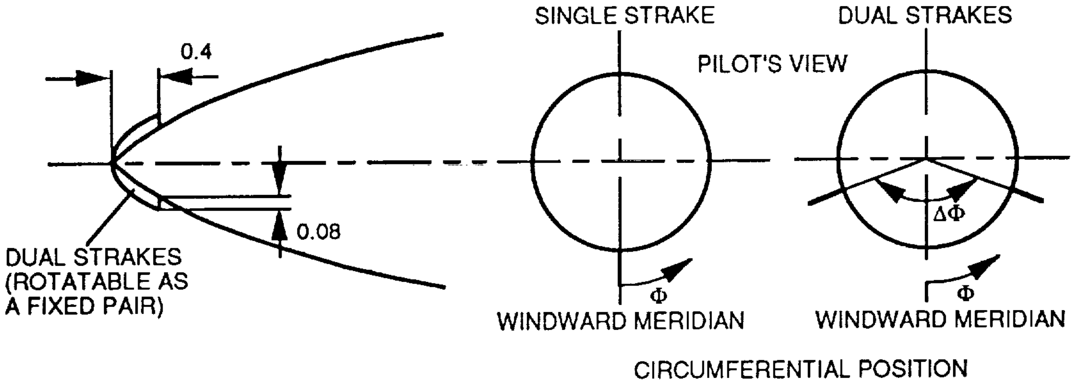

(c) Rotatable tip-strakes

VERTICAL NOSE STRAKE GEOMETRY AND LOCATION

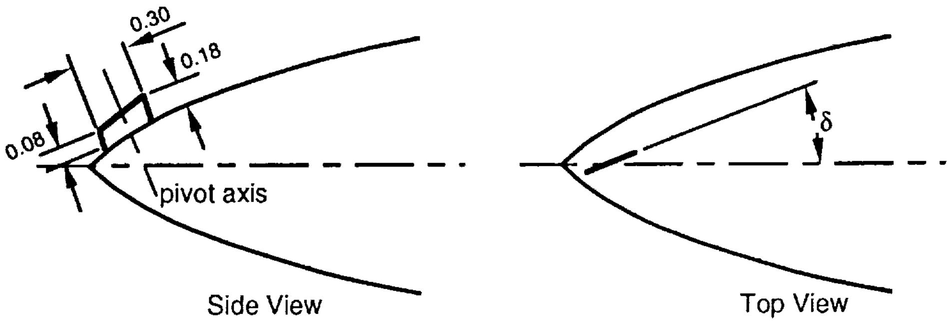

(d) Vertical nose strake (Rhino-horn)

Figure 5 - Concluded

(a) Model Components and instrumentation

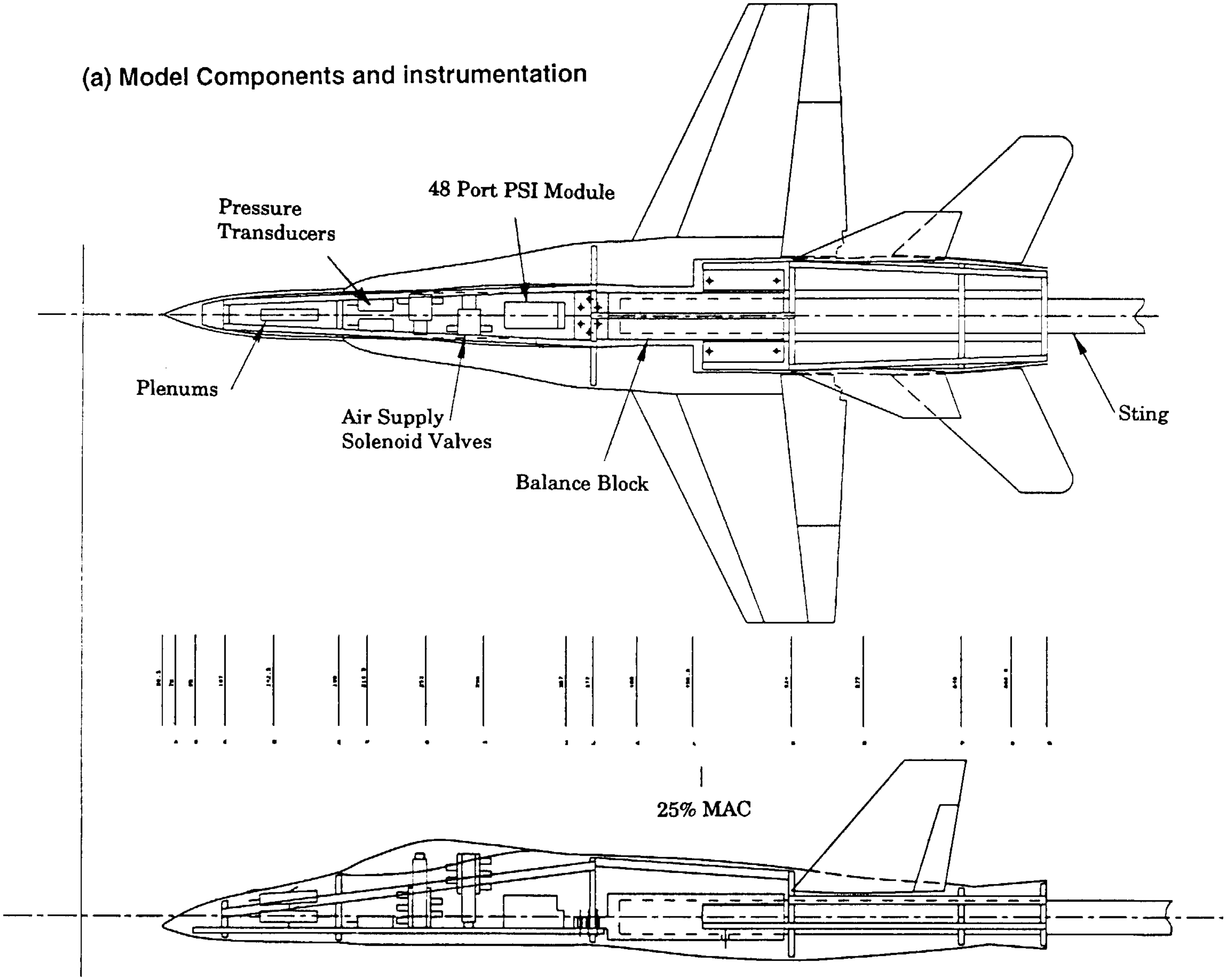

Figure 6 - 6% F/A-18 wind tunnel model details

(b) Pressure tap location

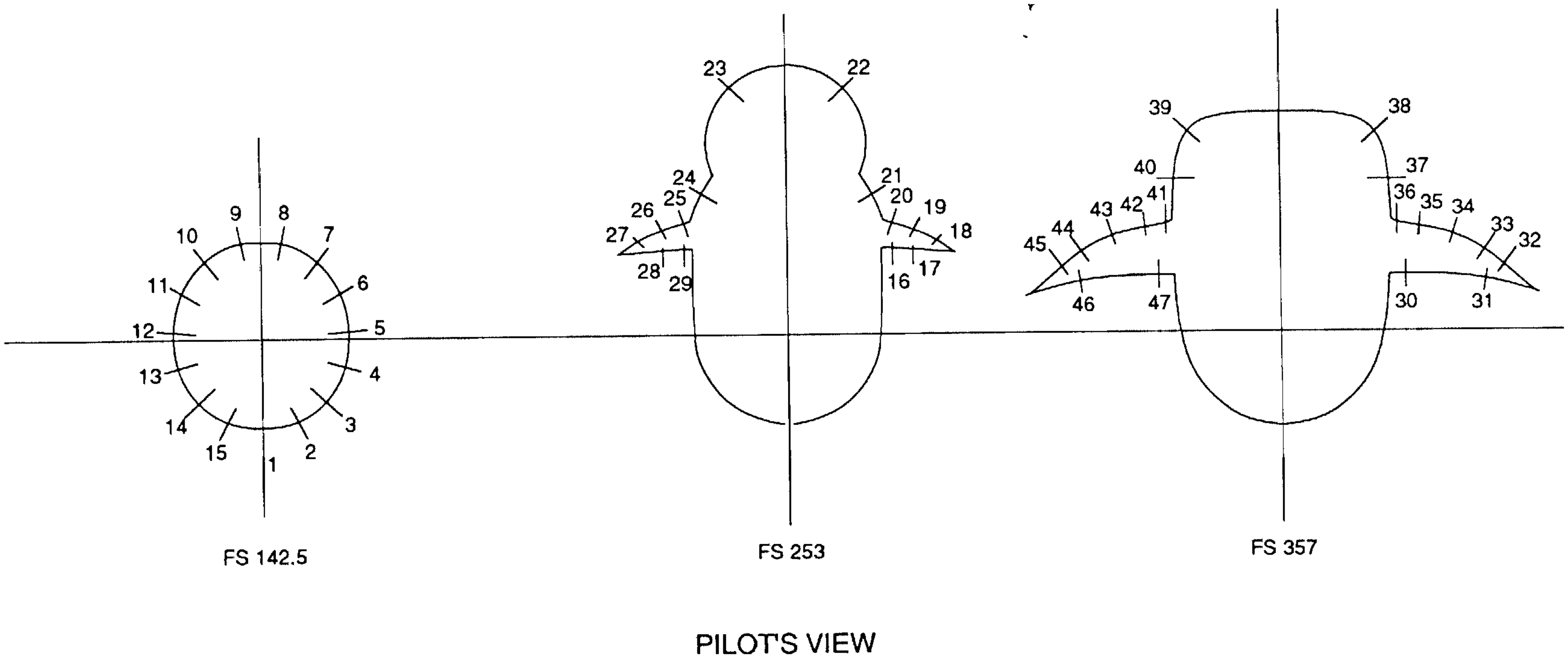

Figure 6 - Continued

F/A-18 PRESSURE TAP LOCATIONS

PORT #	FS	LOCATION	THETA	Y	Z
1	142.5	lower starboard	0	0	-1.180
2		lower starboard	24	0.0488	-1.077
3		lower starboard	45	0.818	-0.807
4		lower starboard	72	1.022	-0.33
5		upper starboard	95	1.047	0.0888
6		upper starboard	120	0.967	0.554
7		upper starboard	144	0.700	0.955
8		upper starboard	168	0.247	1.157
9		upper port	192	-0.250	1.155
10		upper port	216	-0.695	0.944
11		upper port	240	-0.953	0.542
12		upper port	265	-1.033	0.0948
13		lower port	288	-1.011	-0.325
14		lower port	315	-0.801	-0.801
15		lower port	336	-0.482	-1.075

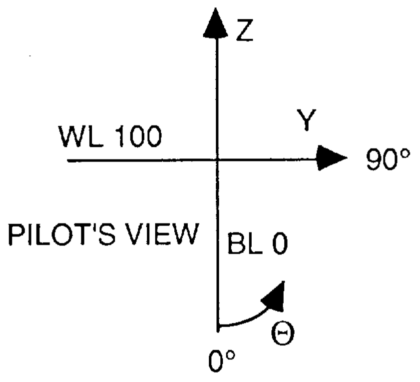

PORT #	FS	LOCATION	Y*	Y/S'	Y	Z
16	253	lower starboard	0.136	0.152		
17		lower starboard	0.401	0.45		
18		upper starboard	0.674	0.758		
19		upper starboard	0.409	0.46		
20		upper starboard	0.119	0.134		
21					-1.06	1.66
22					-0.77	2.99
23					0.77	2.99
24					1.06	1.66

Figure 6 - Continued

25		upper port	0.119	0.134		
26		upper port	0.409	0.46		
27		upper port	0.674	0.758		
28		lower port	0.401	0.45		
29		lower port	0.136	0.152		
30	357	lower starboard	0.214	0.123		
31		lower starboard	1.201	0.691		
32		upper starboard	1.448	0.883		
33		upper starboard	1.195	0.689		
34		upper starboard	0.788	0.454		
35		upper starboard	0.374	0.215		
36		upper starboard	0.08	0.046		
37					-1.36	1.91
38					-1.13	2.52
39					1.13	2.52
40					1.36	1.91
41		upper port	0.08	0.046		
42		upper port	0.374	0.215		
43		upper port	0.788	0.454		
44		upper port	1.195	0.689		
45		upper port	1.448	0.883		
46		lower port	1.201	0.691		
47		lower port	0.214	0.123		

Y* is 6% scale from inboard edge of LEX

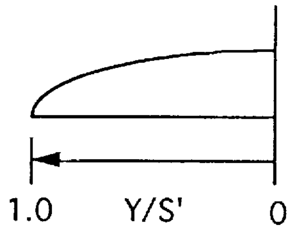

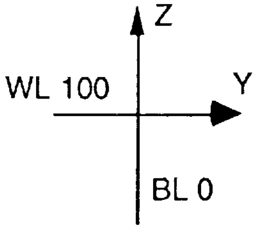

PILOT'S VIEW

Figure 6 - Continued

(c) Endevco pressure transducer location

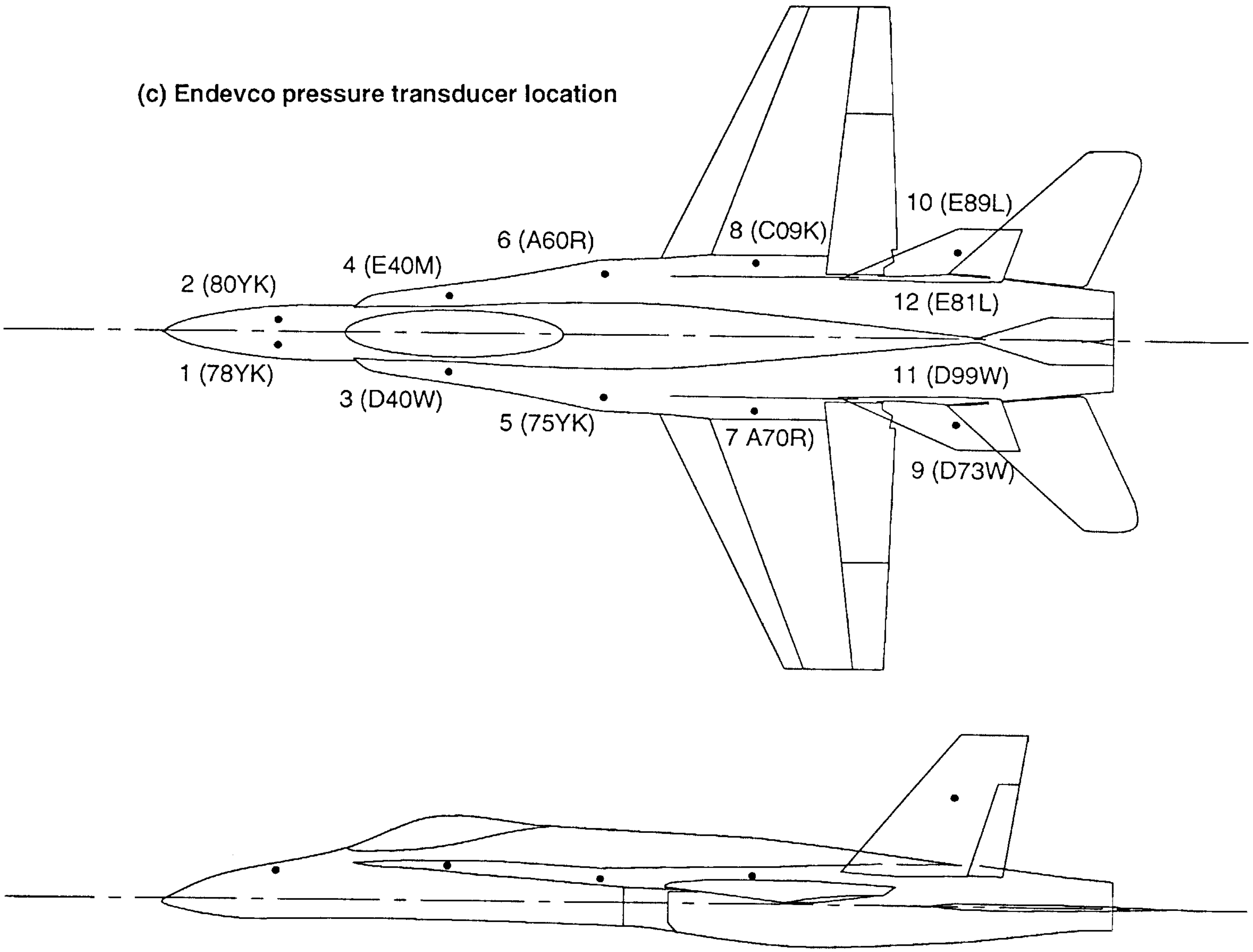

Figure 6 - Continued

F/A-18 ENDEVCO SENSOR LOCATION

END. #	FS	LOCATION	THETA	Y/S'	BL
2	142.5+	upper starboard	135		
1		upper port	225		
4	253+	upper starboard		0.5	
3		upper port		0.5	
6	357+	upper starboard		0.7	
5		upper port		0.7	
8	470	over wing 0.5Cr			54.2
7					-54.2

END. #	LOCATION
9, 10,	Vertical Tail 45% chord 60% span
11, 12	Inboard and outboard of both tails

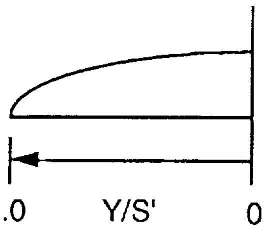

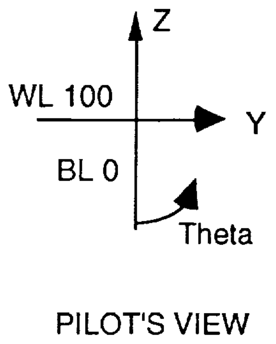

Figure 6 - Concluded

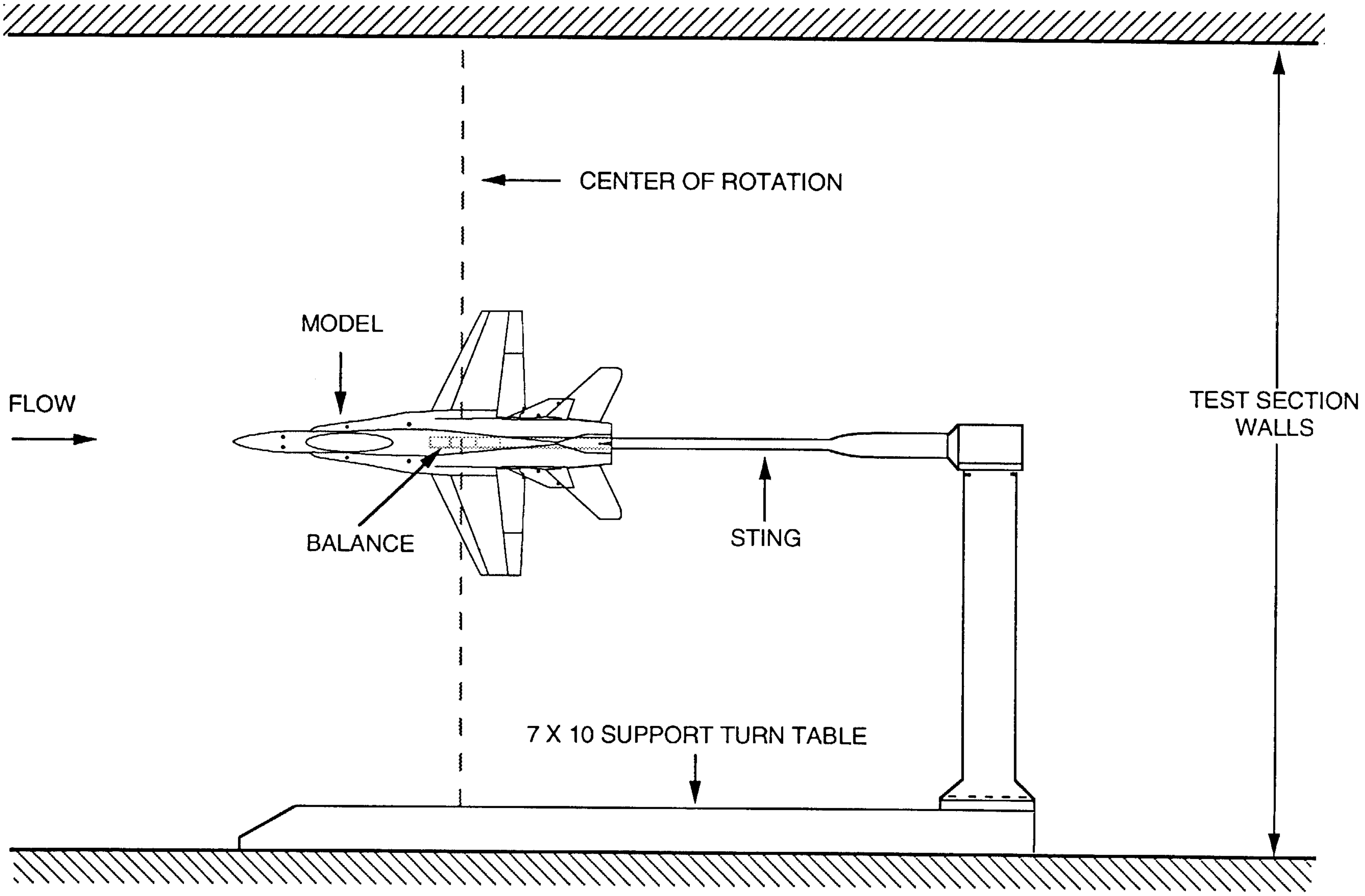

Figure 7 - Installation in NASA AMES 7 x 10' wind tunnel

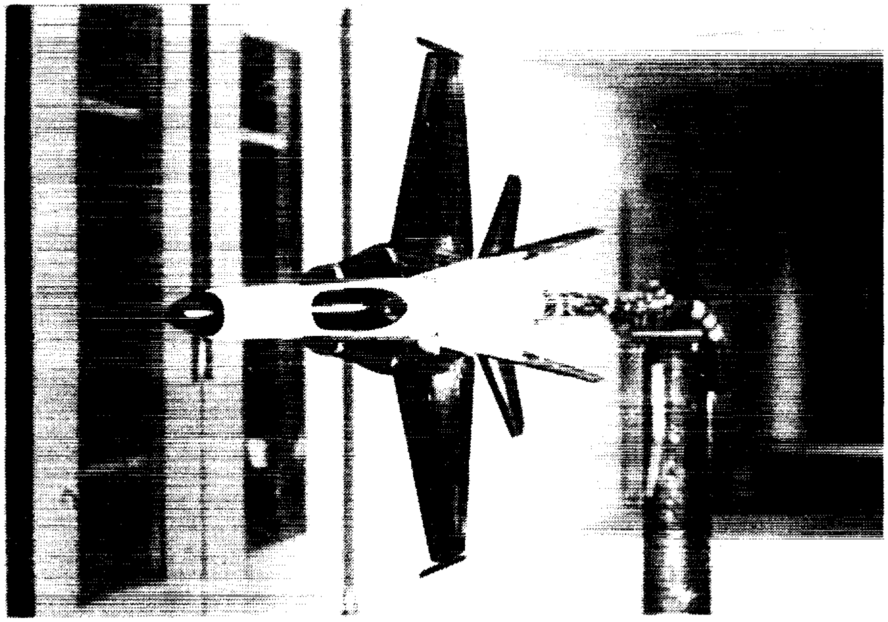

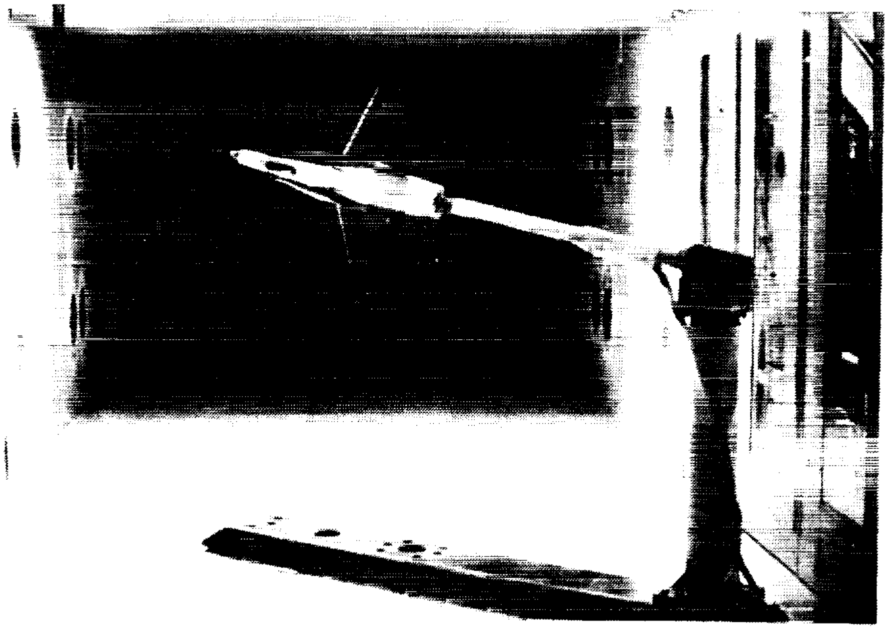

Figure 7 - Concluded

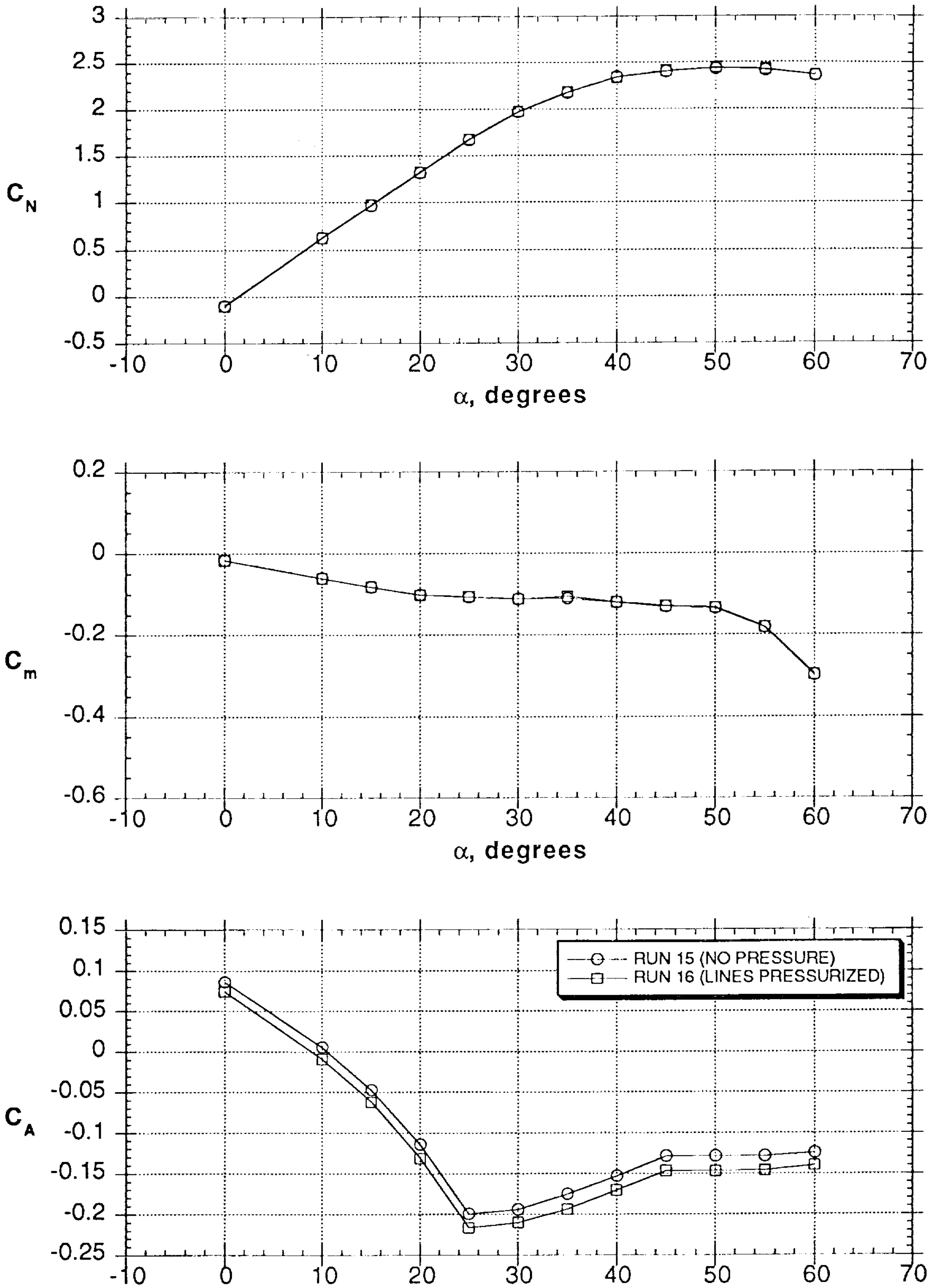

Figure 8 - Effect of pressurizing the blowing lines on forces and moments

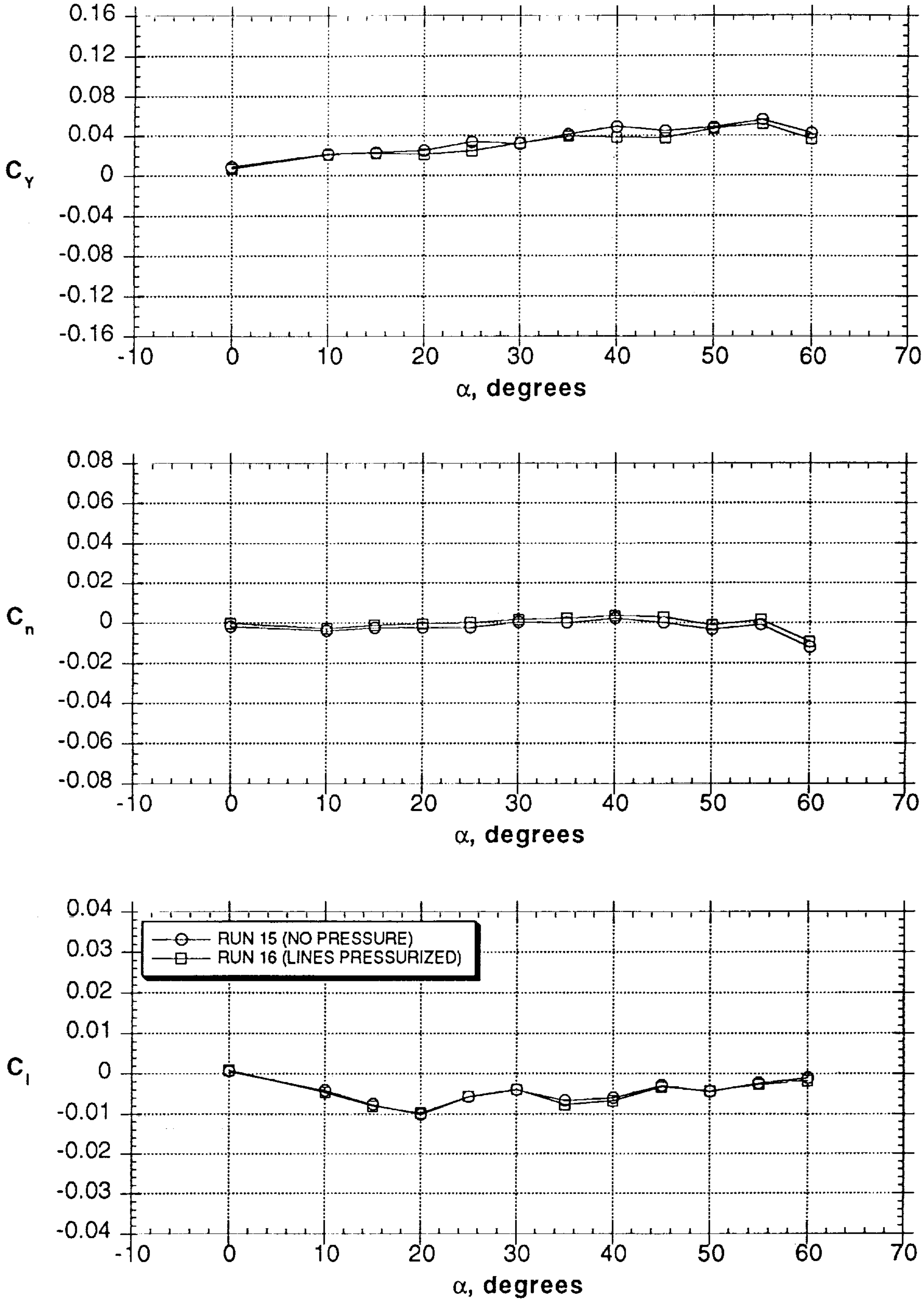

Figure 8 - Concluded

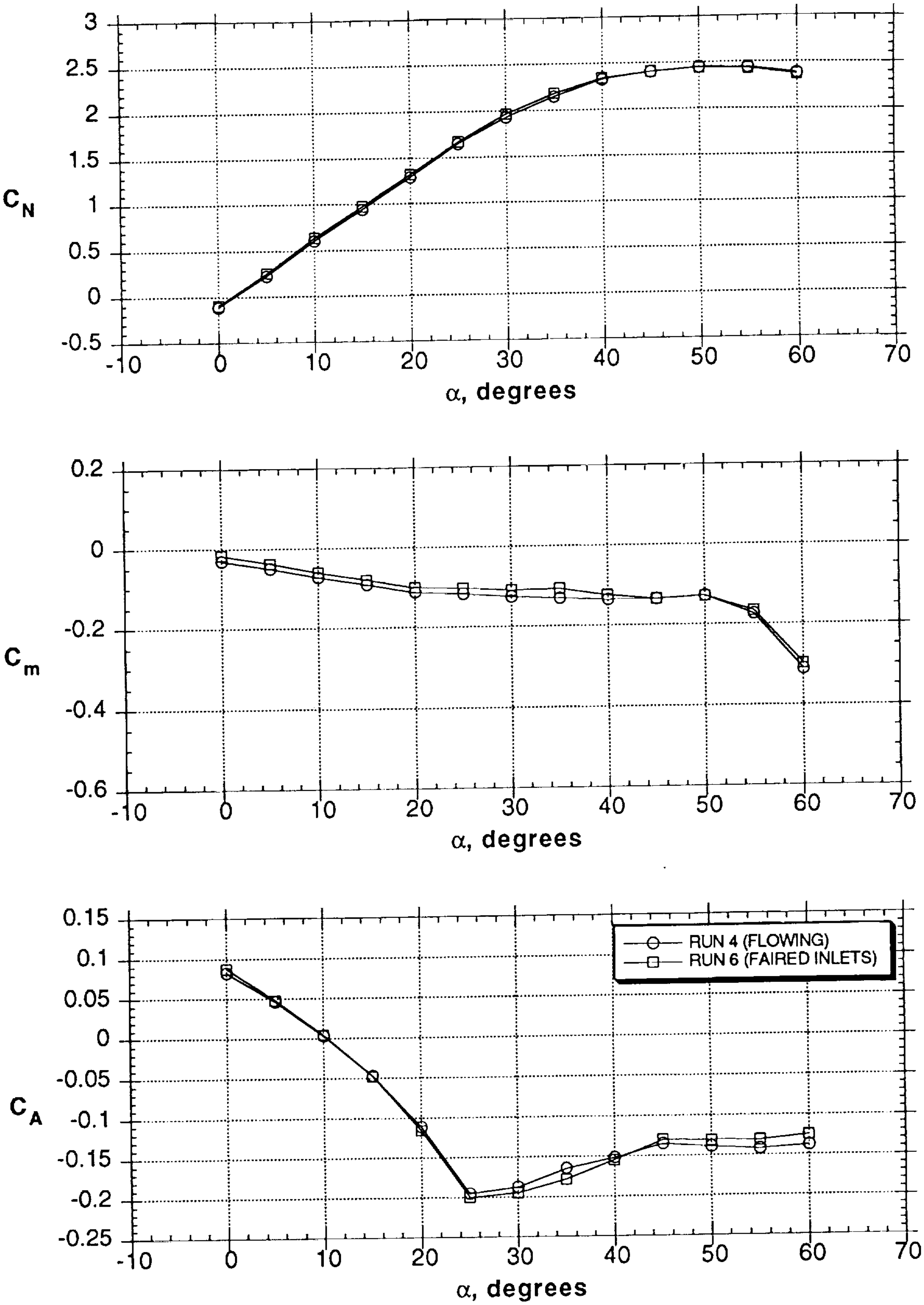

Figure 9 - Effect of fairing over the inlets on forces and moments

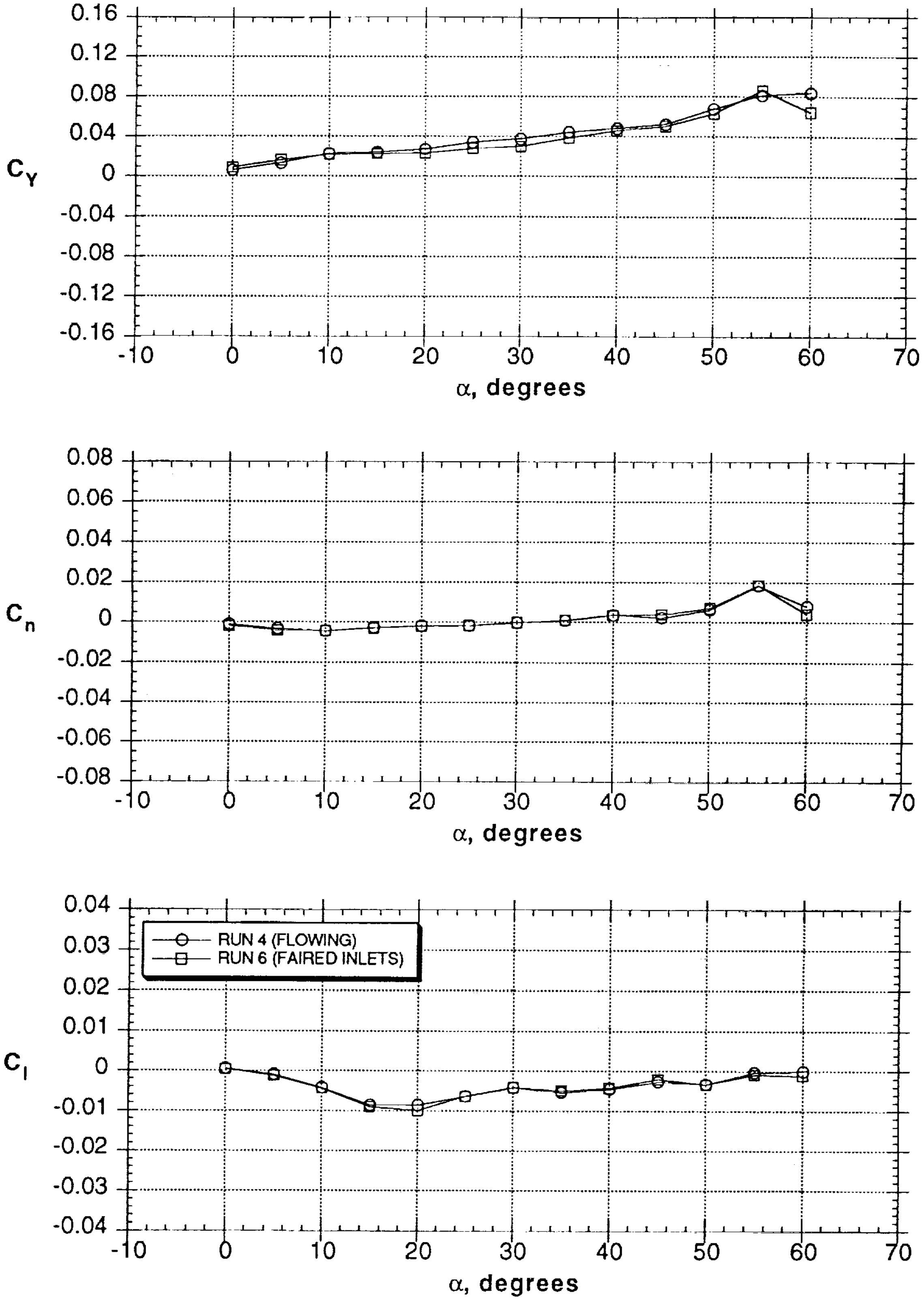

Figure 9 - Concluded

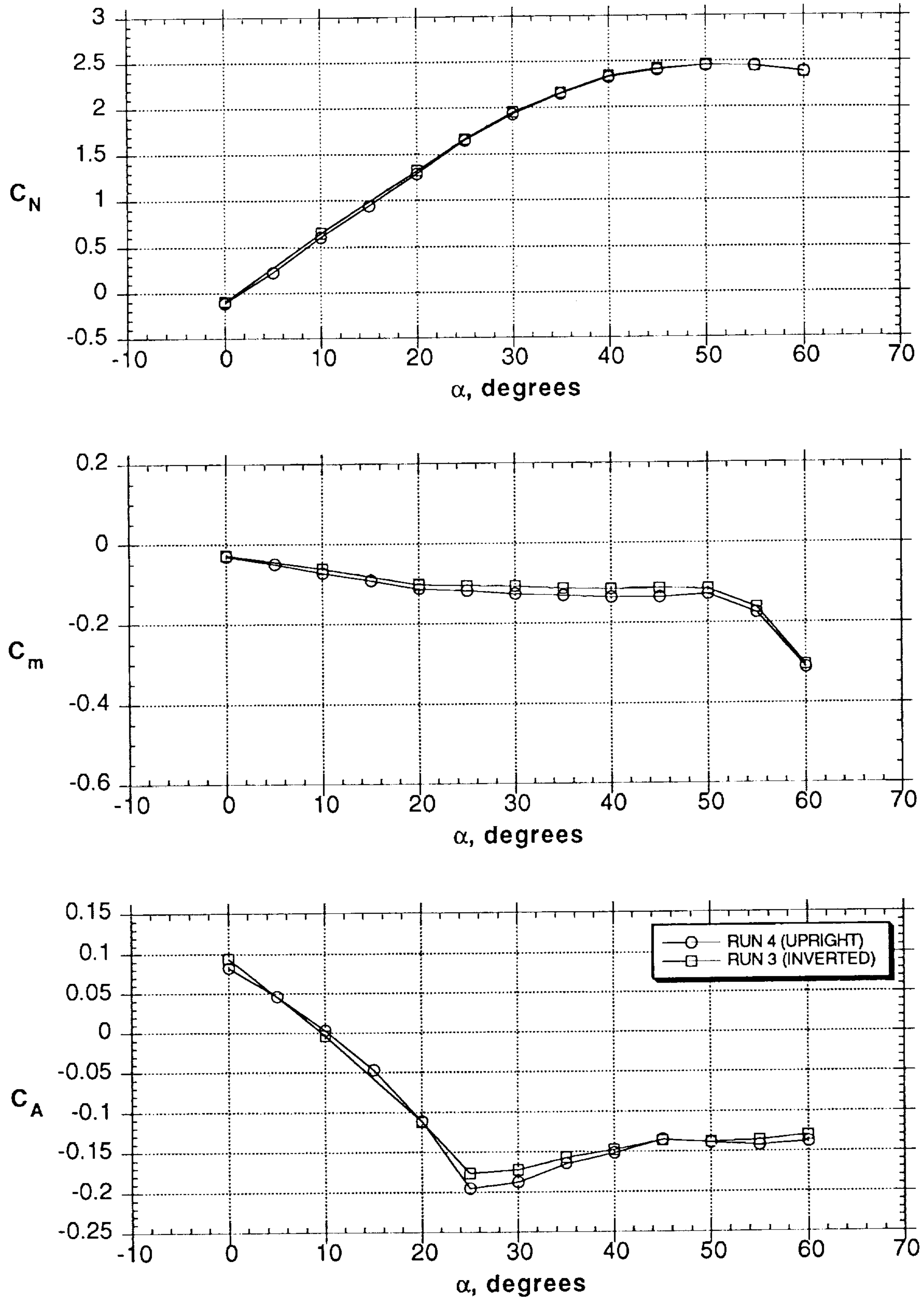

Figure 10 - Effect of running the model "inverted" on forces and moments

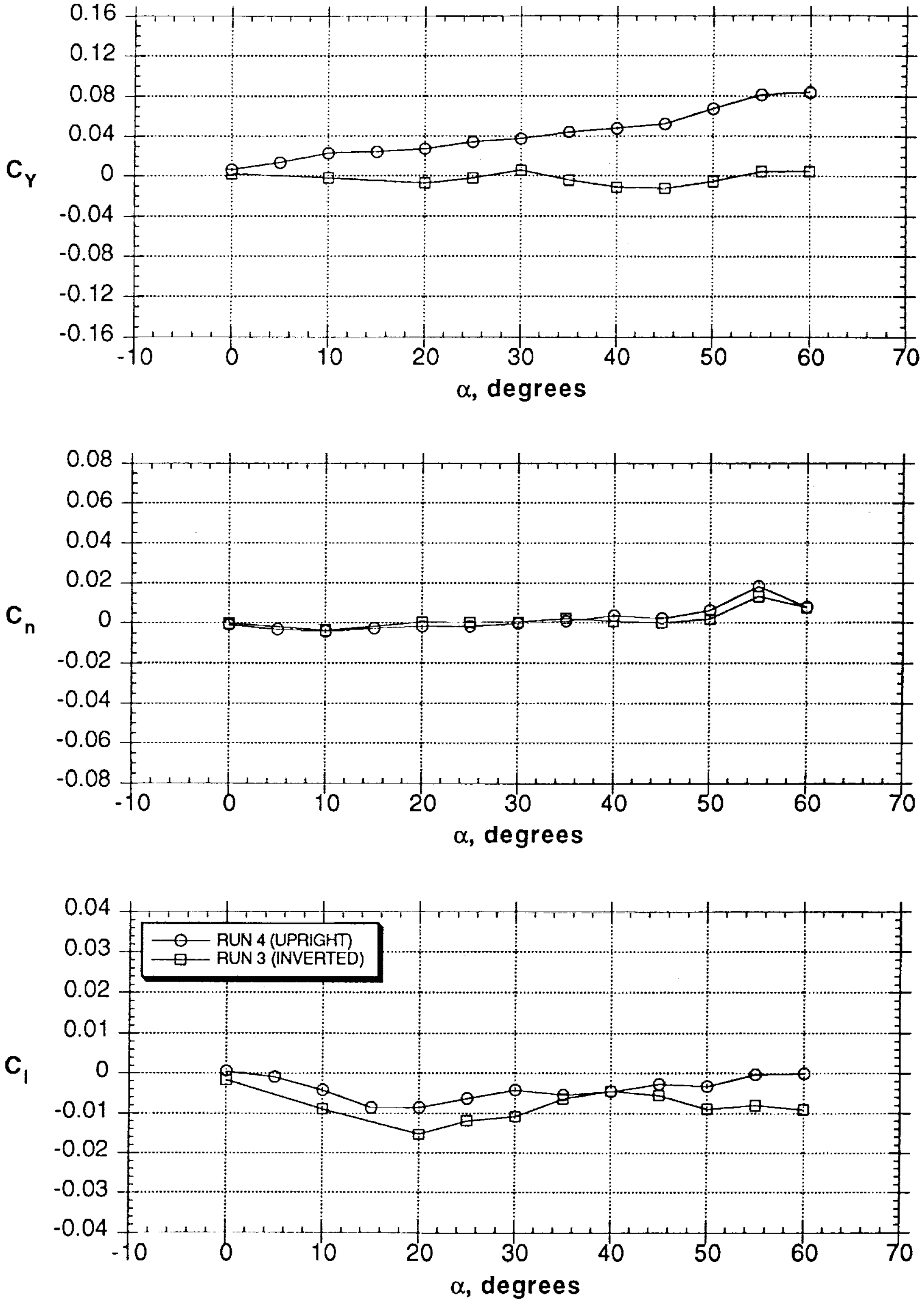

Figure 10 - Concluded

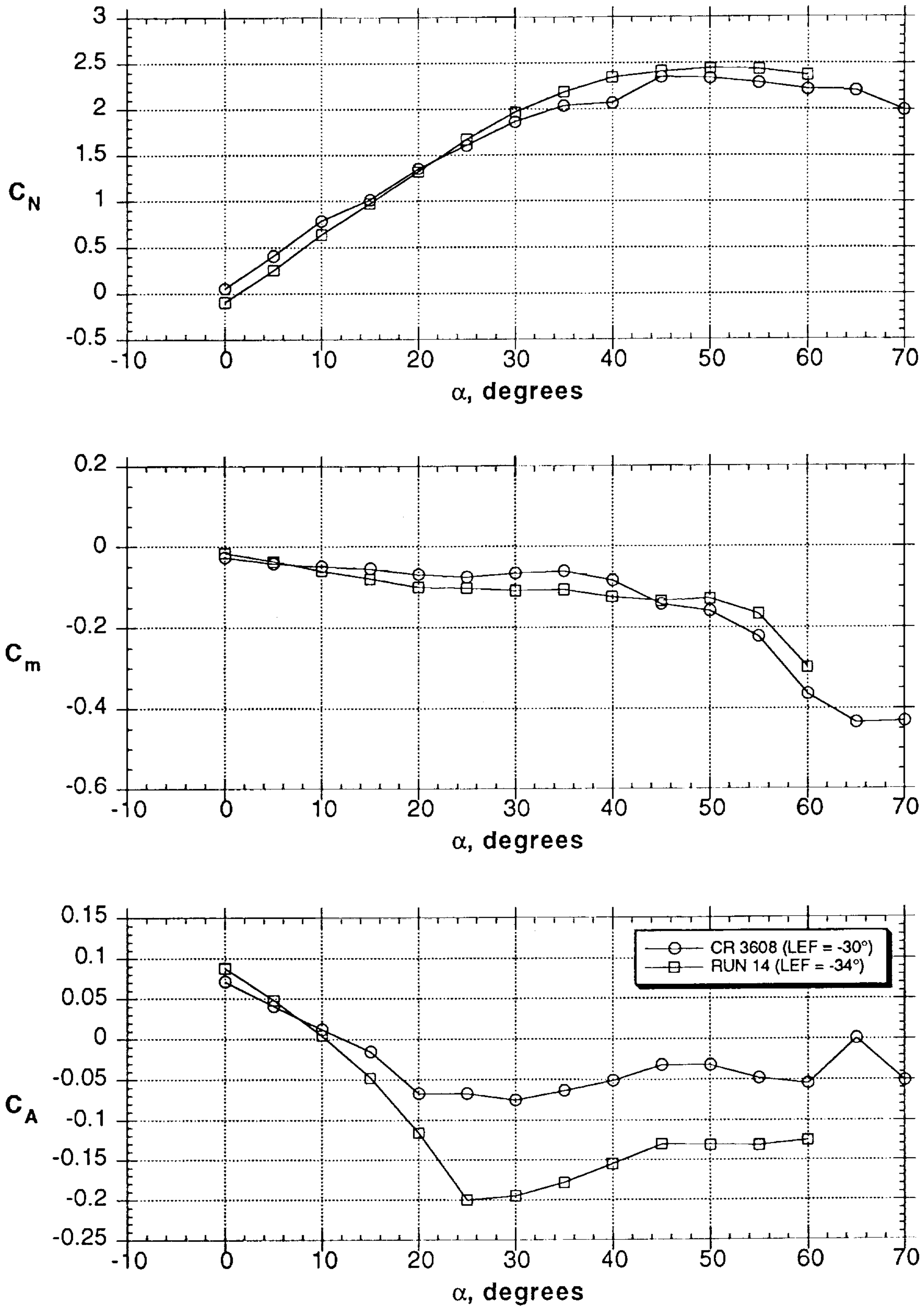

Figure 11 - Comparison of results to data from NASA CR 3608 (Ref. 38)

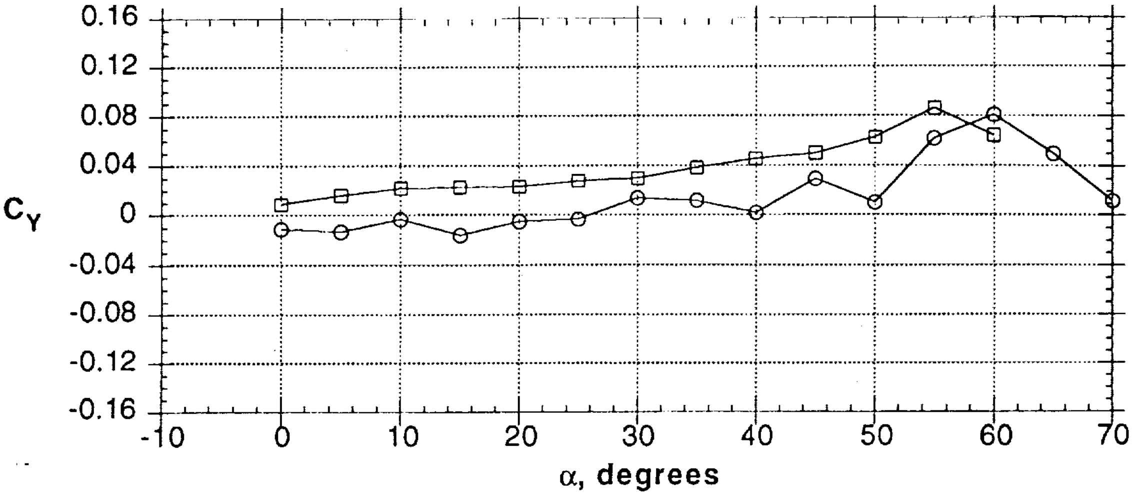

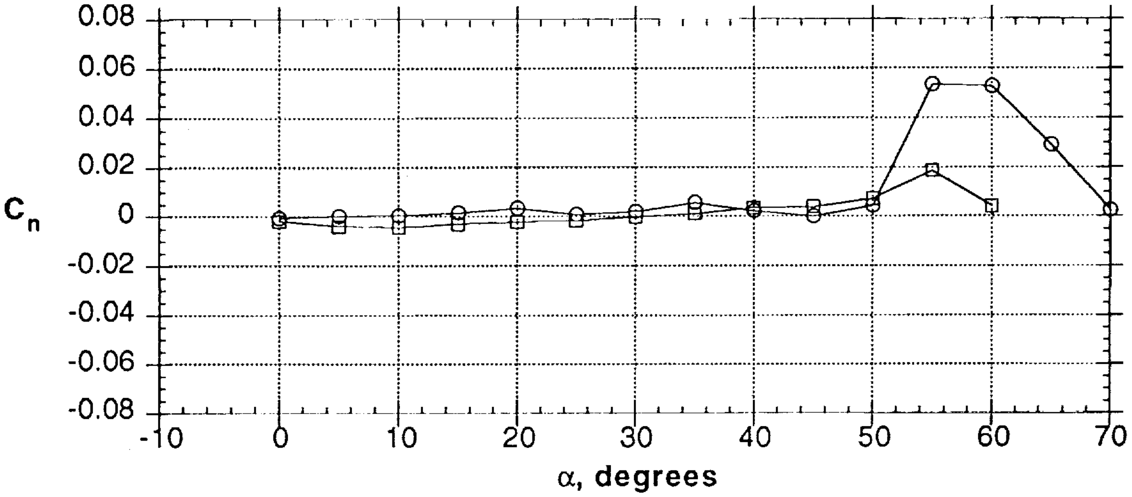

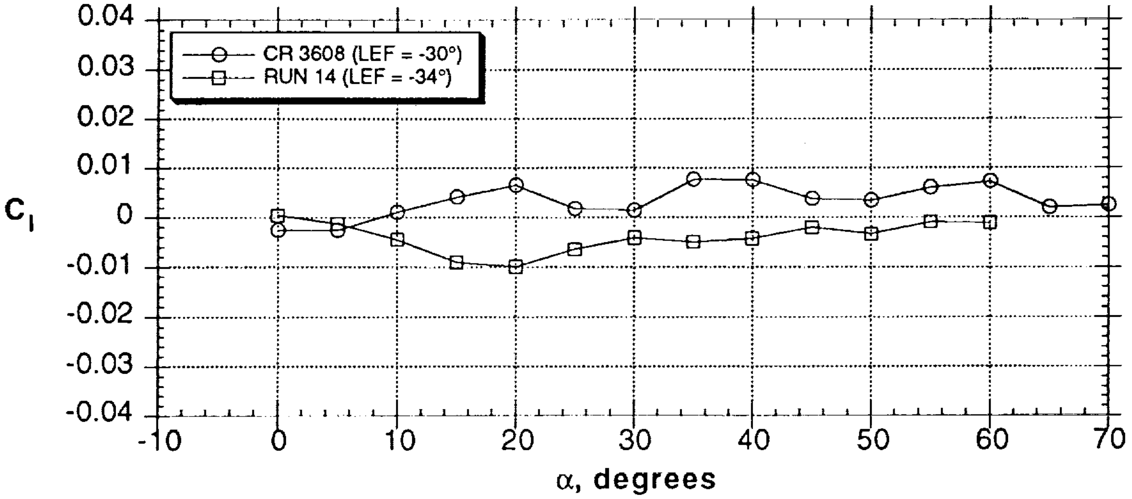

Figure 11 - Concluded

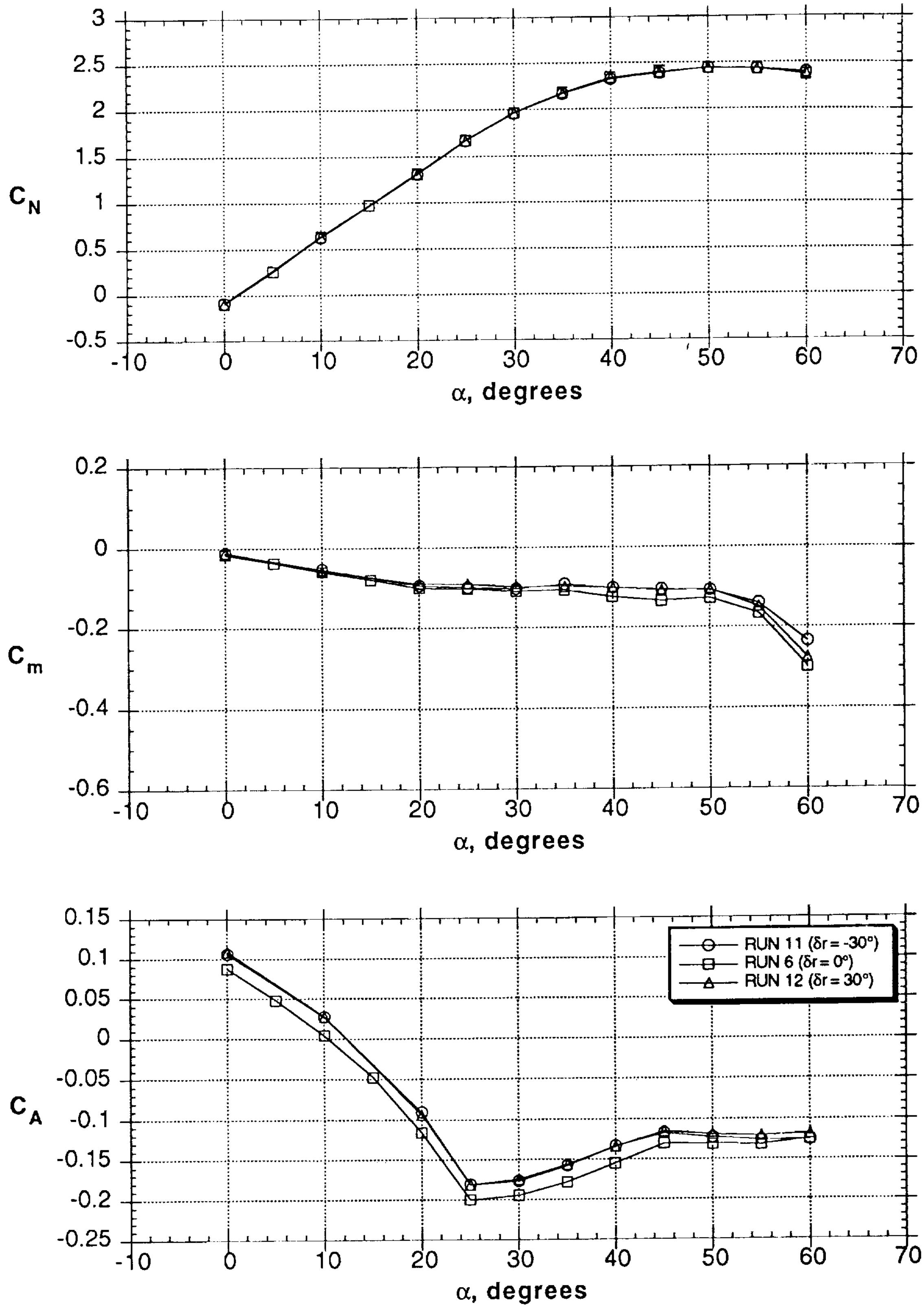

Figure 12 - Rudder control power

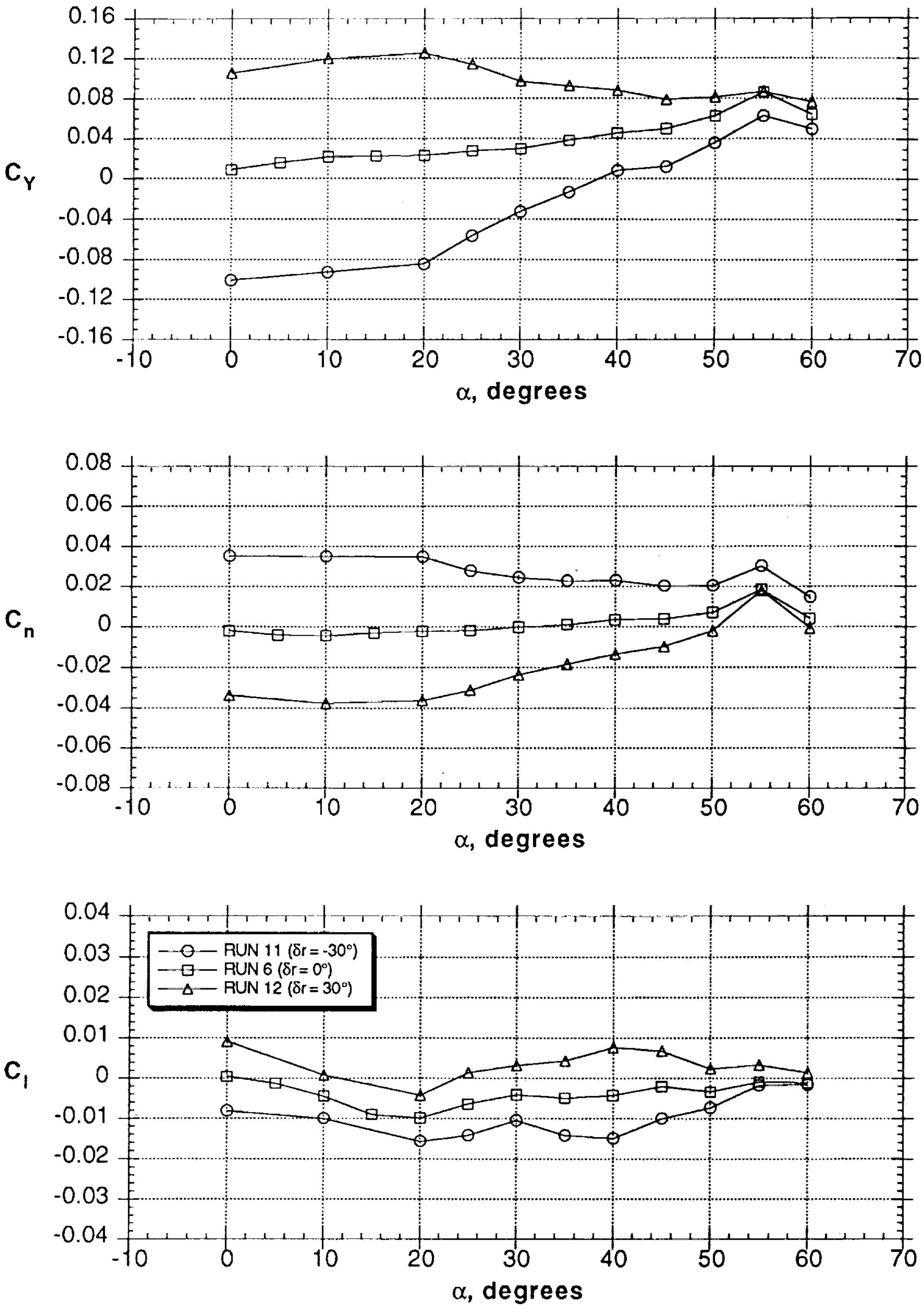

Figure 12 - Concluded

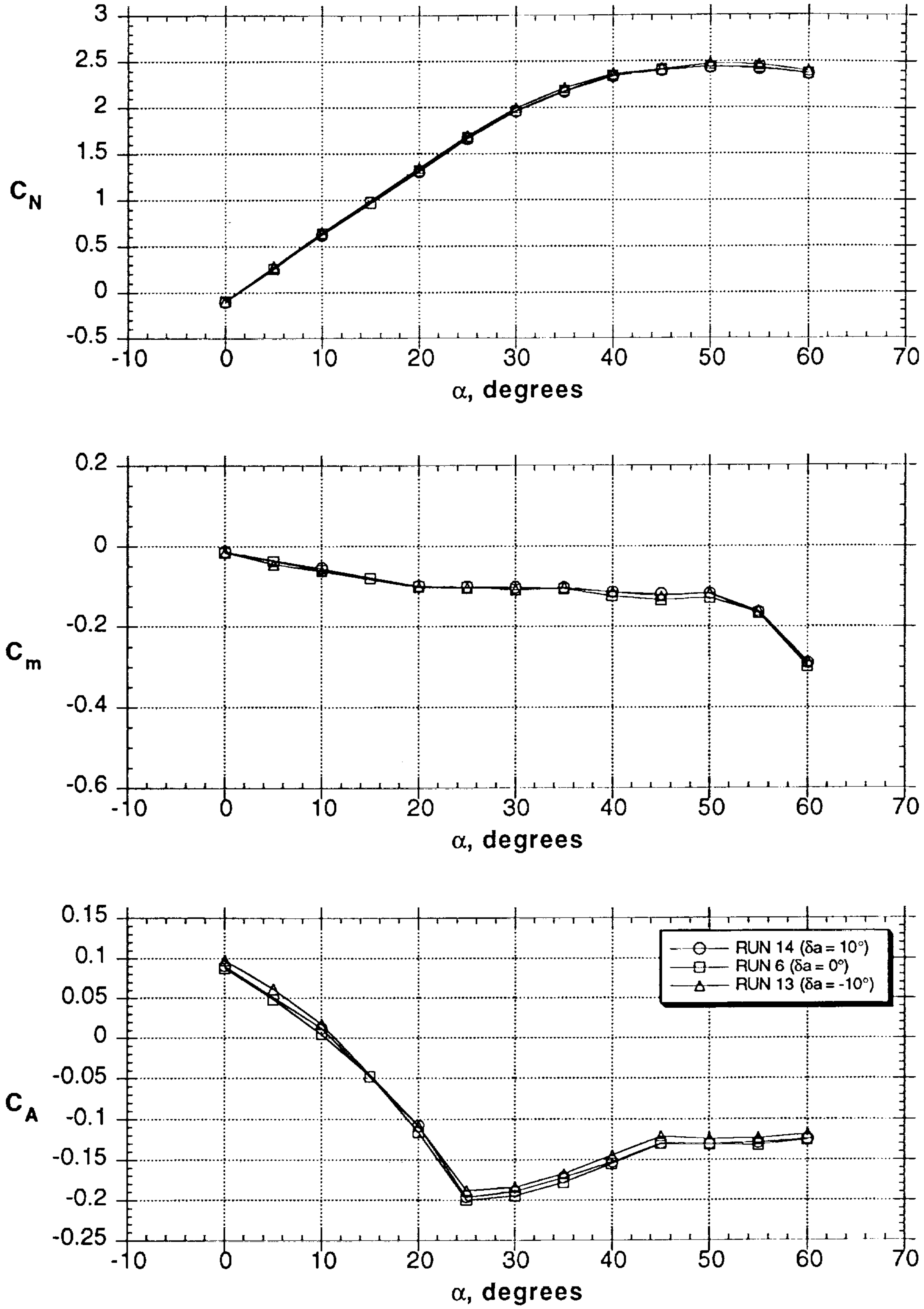

Figure 13 - Aileron control power

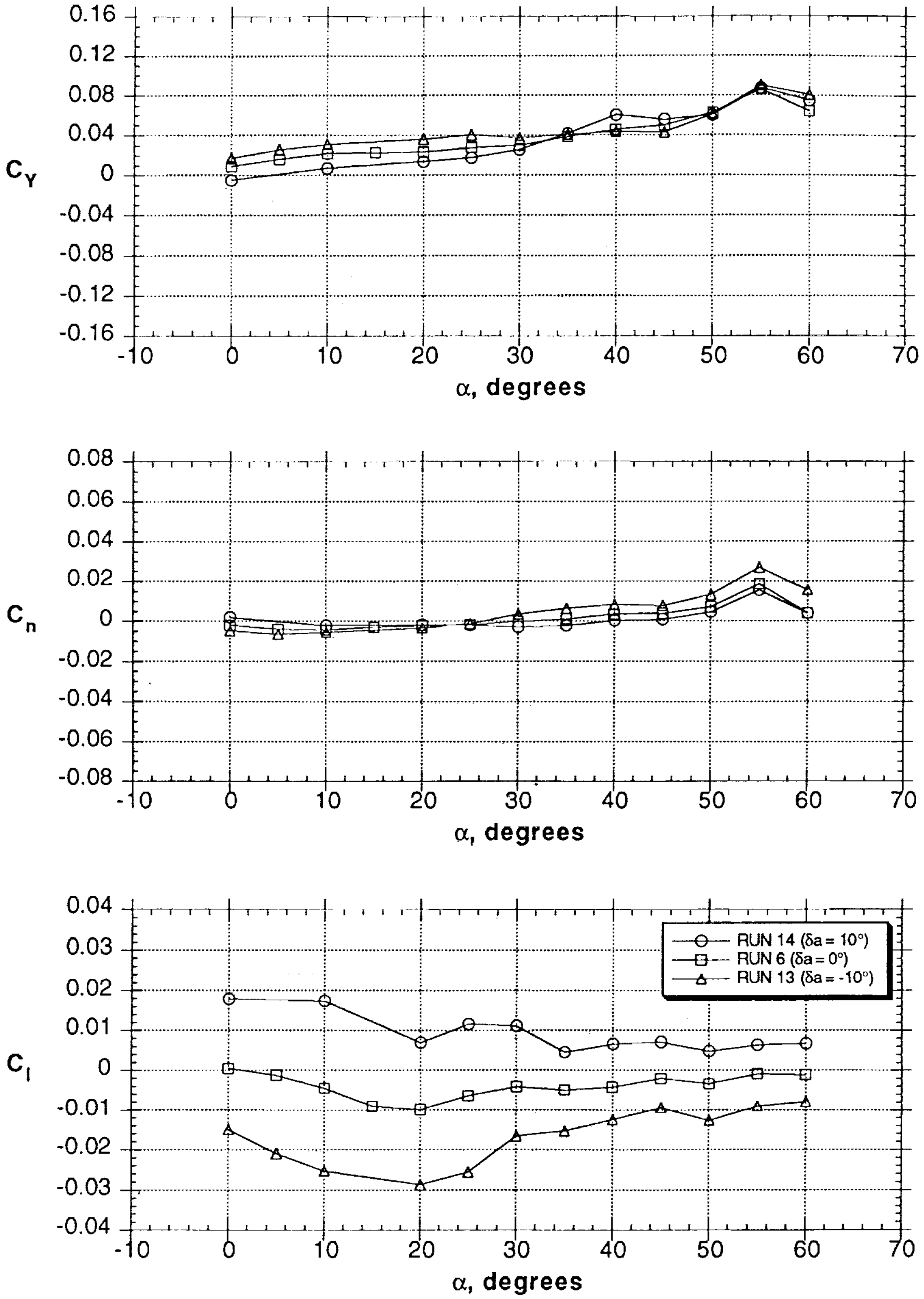

Figure 13 - Concluded

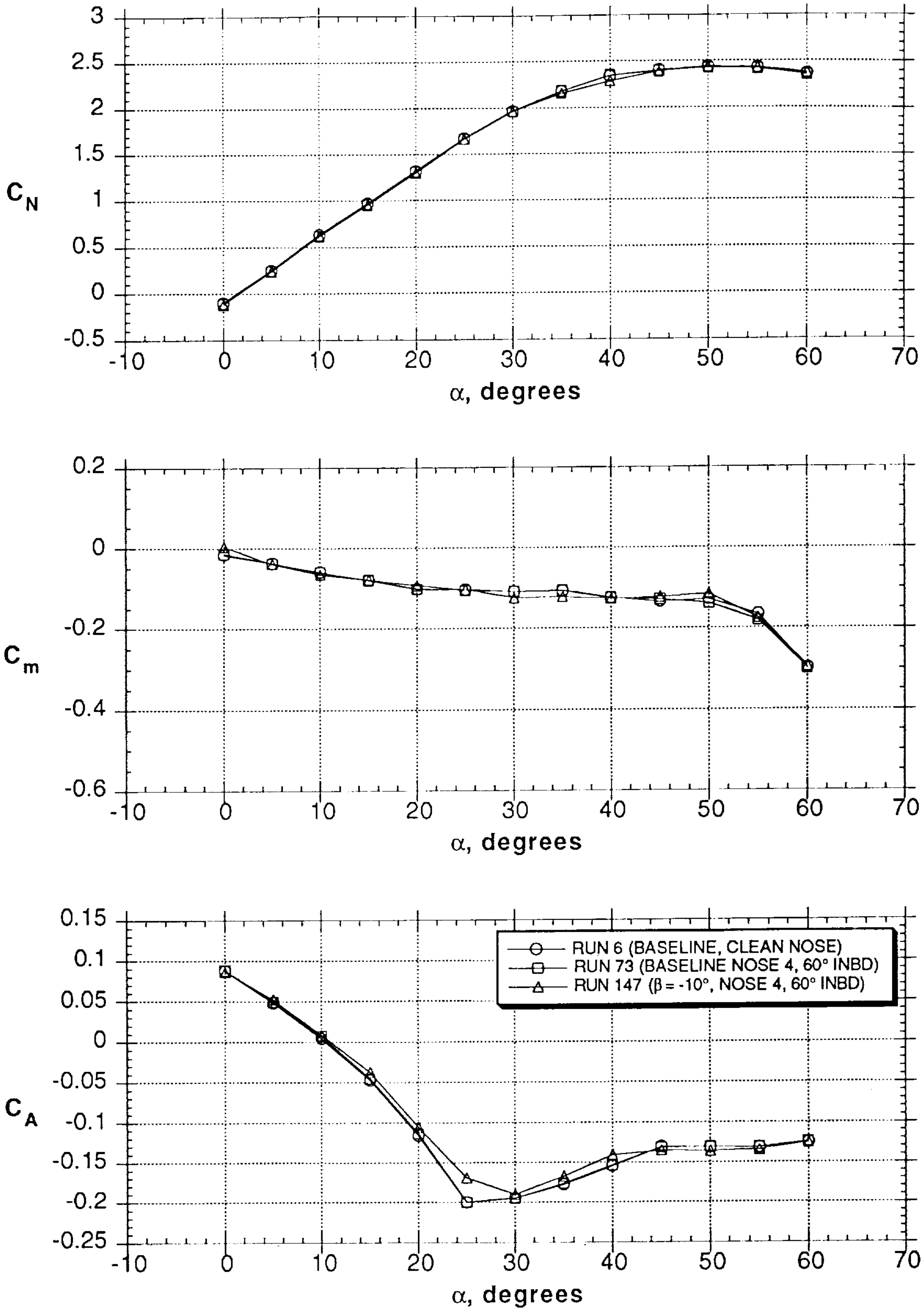

Figure 14 - Effect of sideslip (nose 4)

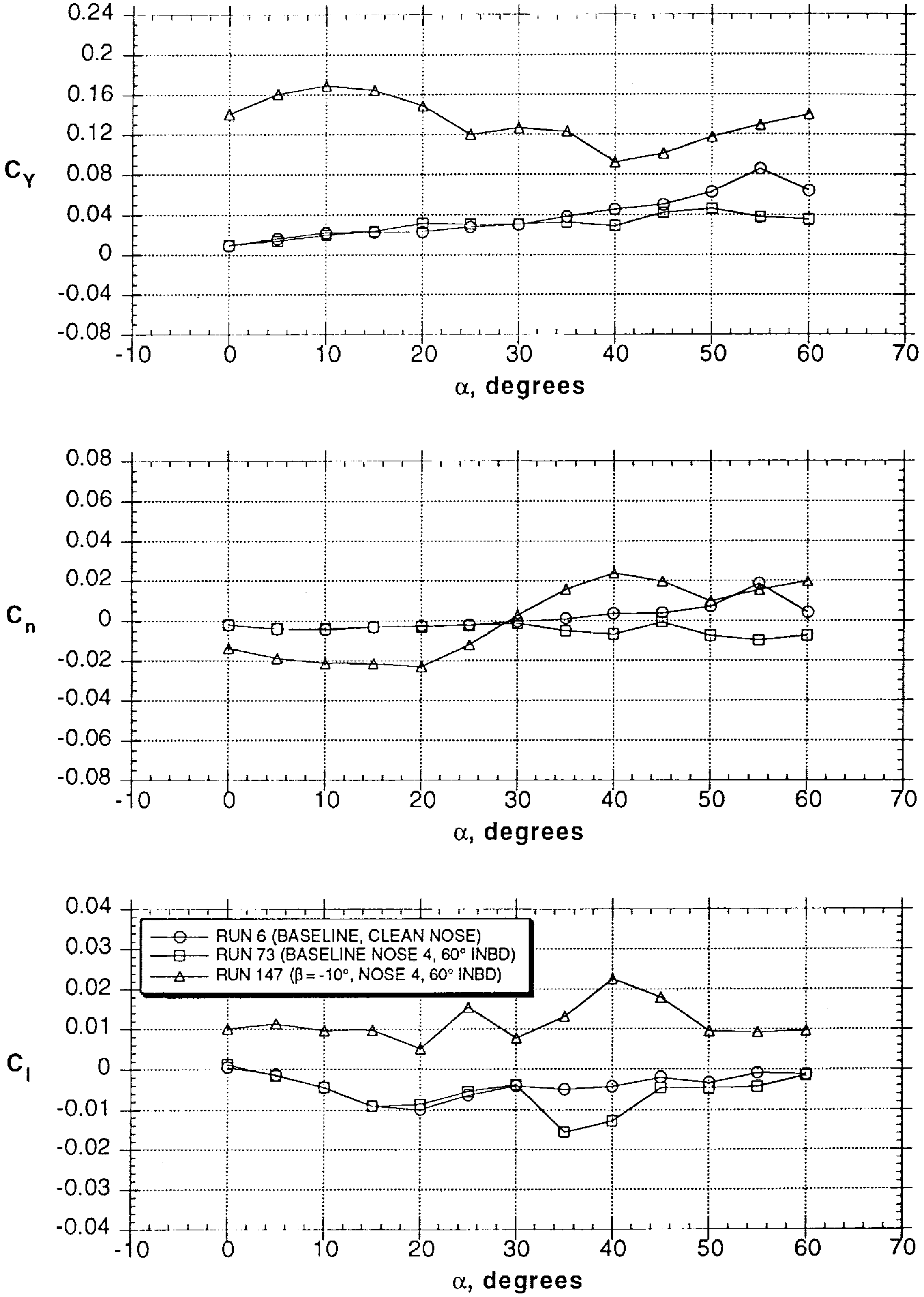

Figure 14 - Concluded

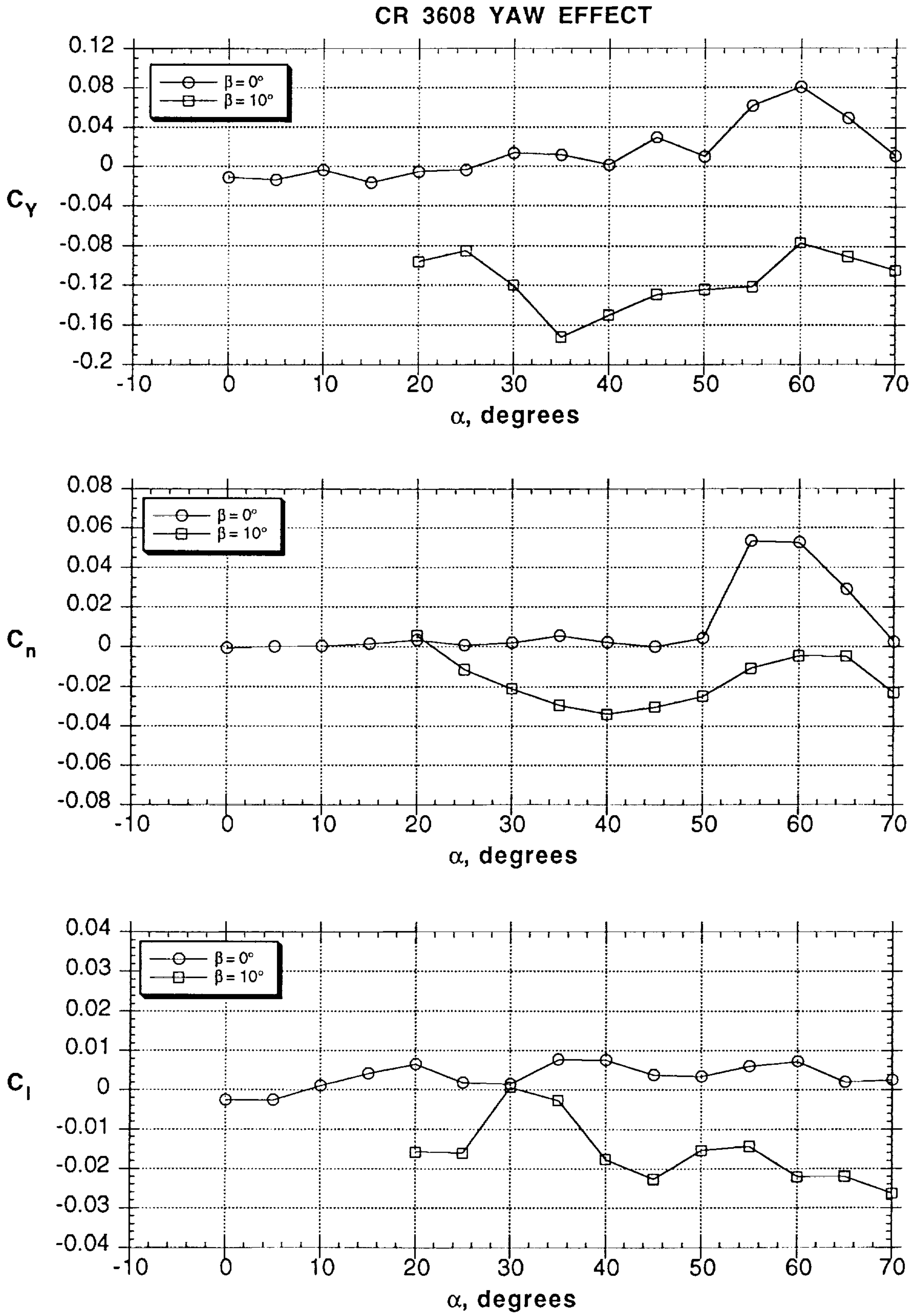

Figure 15 - Effect of sideslip (data from NASA CR 3608, Ref. 38)

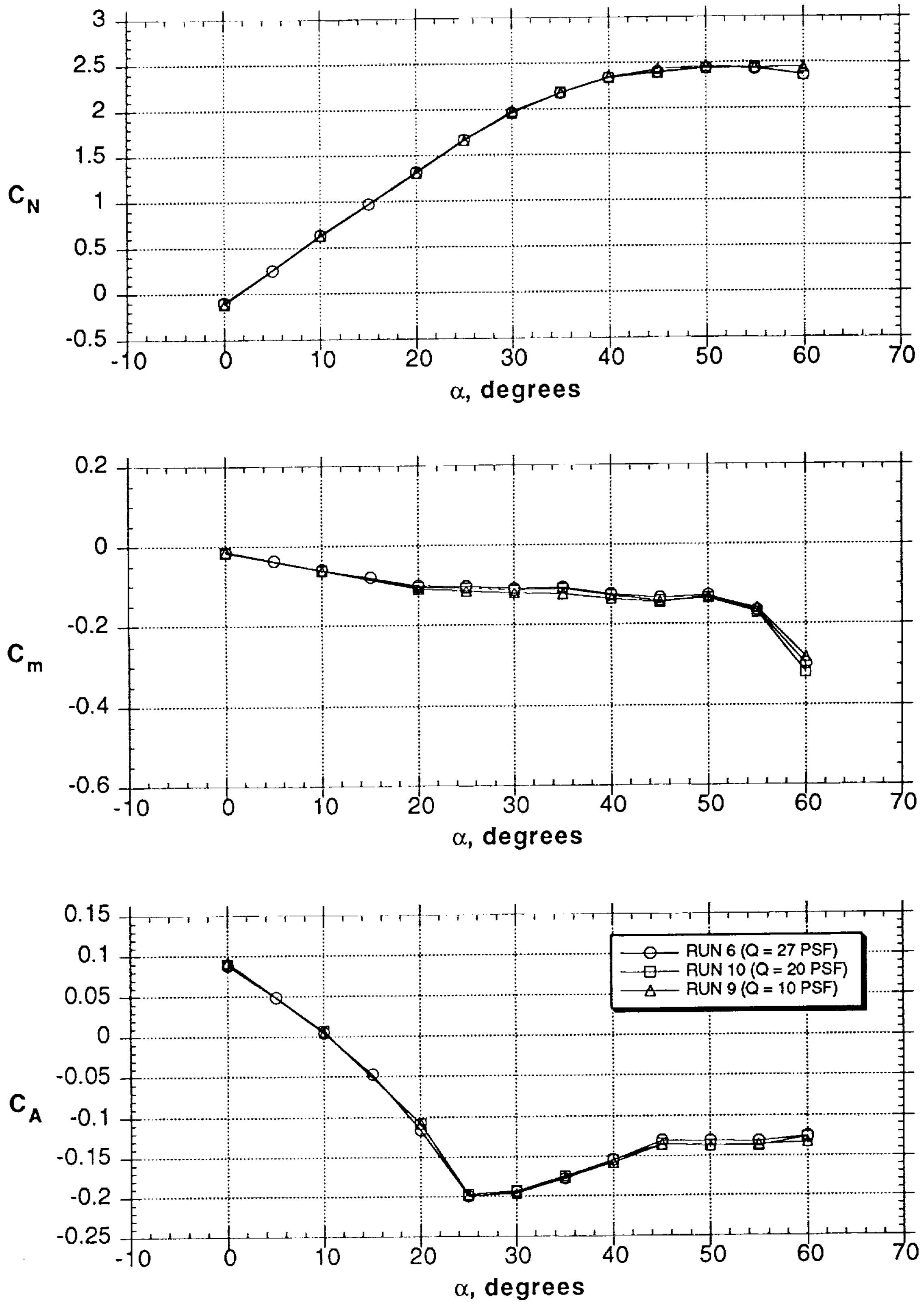

Figure 16 - Effect of Reynolds number

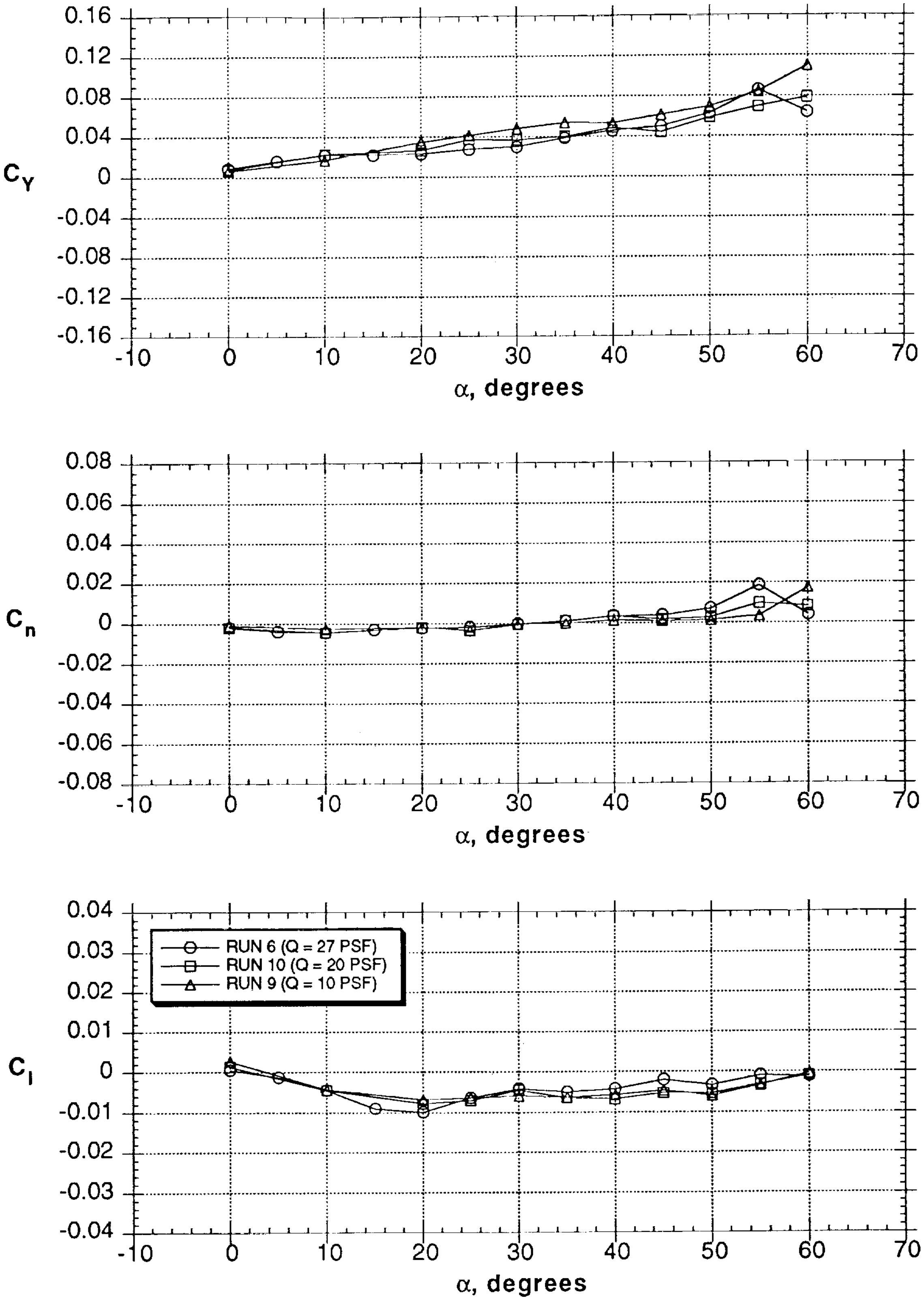

Figure 16 - Concluded

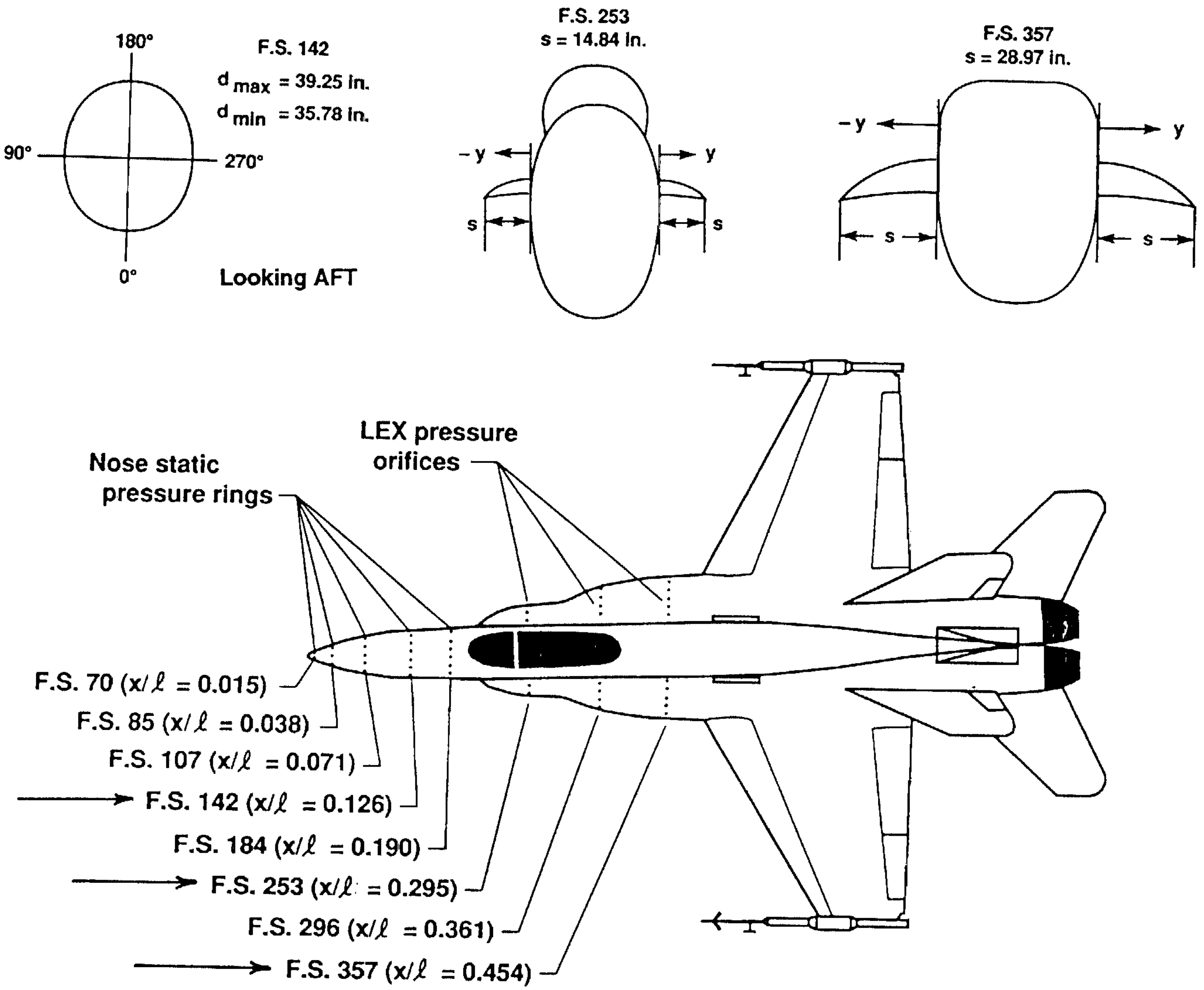

Figure 17 - Pressure tap station location on full-scale F/A-18 model and on F/A-18 HARV

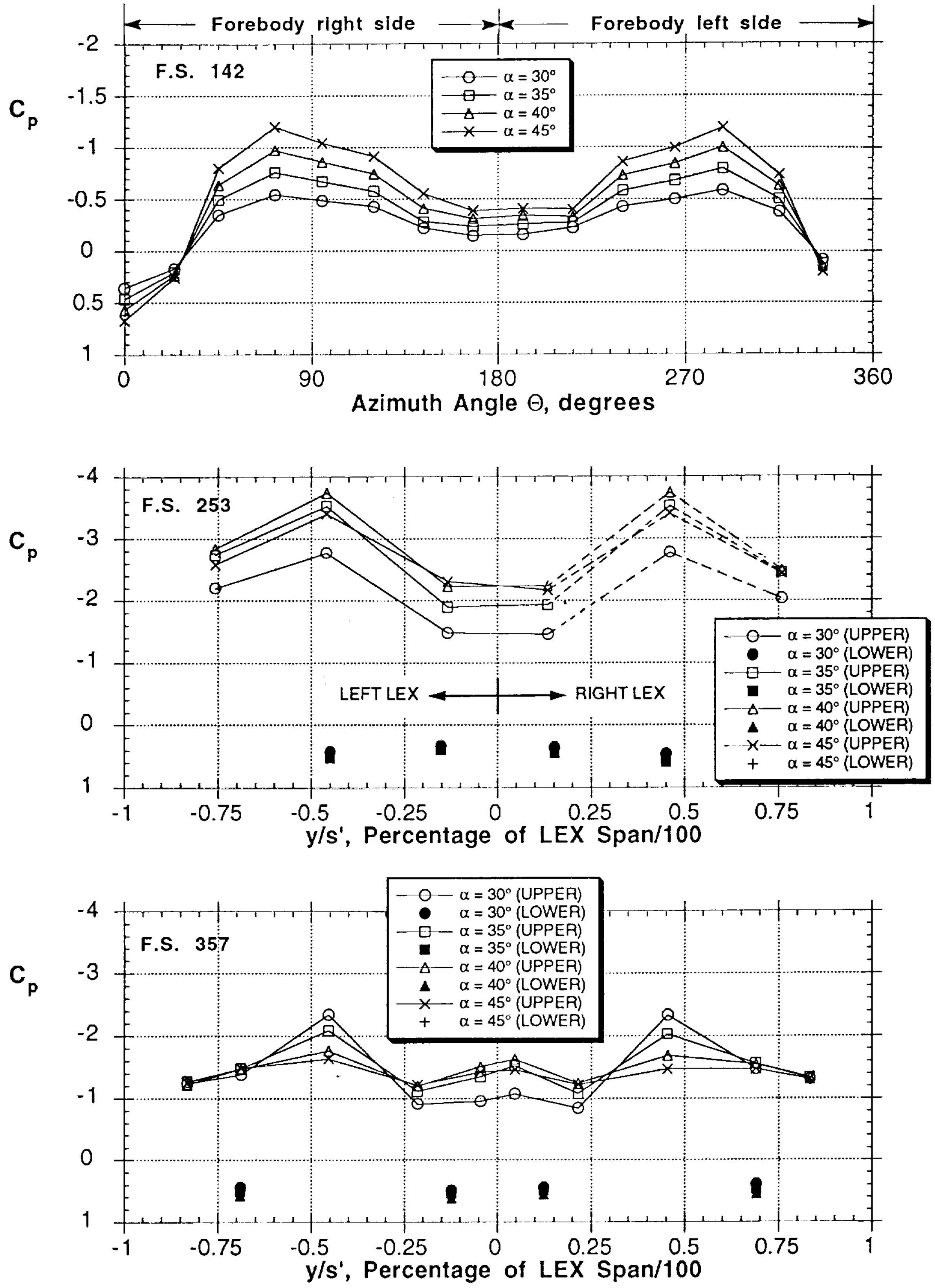

Figure 18 - Forebody and LEX pressure distributions (baseline nose)

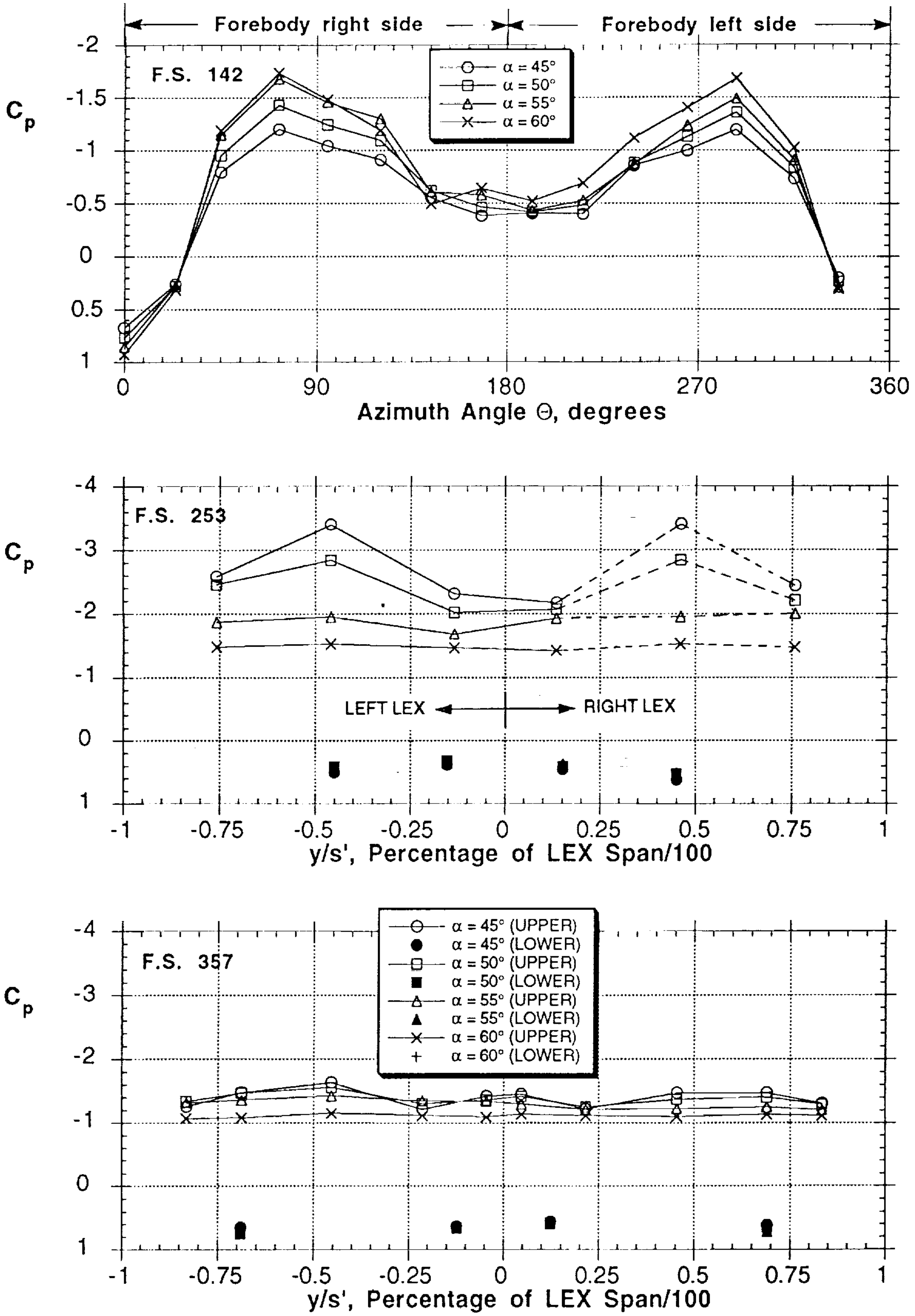

Figure 18 - Concluded

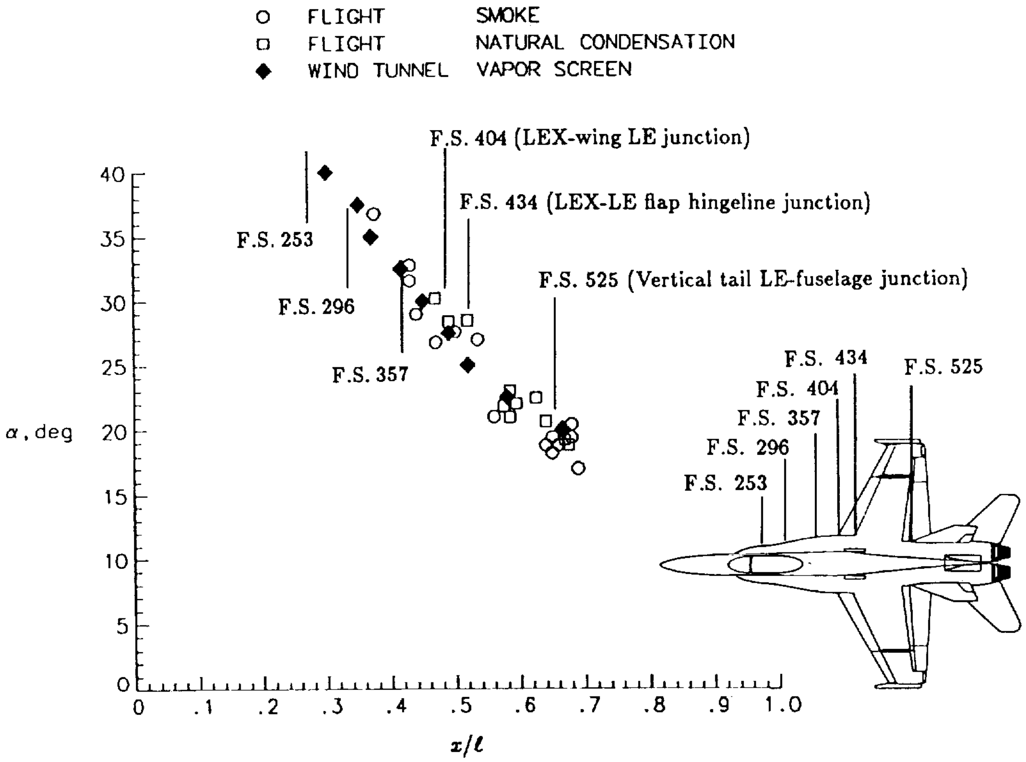

Figure 19 - LEX vortex breakdown progression with angle of attack on a 6% F/A-18 model (M = 0.4) and the F/A-18 HARV (M = 0.3) (Ref. 33)

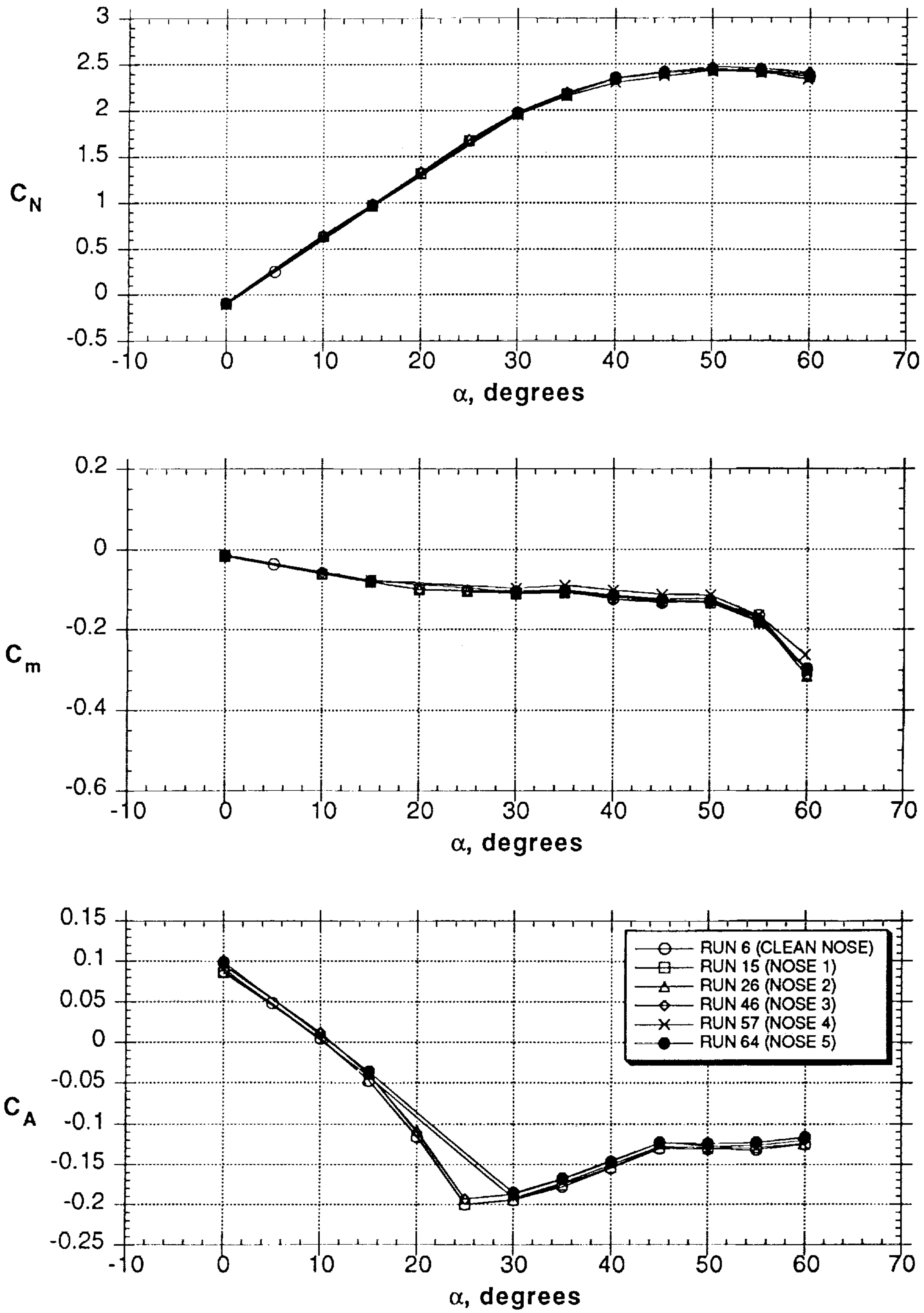

Figure 20 - Effect of jet nozzles on forces and moments

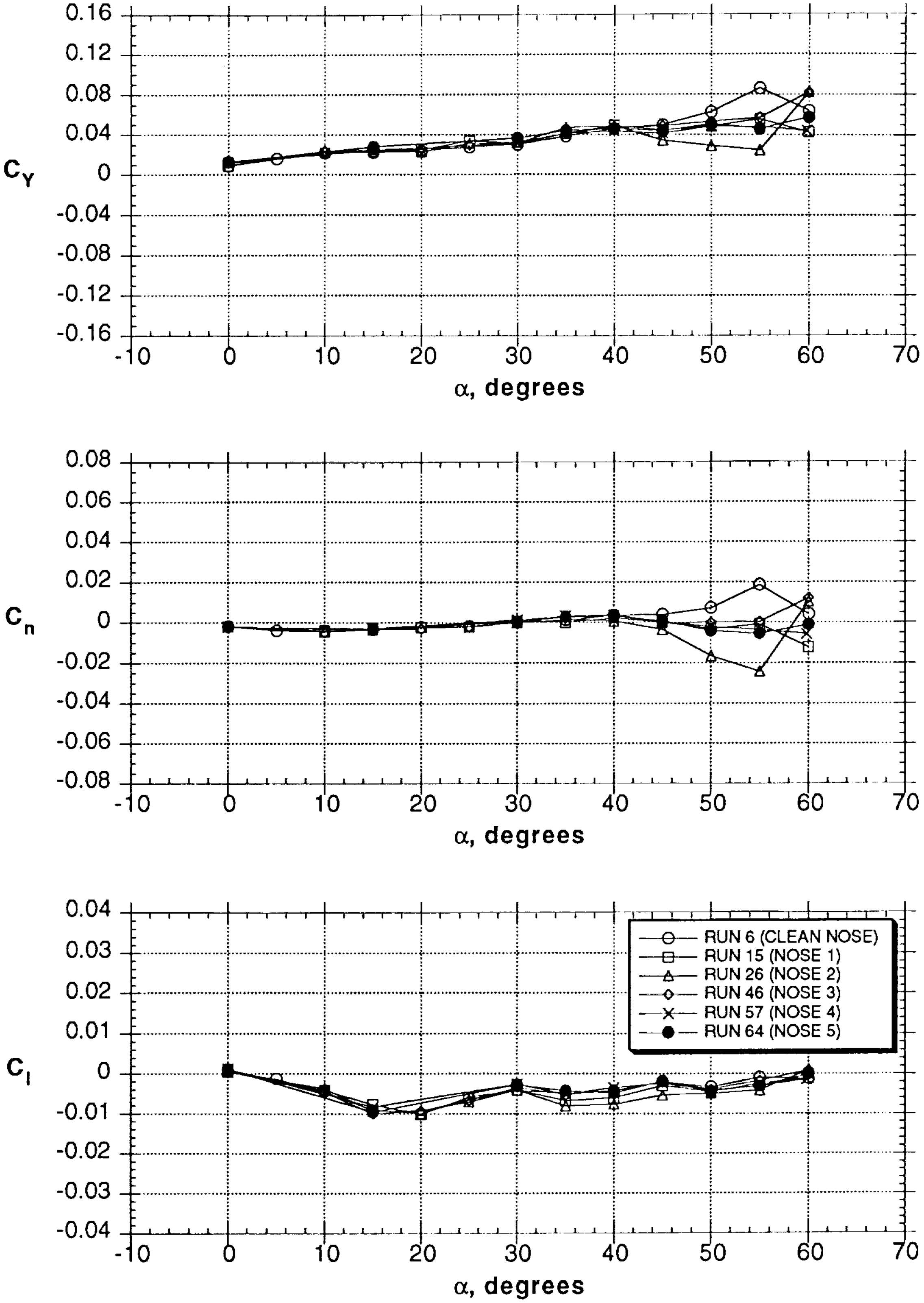

Figure 20 - Concluded

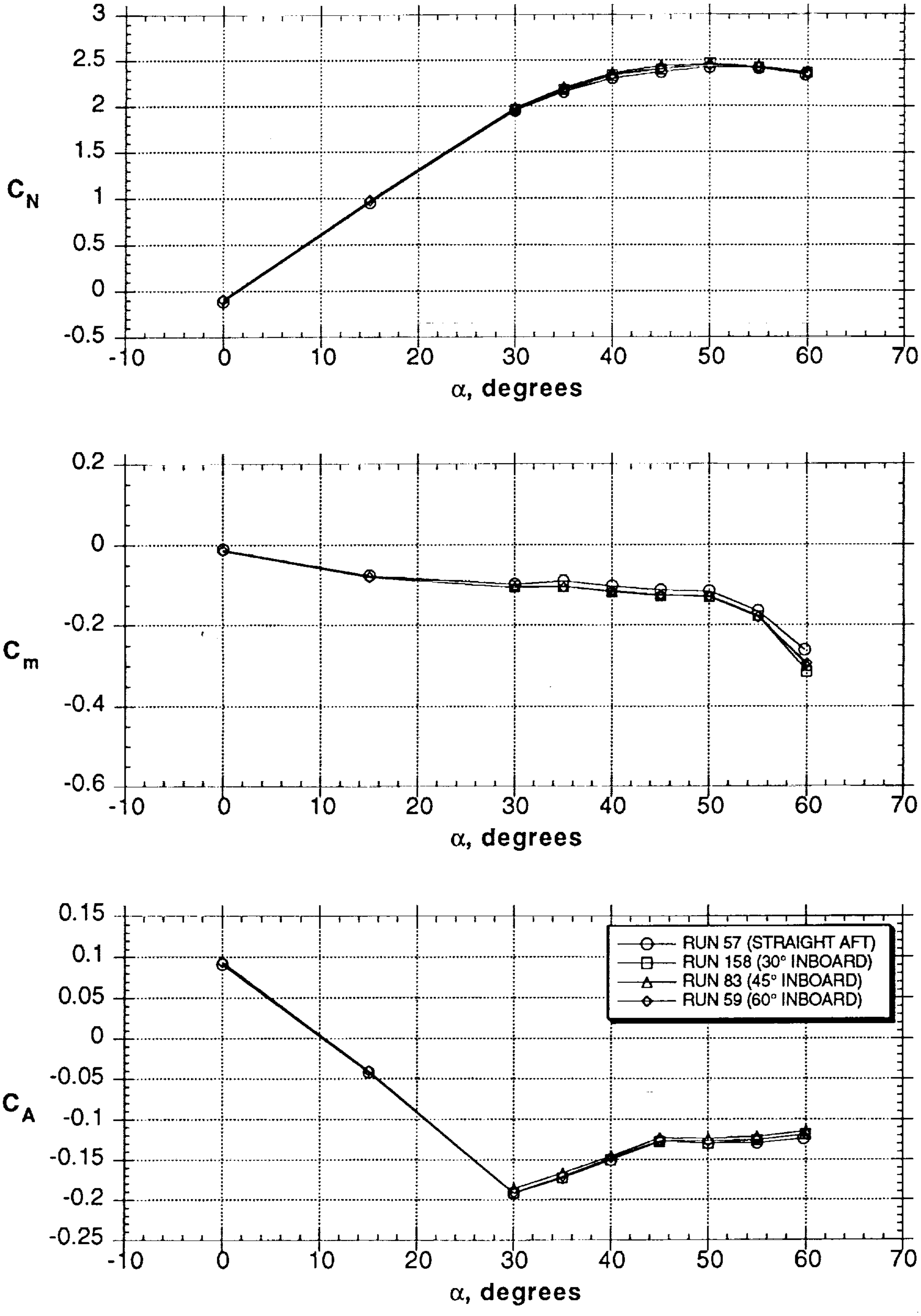

Figure 21 - Effect of jet nozzle cant angle on forces and moments (nose 4)

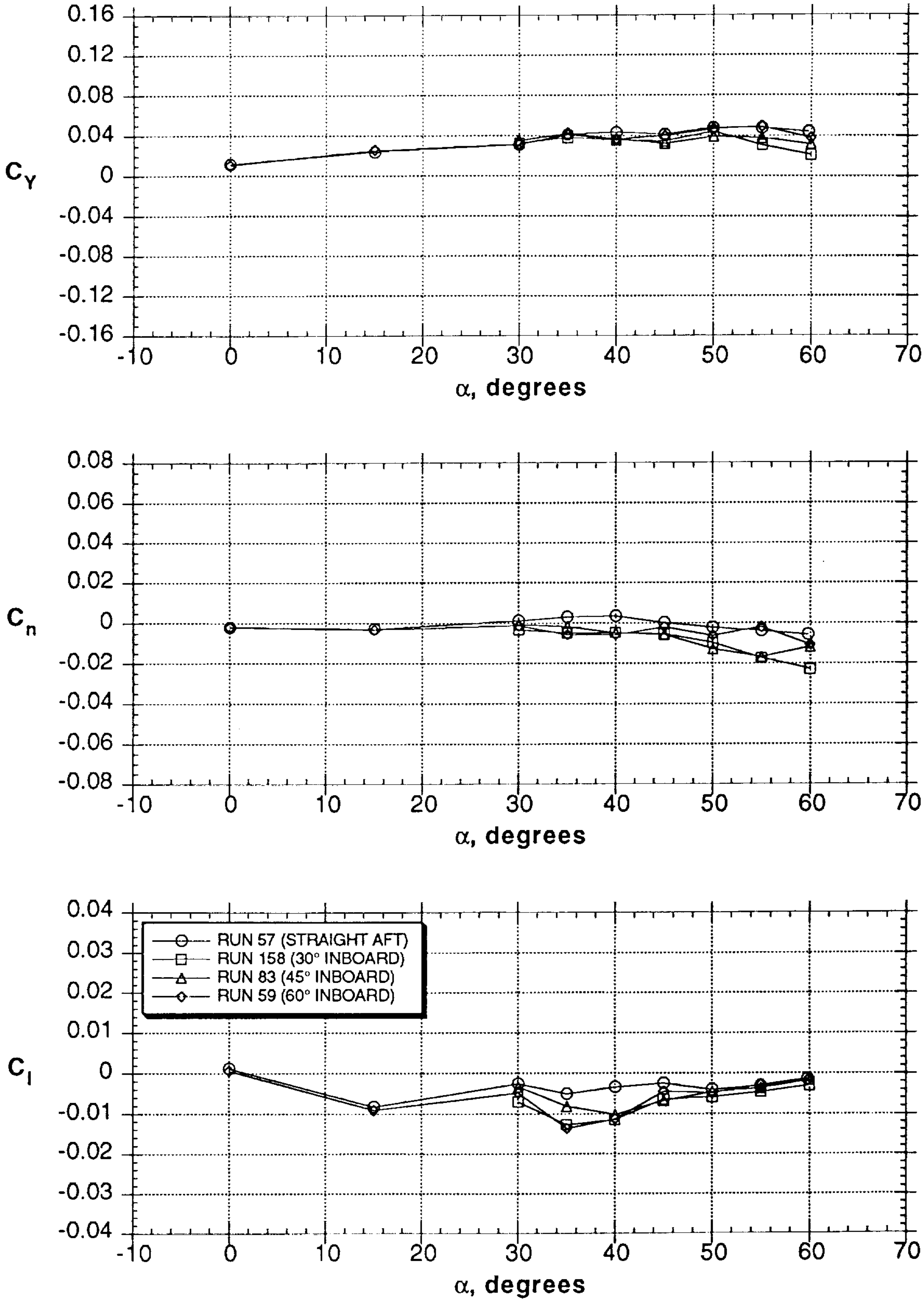

Figure 21 - Concluded

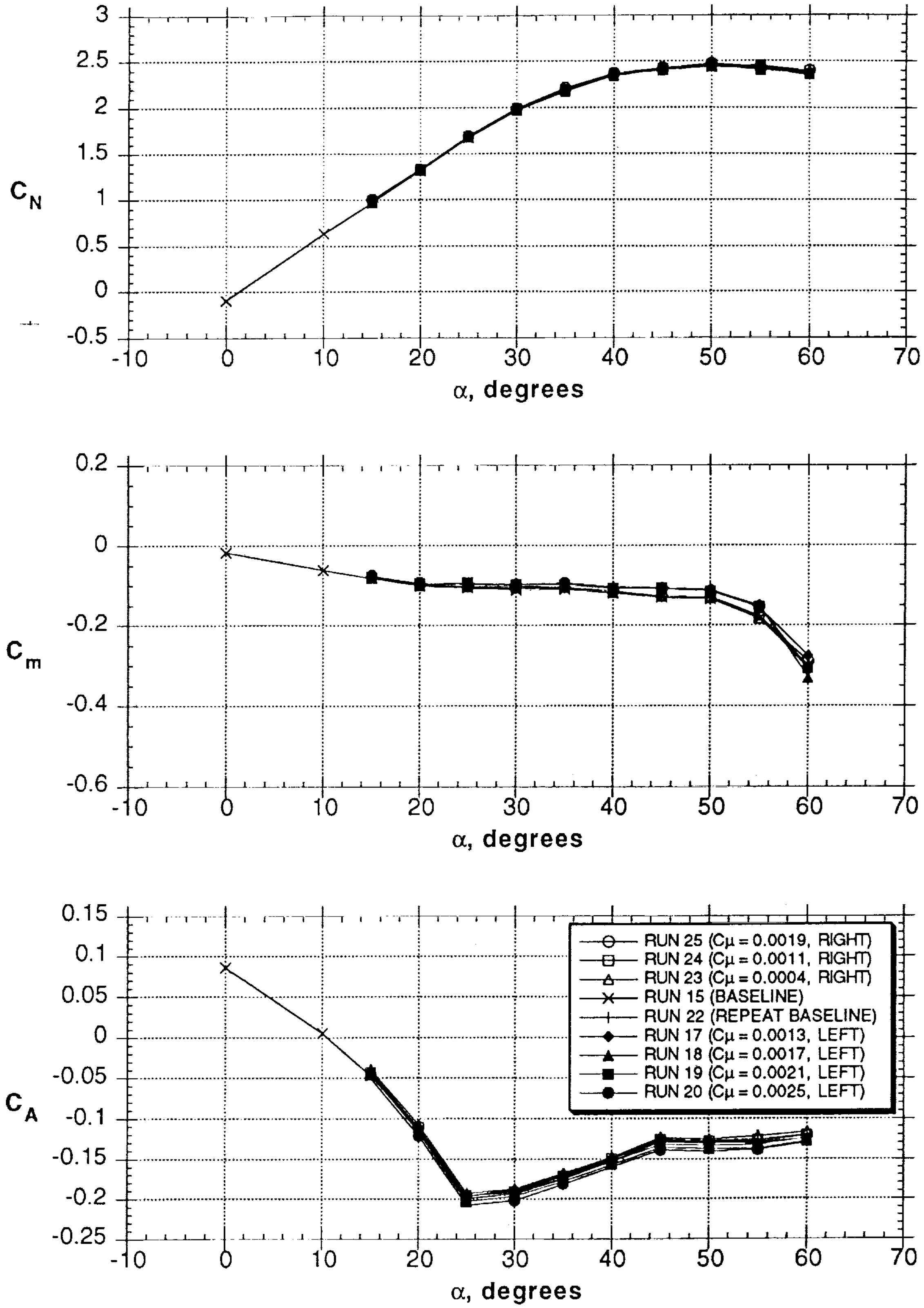

Figure 22 - Effect of jet blowing (straight aft, nose 1)

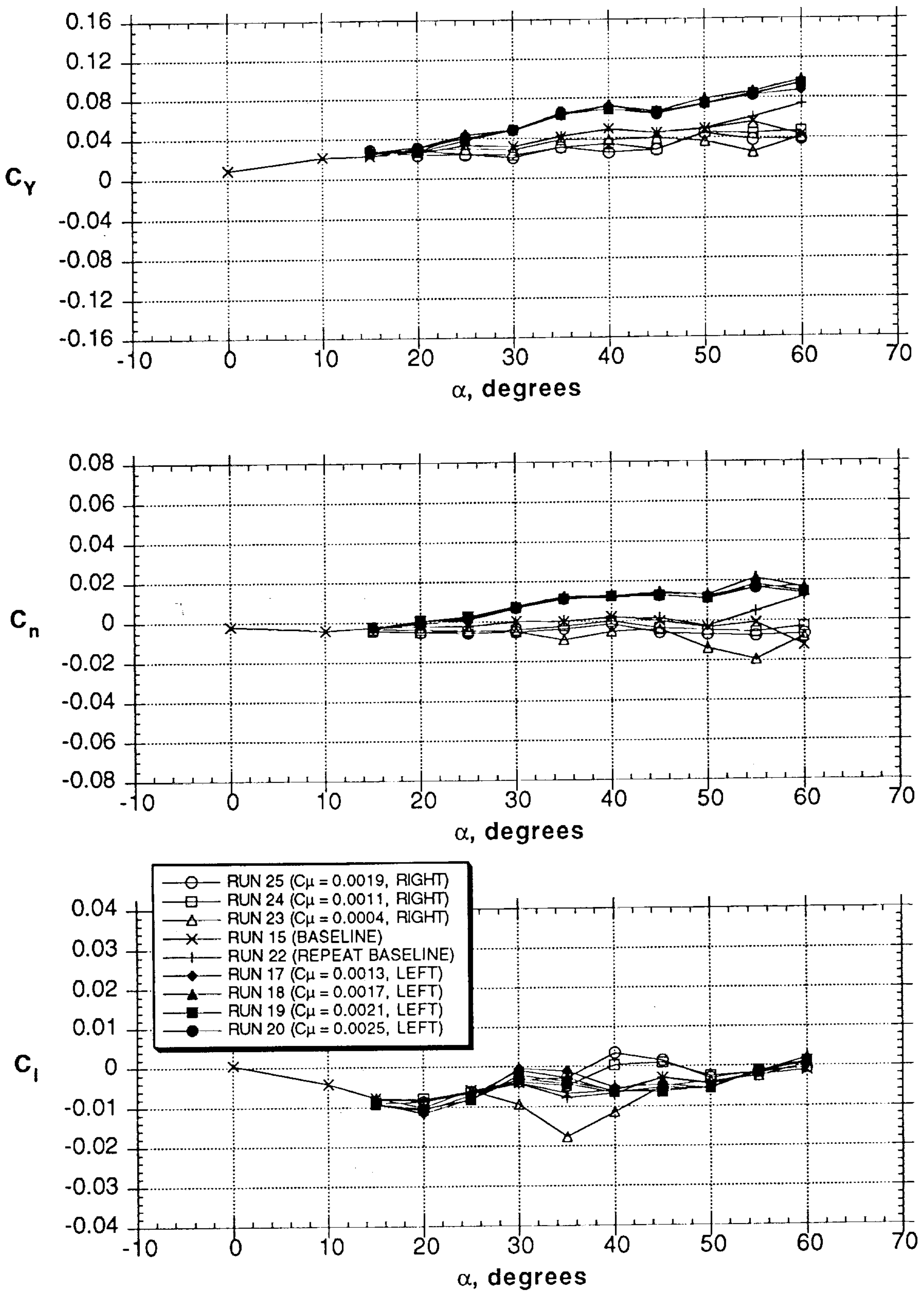

Figure 22 - Concluded

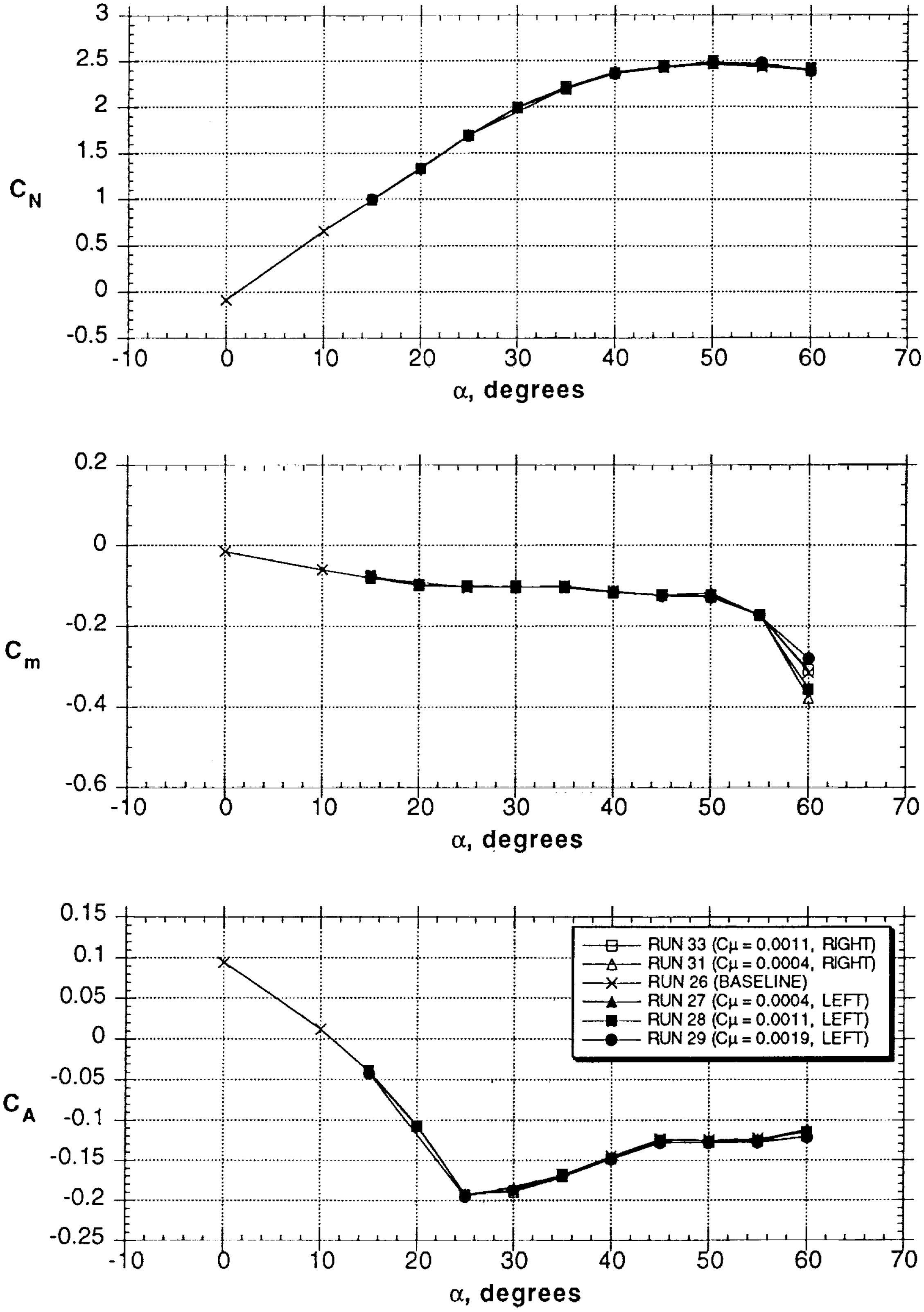

Figure 23 - Effect of jet blowing (straight aft, nose 2)

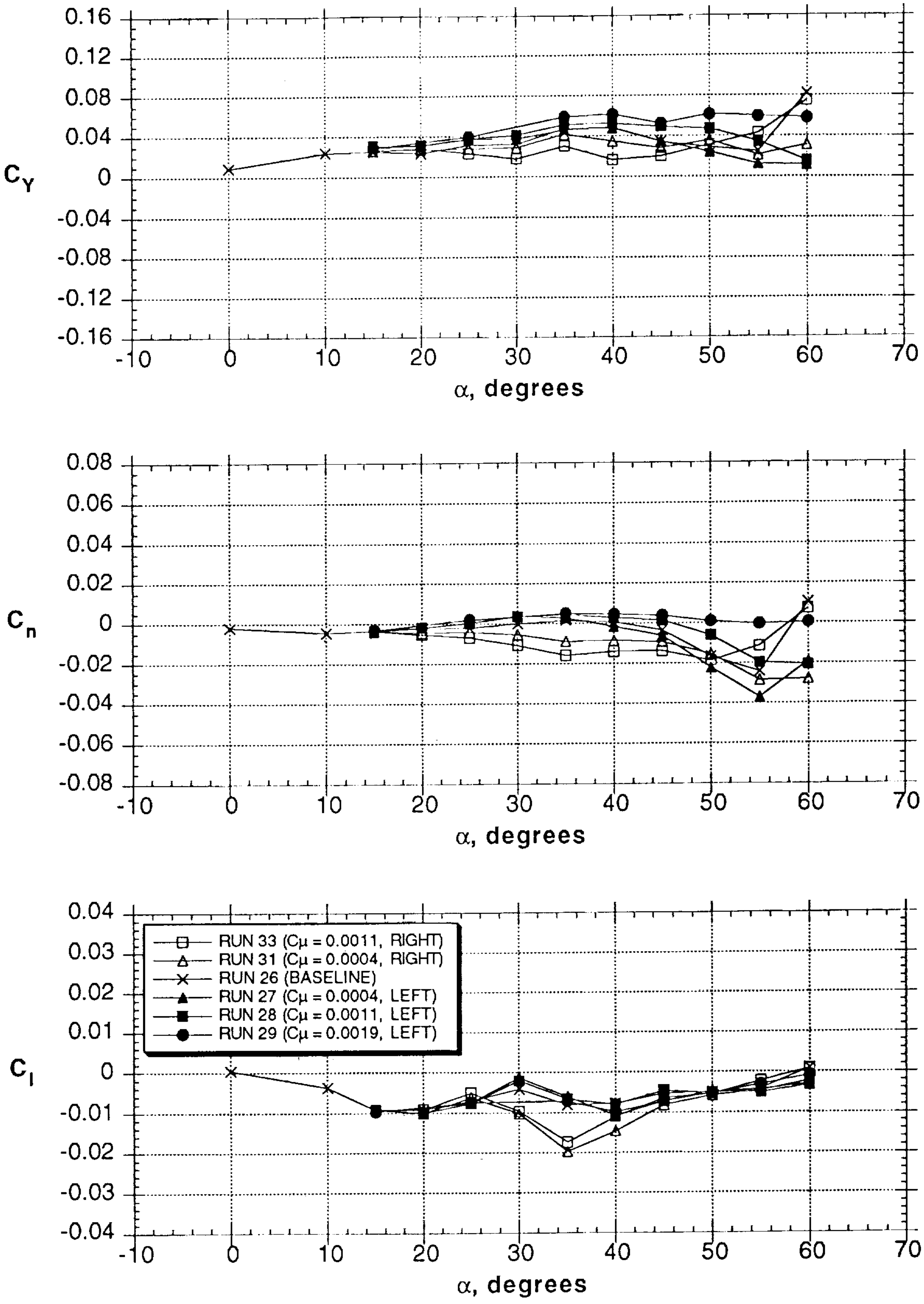

Figure 23 - Concluded

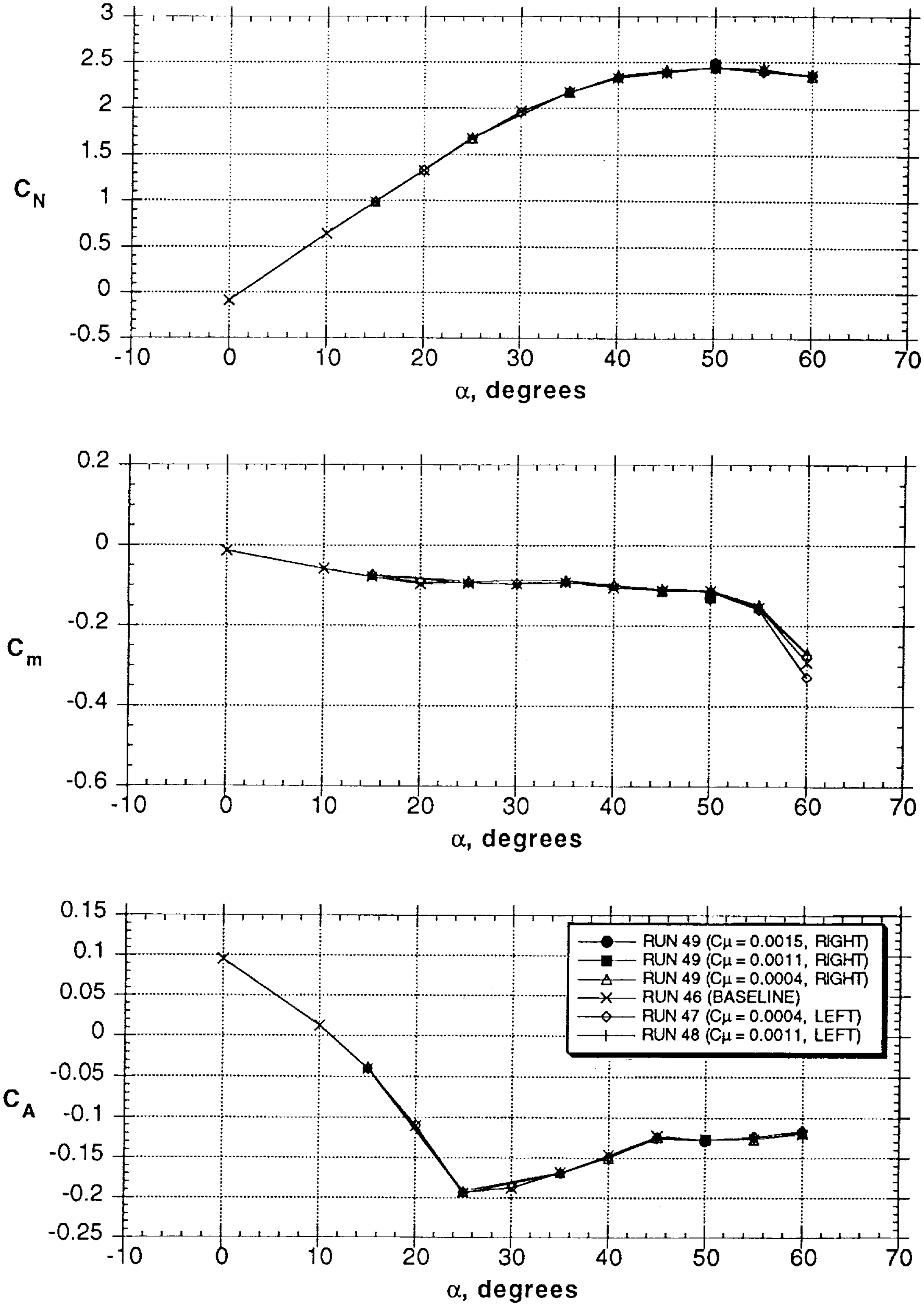

Figure 24 - Effect of jet blowing (straight aft, nose 3)

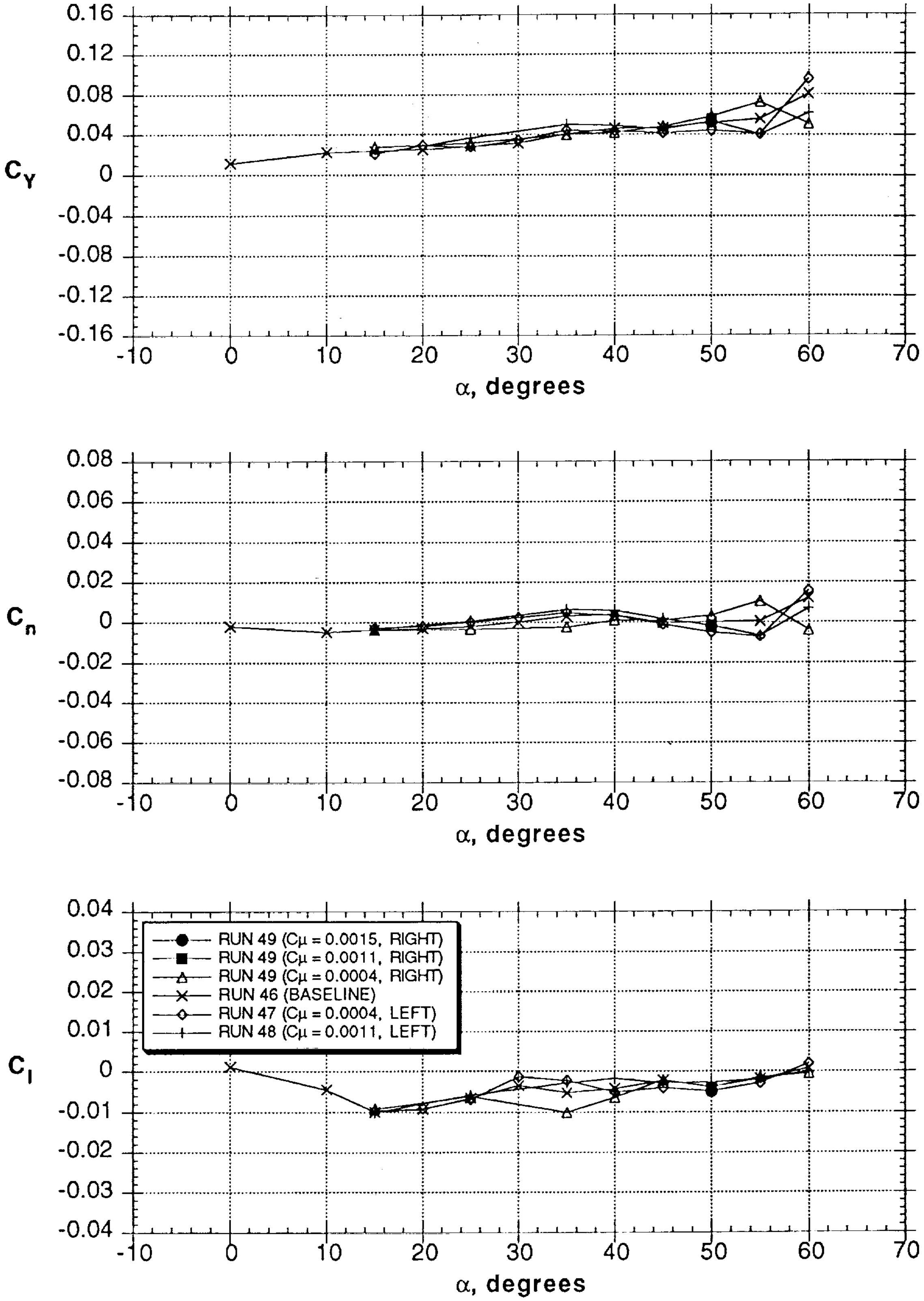

Figure 24 - Concluded

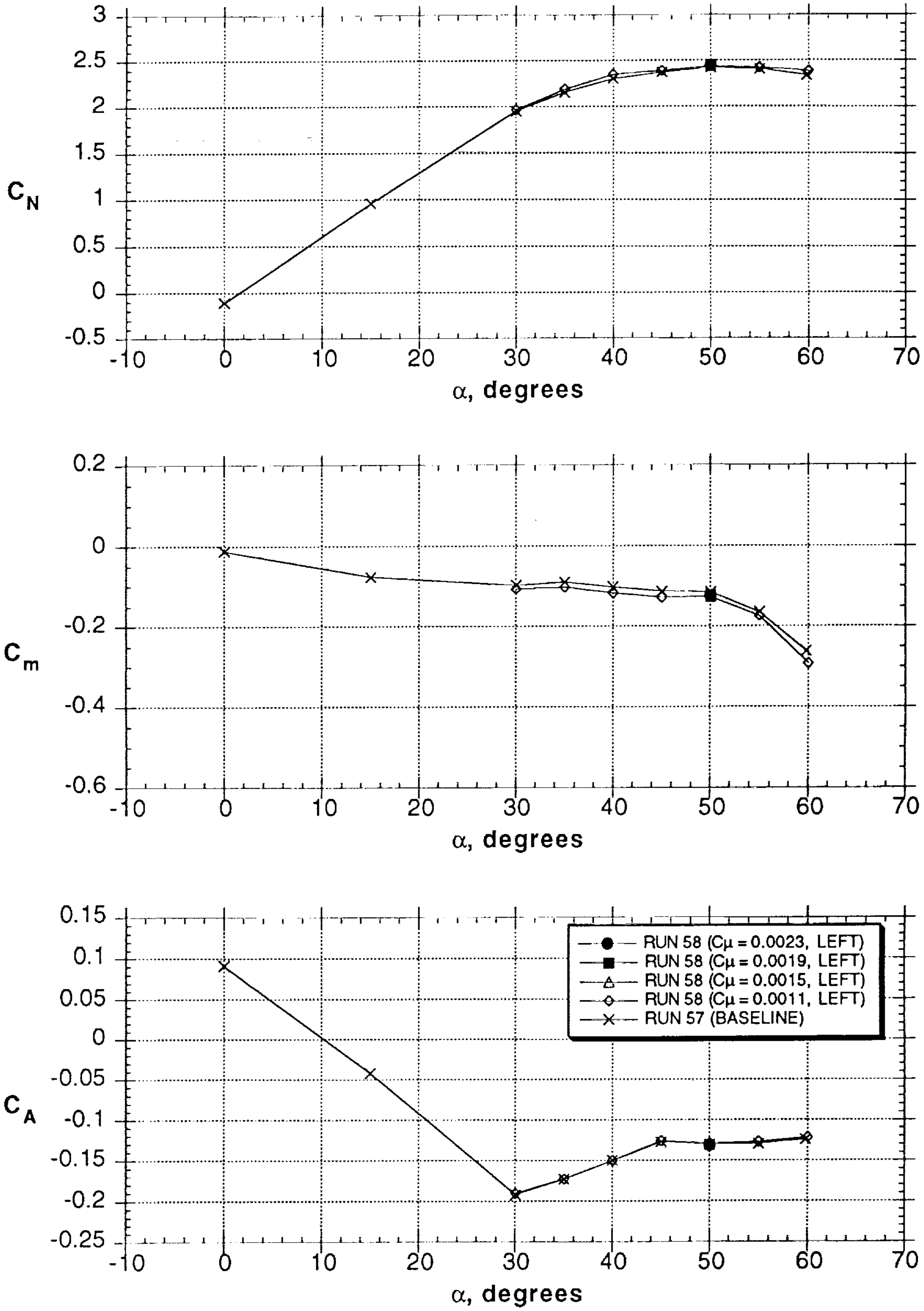

Figure 25 - Effect of jet blowing (straight aft, nose 4)

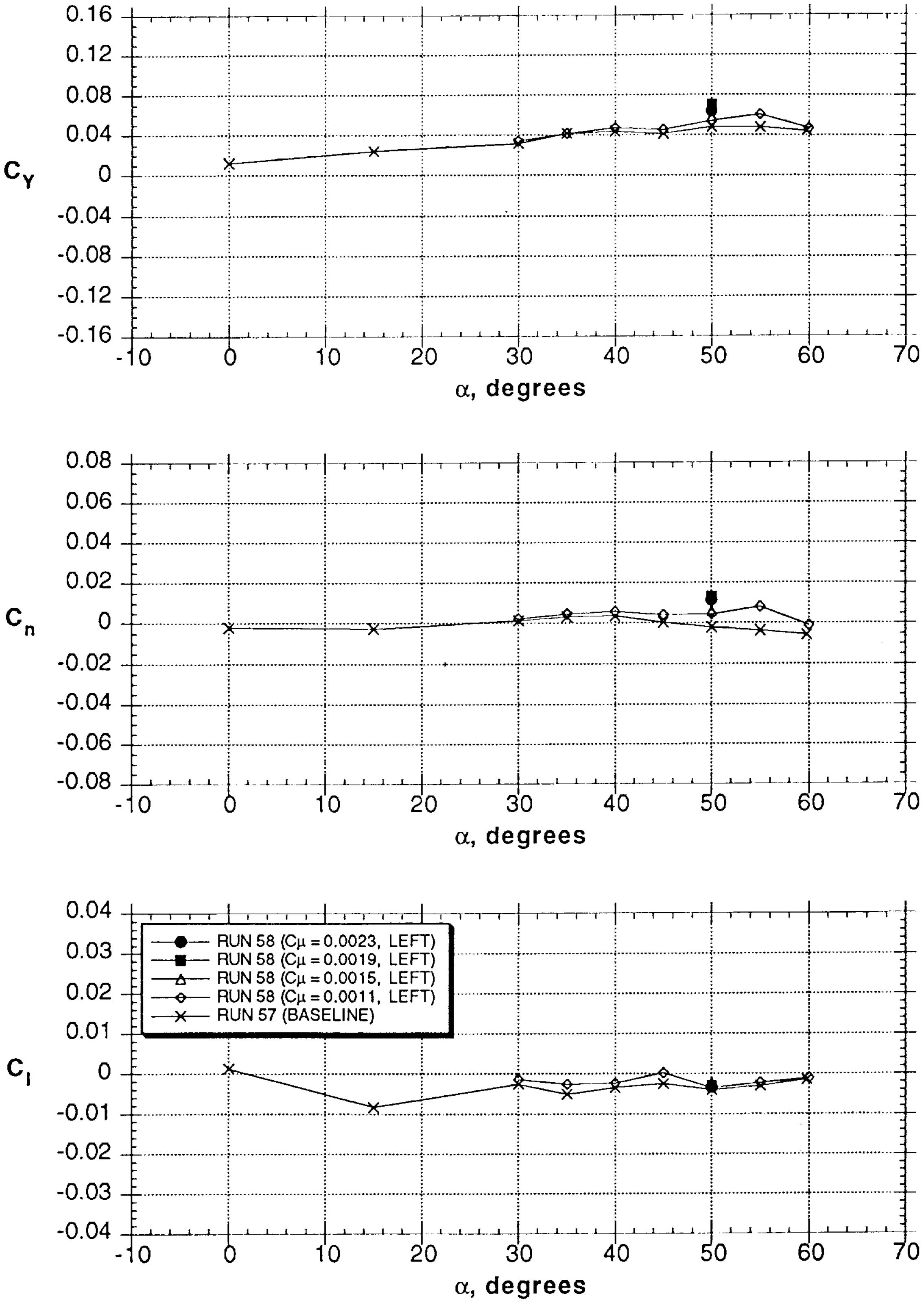

Figure 25 - Concluded

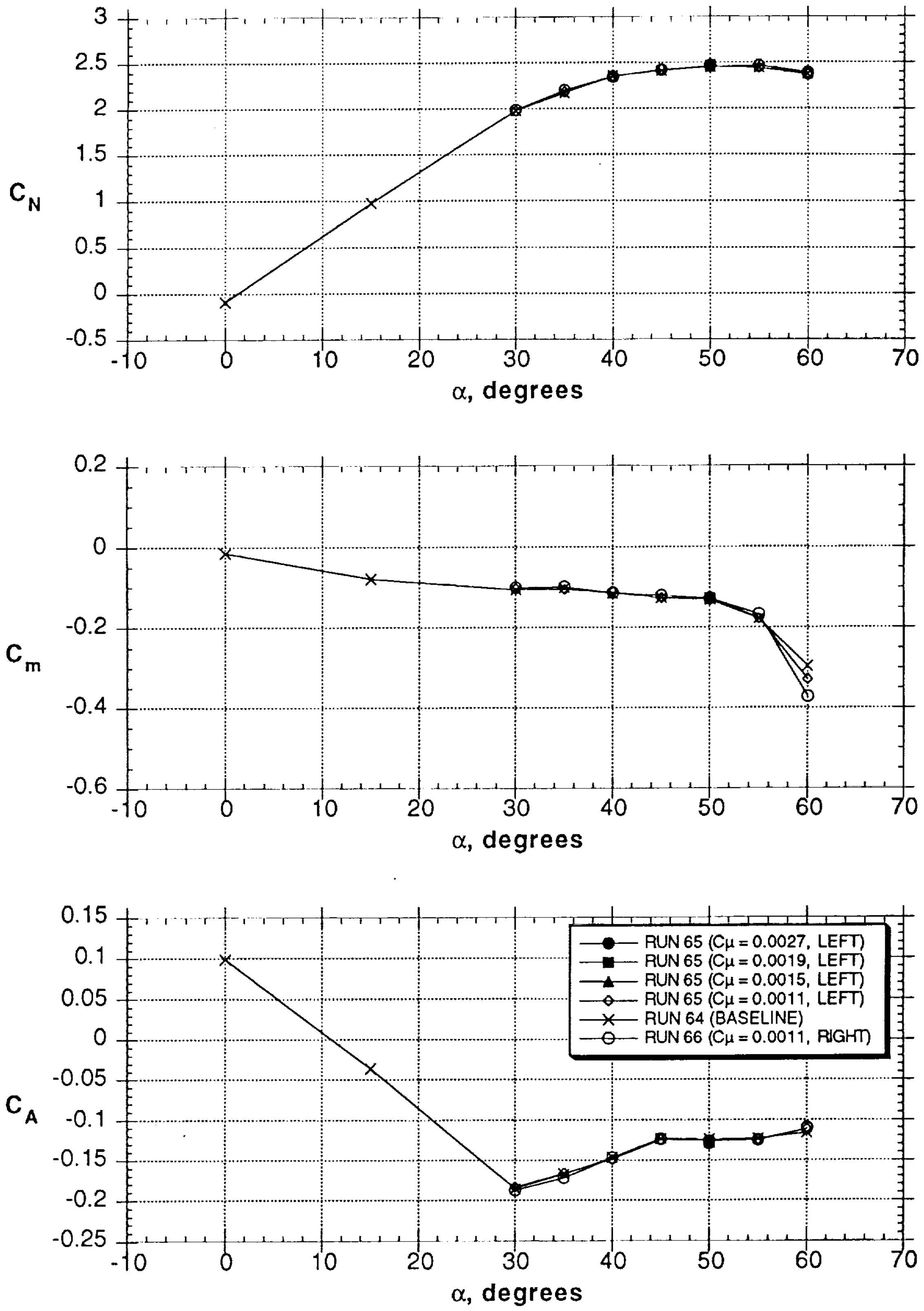

Figure 26 - Effect of jet blowing (straight aft, nose 5)

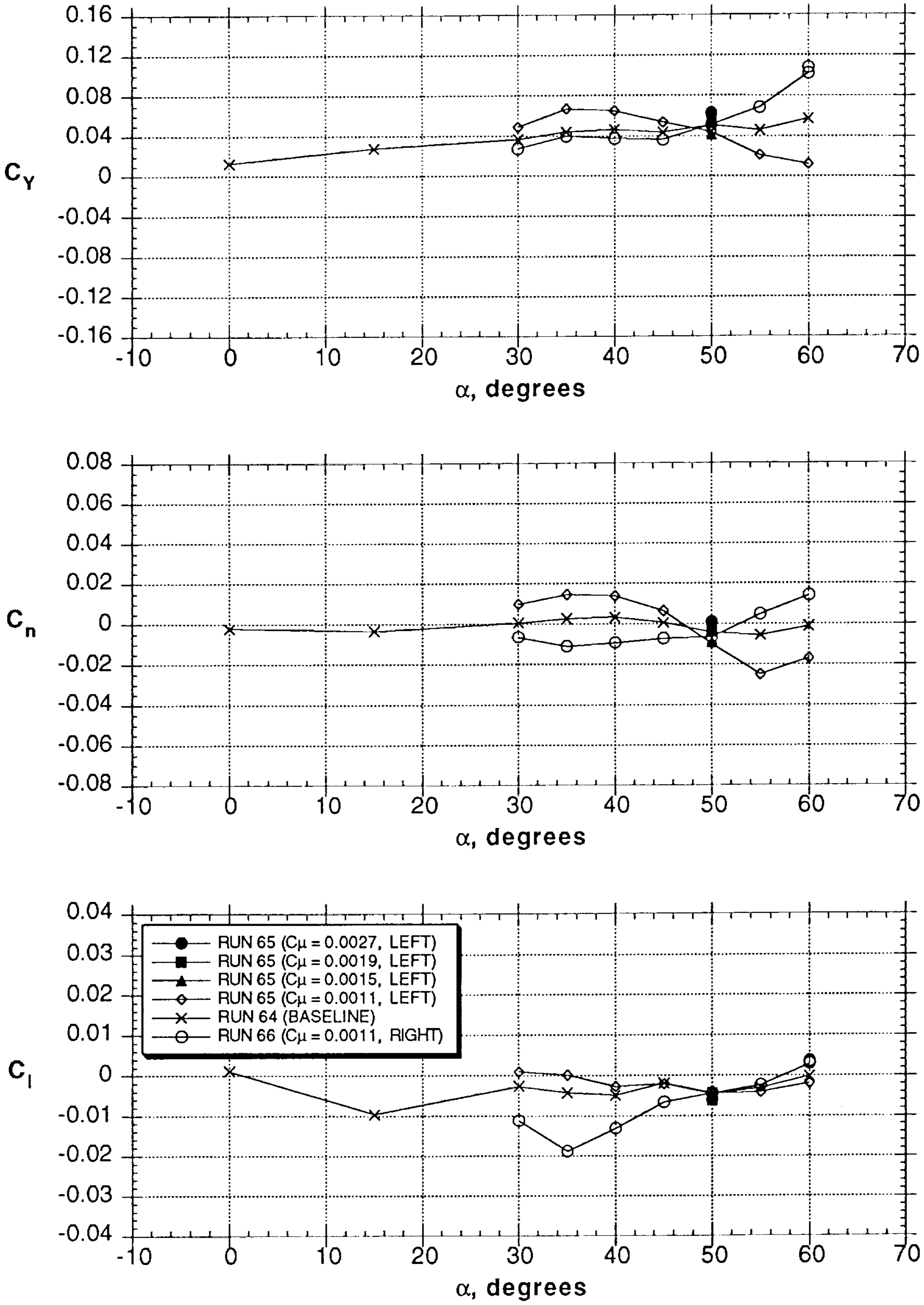

Figure 26 - Concluded

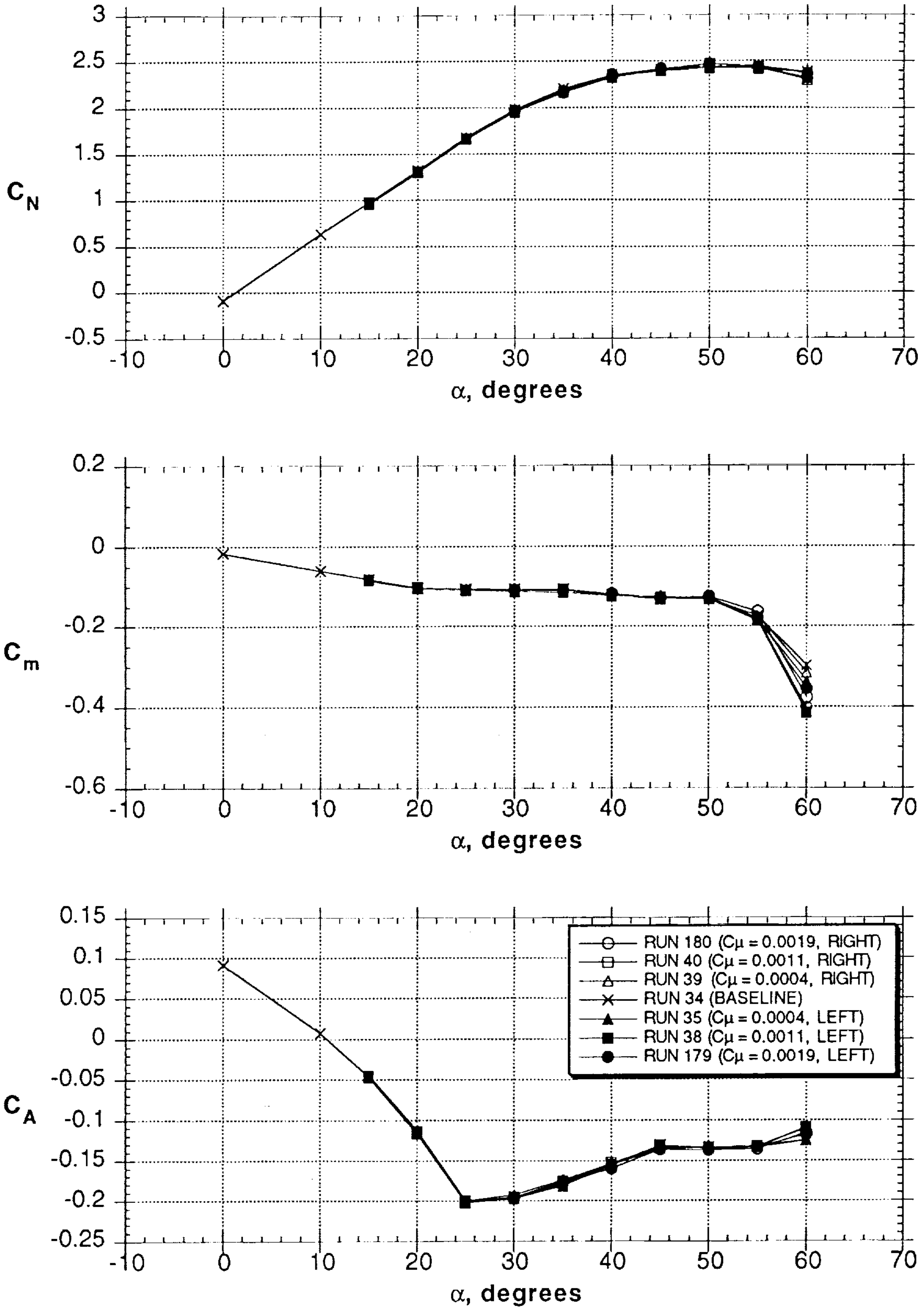

Figure 27 - Effect of jet blowing (60° inboard, nose 2)

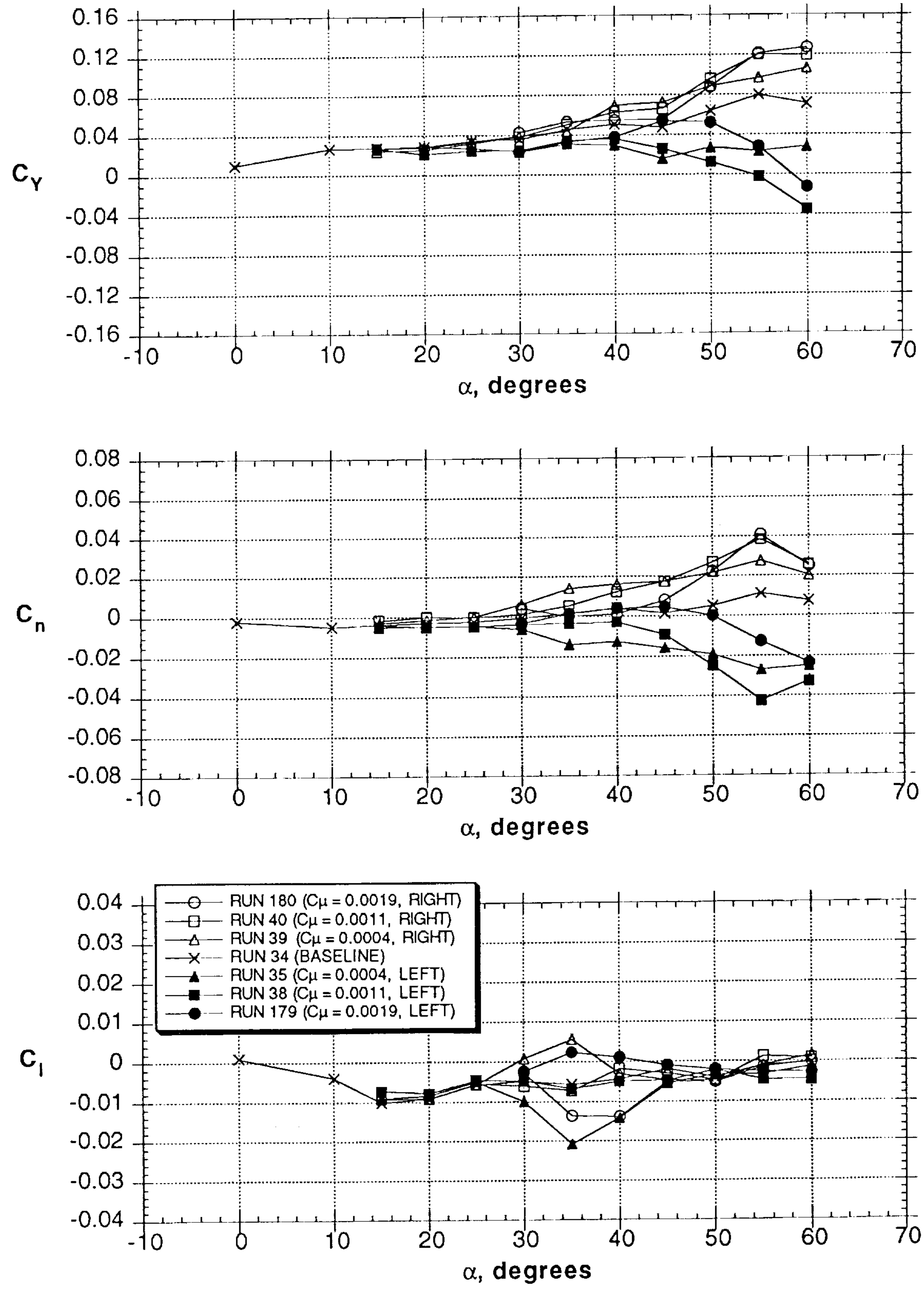

Figure 27 - Concluded

C-2

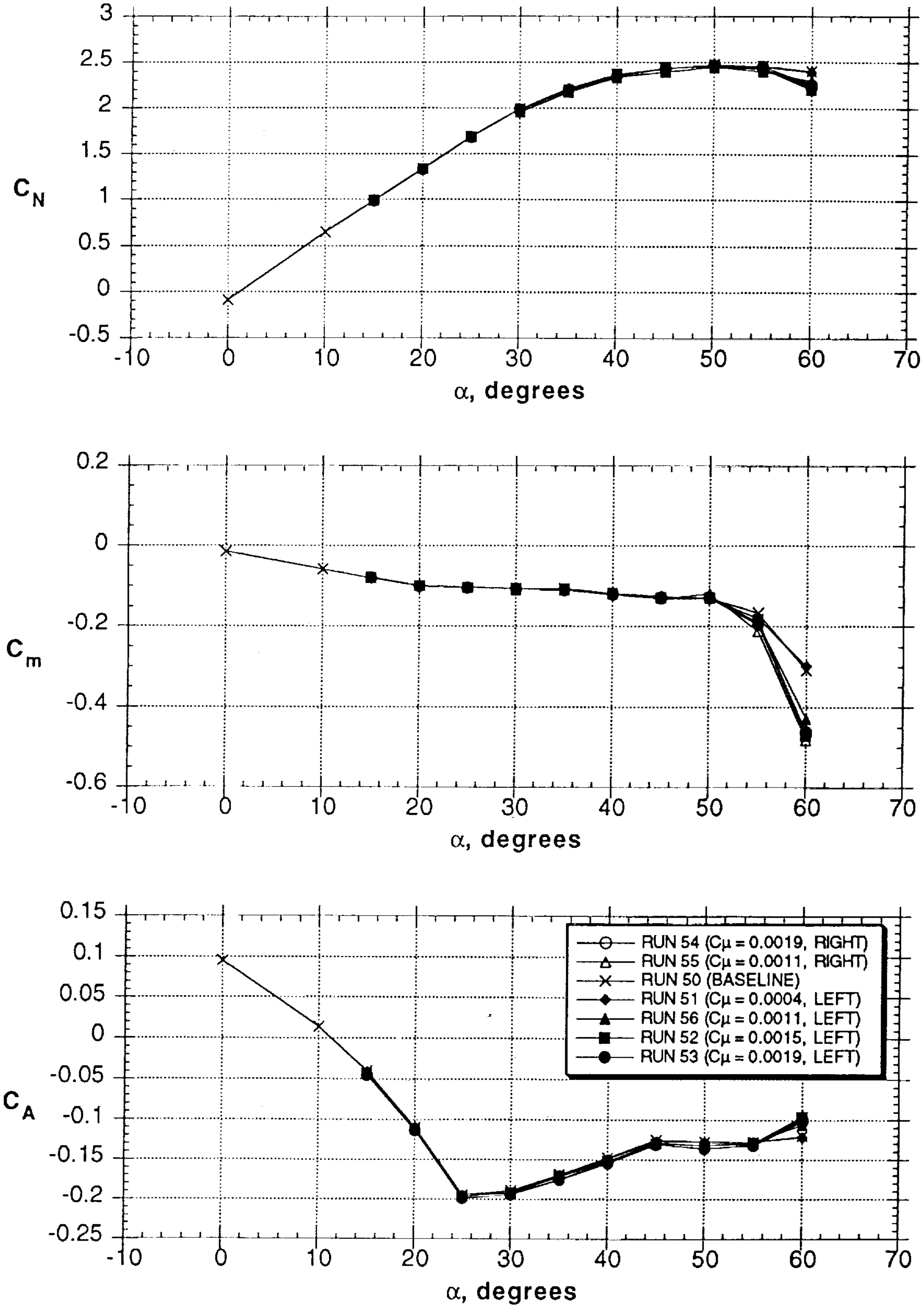

Figure 28 - Effect of jet blowing (60° inboard, nose 3)

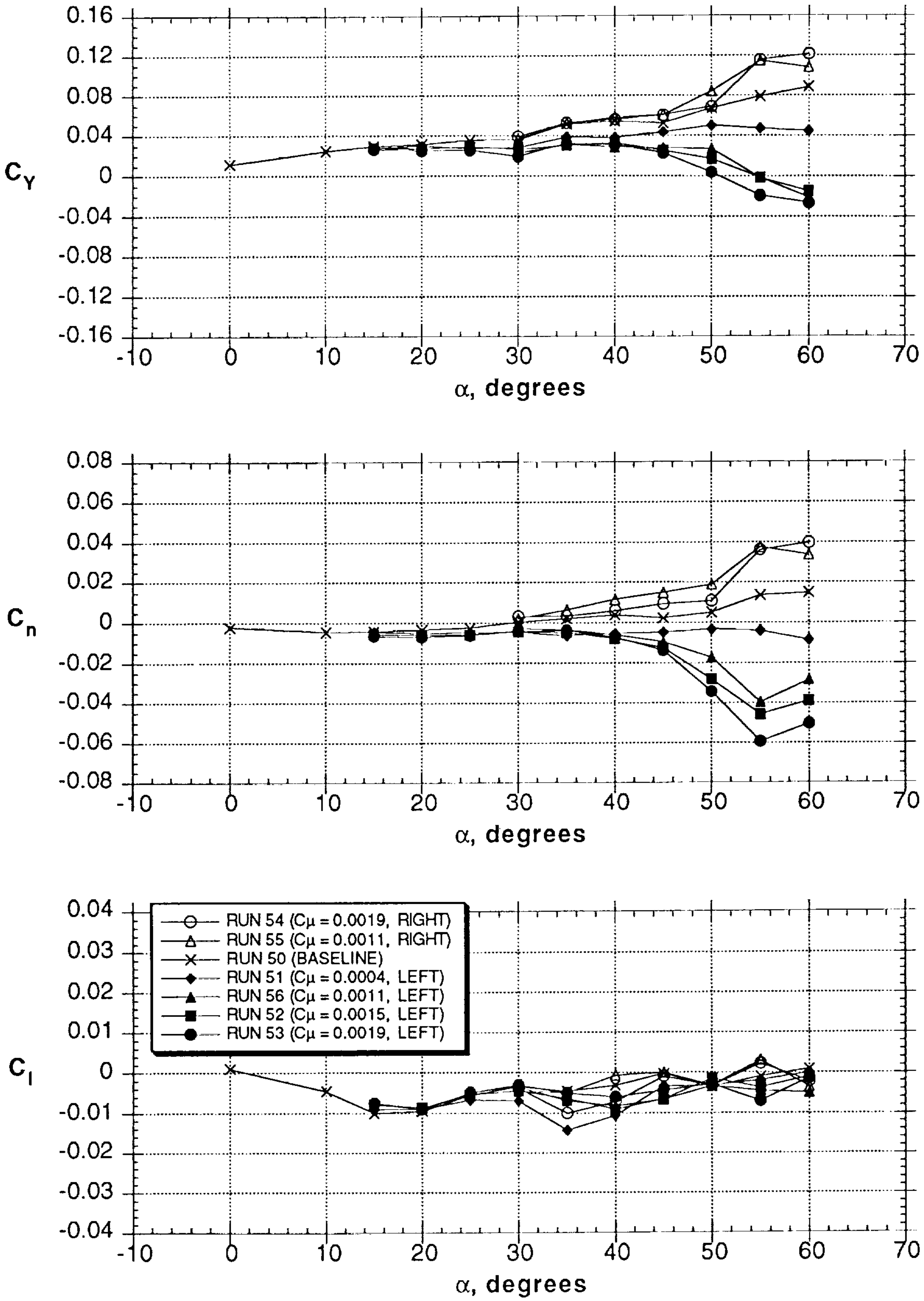

Figure 28 - Concluded

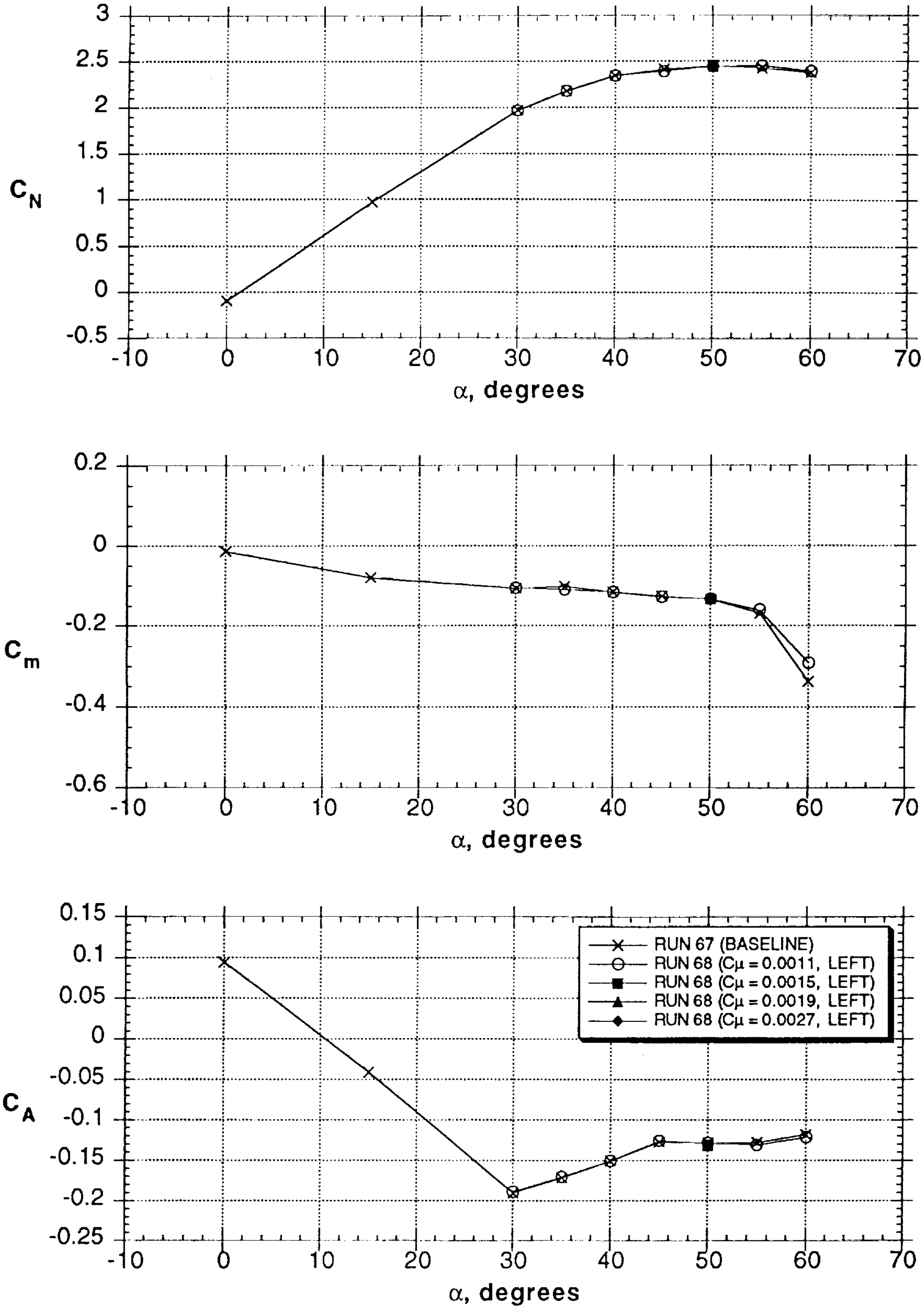

Figure 29 - Effect of jet blowing (60° inboard, nose 5)

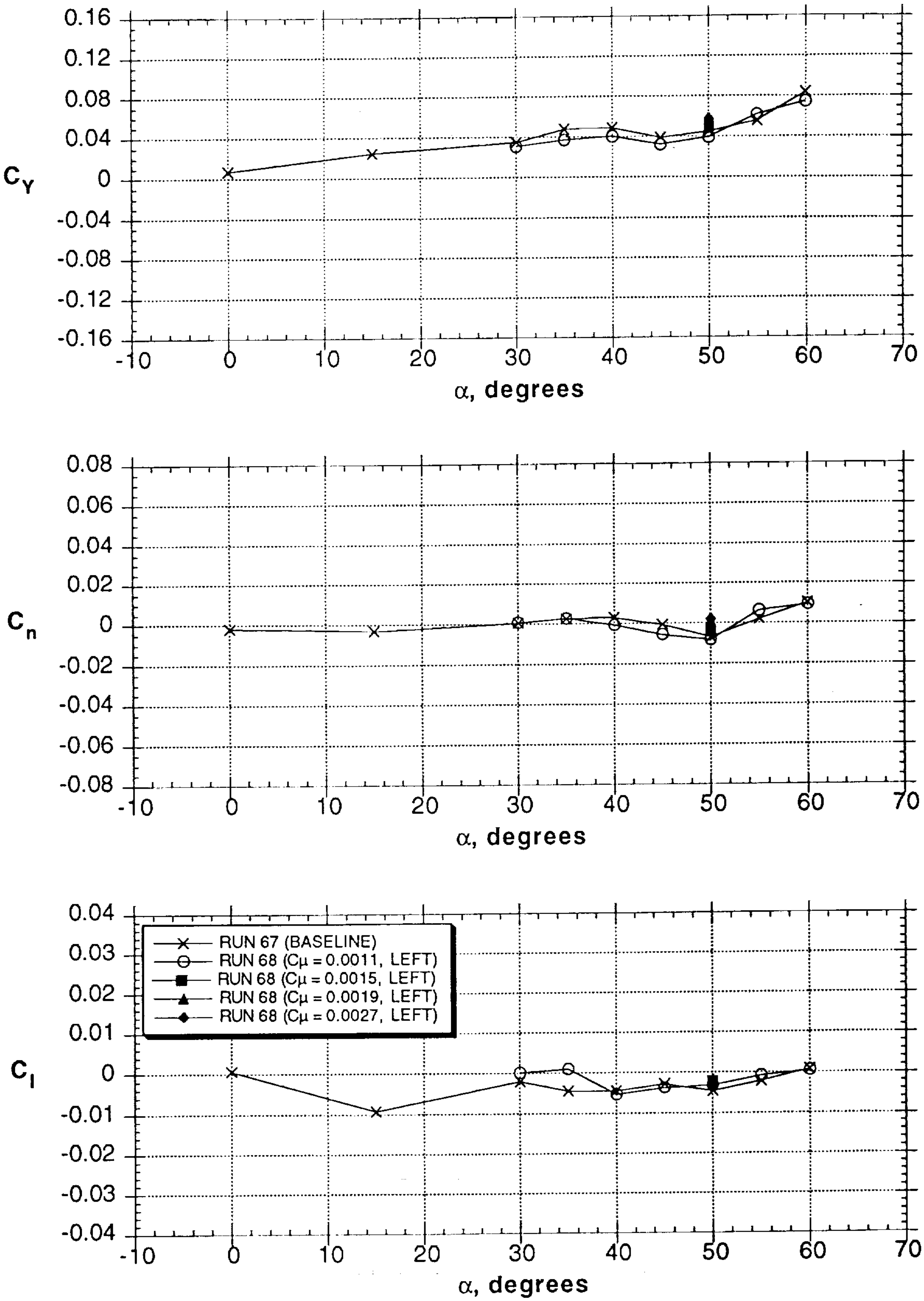

Figure 29 - Concluded

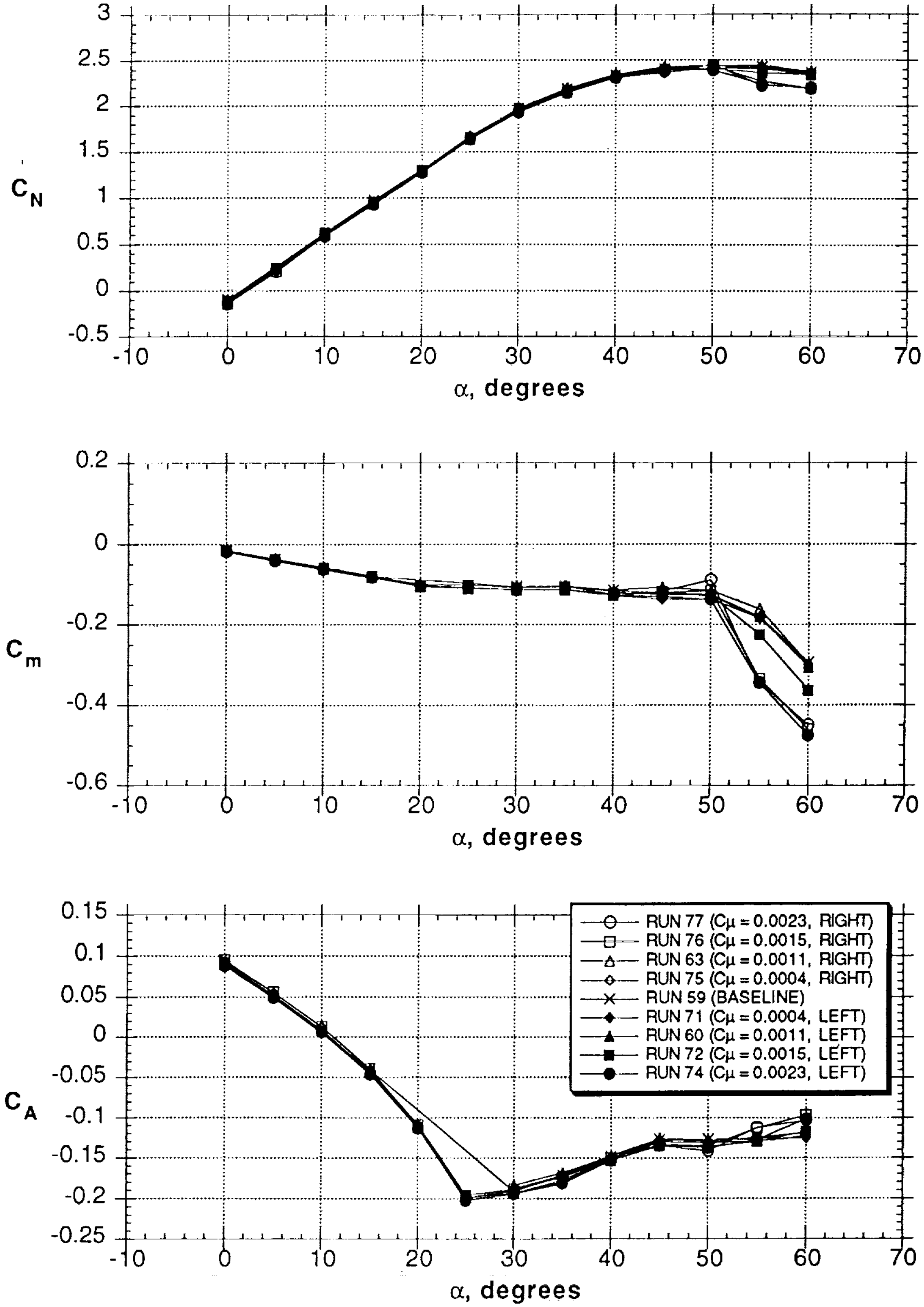

Figure 30 - Effect of jet blowing (60° inboard, nose 4)

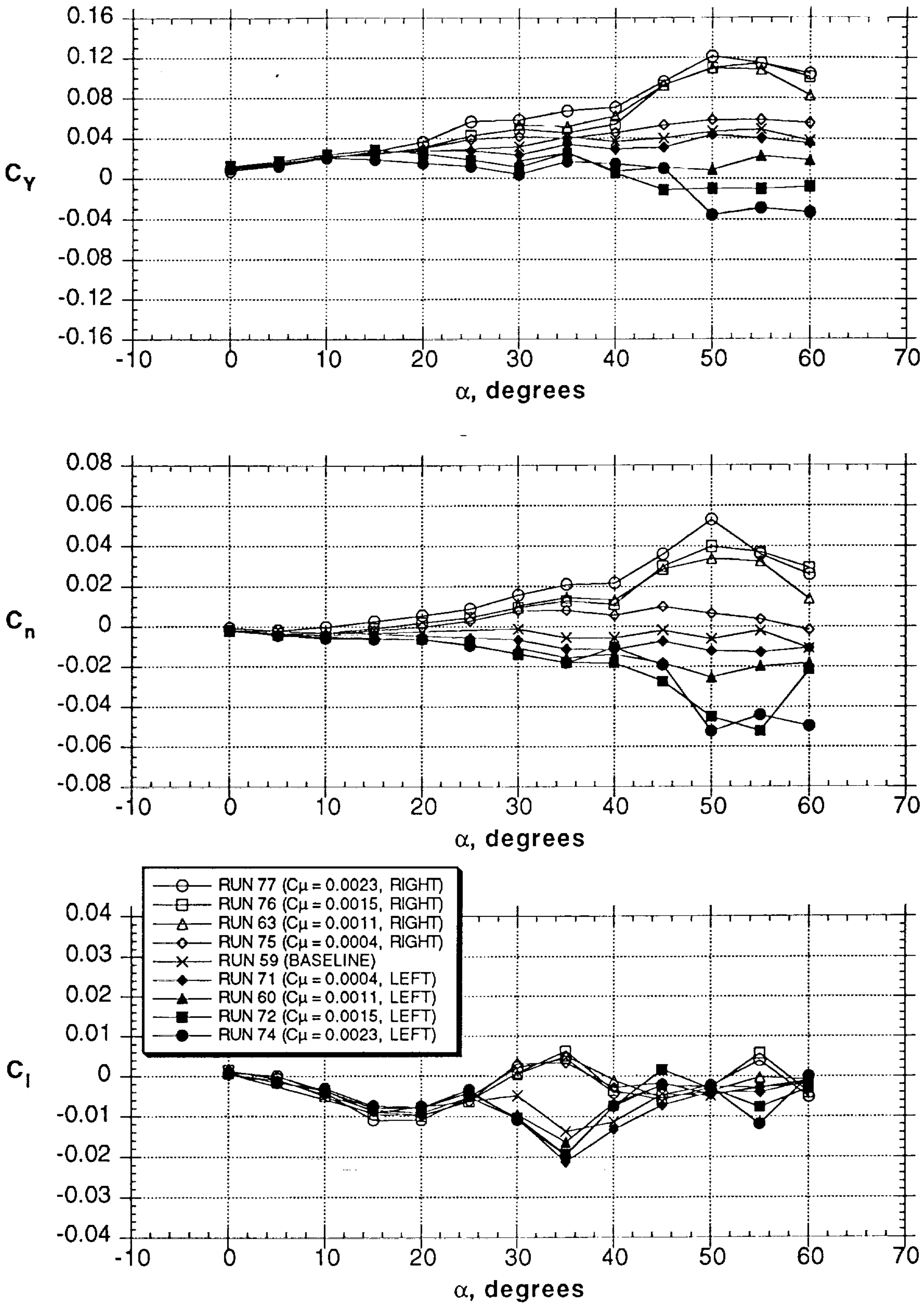

Figure 30 - Concluded

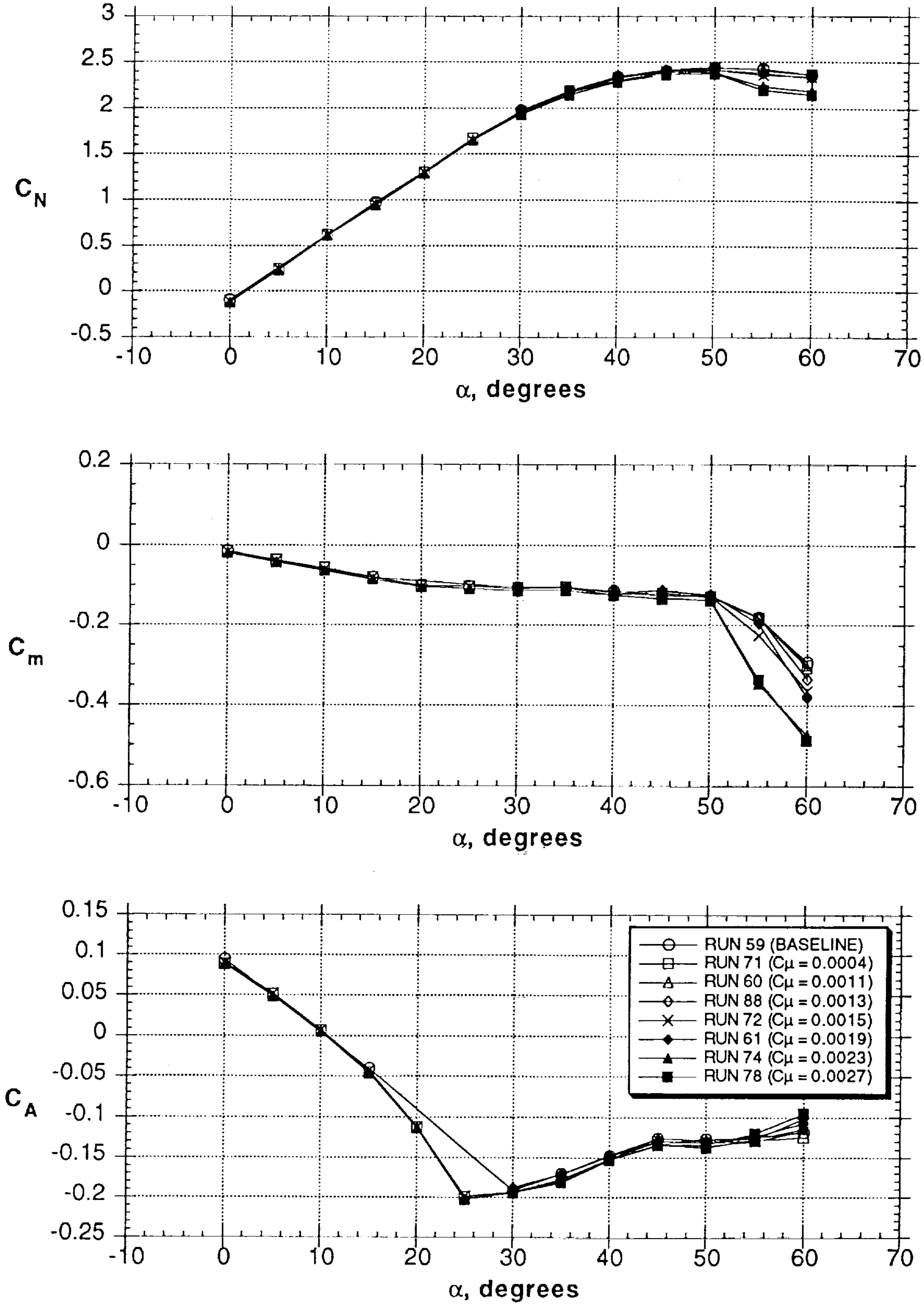

Figure 31 - Effect of jet blowing (60° inboard, nose 4, left side only)

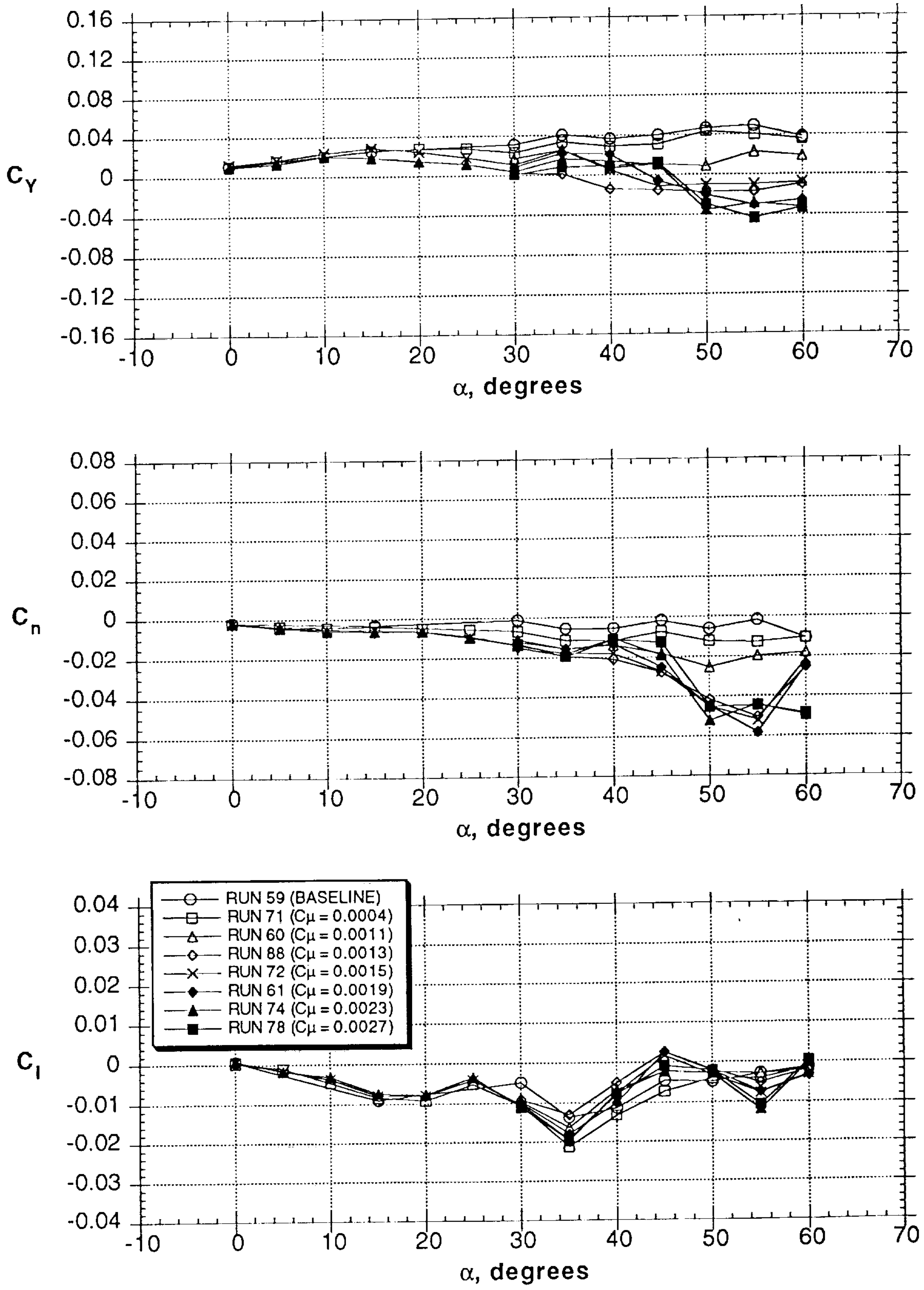

Figure 31 - Concluded

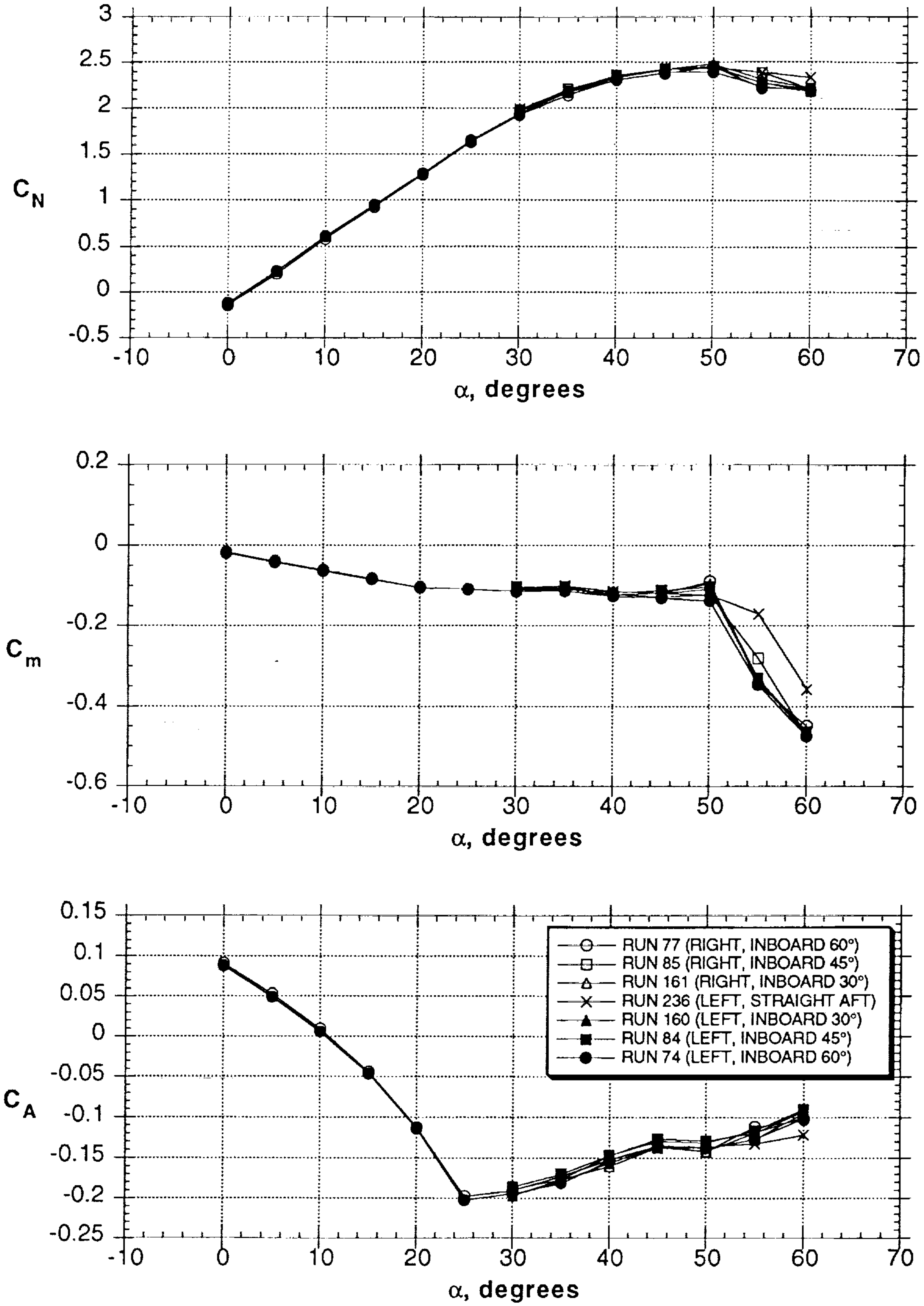

Figure 32 - Effect of nozzle cant angle on jet blowing (nose 4, $C\mu = 0.0023$)

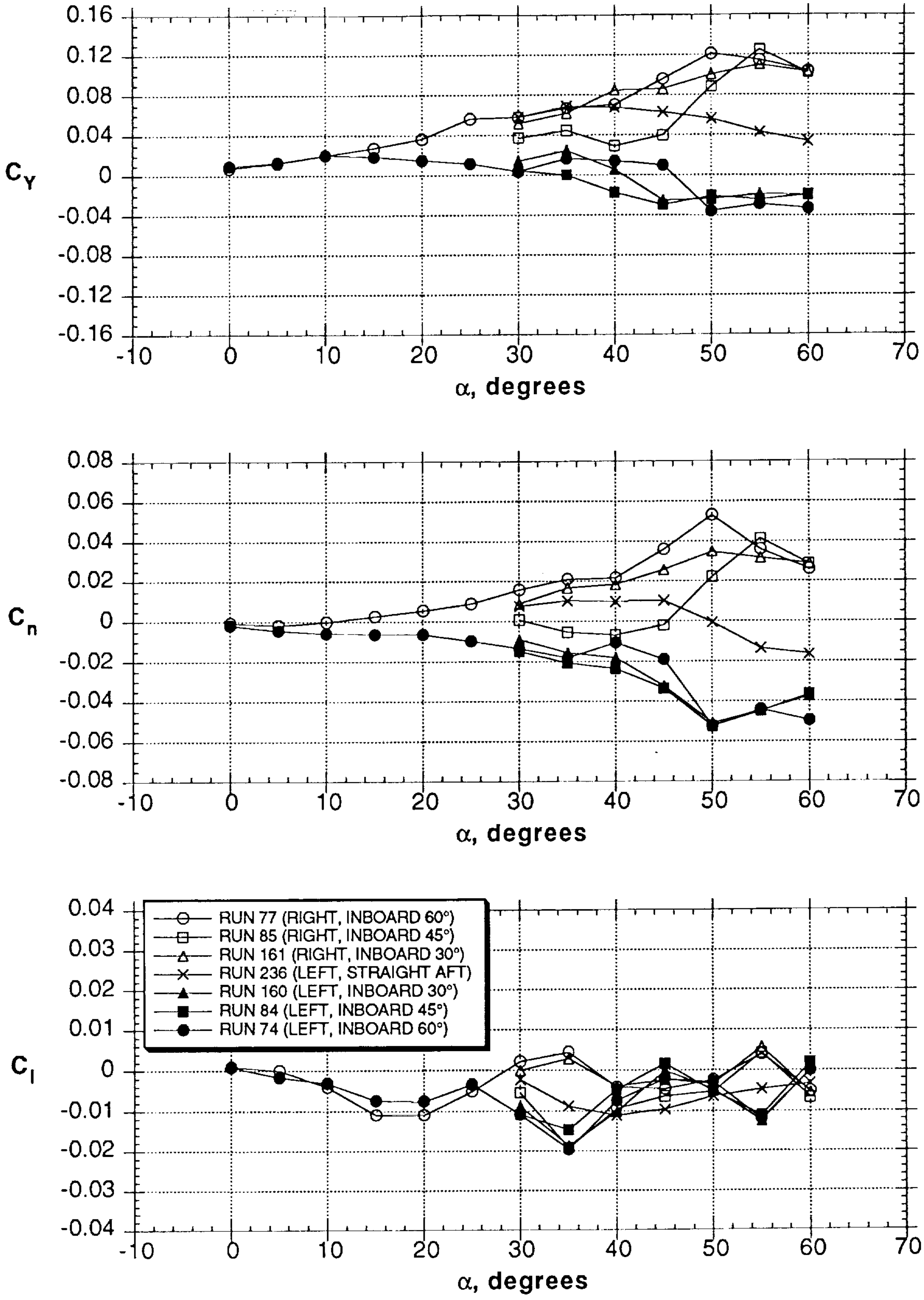

Figure 32 - Concluded

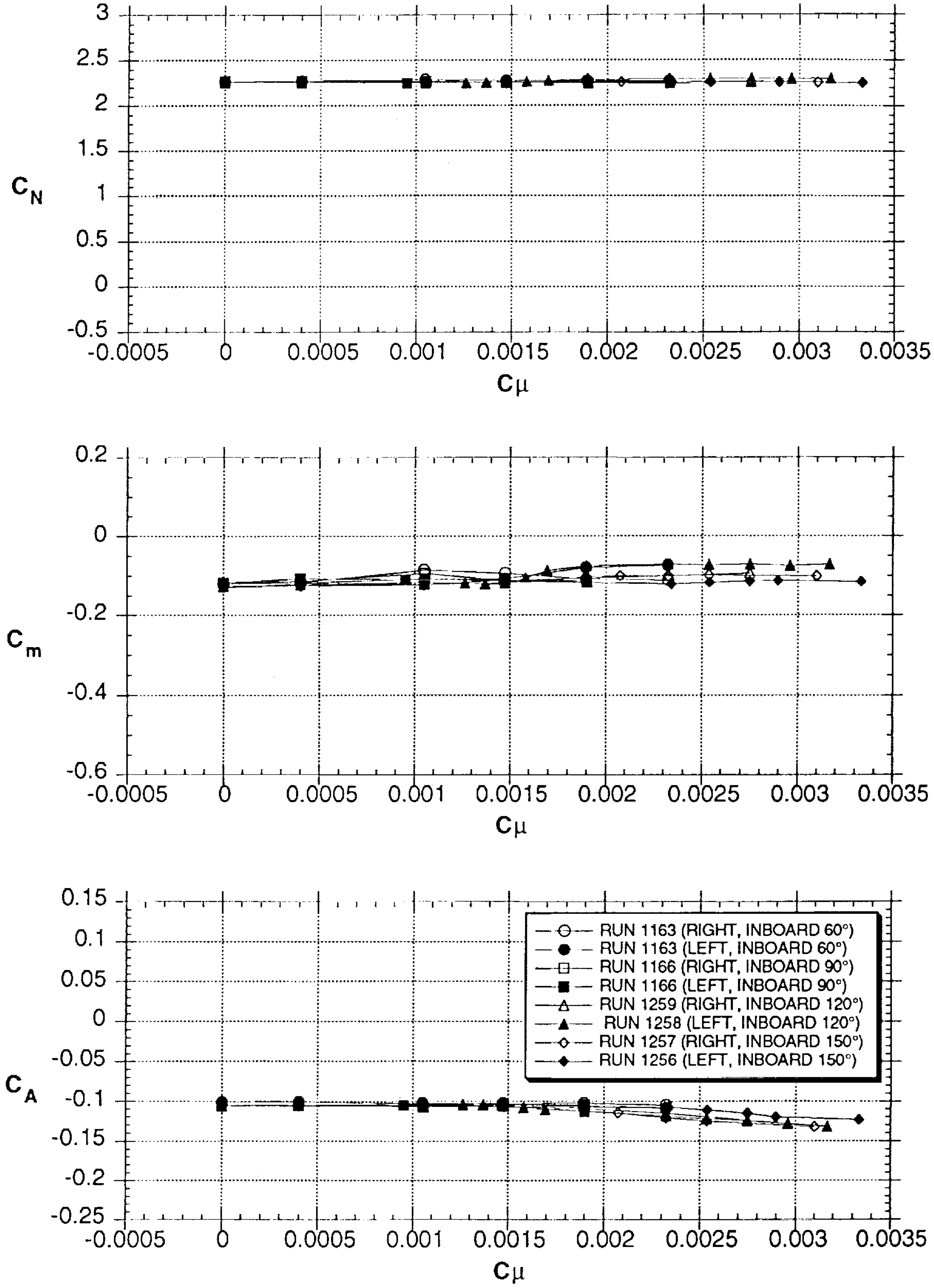

Figure 33 - Effect of nozzle cant angle on jet blowing (nose 4, $\alpha = 51°$)

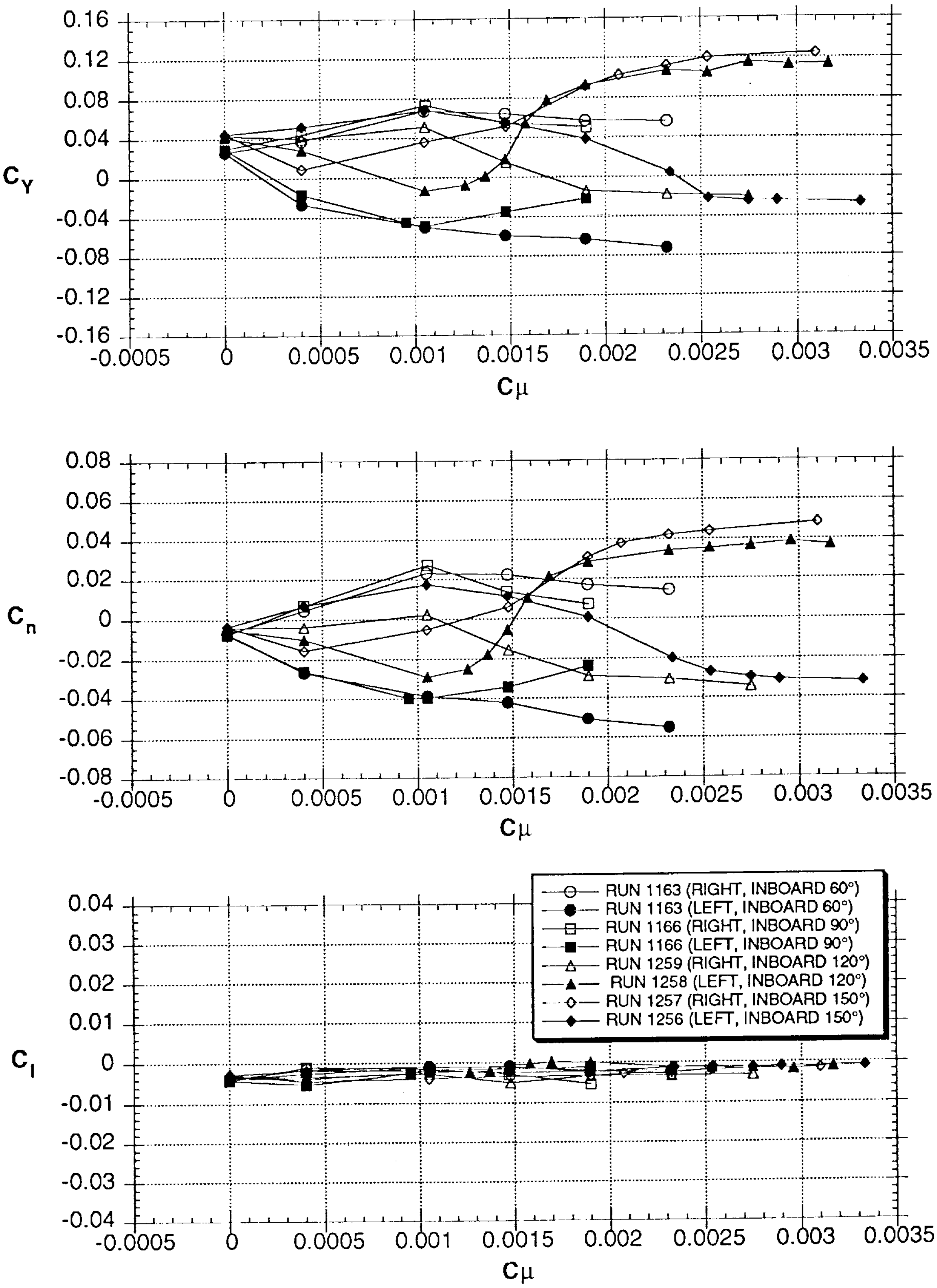

Figure 33 - Concluded

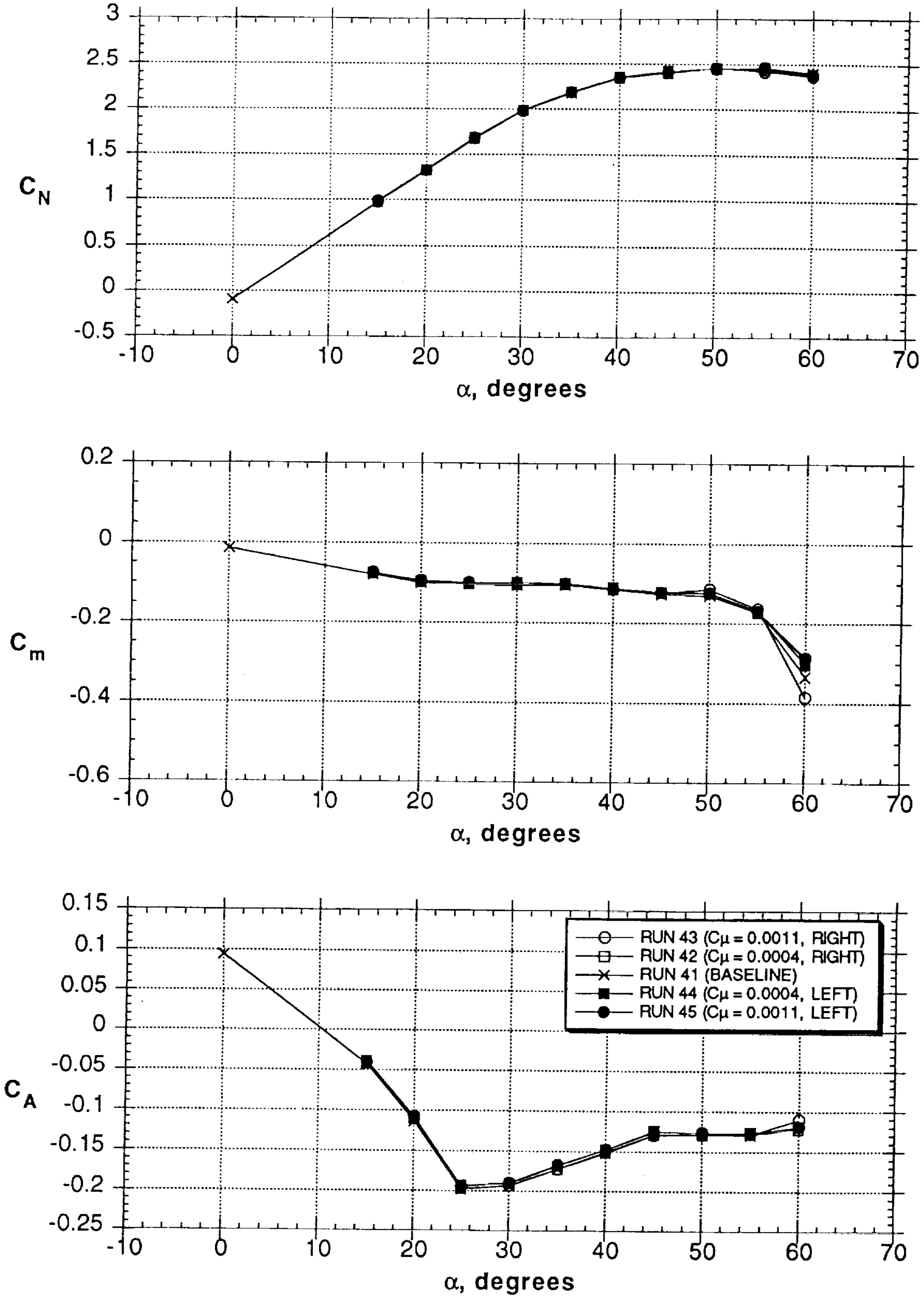

Figure 34 - Effect of nozzle cant angle on jet blowing (30° inboard, nose 2)

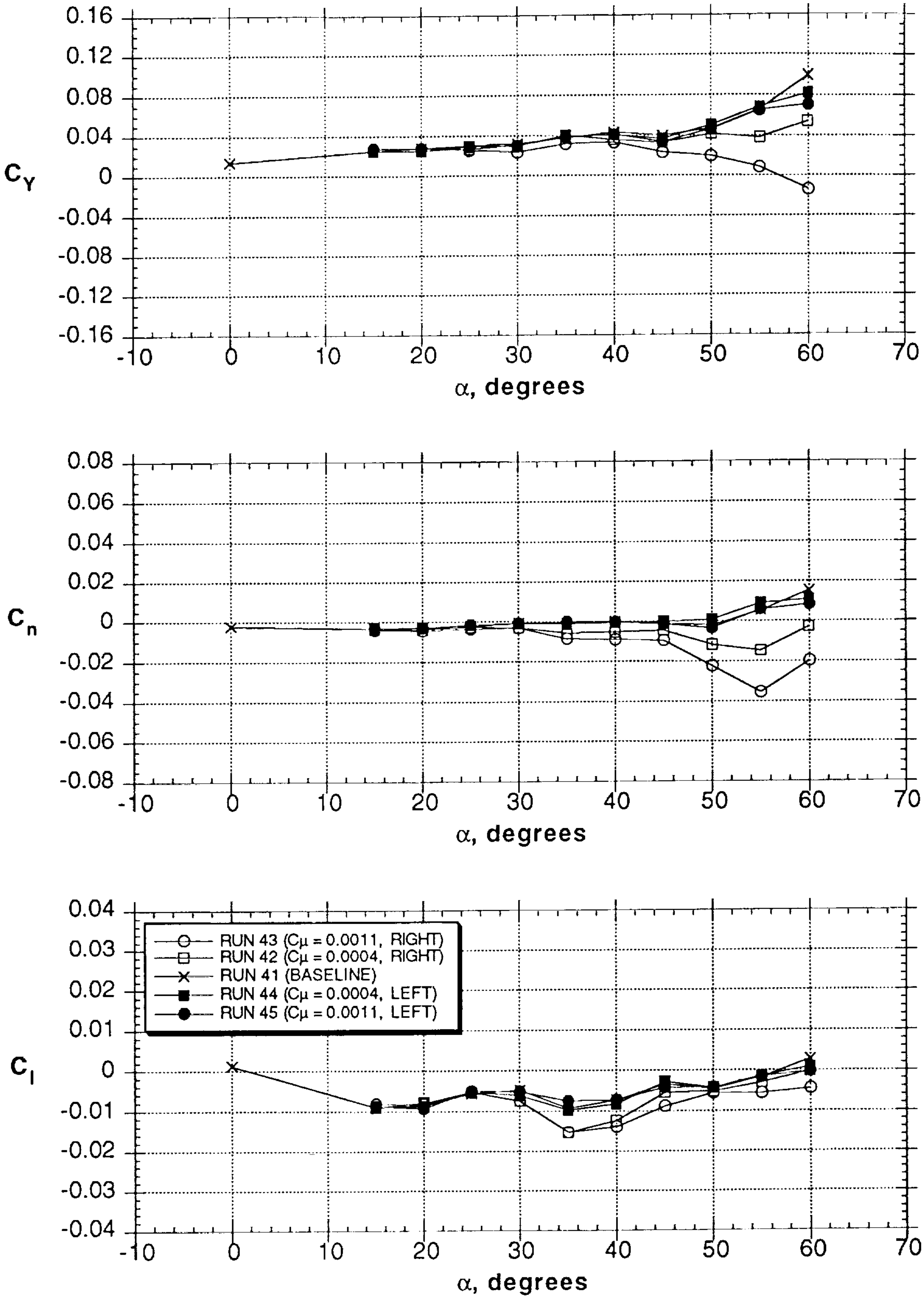

Figure 34 - Concluded

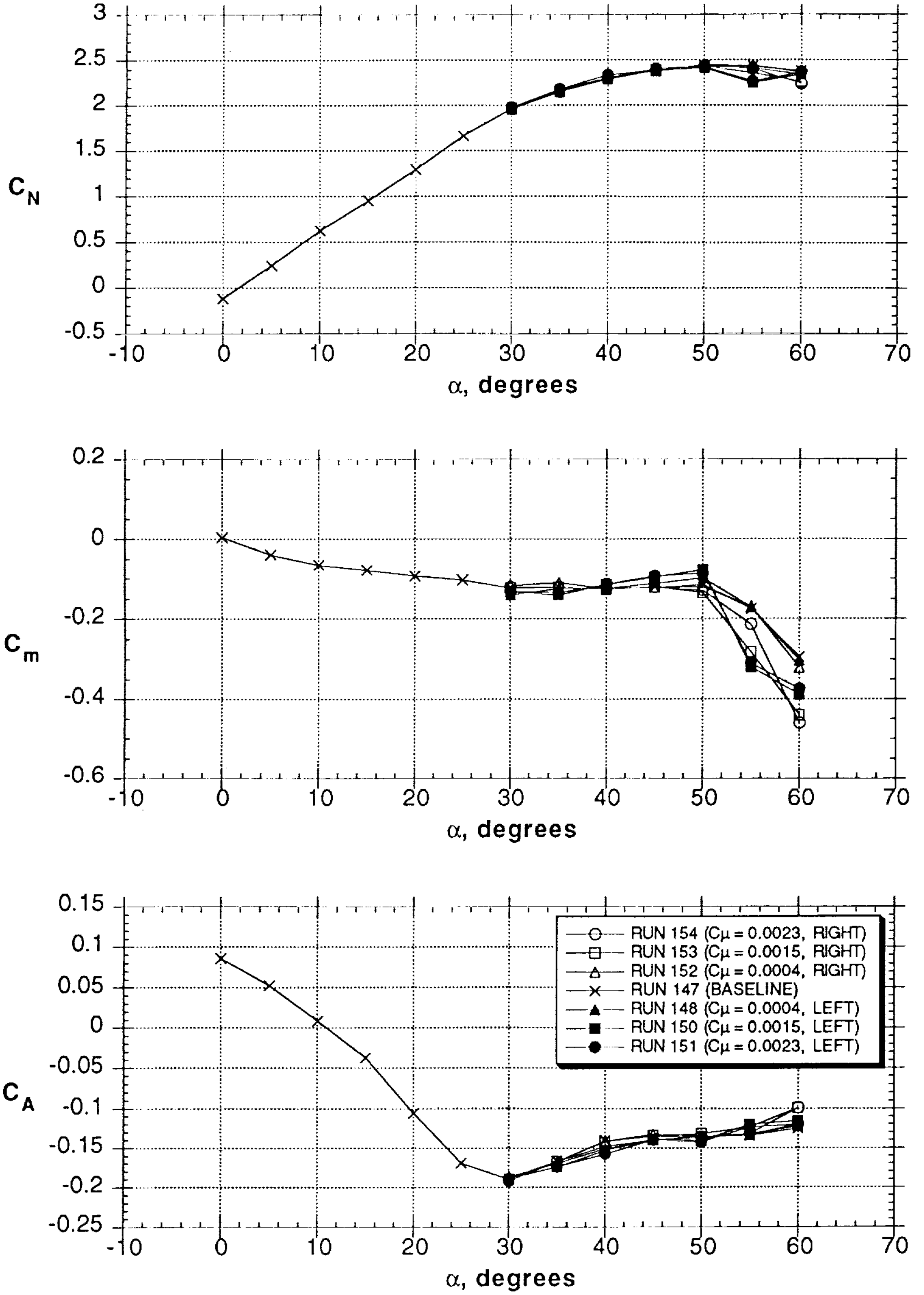

Figure 35 - Effect of sideslip on jet blowing effectiveness (60° inboard, nose 4, $\beta = -10°$)

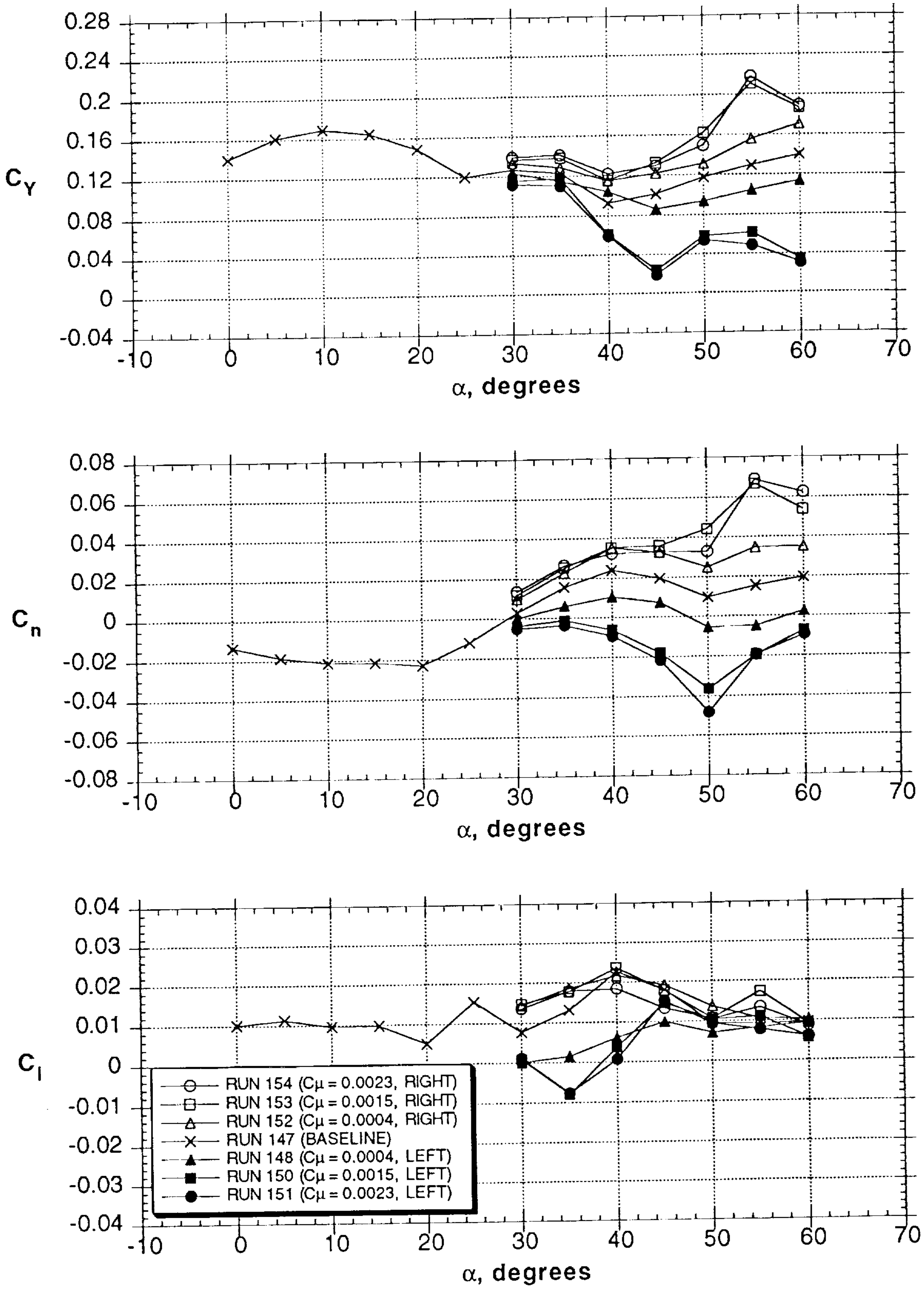

Figure 35 - Concluded

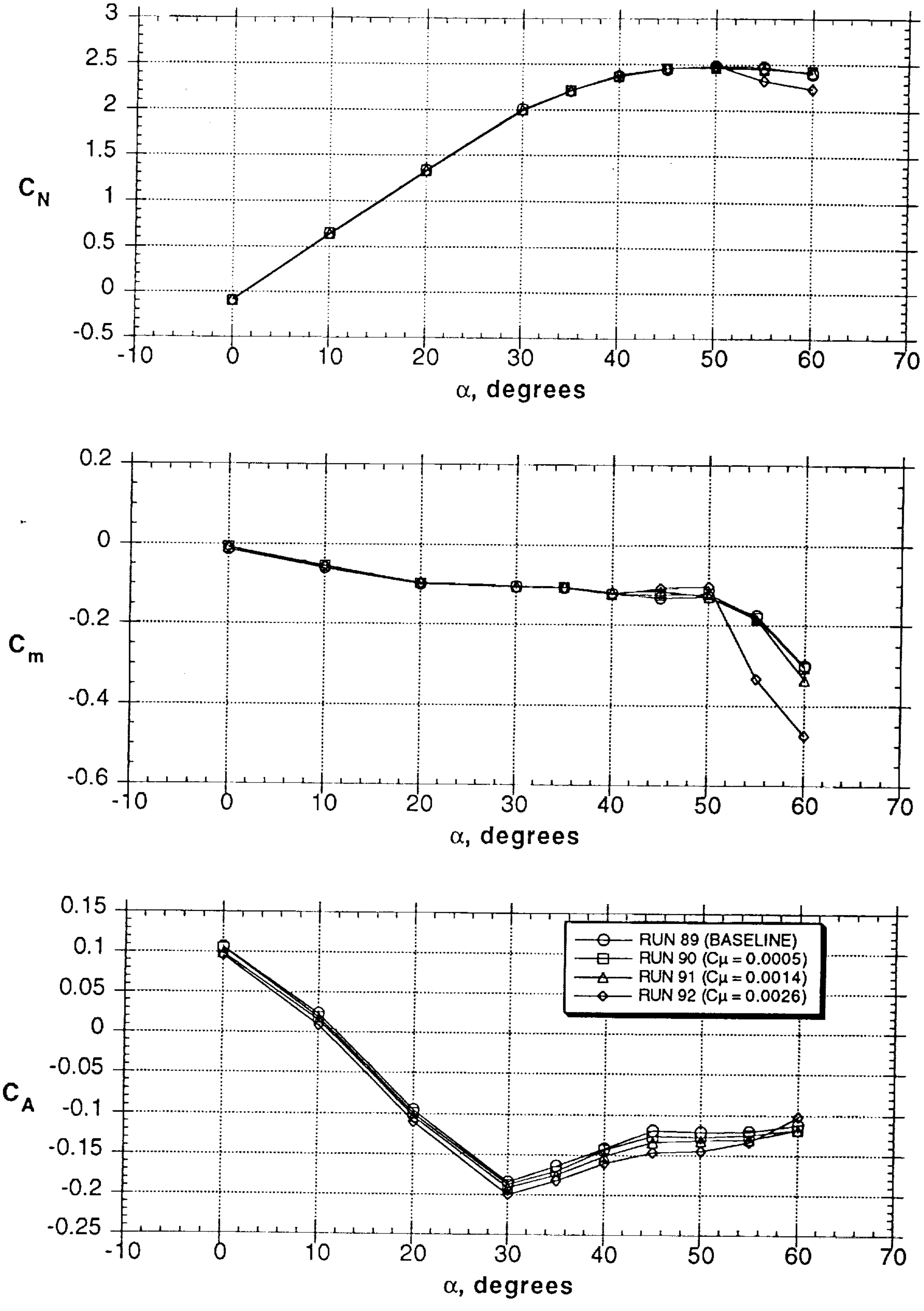

Figure 36 - Effect of Reynolds number on jet blowing (60° inboard, nose 4, Rn = 0.8 x 10^6, Q = 20 psf, left side only)

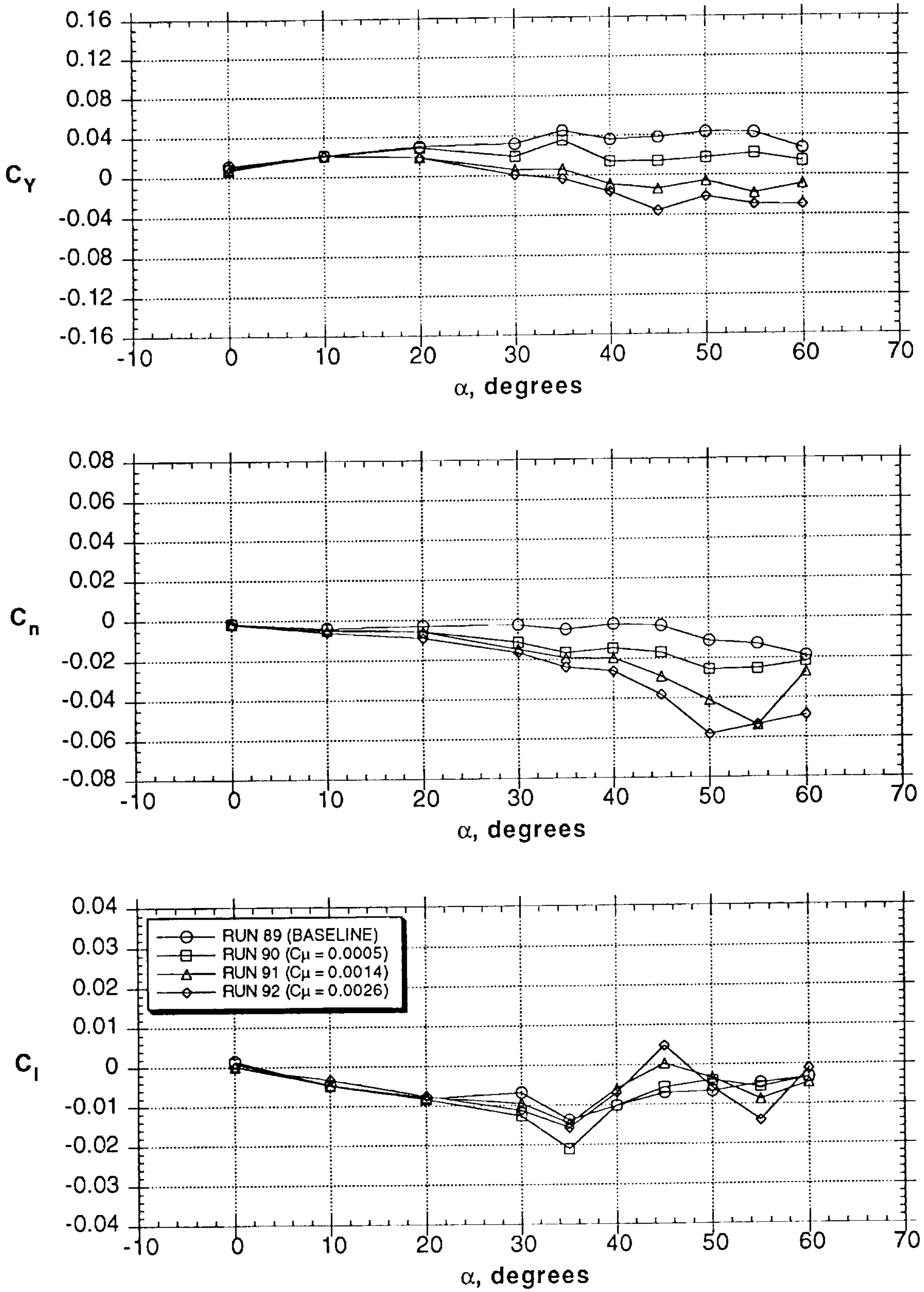

Figure 36 - Concluded

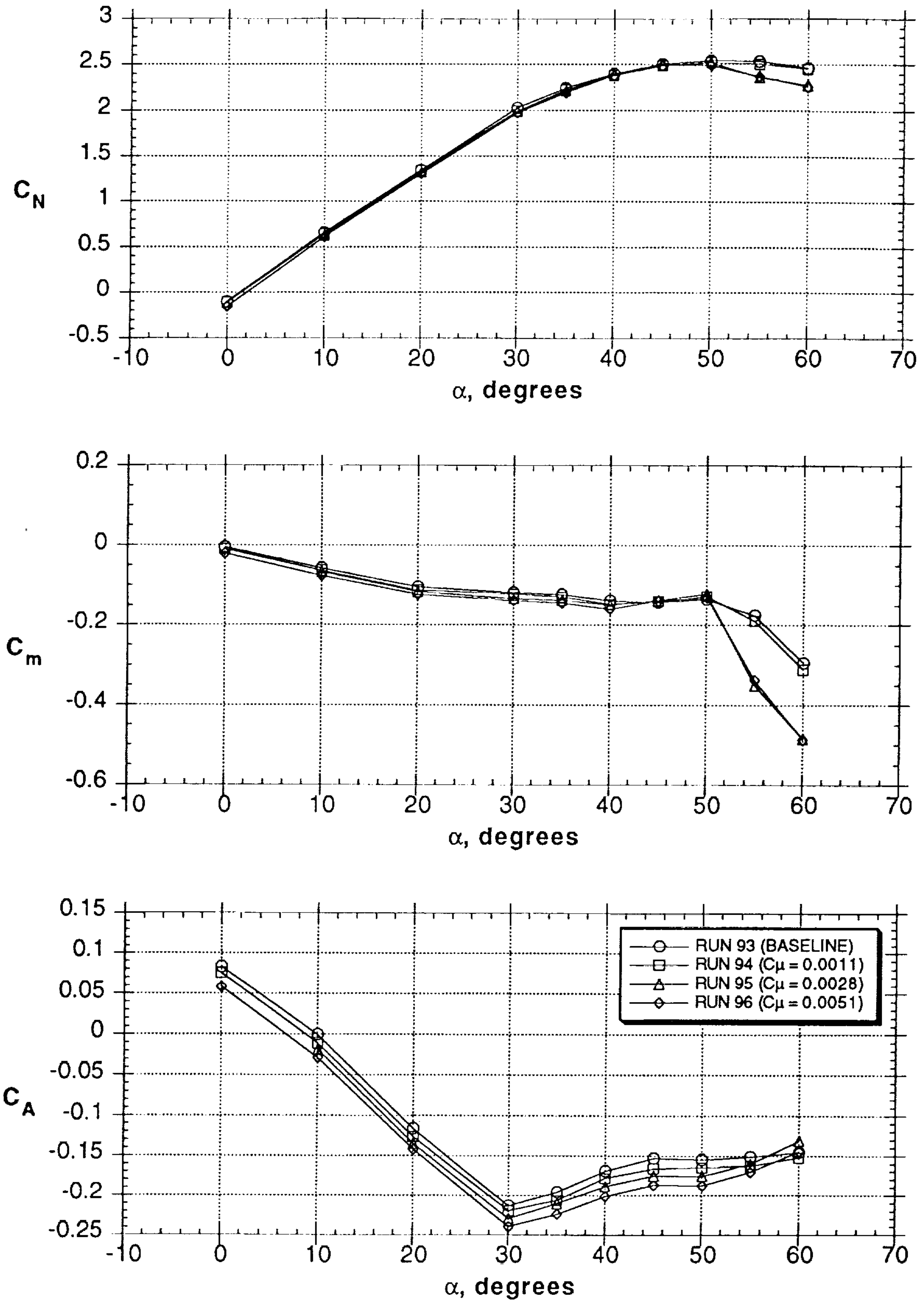

Figure 37 - Effect of Reynolds number on jet blowing (60° inboard, nose 4, Rn = 0.56 x 10^6, Q = 10 psf, left side only)

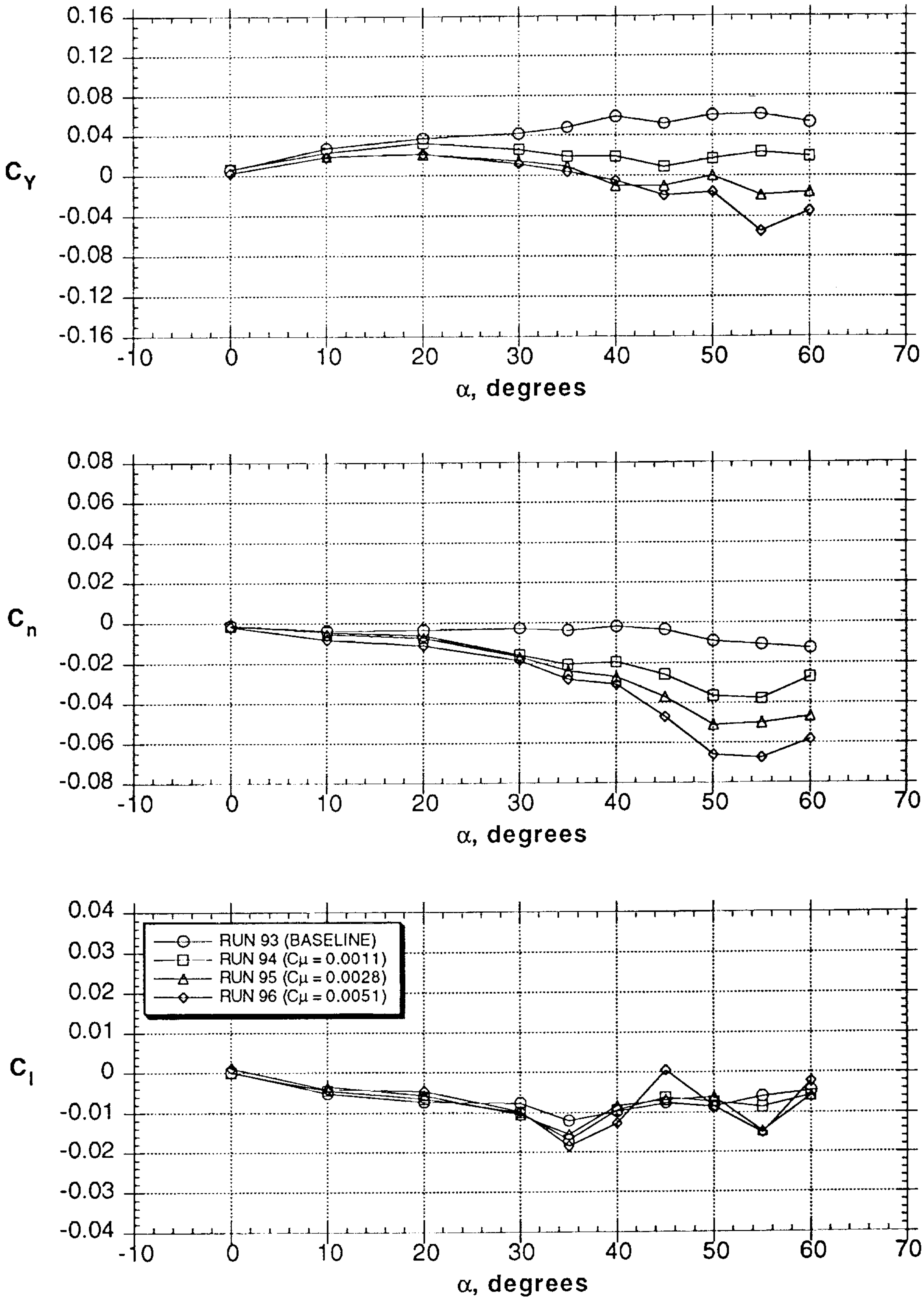

Figure 37 - Concluded

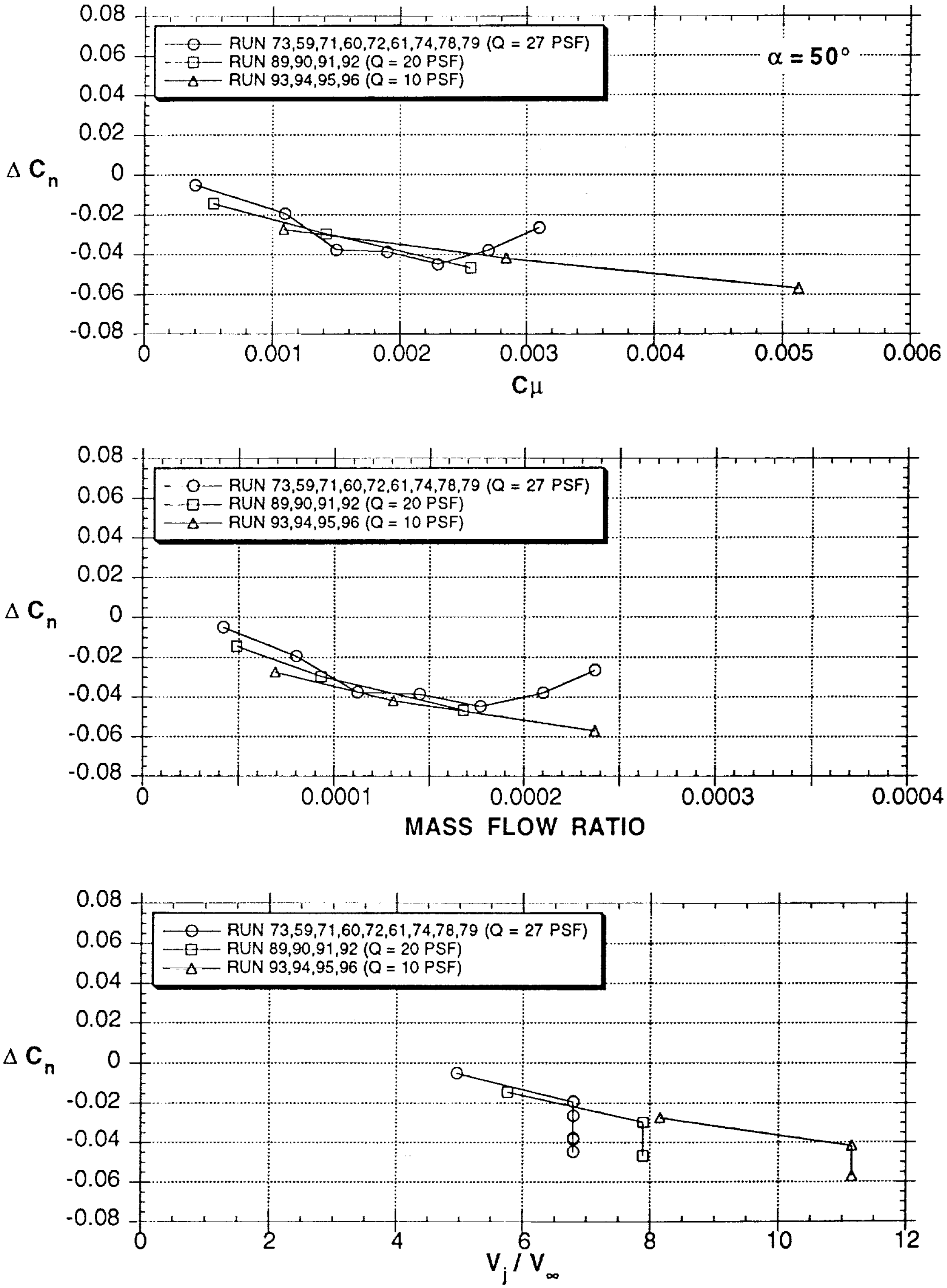

Figure 38 - Effect of correlation parameters (jet blowing, 60° inboard, nose 4, α = 50°)

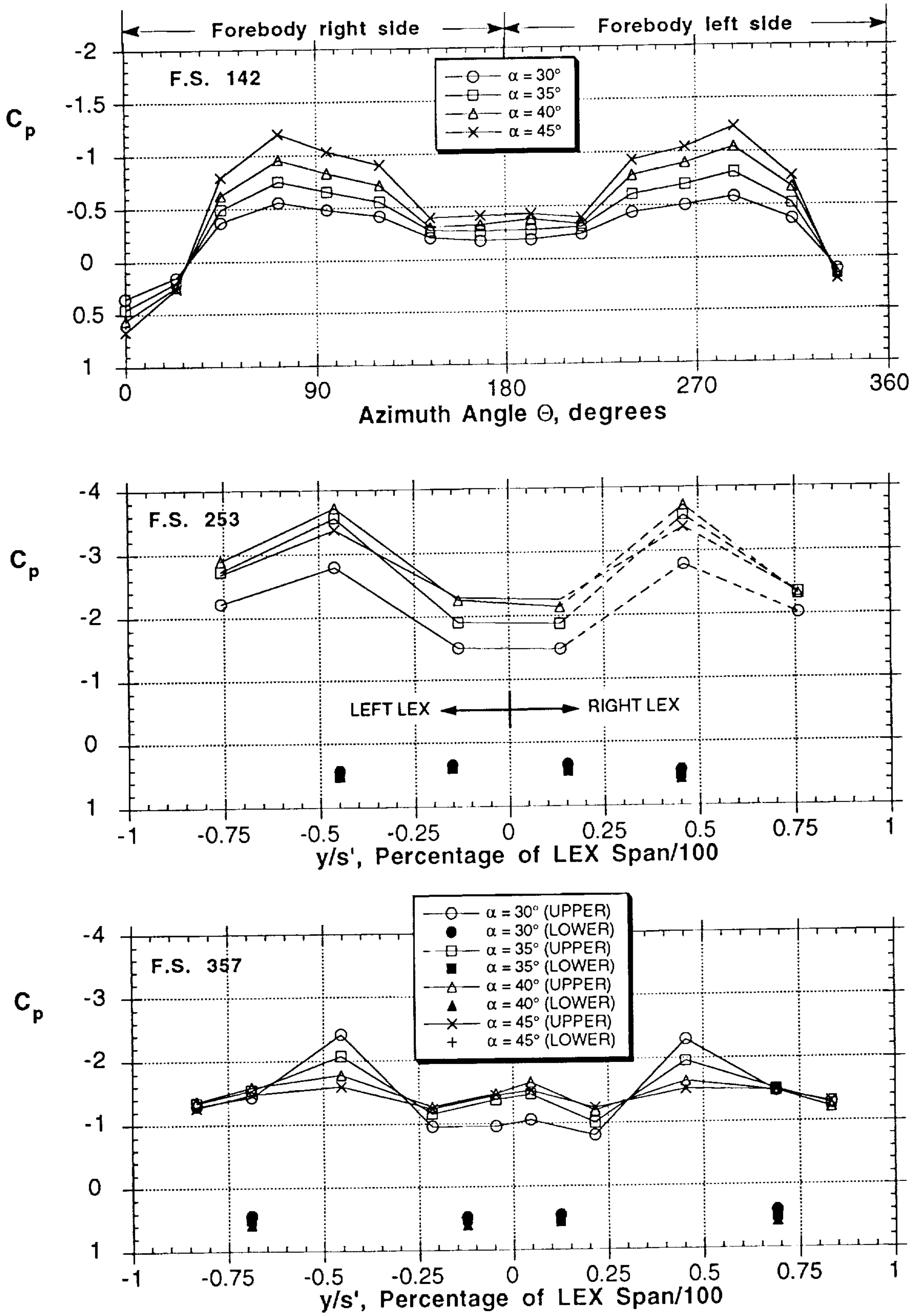

Figure 39 - Effect of jet nozzles on pressure distributions (60° inboard, nose 4)

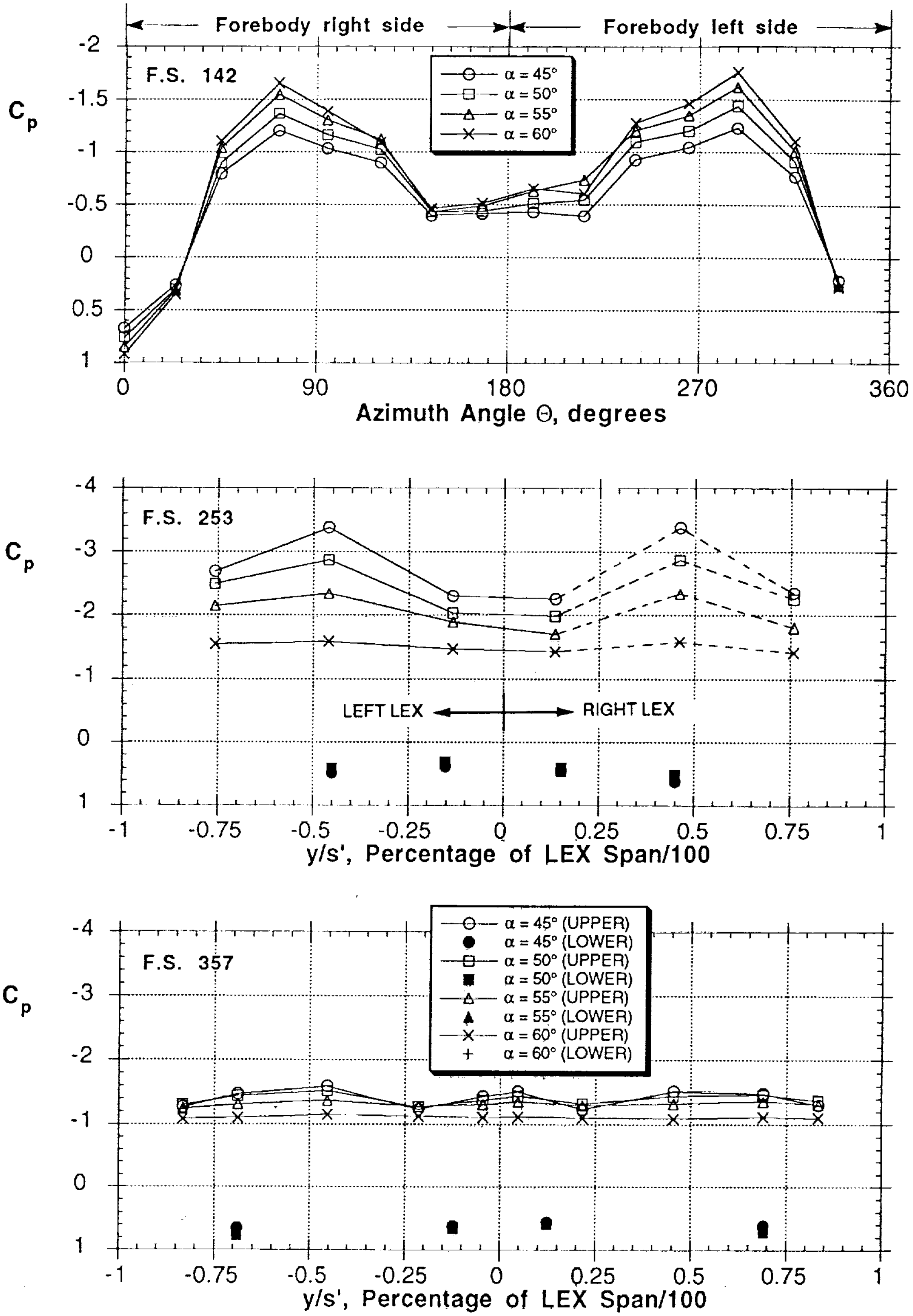

Figure 39 - Concluded

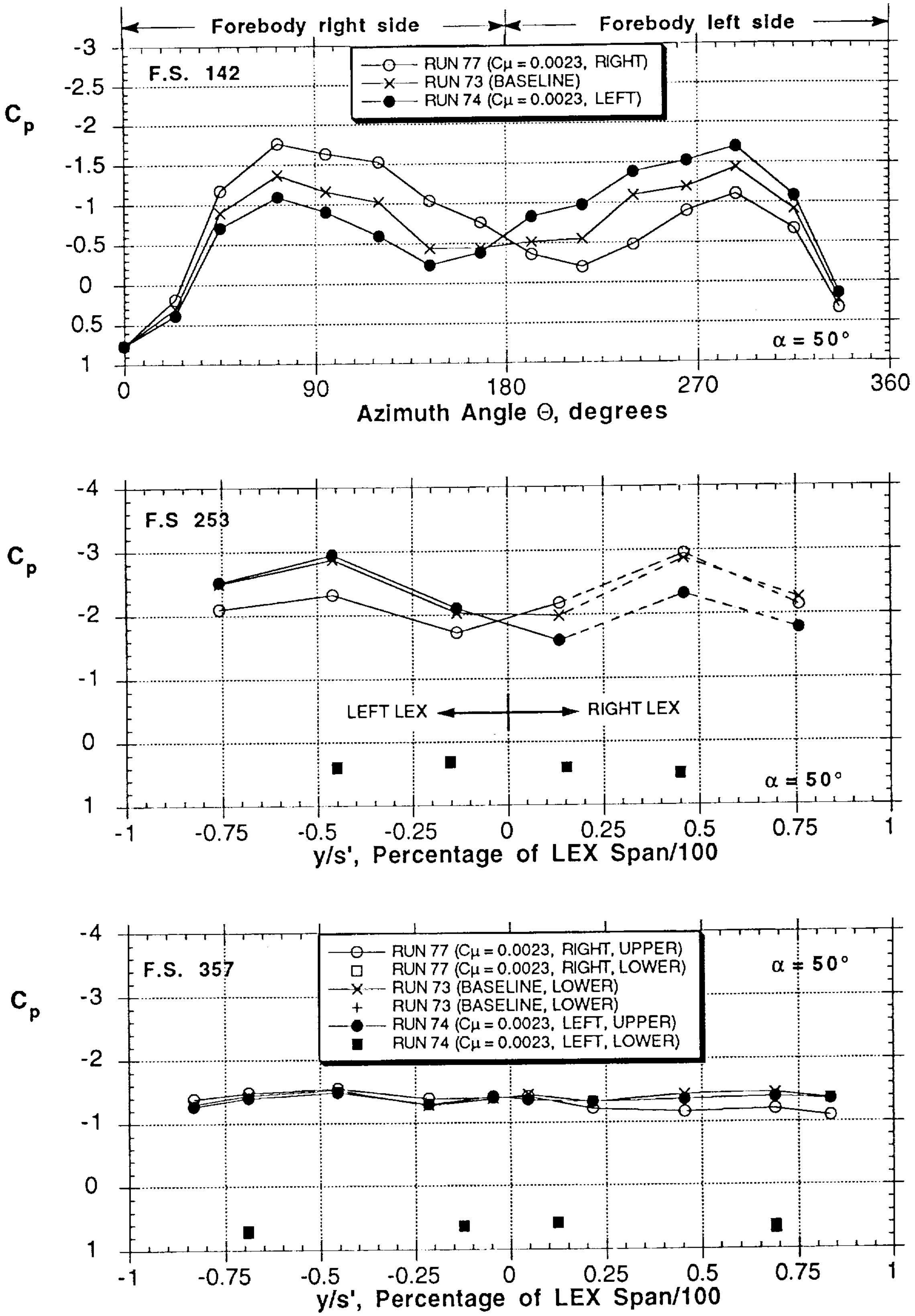

Figure 40 - Effect of jet blowing (60° inboard, nose 4) on pressure distributions at α = 50°

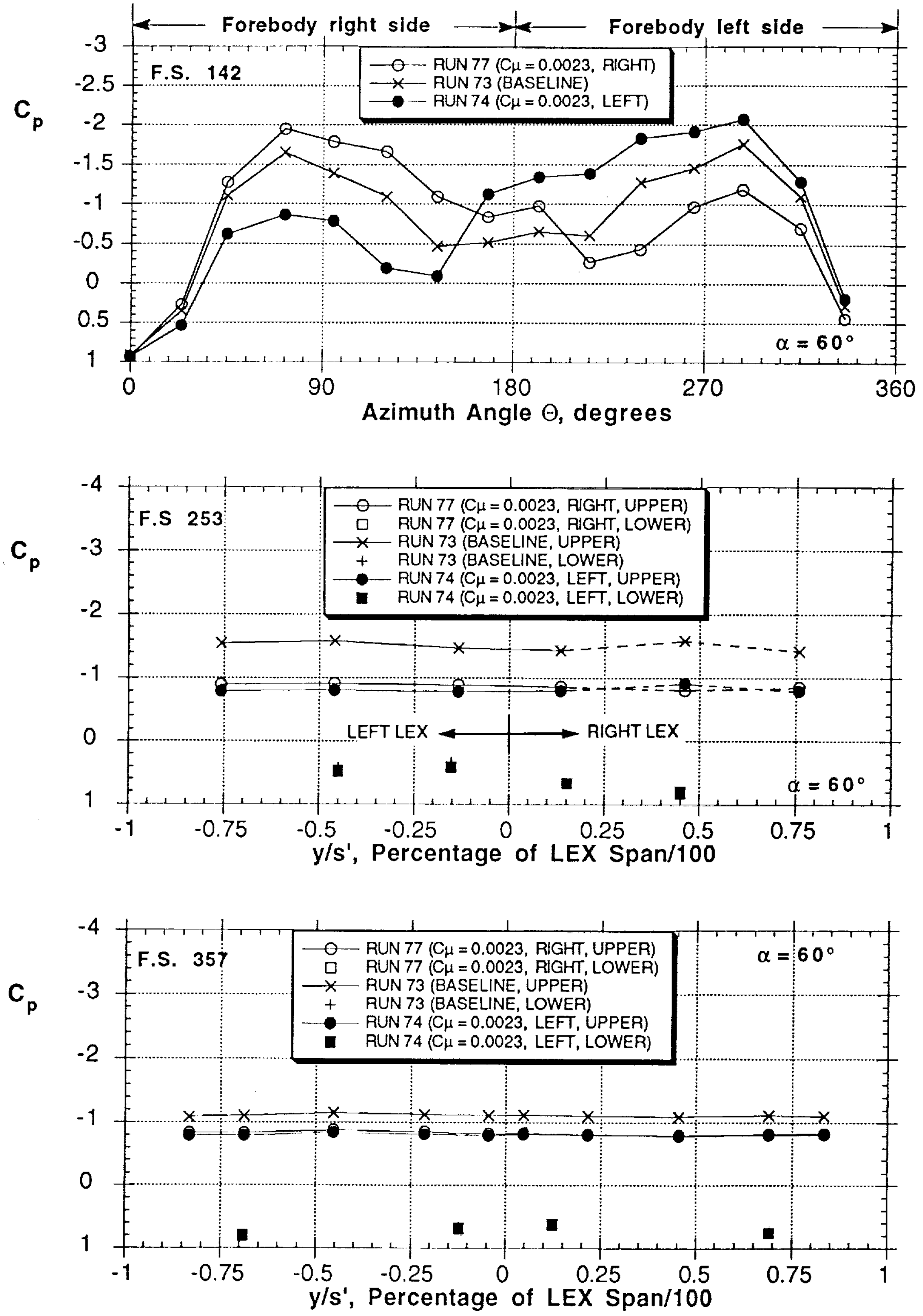

Figure 41 - Effect of jet blowing (60° inboard, nose 4) on pressure distributions at $\alpha = 60°$

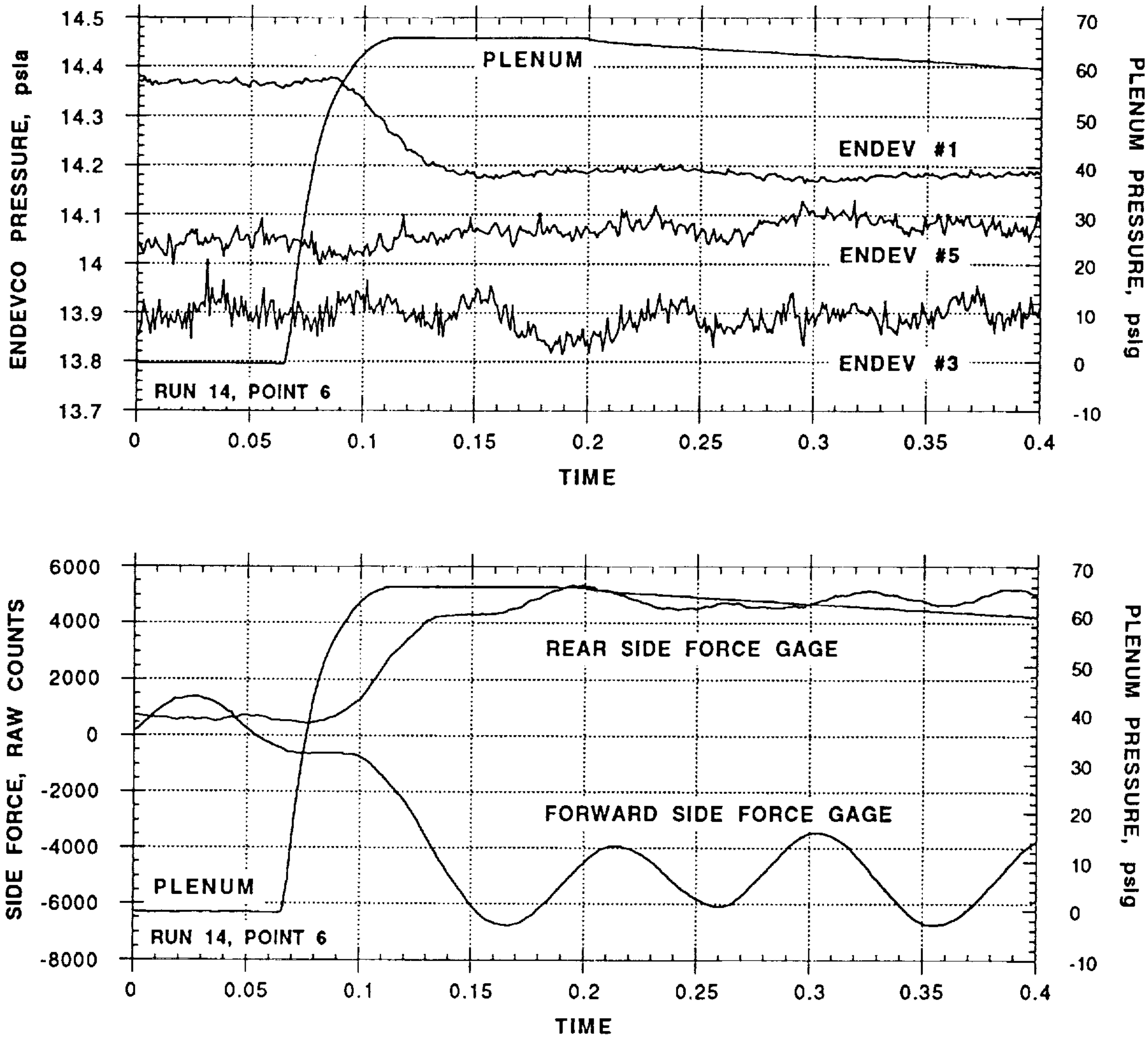

Figure 42 - Time lag effects (jet blowing onset, 60° inboard, nose 4, $\alpha = 50°$)

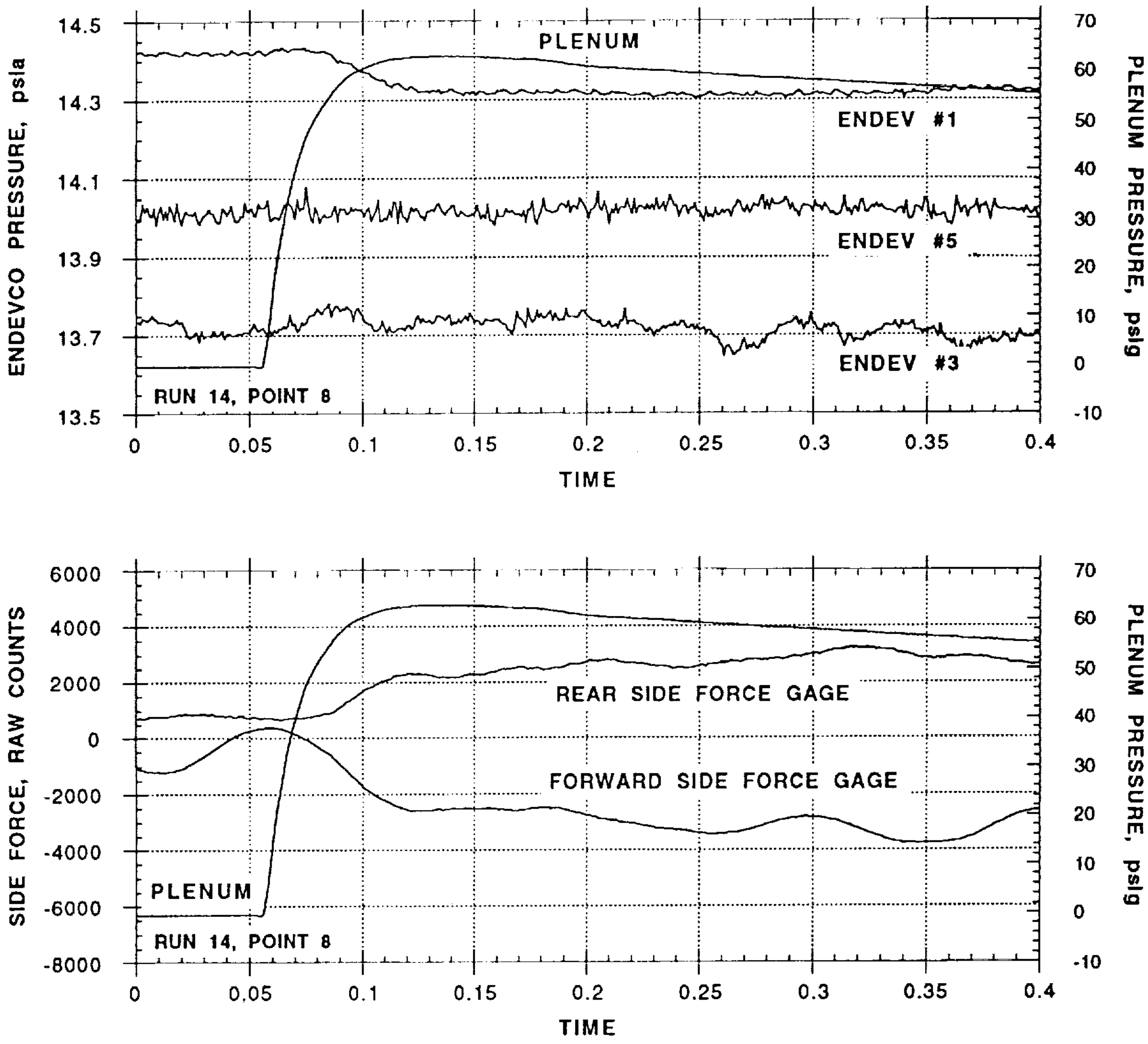

Figure 43 - Time lag effects (jet blowing onset, 60° inboard, nose 4, $\alpha = 40°$)

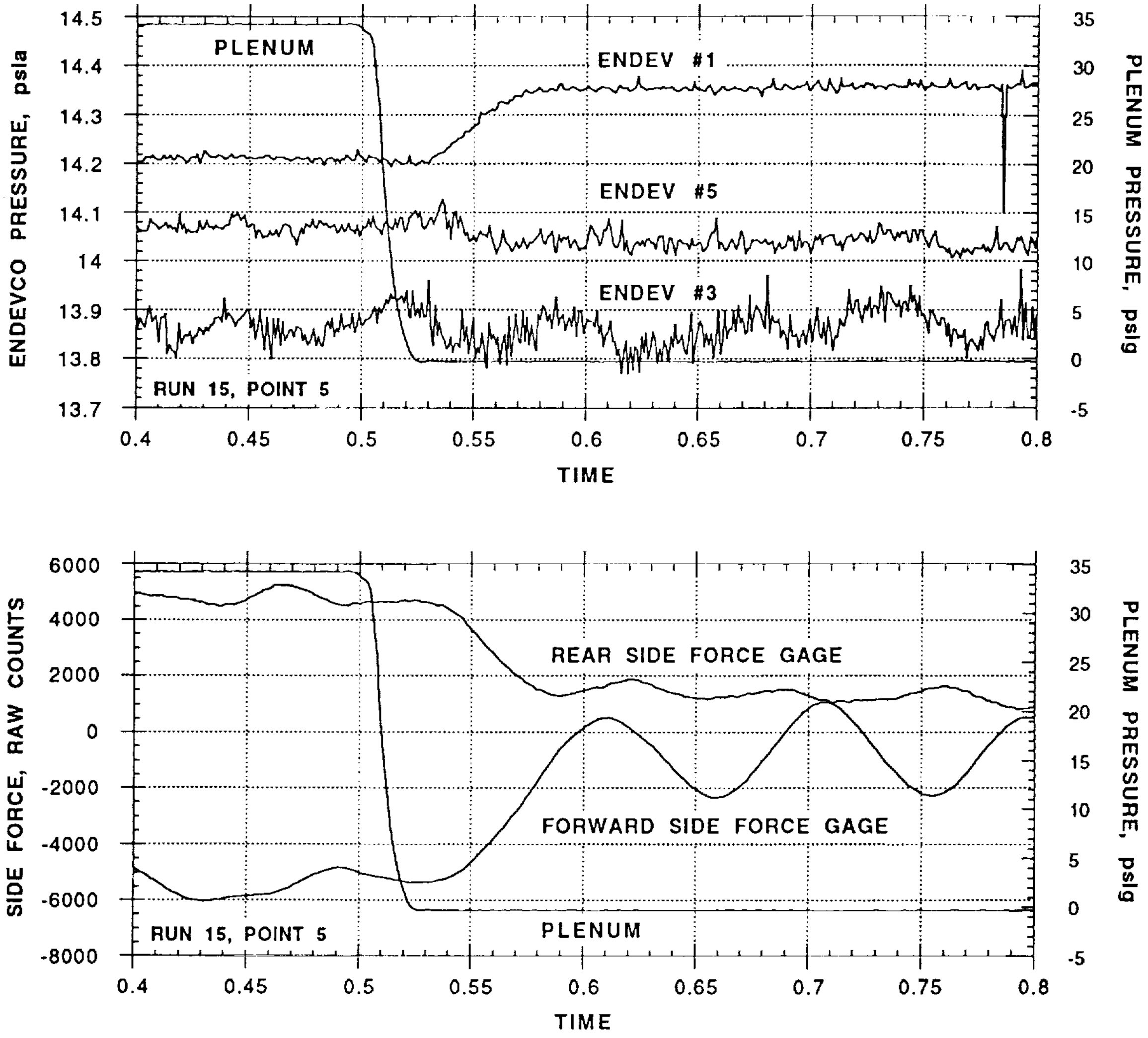

Figure 44 - Time lag effects (jet blowing decay, 60° inboard, nose 4, $\alpha = 50°$)

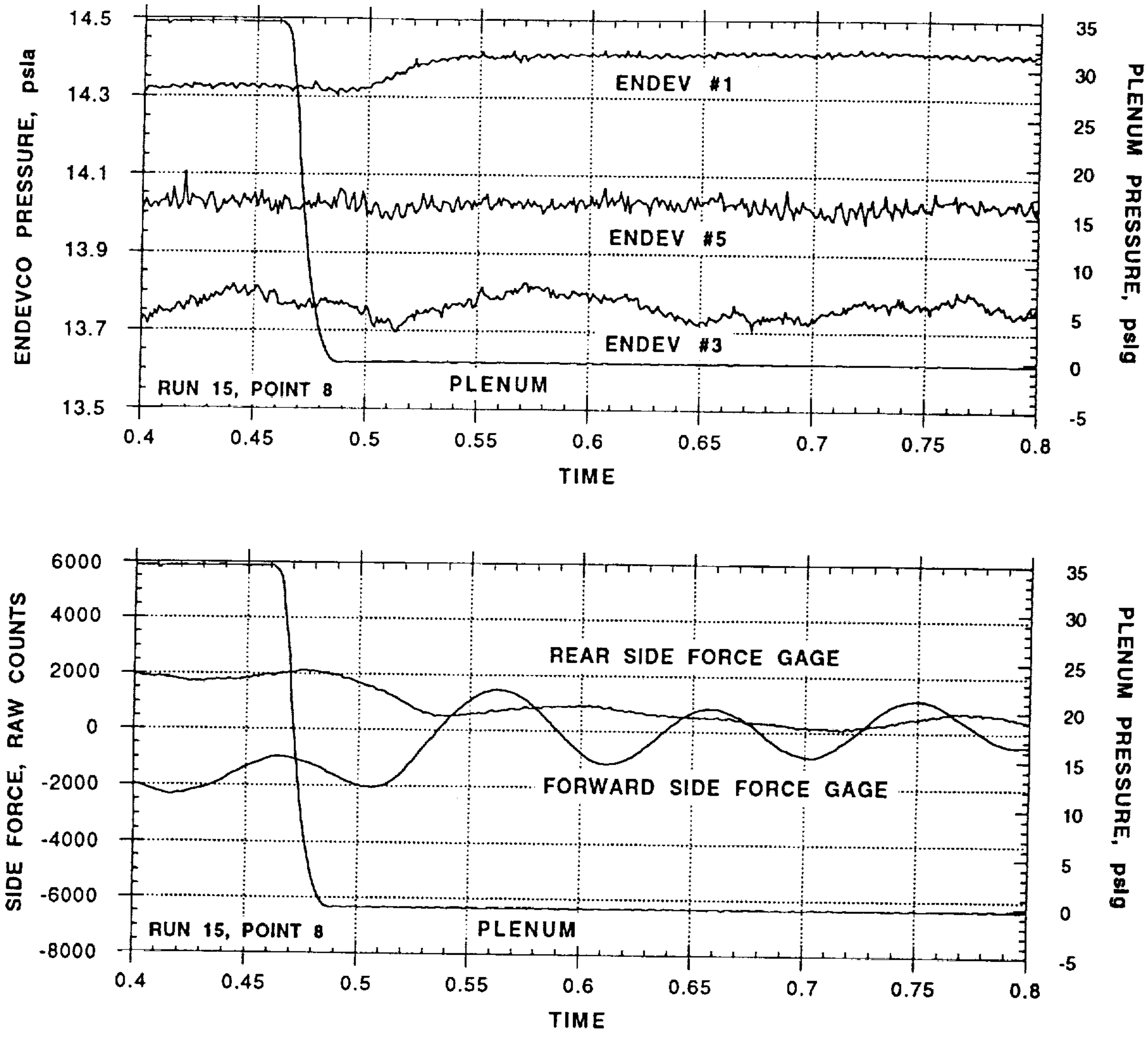

Figure 45 - Time lag effects (jet blowing decay, 60° inboard, nose 4, α = 40°)

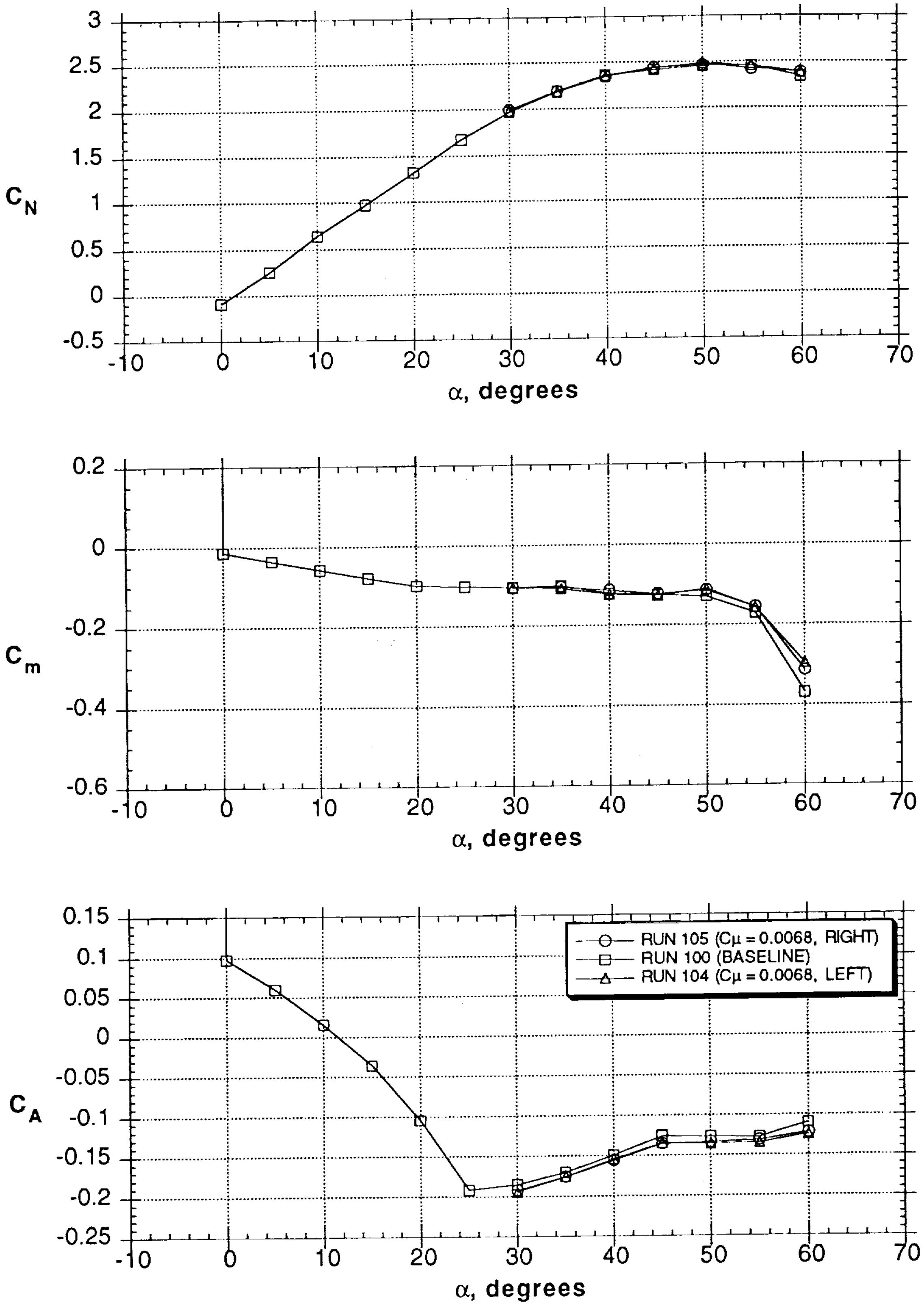

Figure 46 - Effect of slot blowing (slot ABCD)

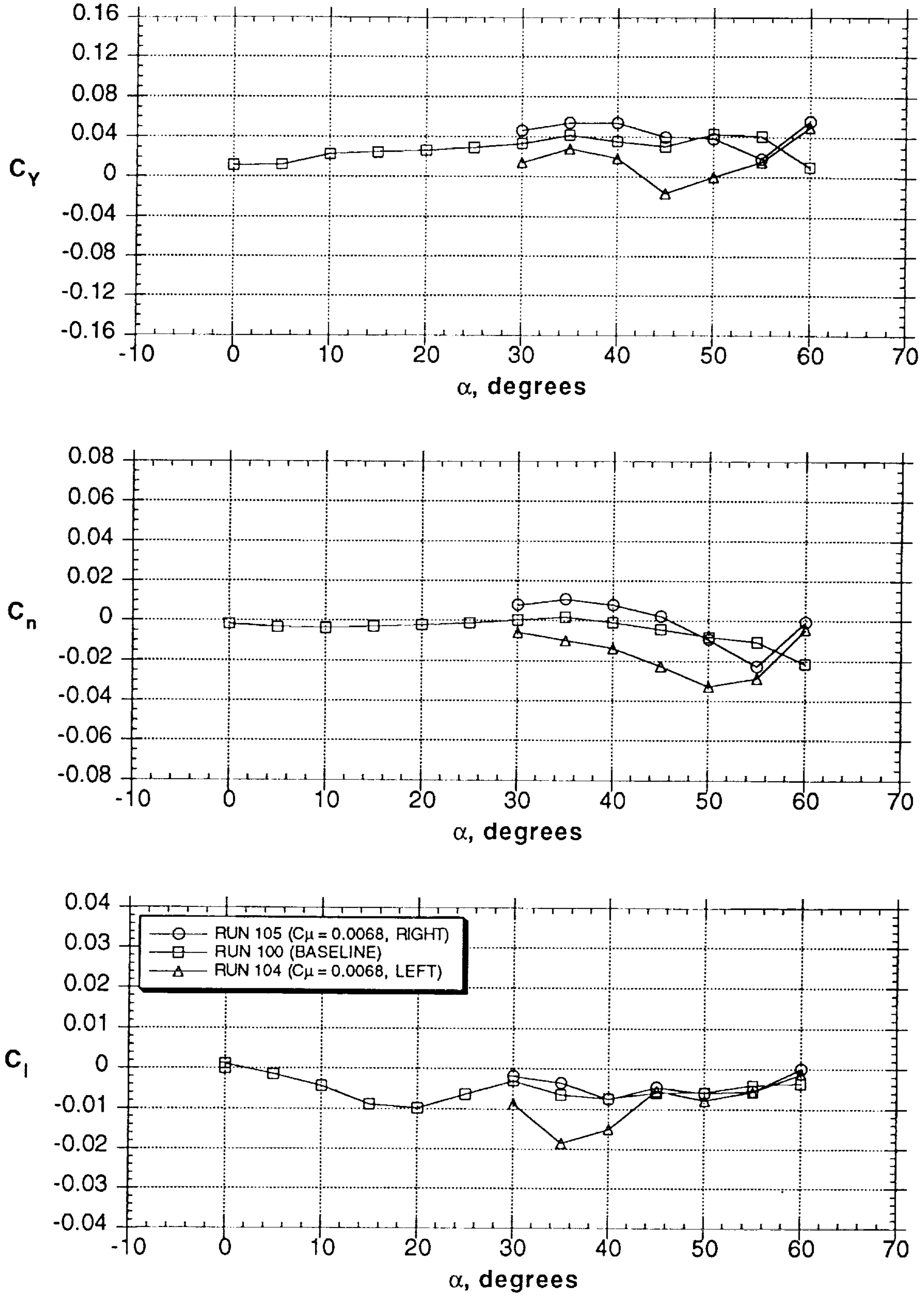

Figure 46 - Concluded

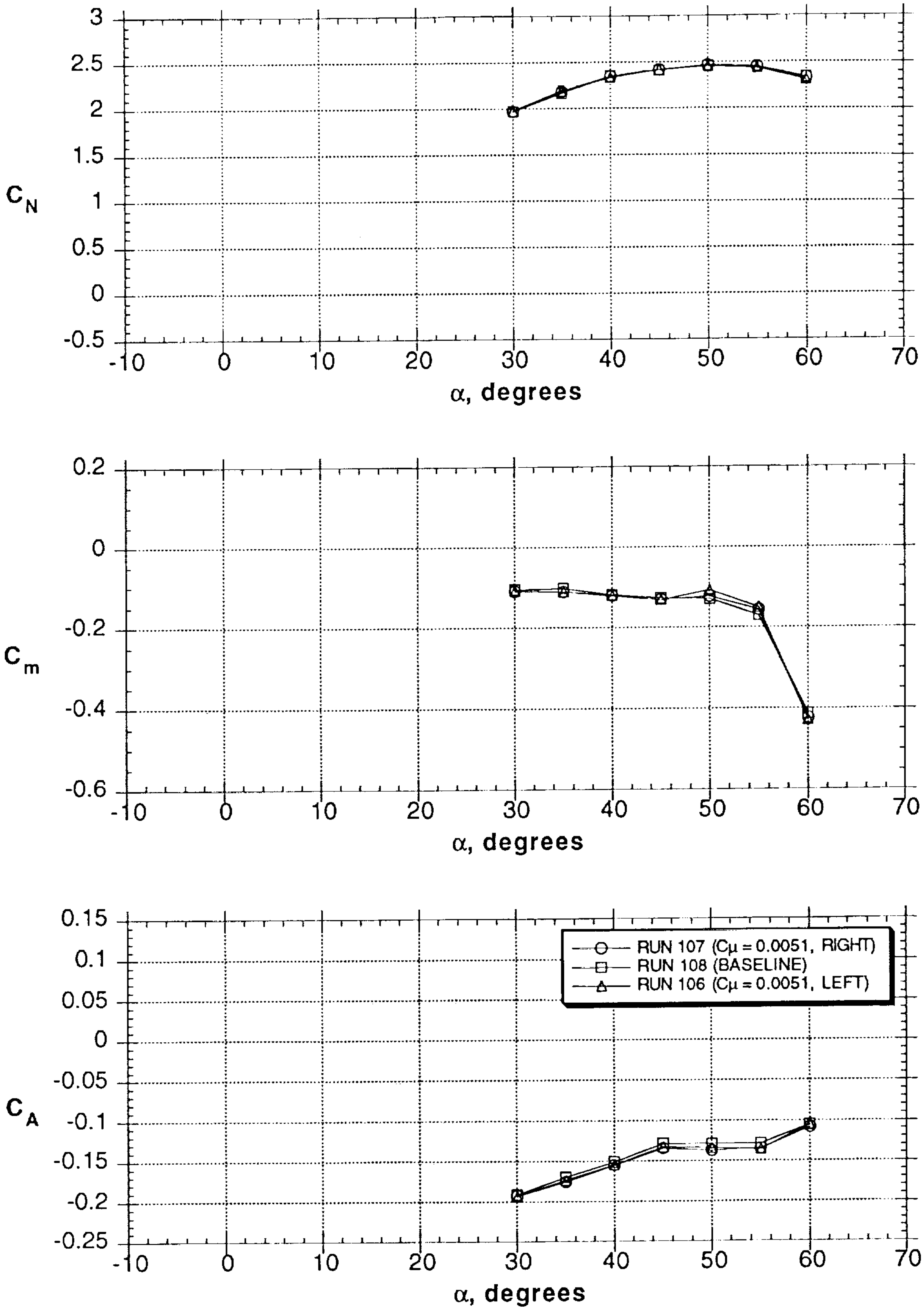

Figure 47 - Effect of slot blowing (slot ABC)

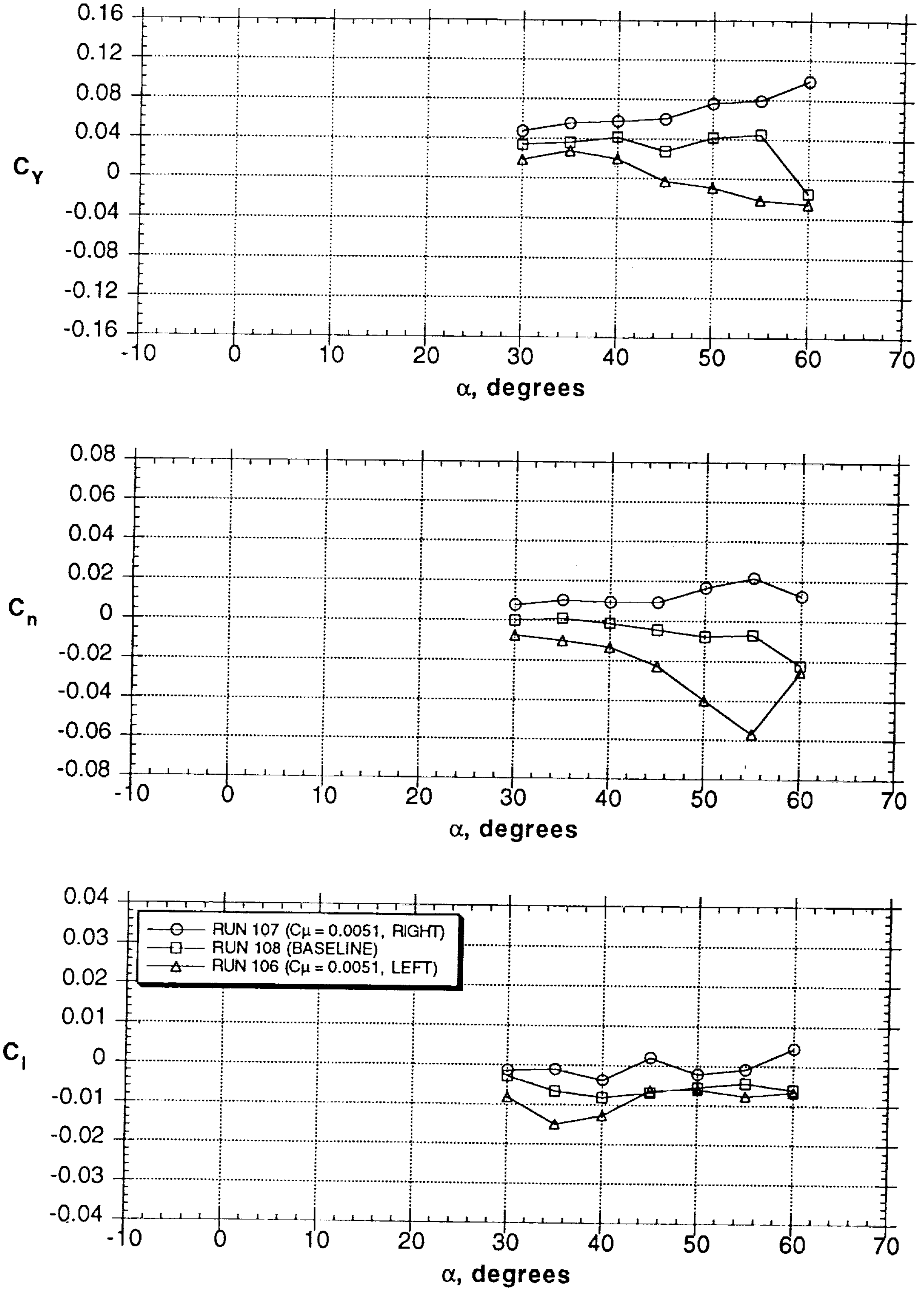

Figure 47 - Concluded

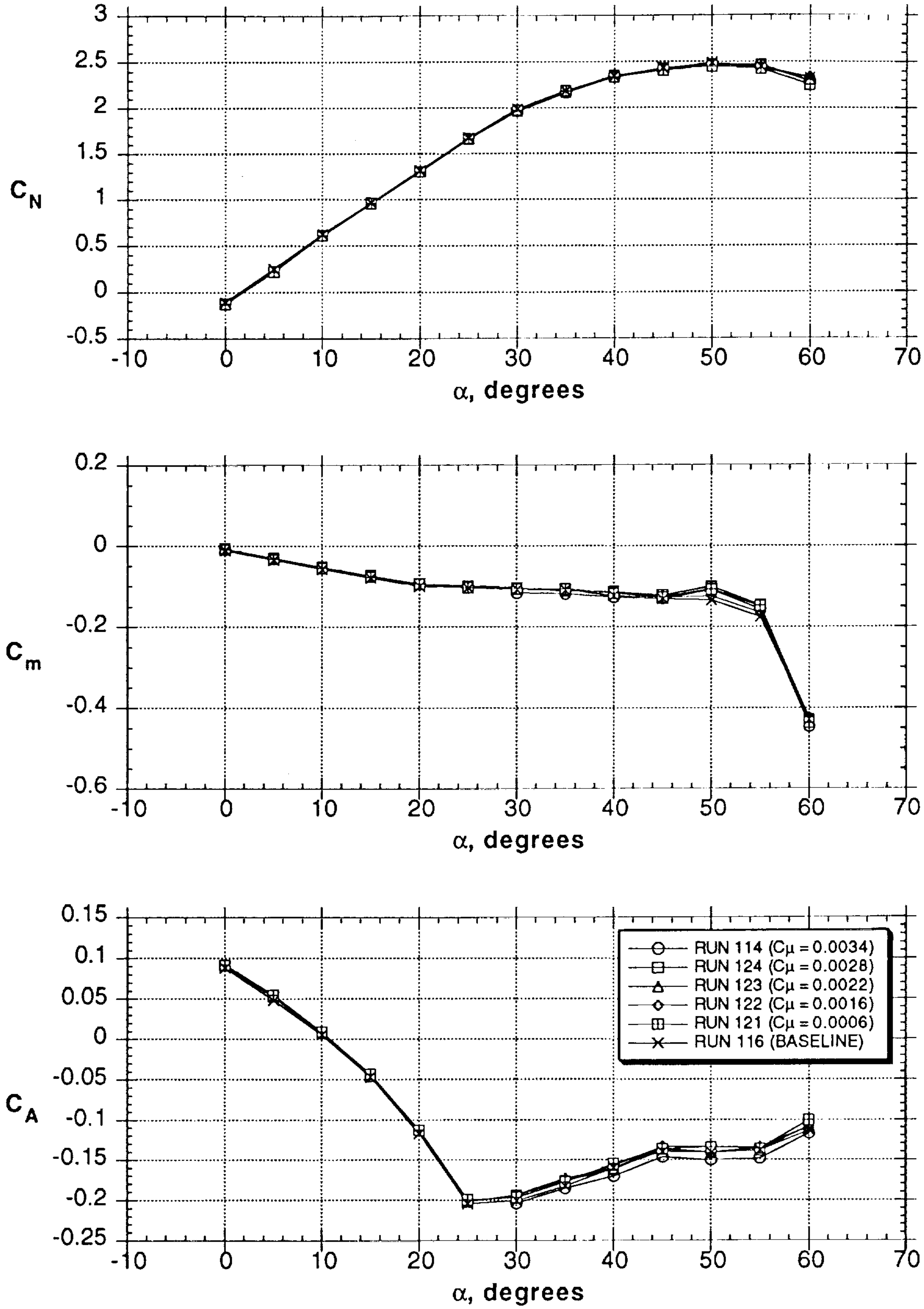

Figure 48 - Effect of slot blowing (slot AB, right side only)

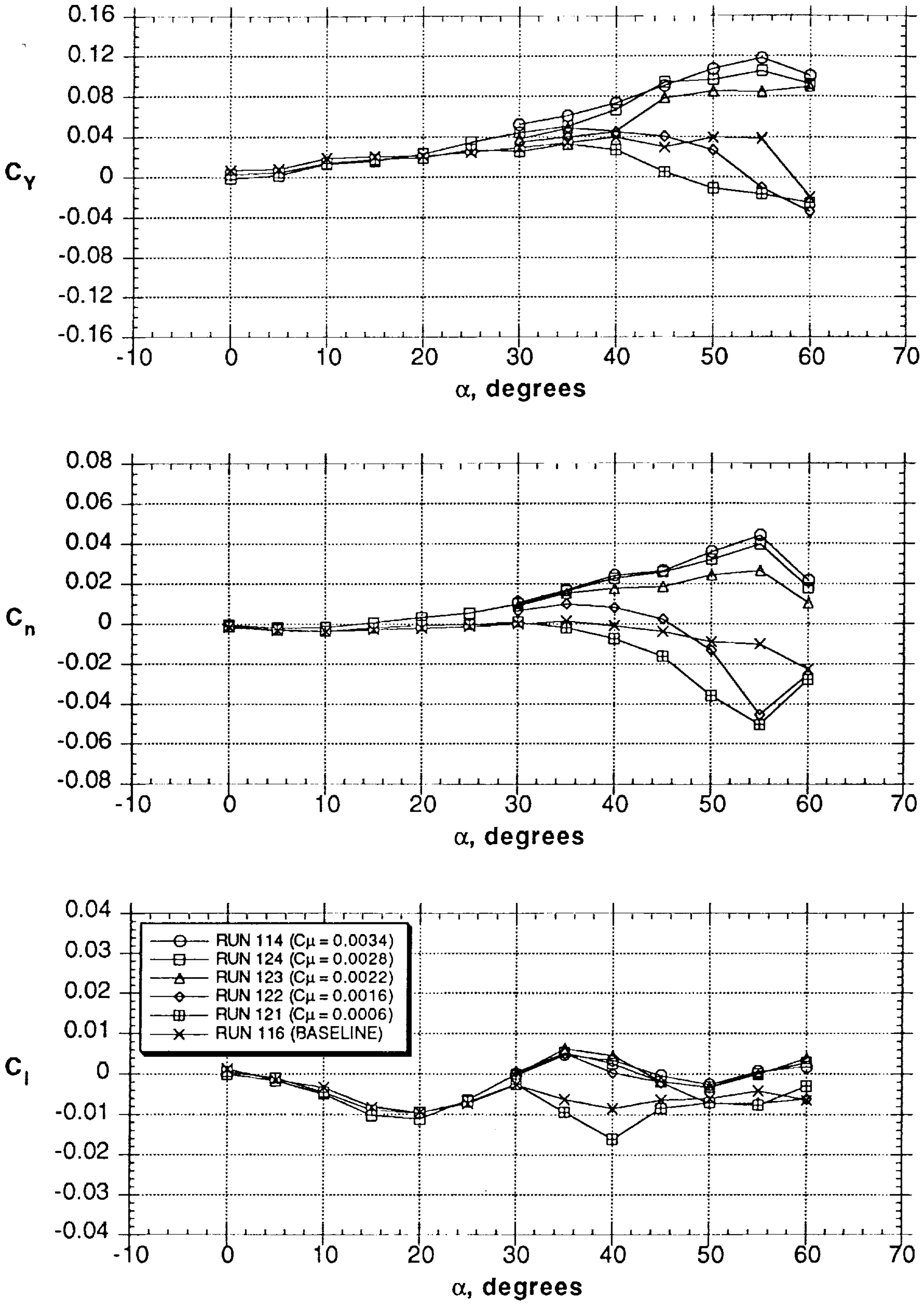

Figure 48 - Concluded

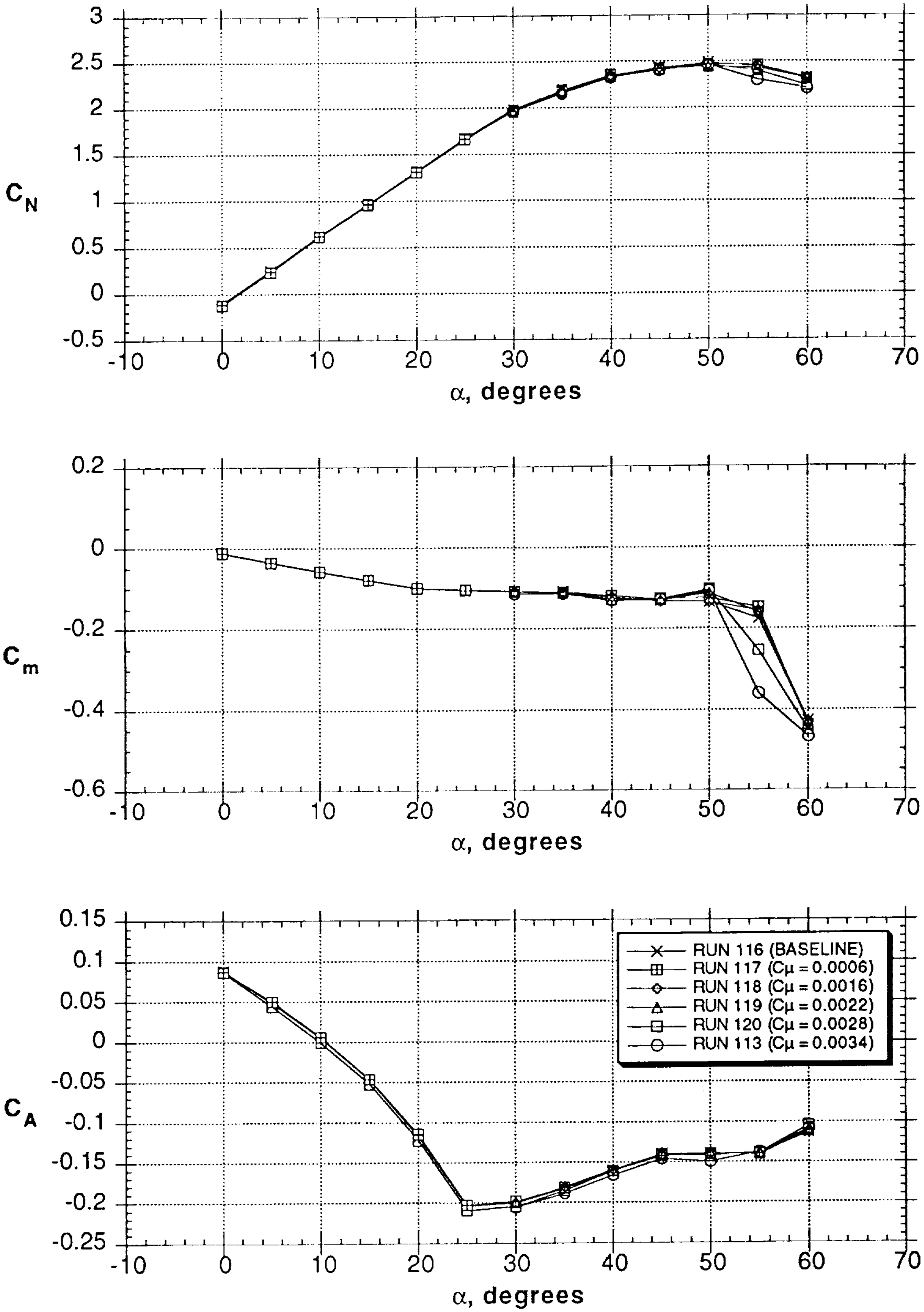

Figure 49 - Effect of slot blowing (slot AB, left side only)

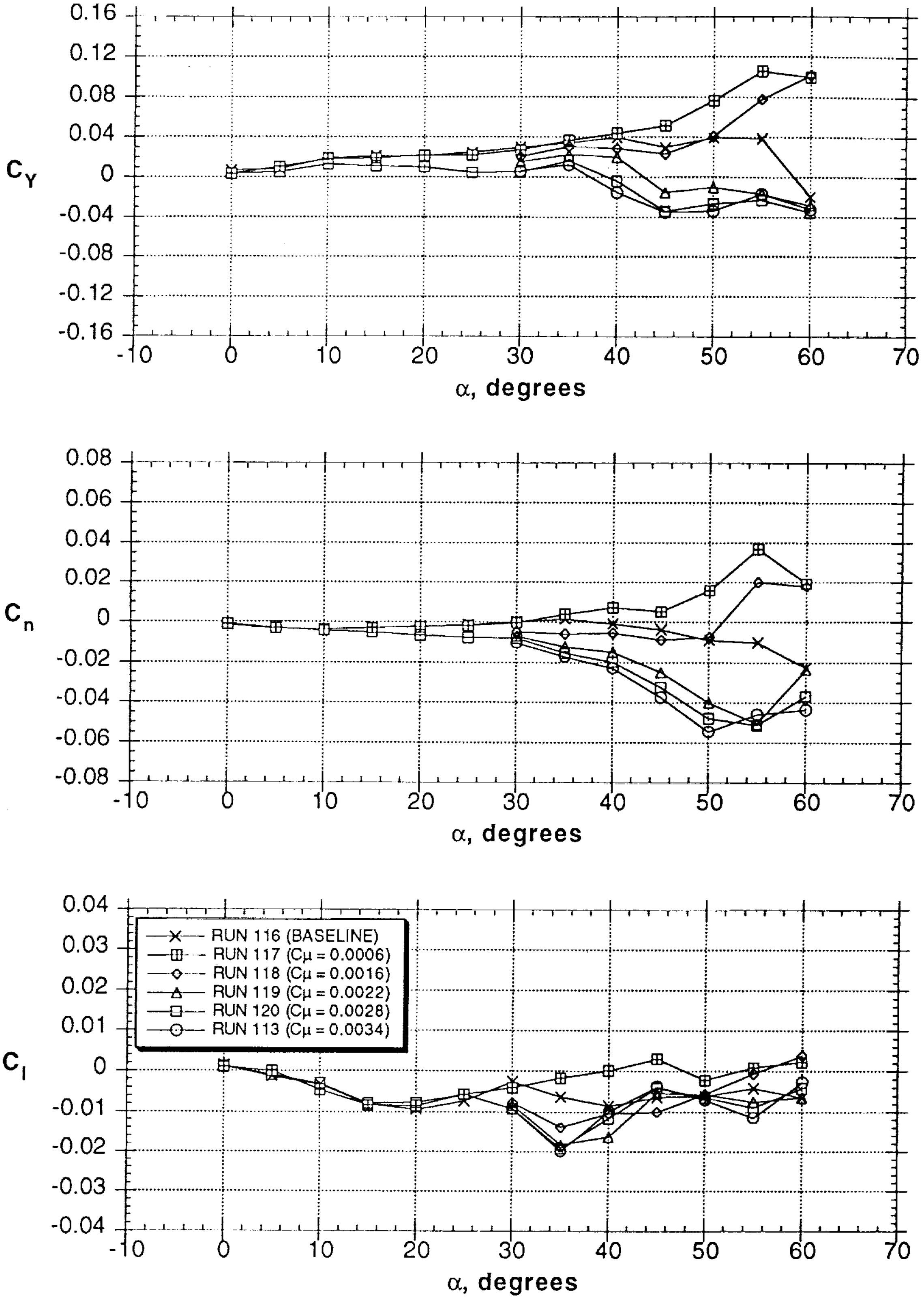

Figure 49 - Concluded

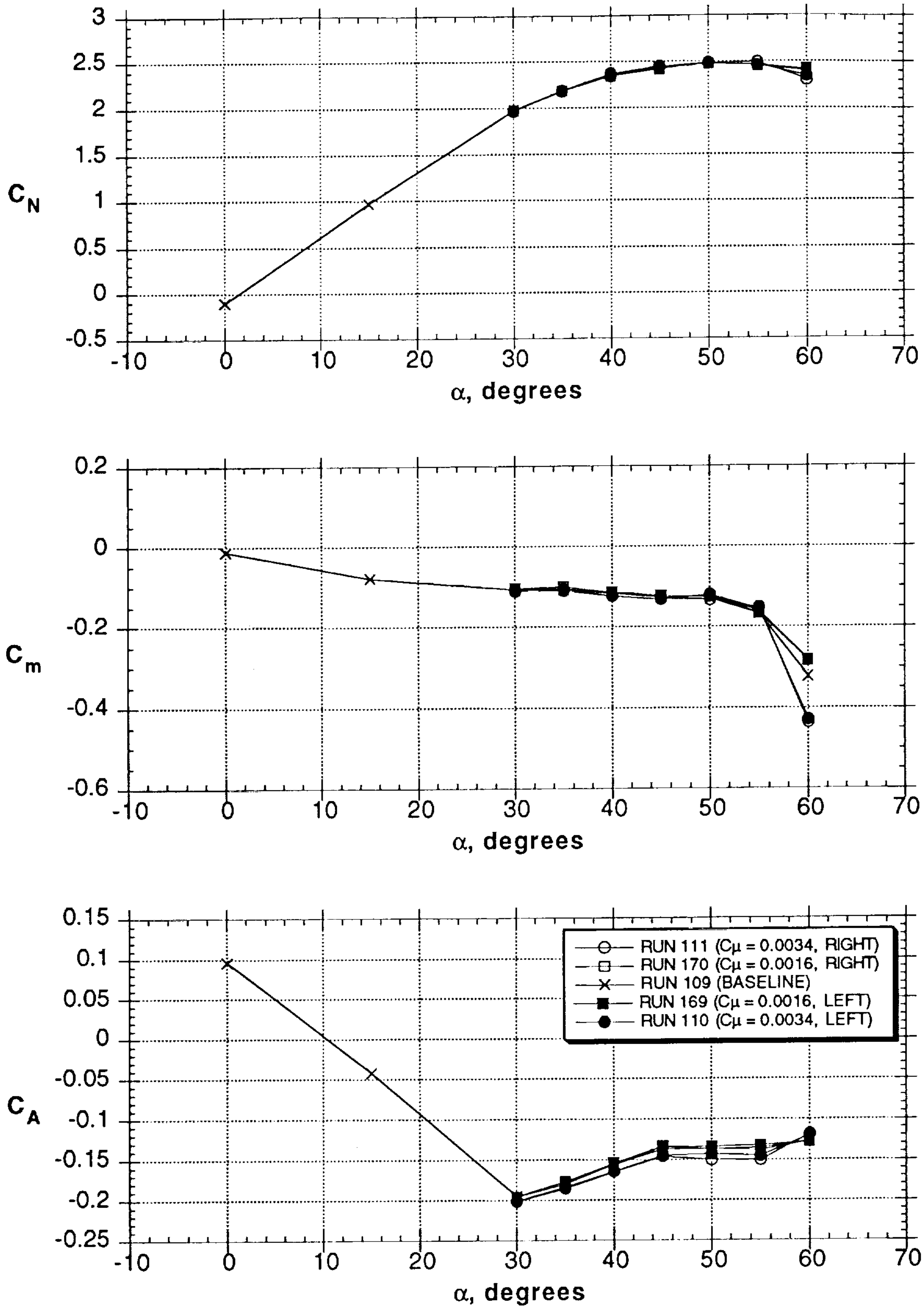

Figure 50 - Effect of slot blowing (slot BC)

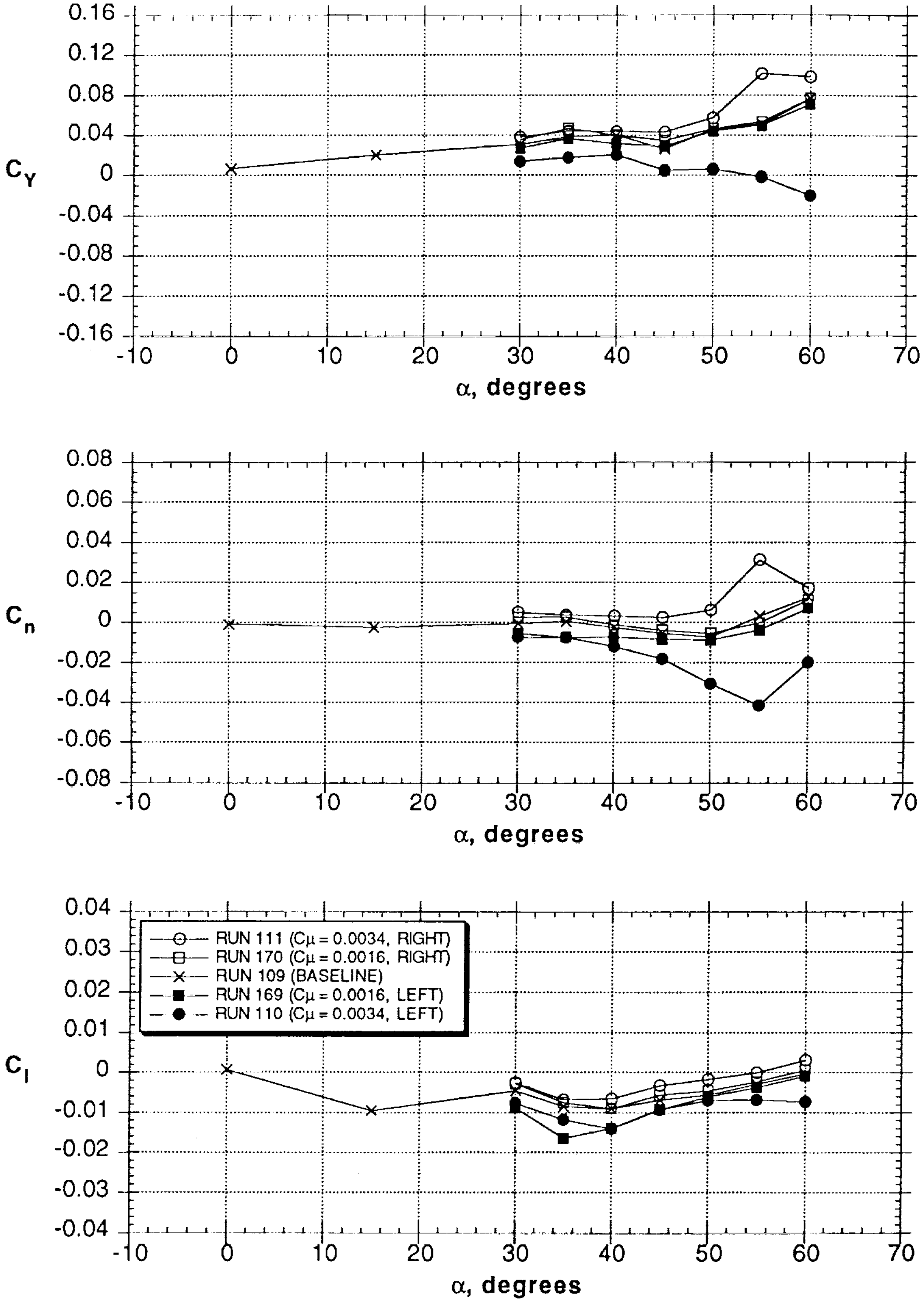

Figure 50 - Concluded

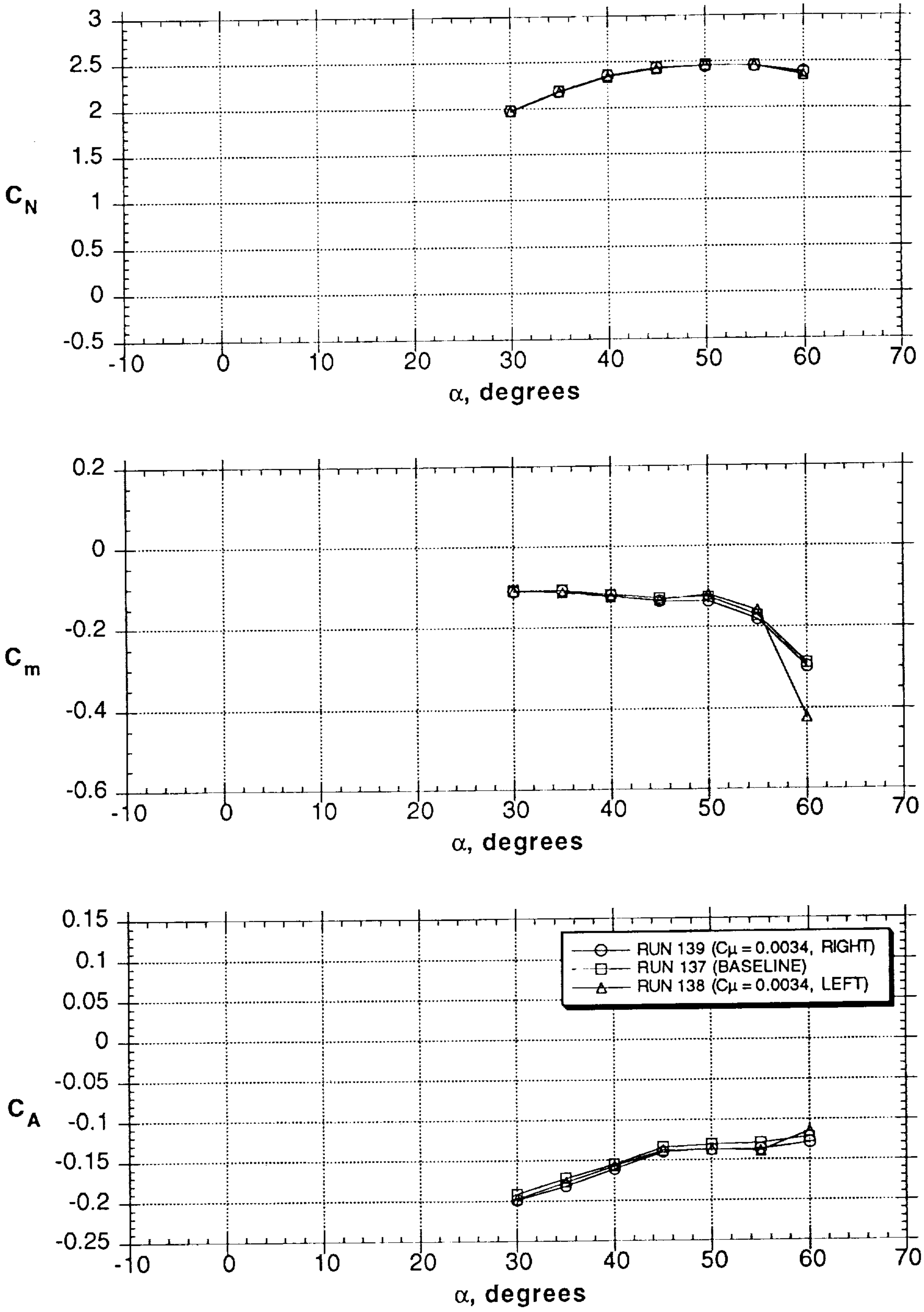

Figure 51 - Effect of slot blowing (slot CD)

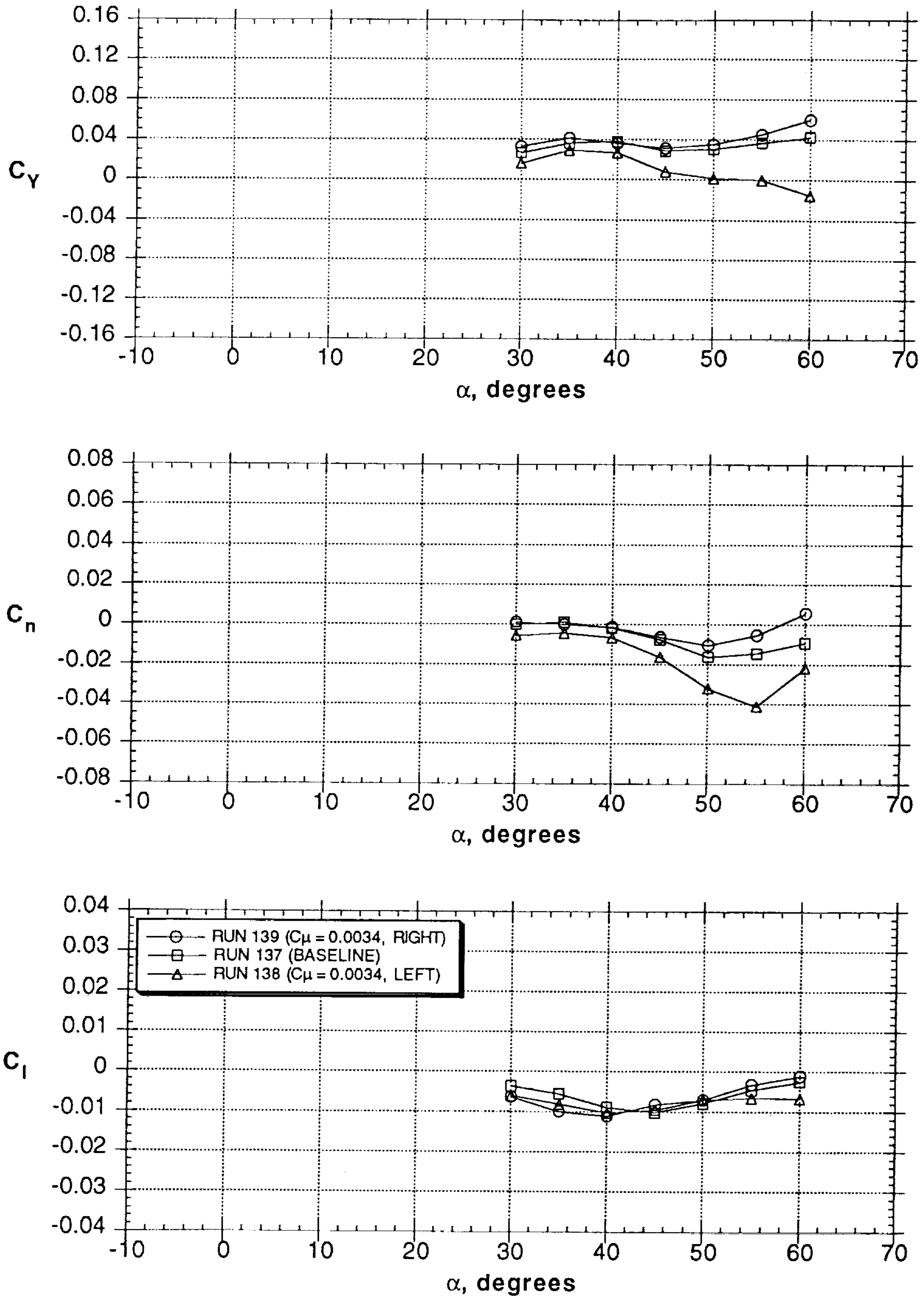

Figure 51 - Concluded

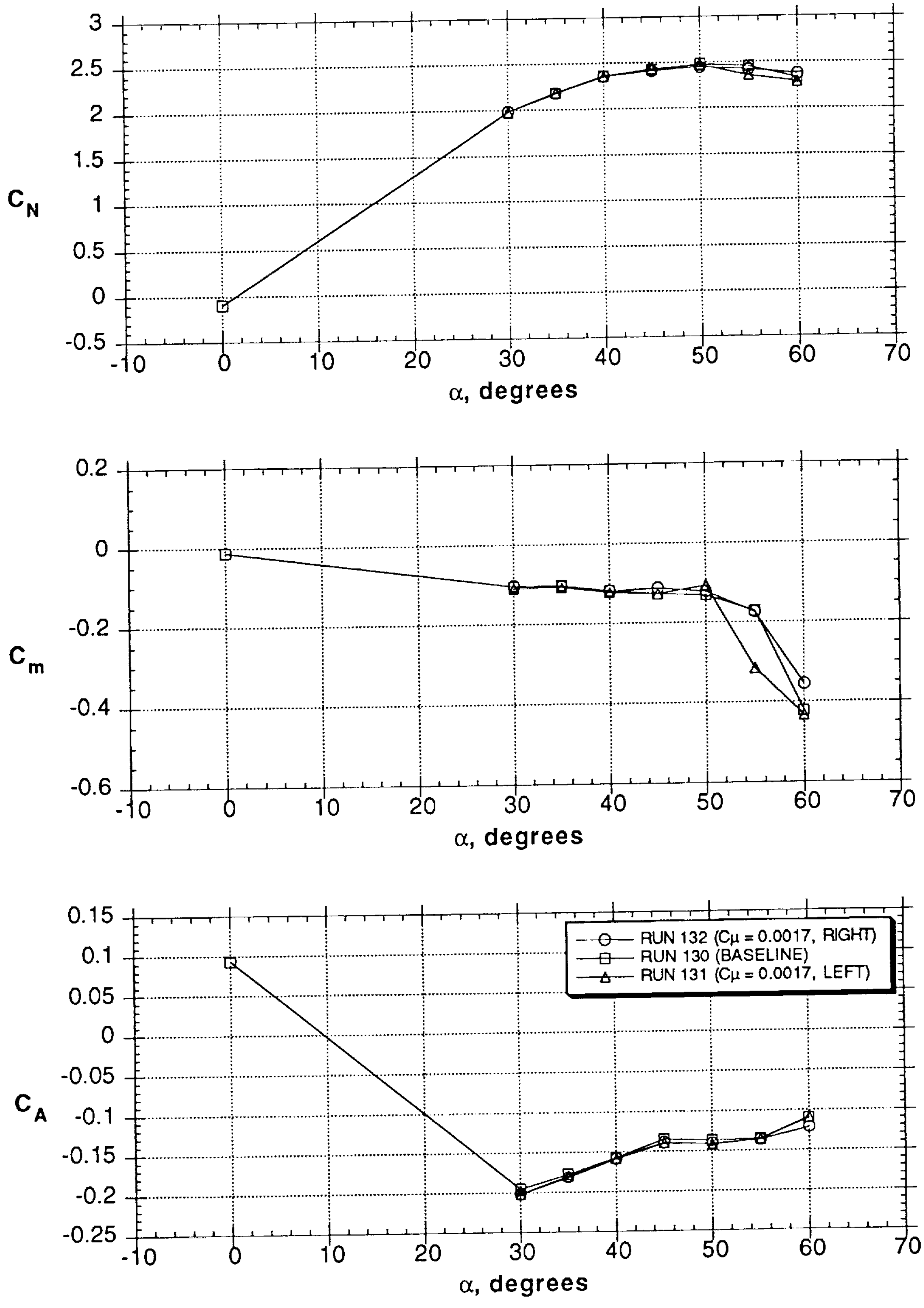

Figure 52 - Effect of slot blowing (slot A)

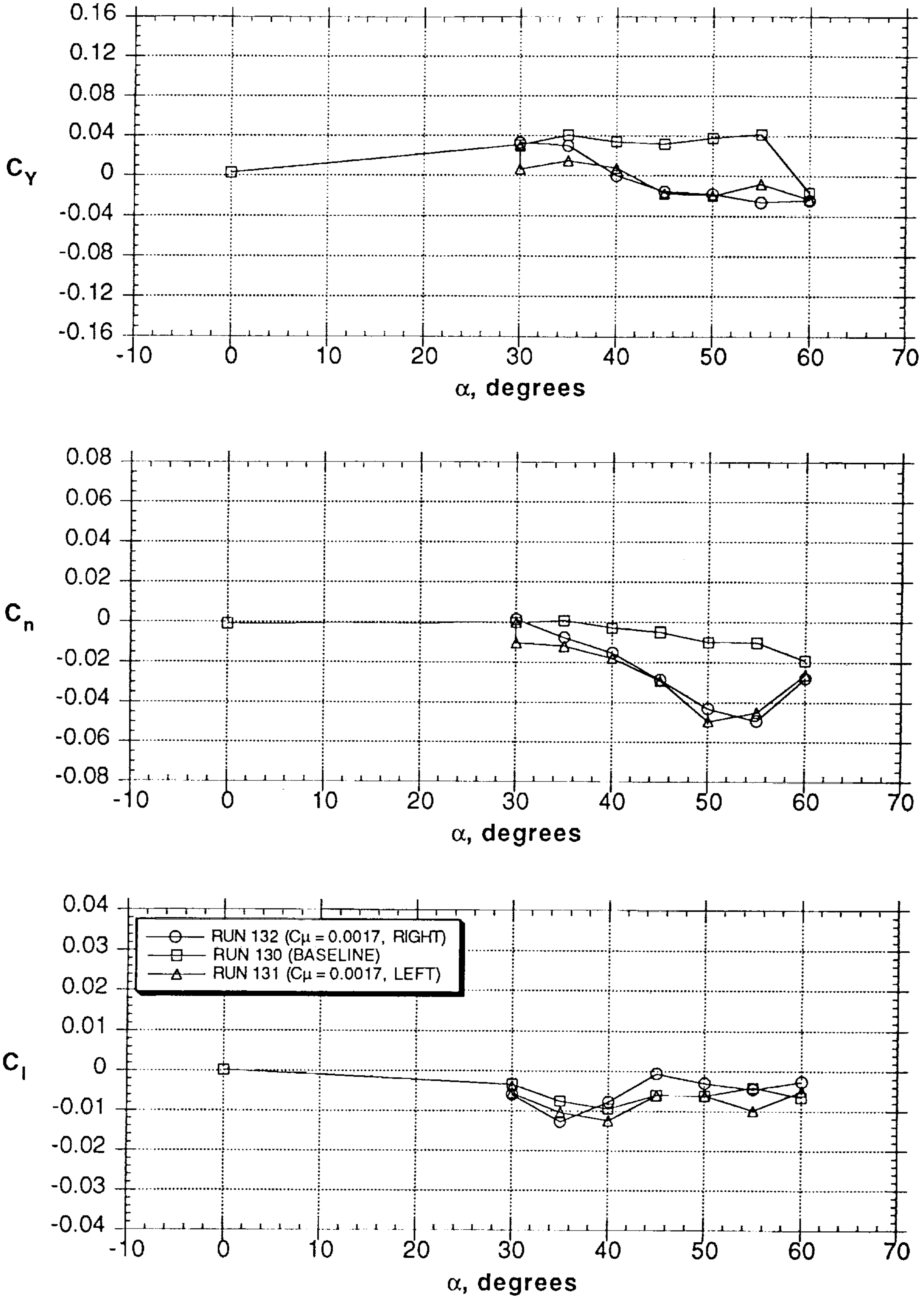

Figure 52 - Concluded

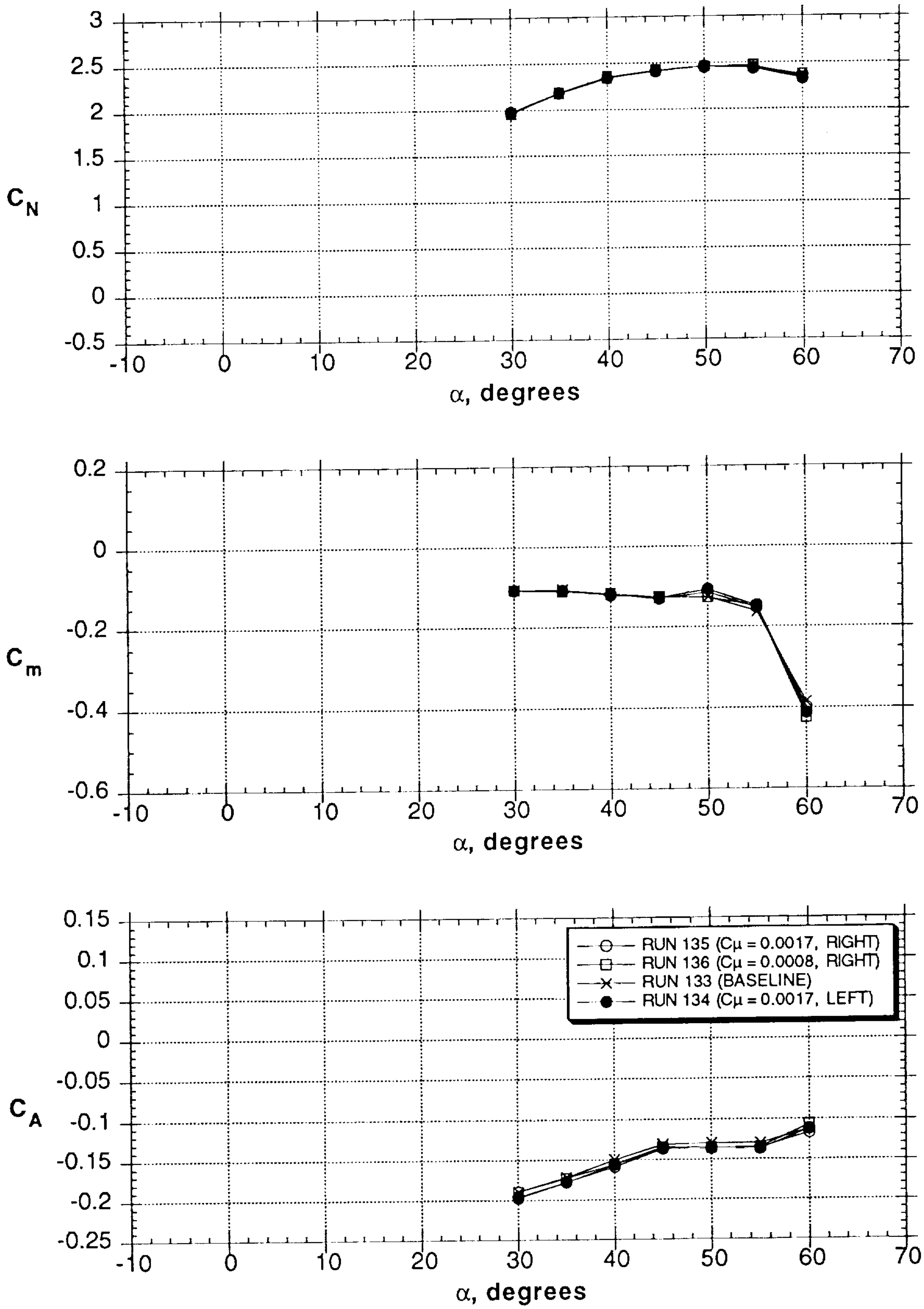

Figure 53 - Effect of slot blowing (slot B)

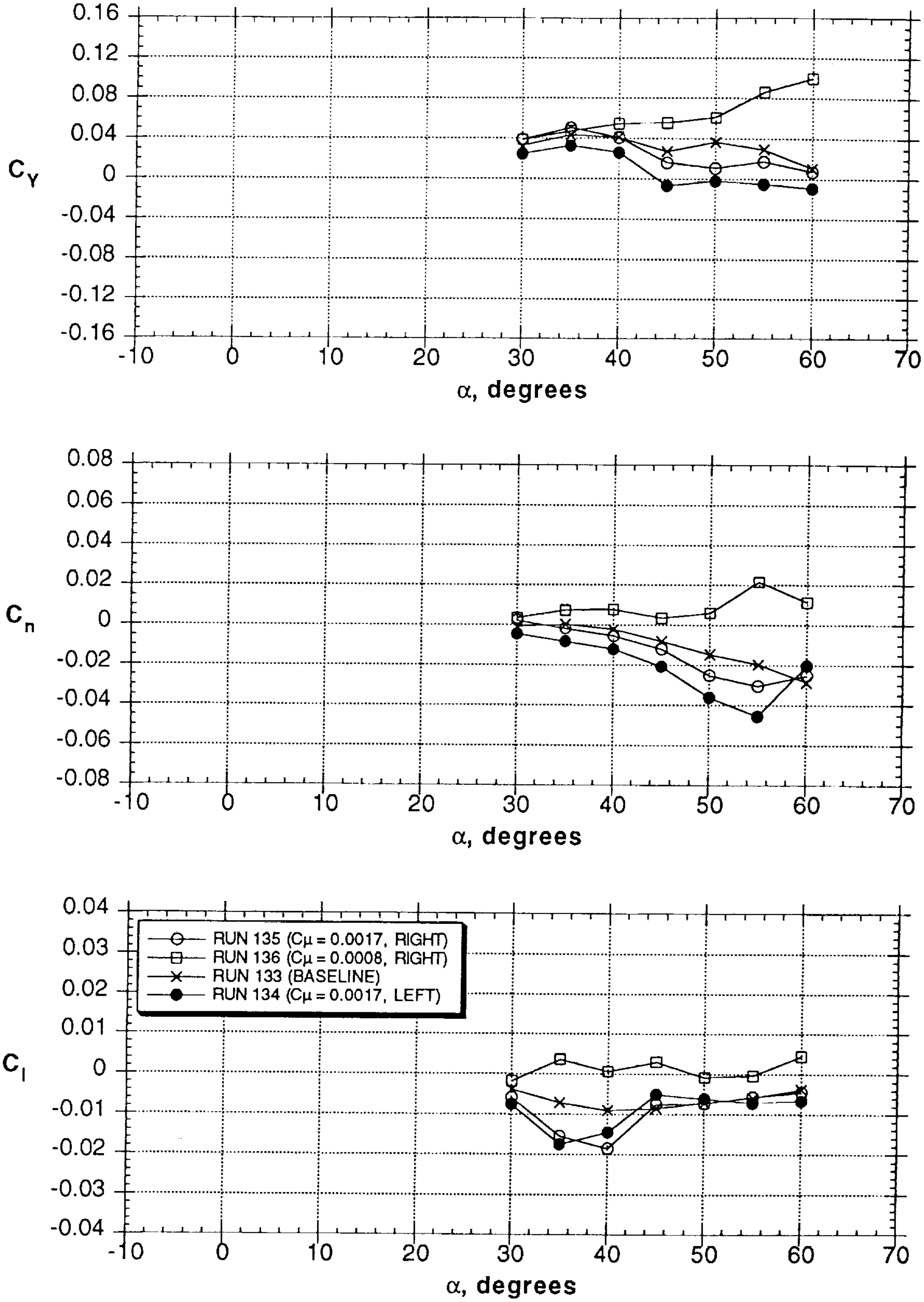

Figure 53 - Concluded

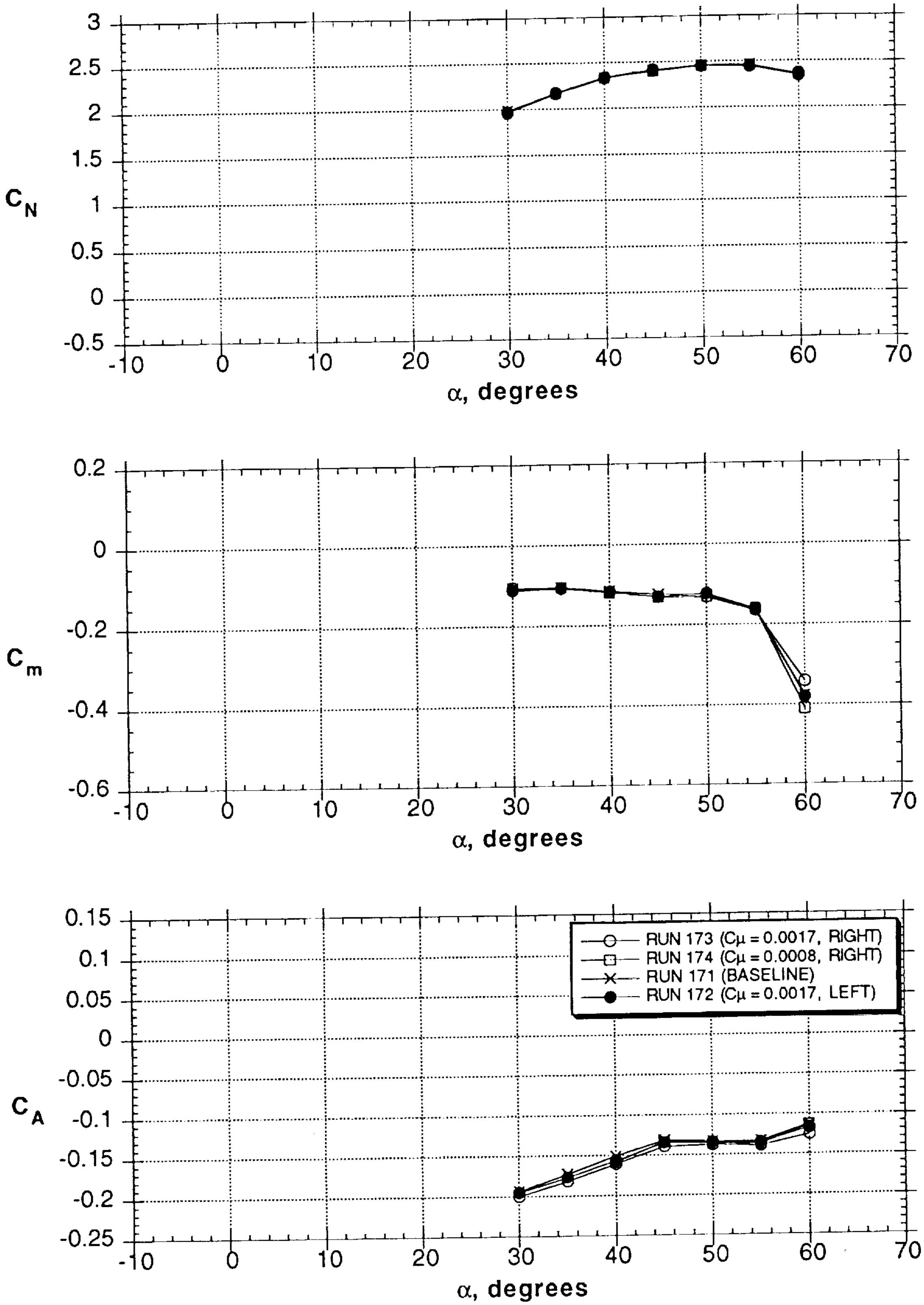

Figure 54 - Effect of slot blowing (slot C)

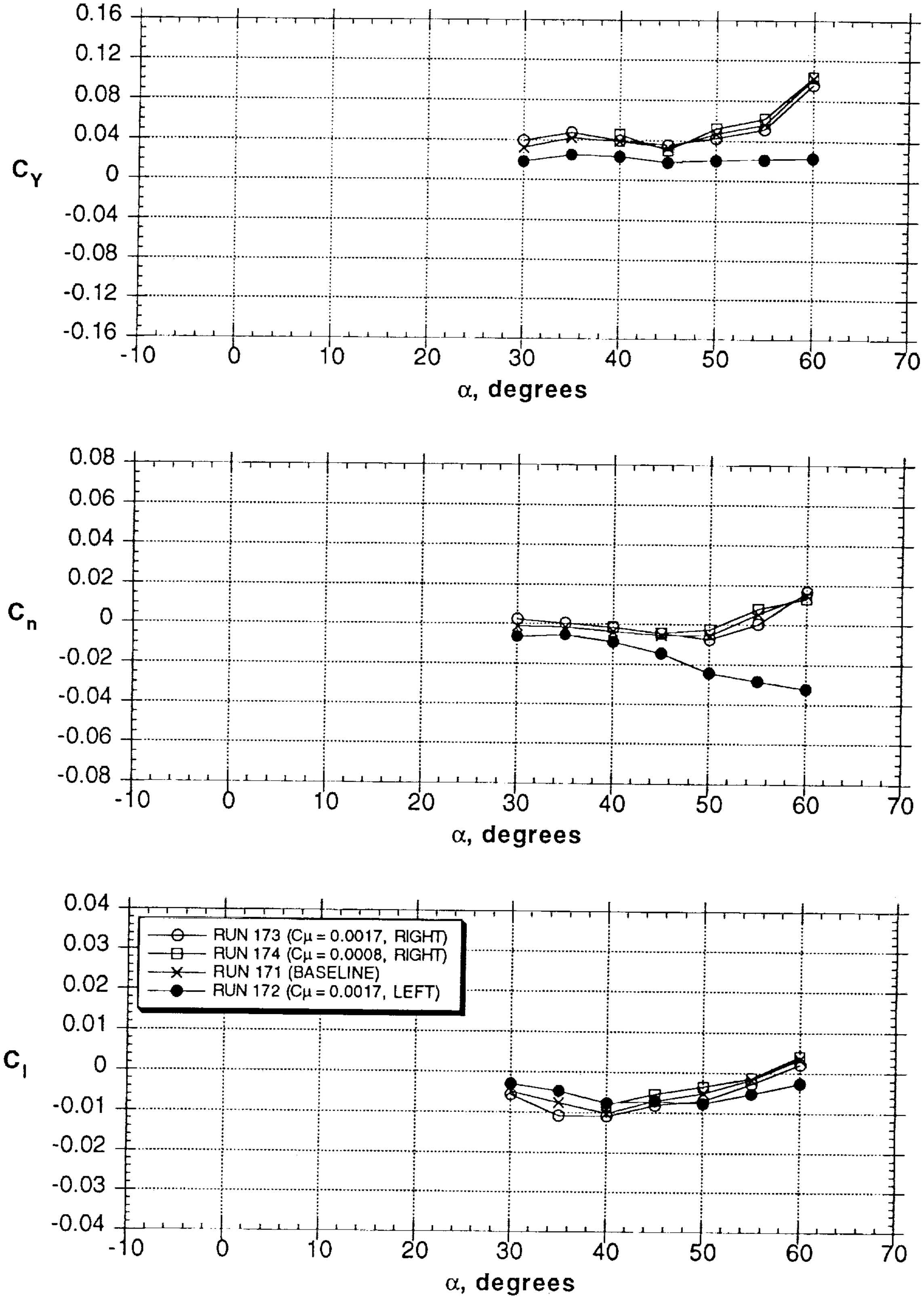

Figure 54 - Concluded

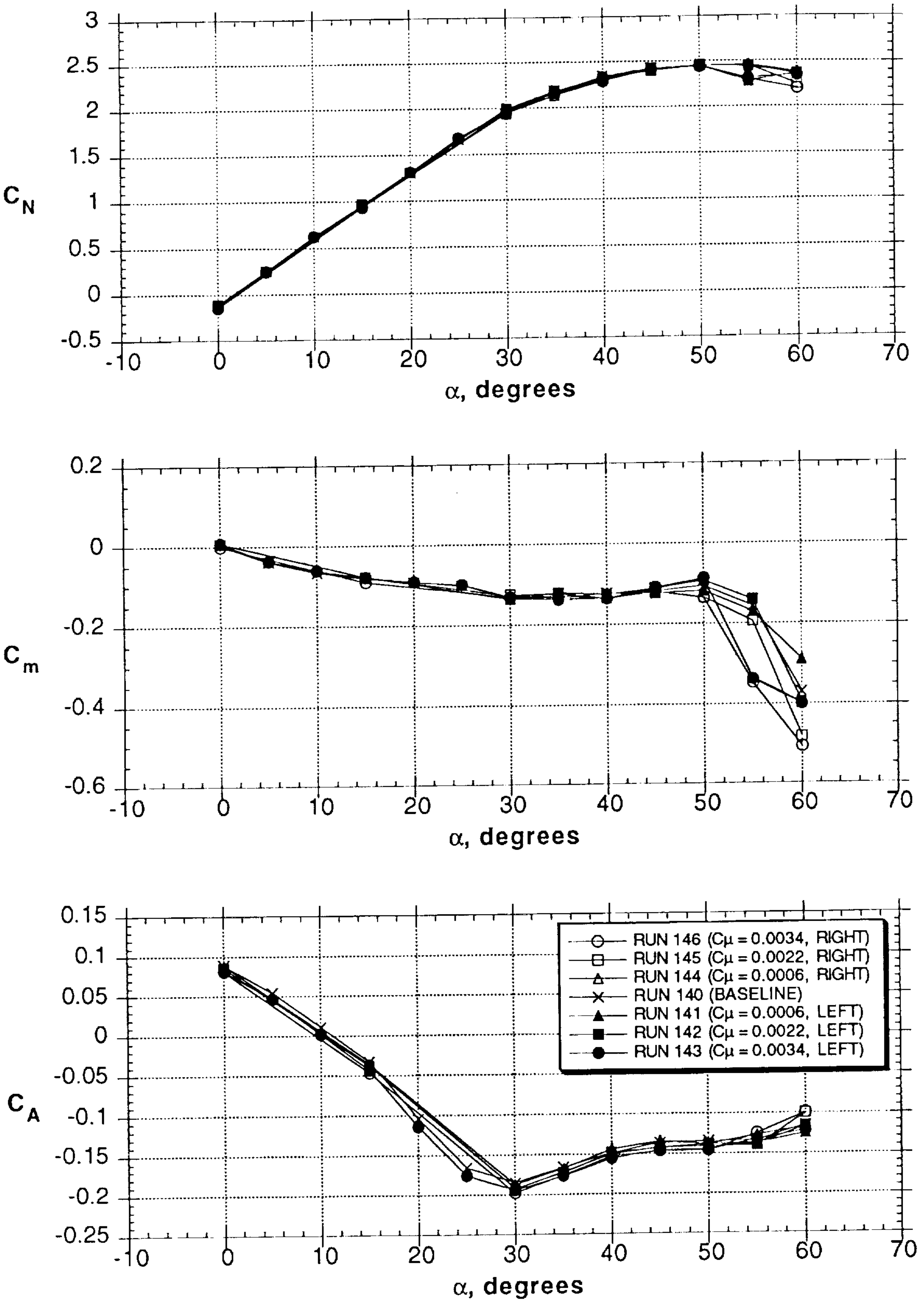

Figure 55 - Effect of sideslip on slot blowing effectiveness (slot AB, $\beta = -10°$)

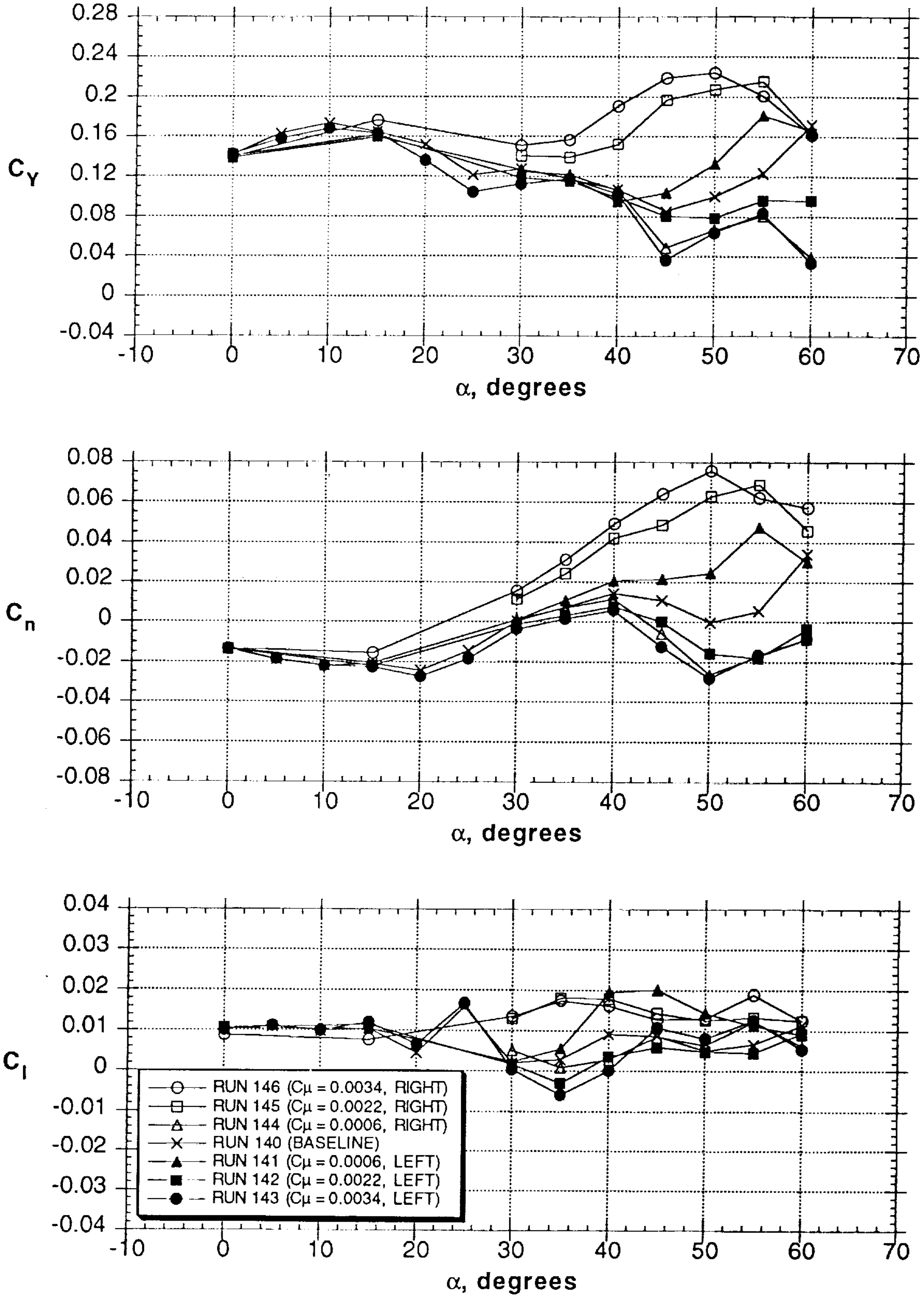

Figure 55 - Concluded

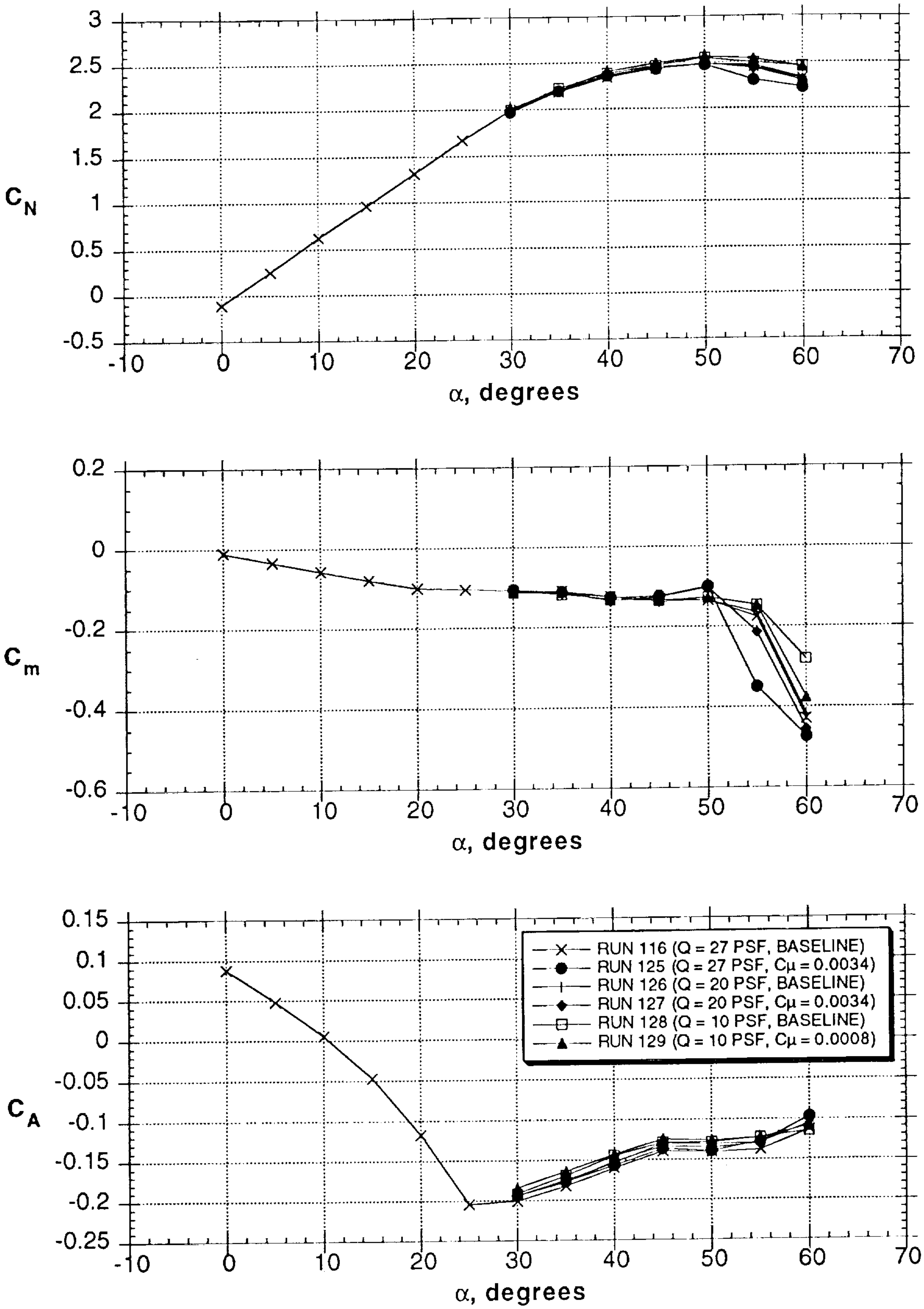

Figure 56 - Effect of Reynolds number on slot blowing (slot AB, left side only)

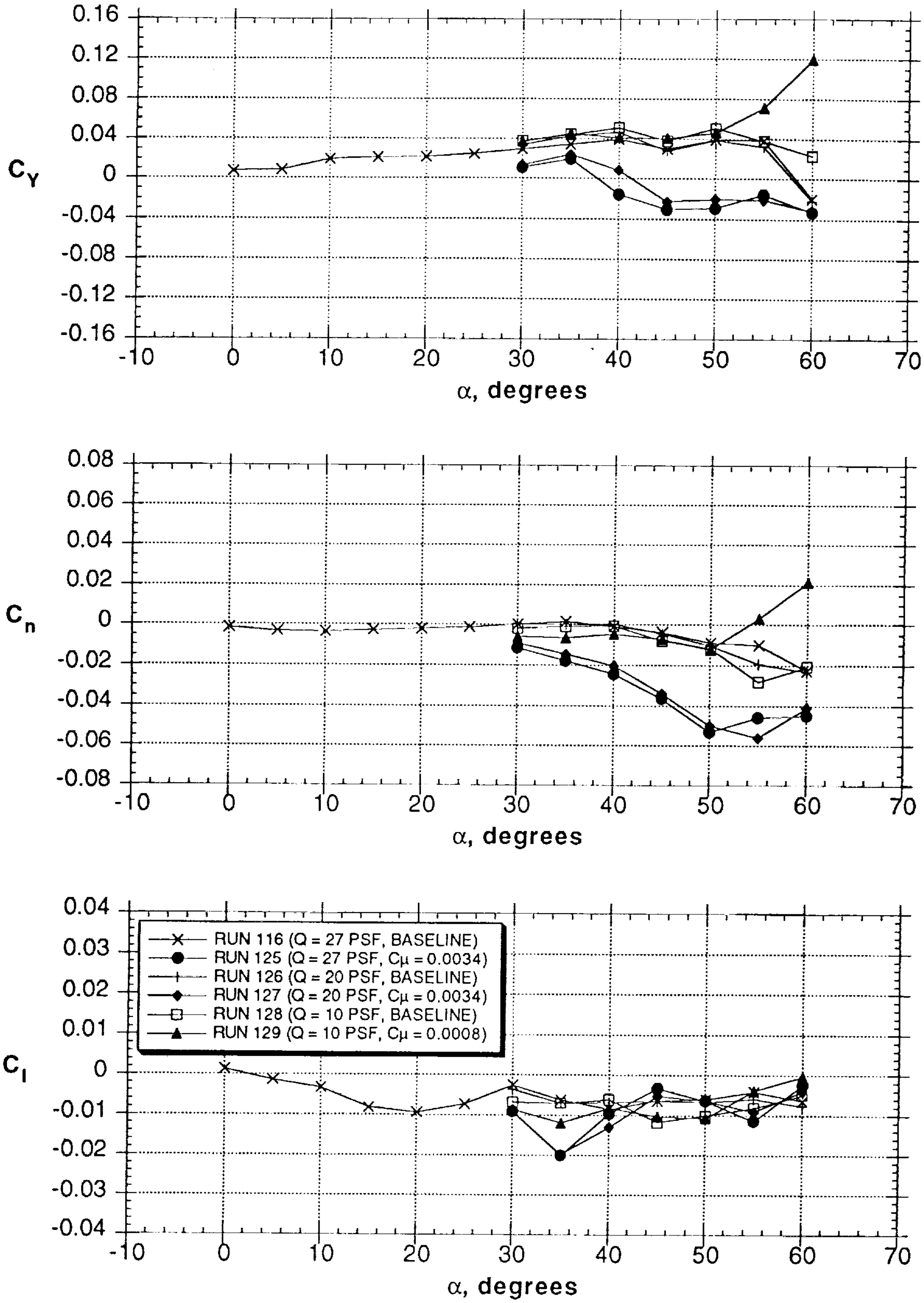

Figure 56 - Concluded

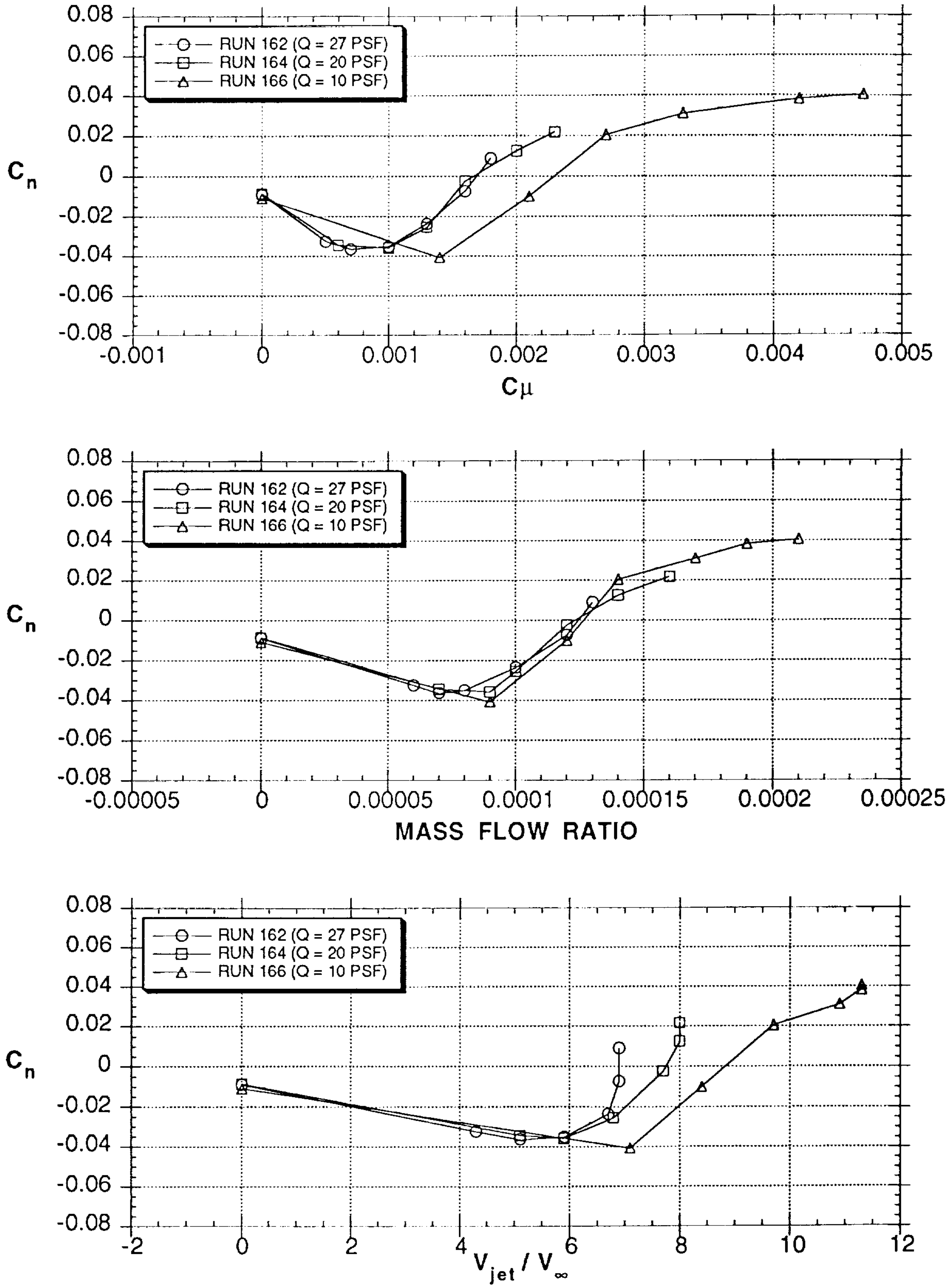

Figure 57 - Effect of correlation parameters (slot blowing, slot AB, right side only, α = 50°)

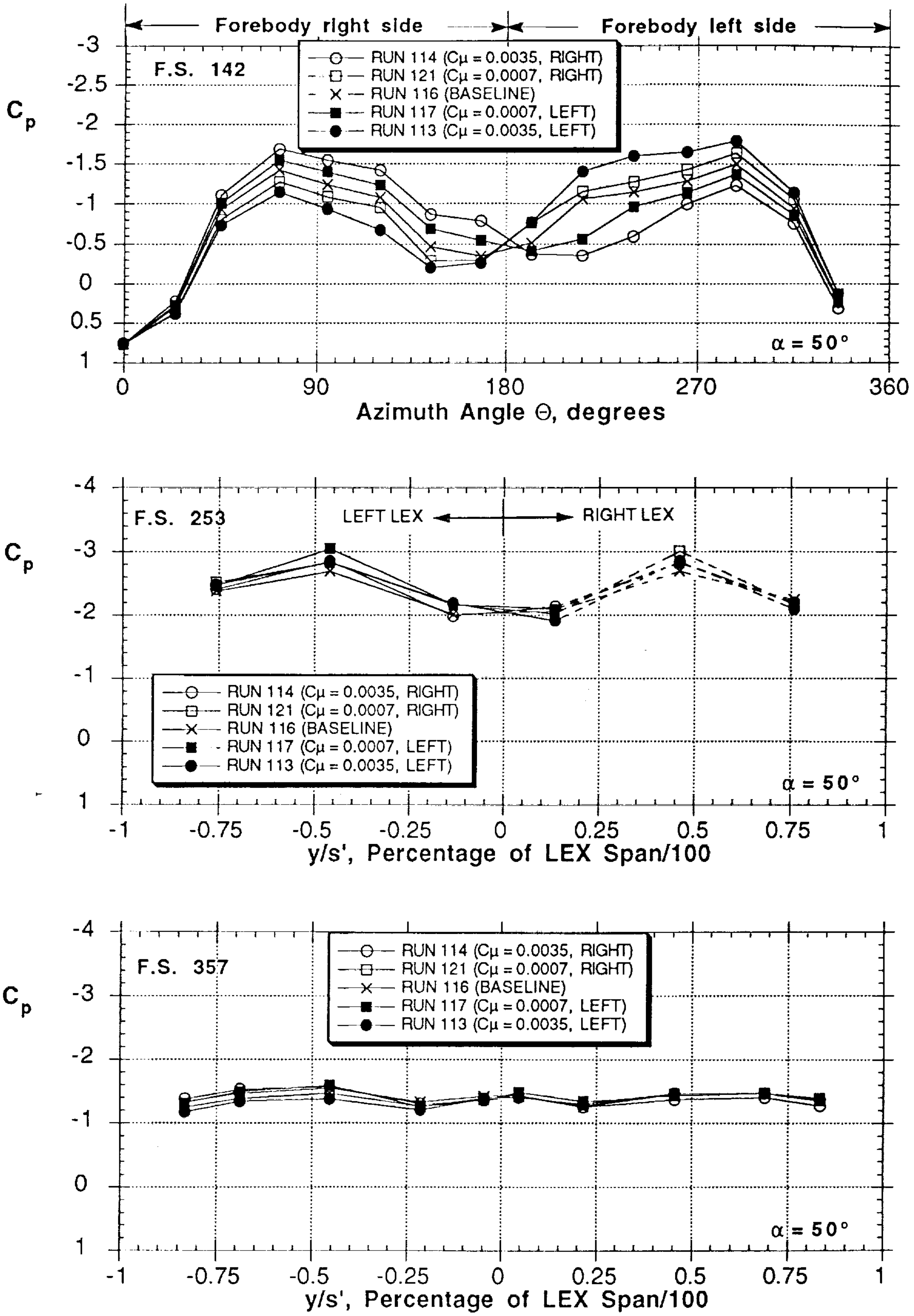

Figure 58 - Effect of slot blowing (slot AB) on pressure distributions at α = 50°

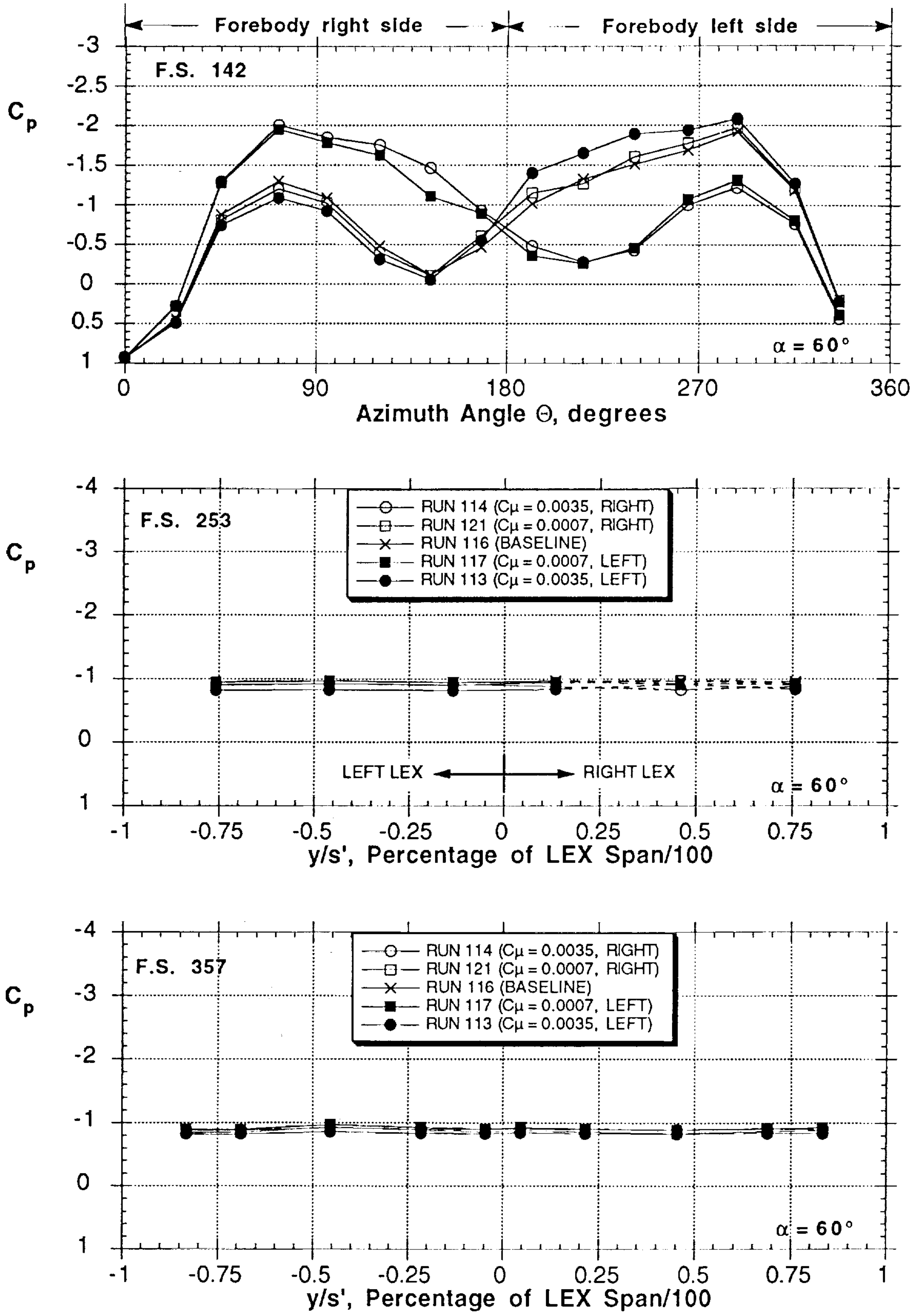

Figure 59 - Effect of slot blowing (slot AB) on pressure distributions at α = 60°

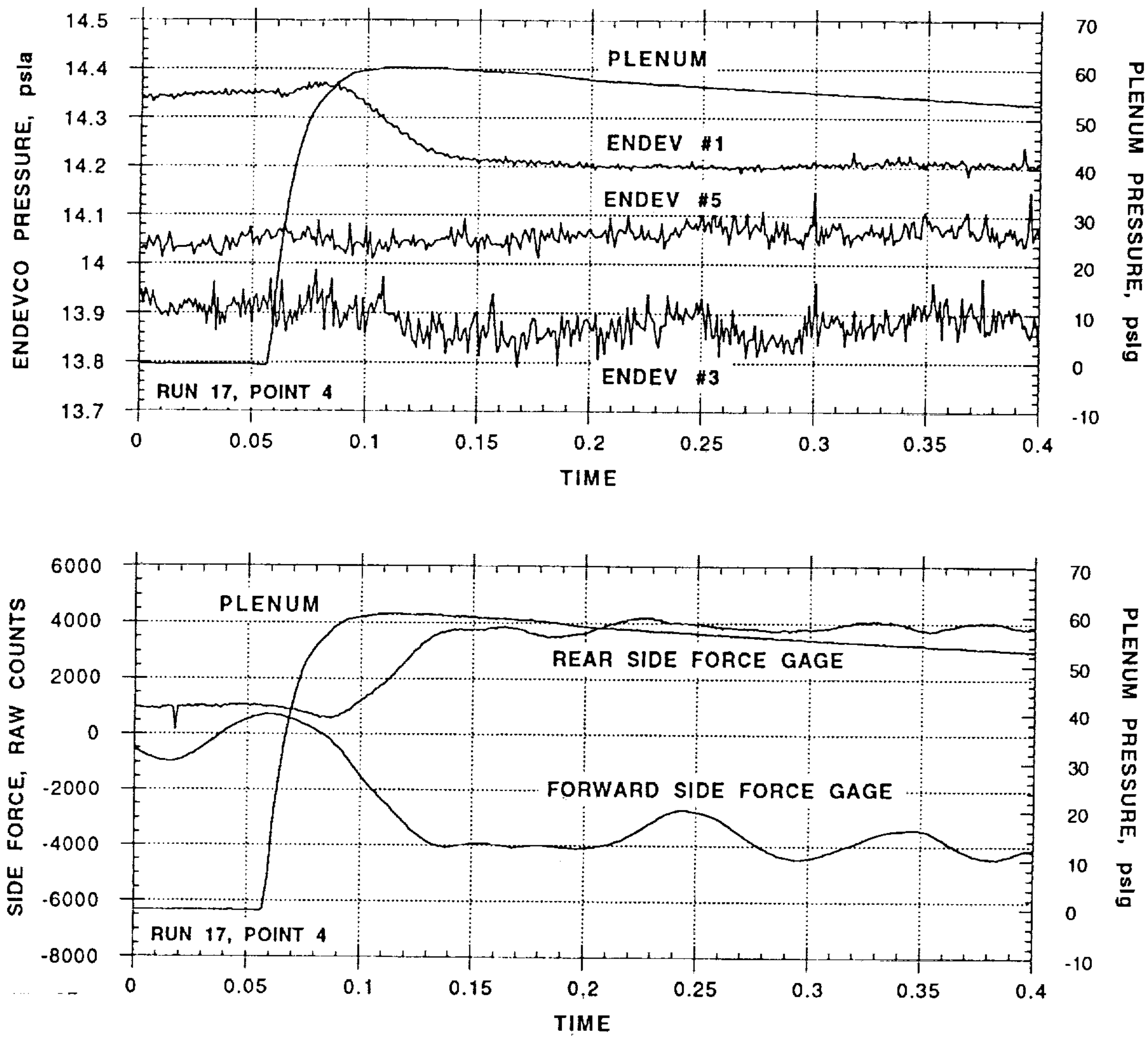

Figure 60 - Time lag effects (slot blowing onset, slot AB, $\alpha = 50°$)

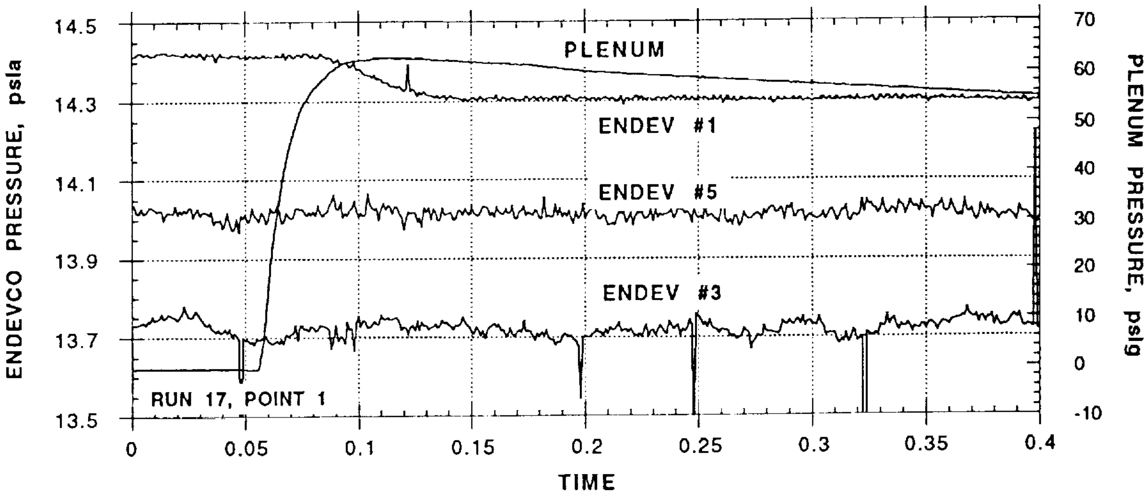

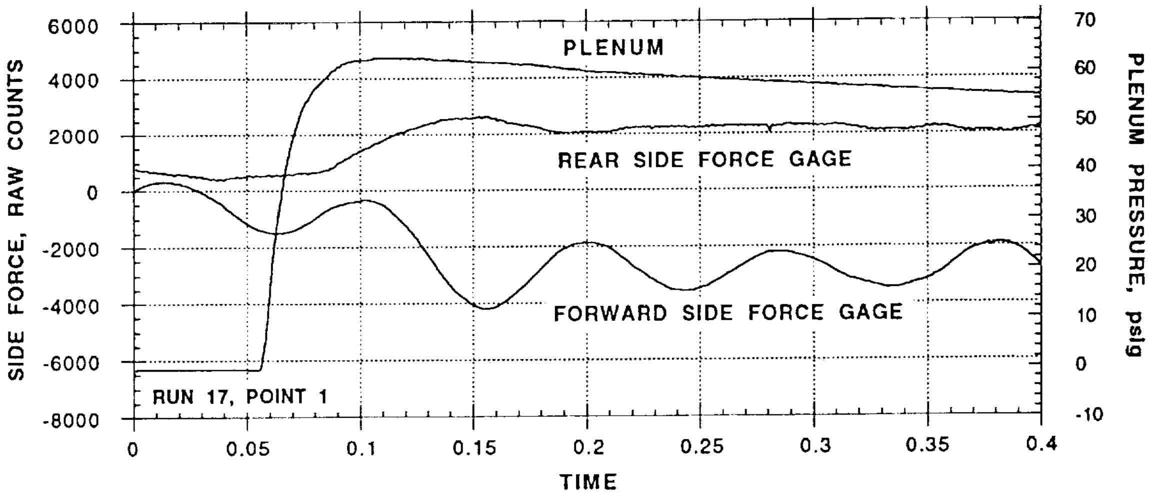

Figure 61 - Time lag effects (slot blowing onset, slot AB, $\alpha = 40°$)

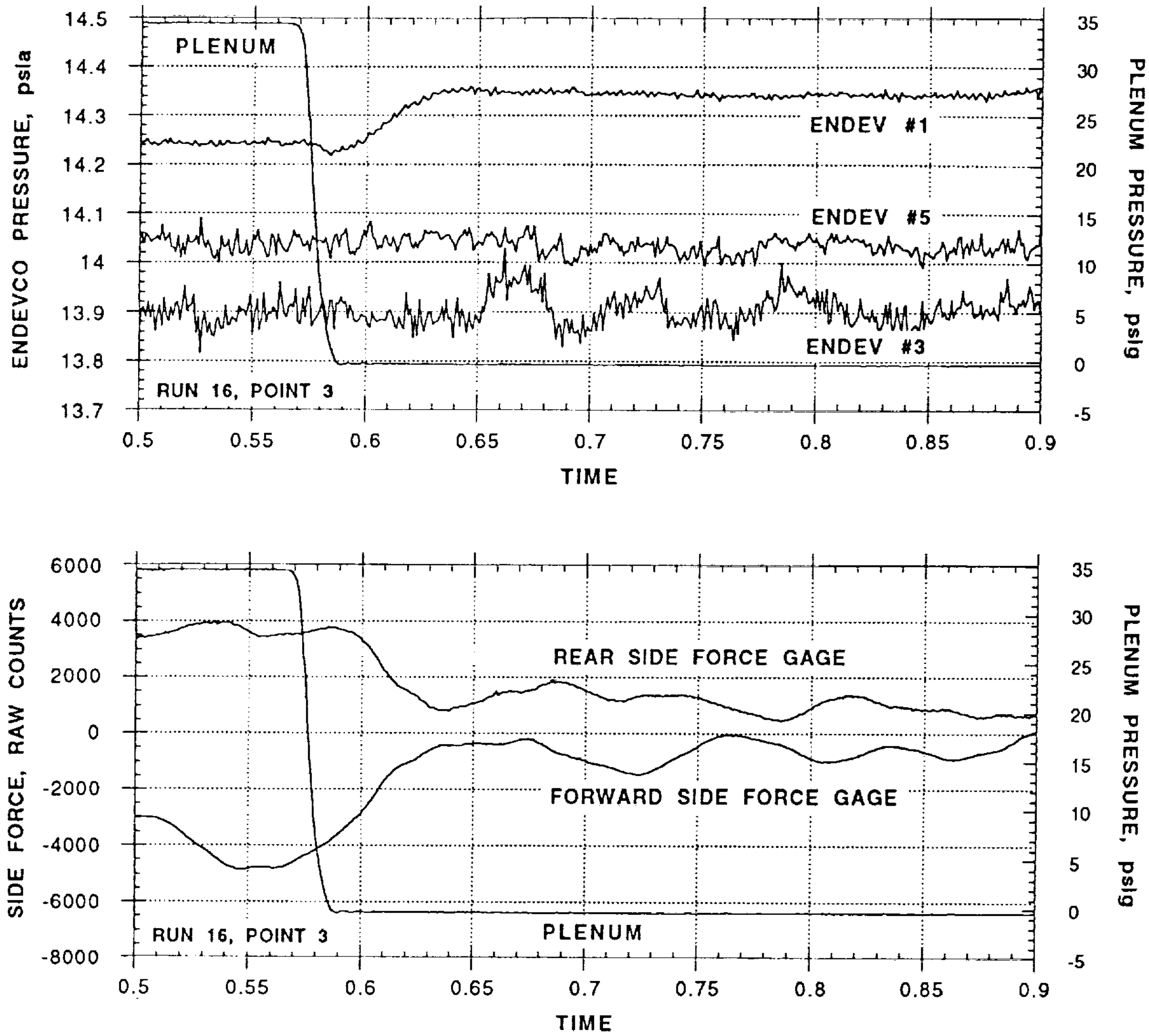

Figure 62 - Time lag effects (slot blowing decay, slot AB, $\alpha = 50°$)

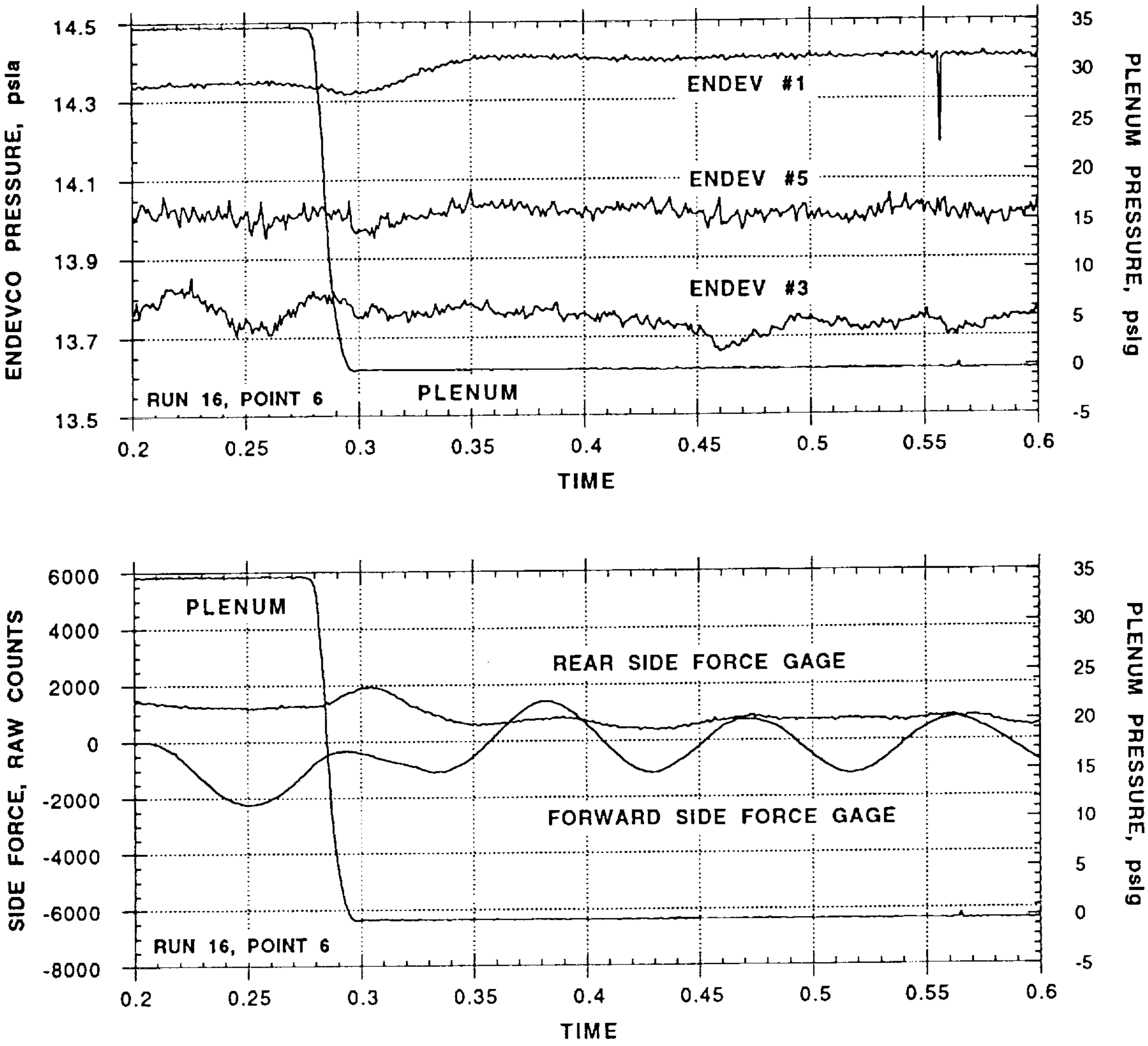

Figure 63 - Time lag effects (slot blowing decay, slot AB, $\alpha = 40°$)

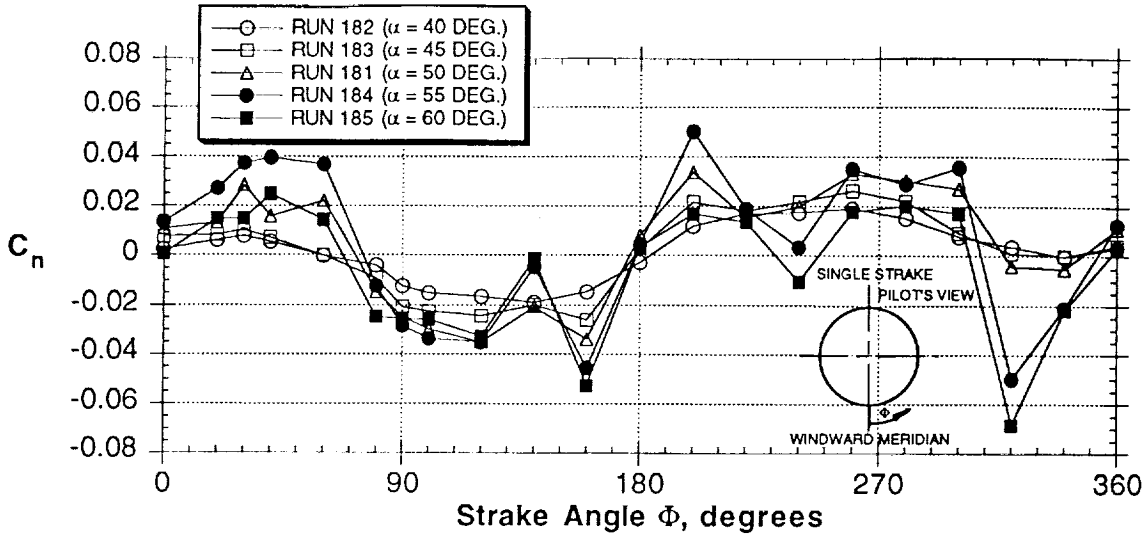

Figure 64 - Effect of rotating a single strake on yawing moment

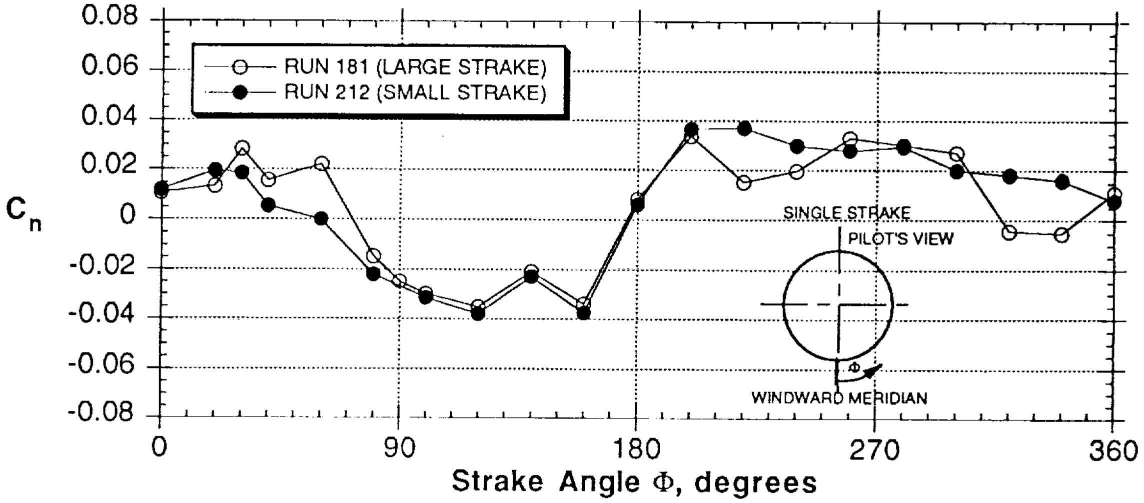

Figure 65 - Effect of strake size (single strake, α = 50°)

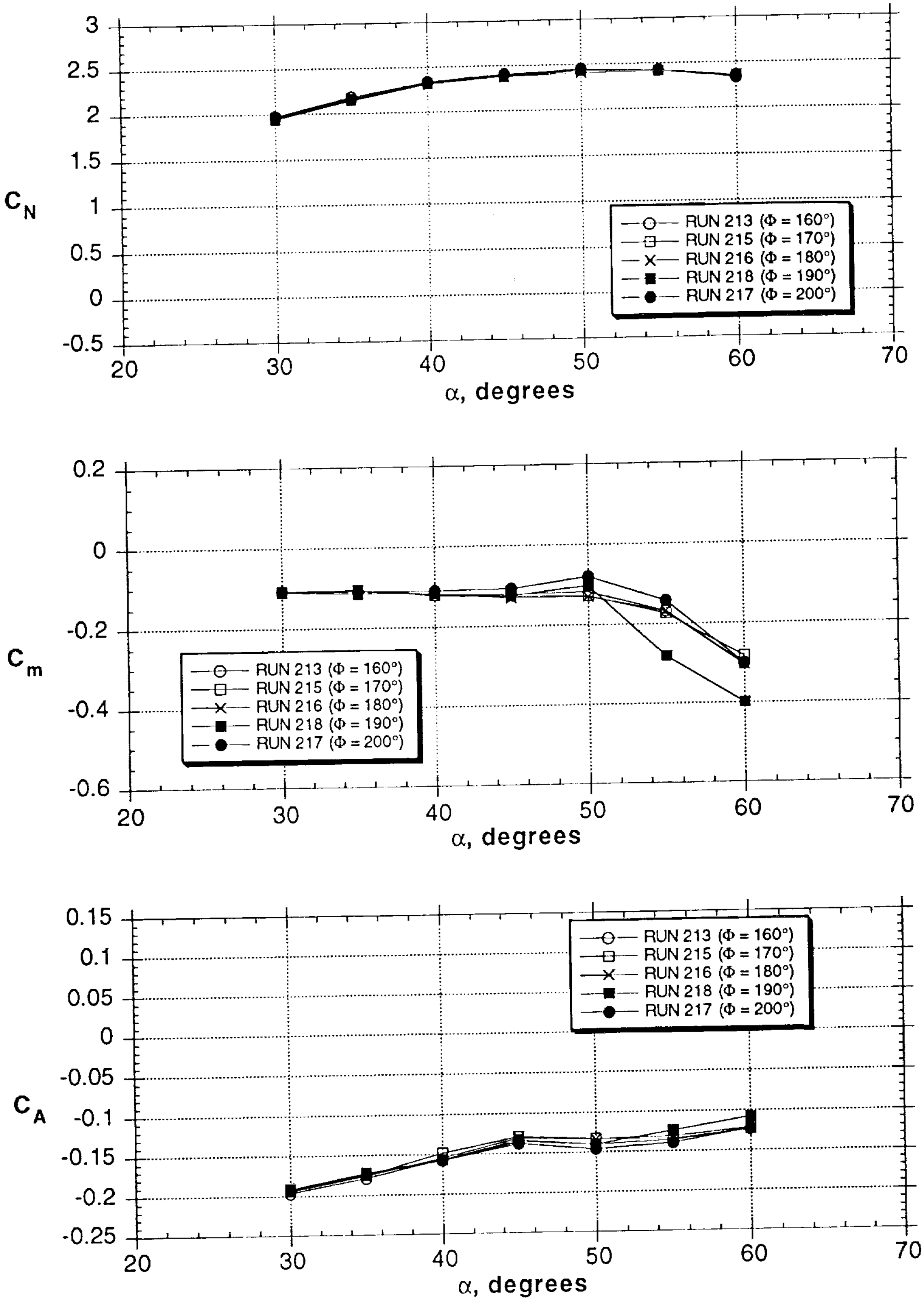

Figure 66 - Effect of a single strake on forces and moments

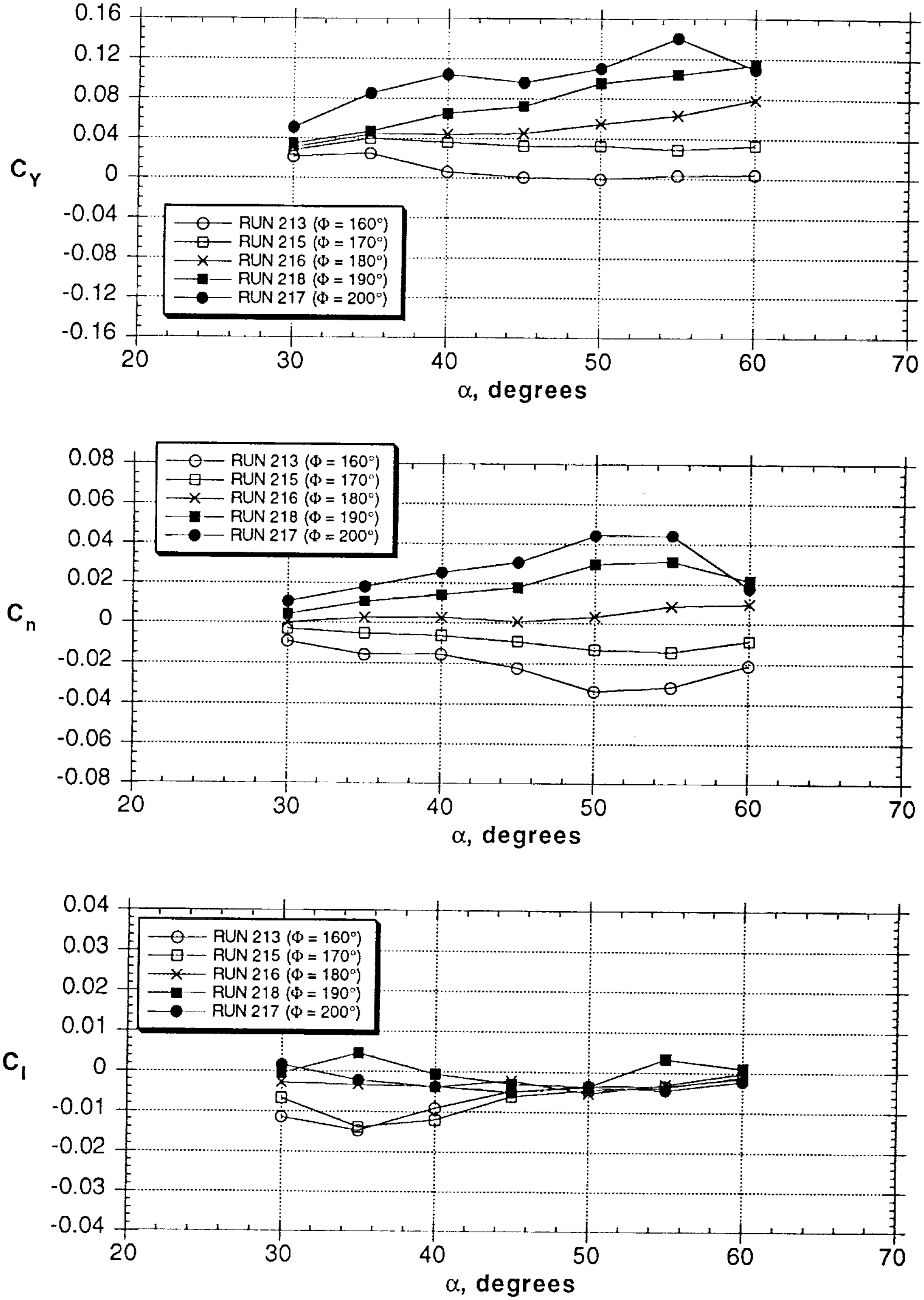

Figure 66 - Concluded

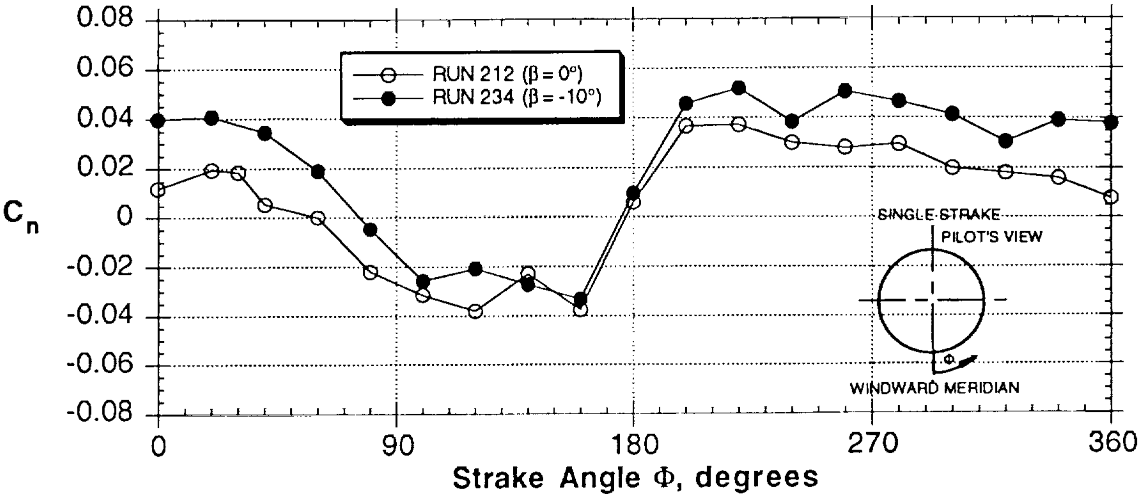

Figure 67 - Effect of sideslip on single strake effectiveness (α = 50°)

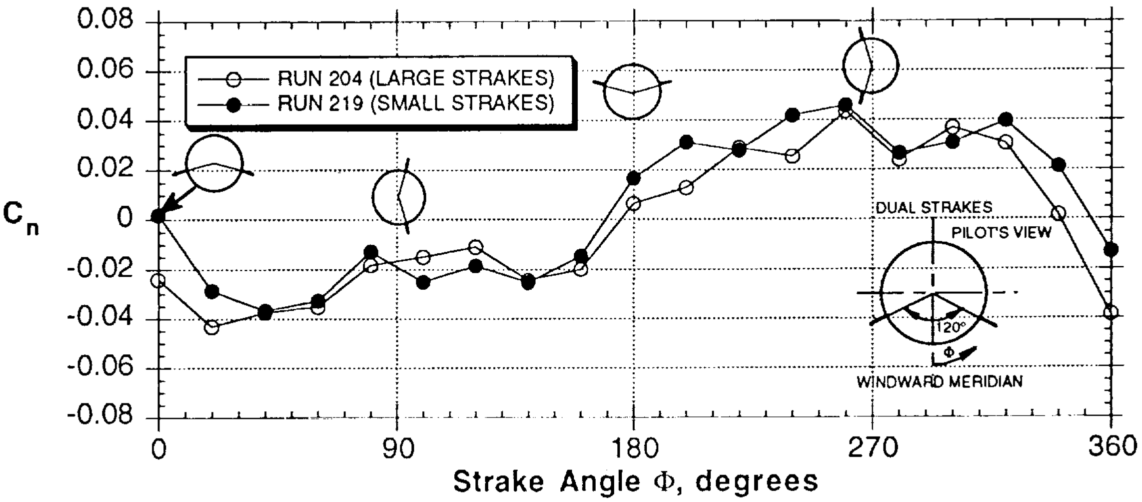

Figure 68 - Effect of strake size (dual strakes, ΔΦ = 120°, α = 50°)

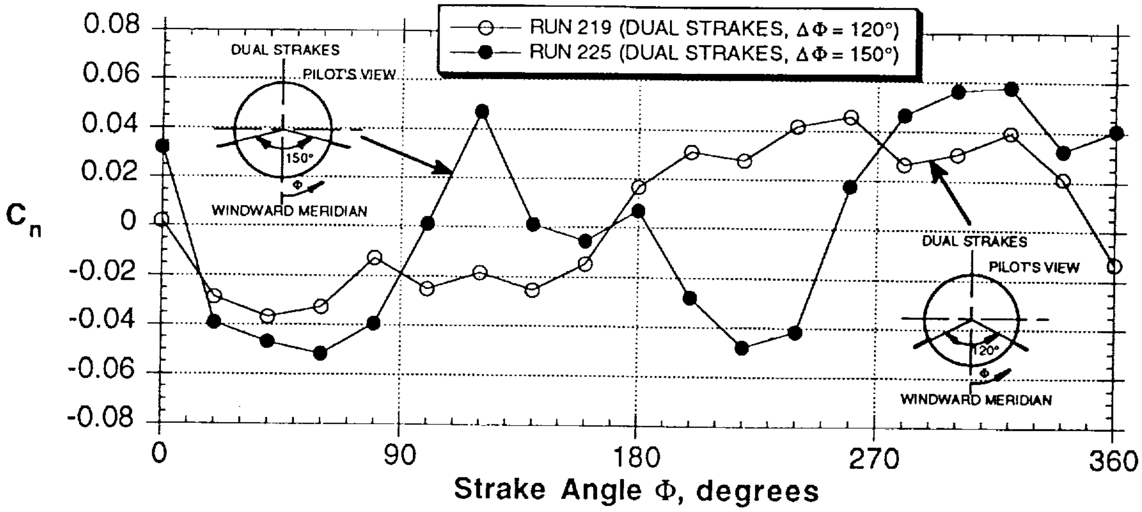

Figure 69 - Effect of strake separation angle ΔΦ (dual strakes, α = 50°)

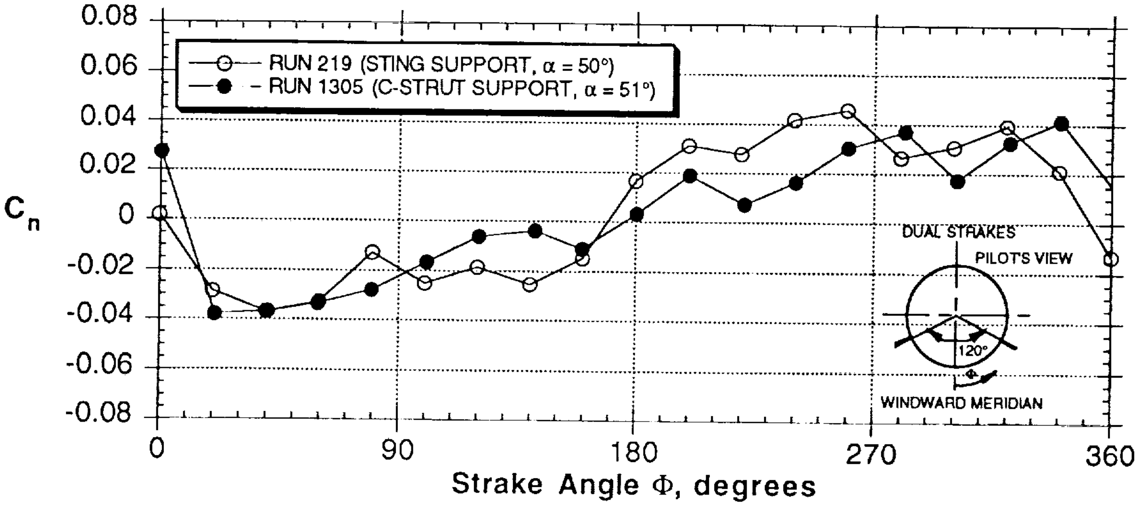

Figure 70 - Comparison of data obtained with the model mounted on the standard sting and on the C-strut of the rotary rig (dual strakes, ΔΦ = 120°, α = 50°)

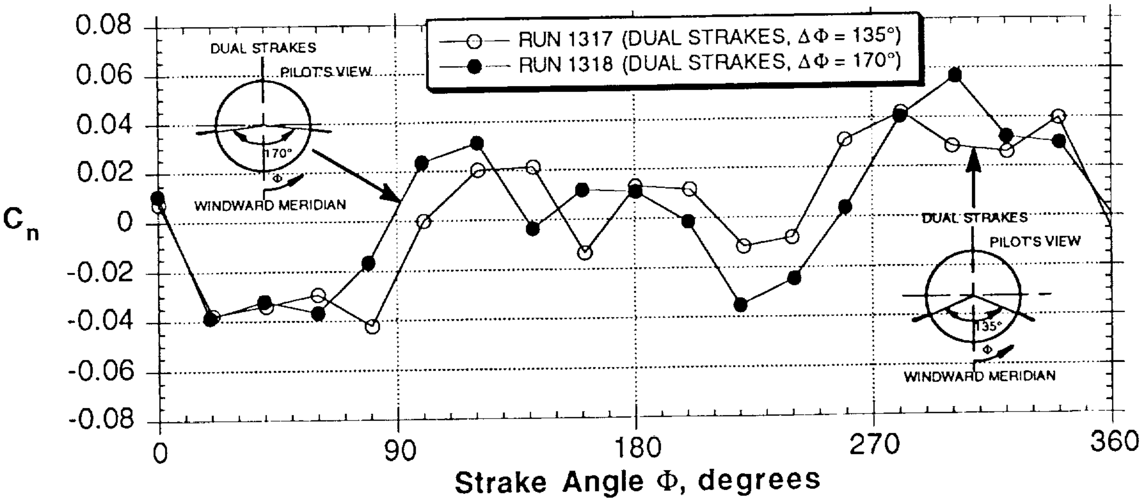

Figure 71 - Effect of strake separation angle ΔΦ (dual strakes, α = 50°)

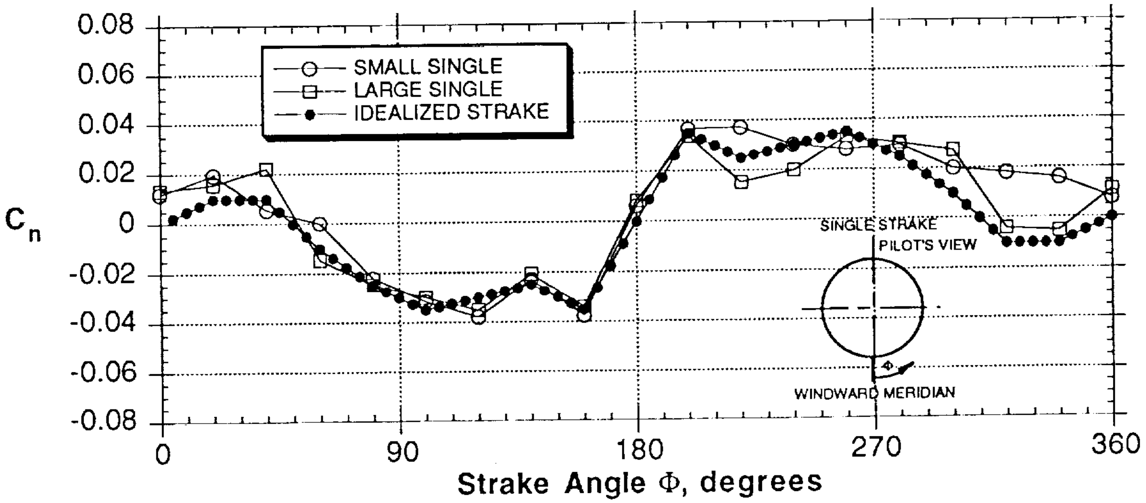

Figure 72 - Comparison of "idealized" single strake data, and actual data for large and small single strake (α = 50°)

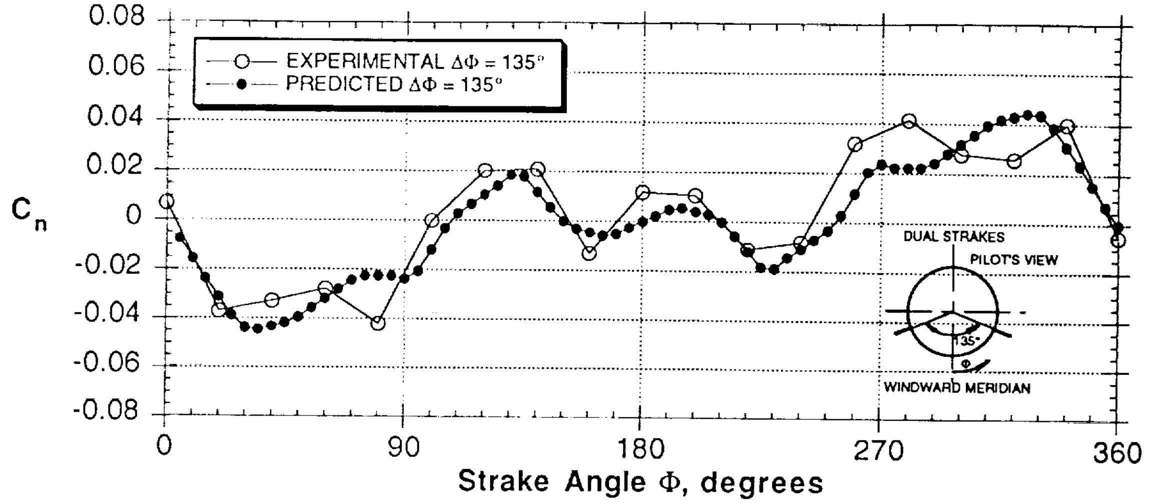

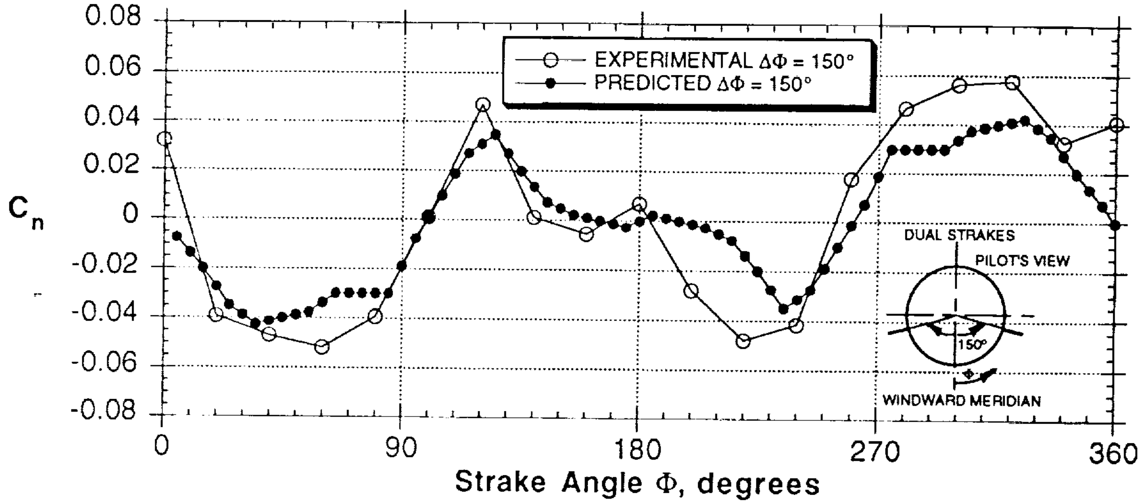

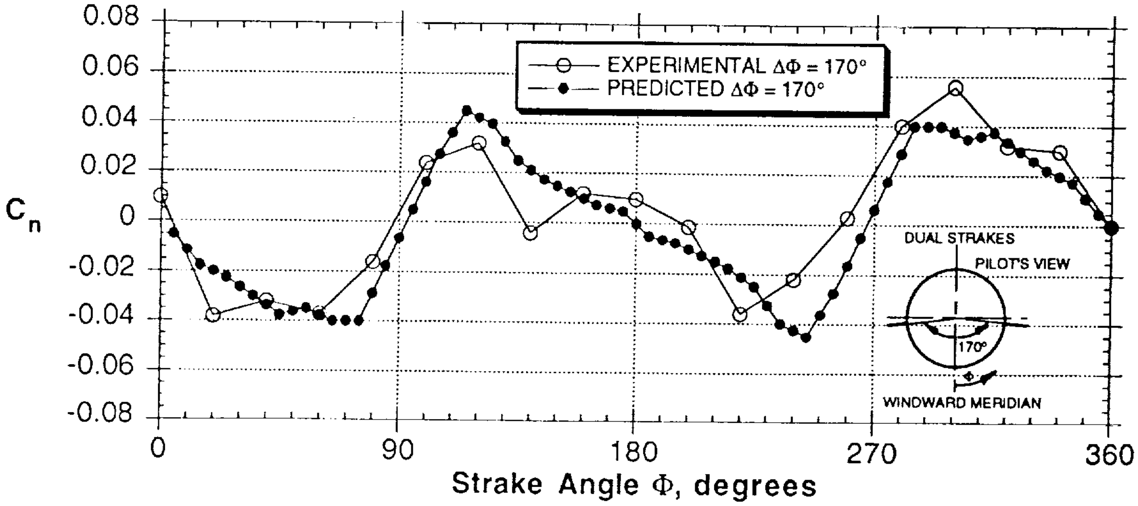

Figure 73 - Comparison of predicted and experimental data for different strake separation angles ΔΦ(dual strakes, $\alpha = 50°$)

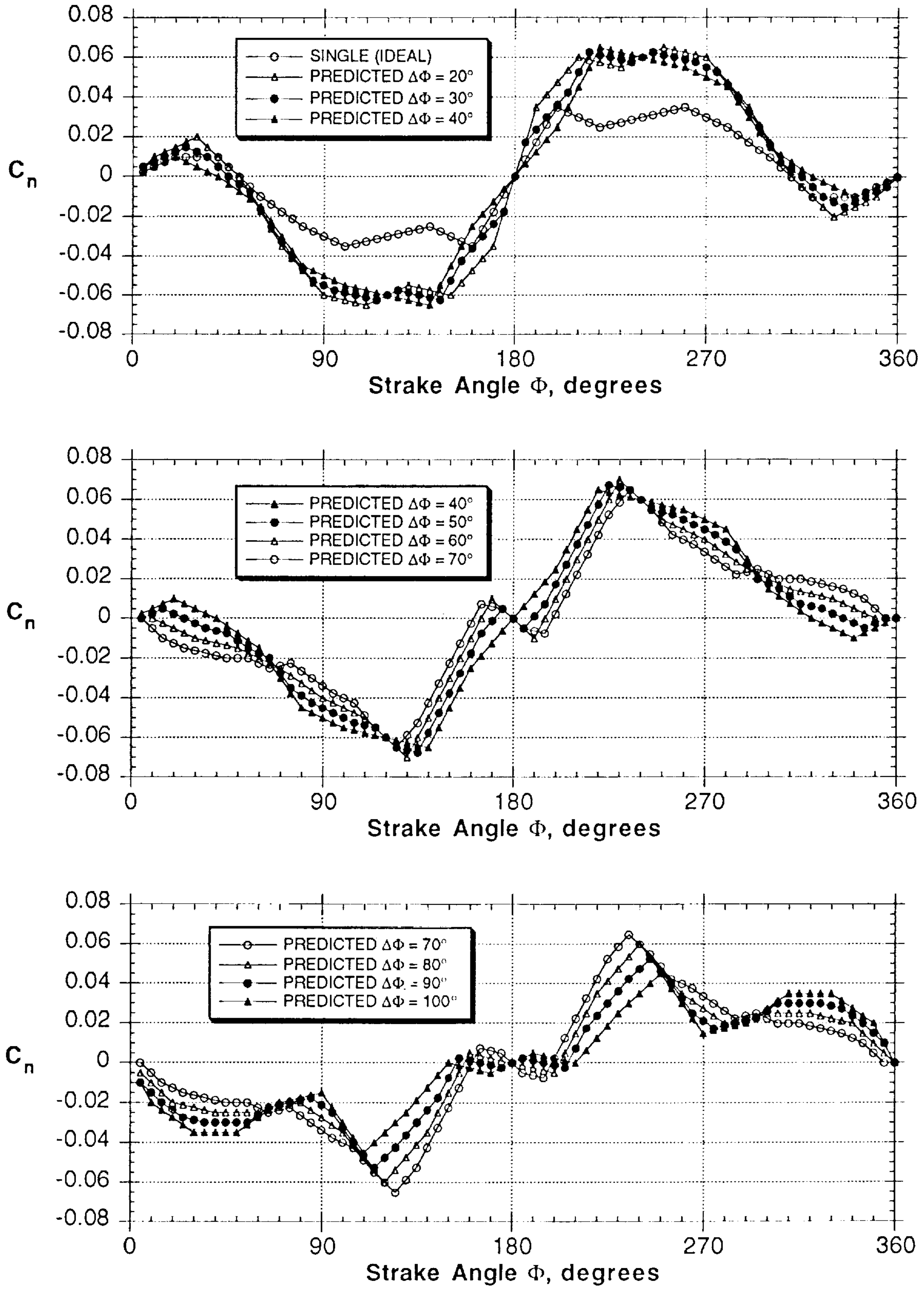

Figure 74 - Predicted performance of dual strakes with different separation angles $\Delta\Phi$ ($\alpha = 50°$)

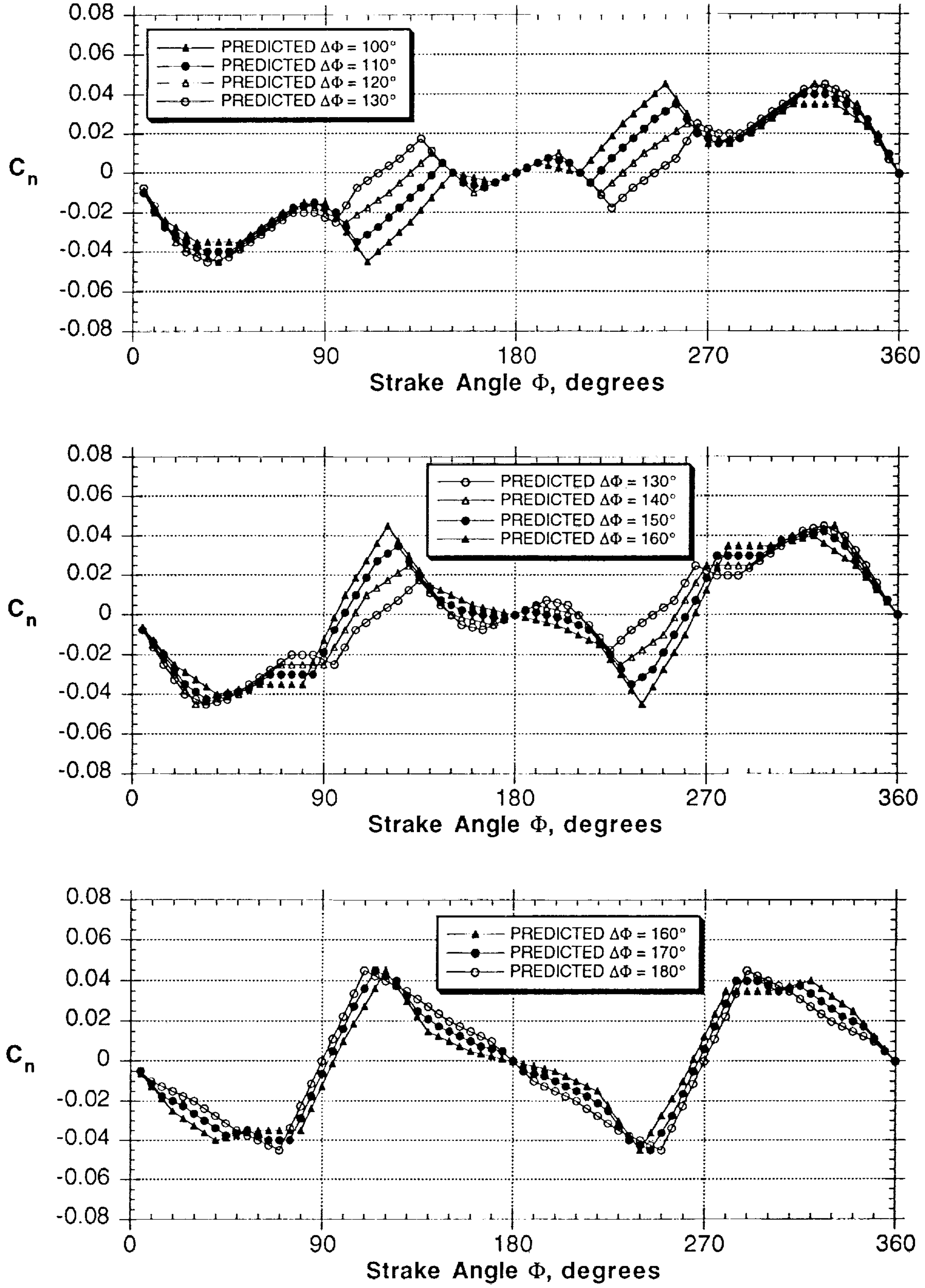

Figure 74 - Concluded

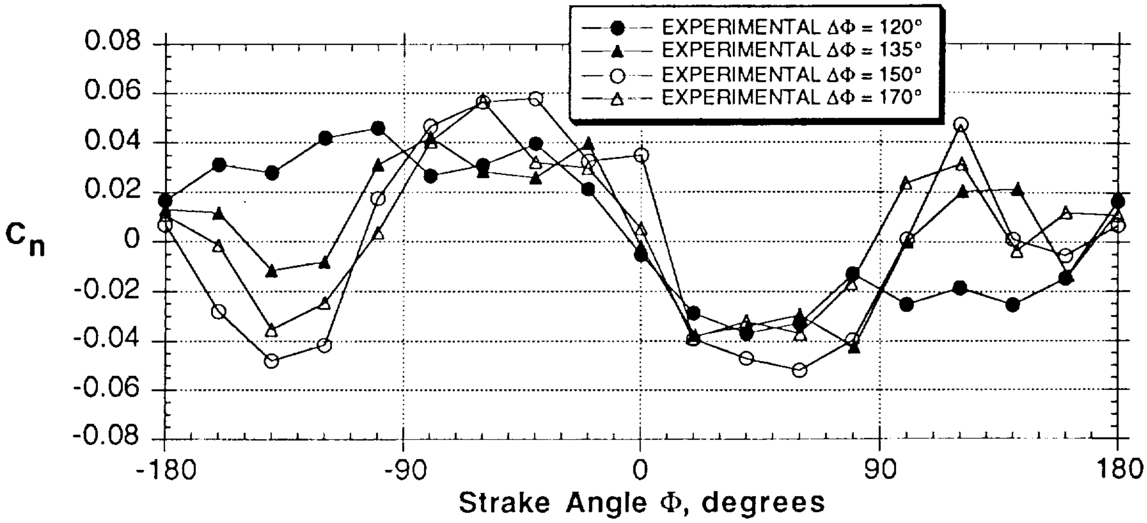

Figure 75 - Effect of strake separation angle ΔΦ (experimental data, dual strakes, α = 50°)

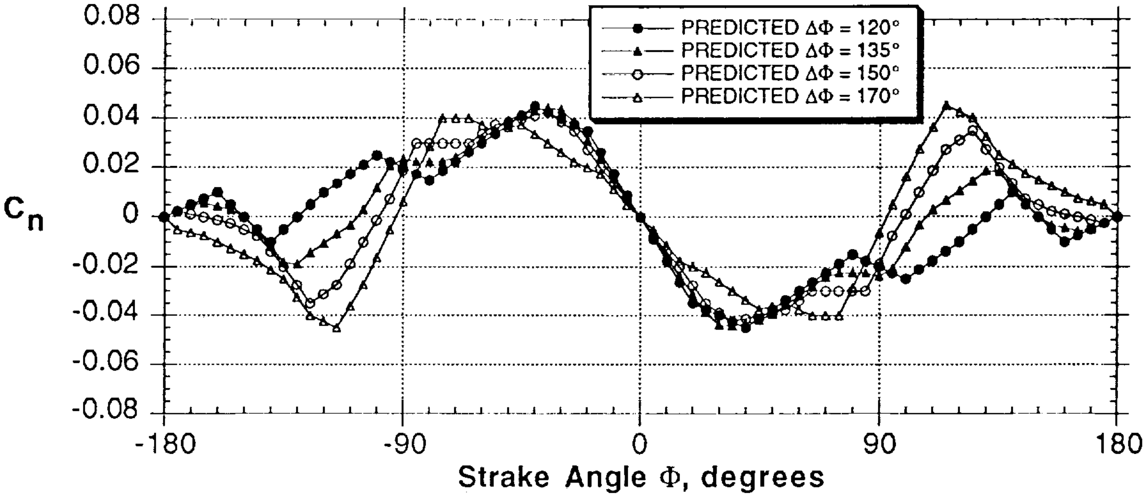

Figure 76 - Effect of strake separation angle ΔΦ (predicted data, dual strakes, α = 50°)

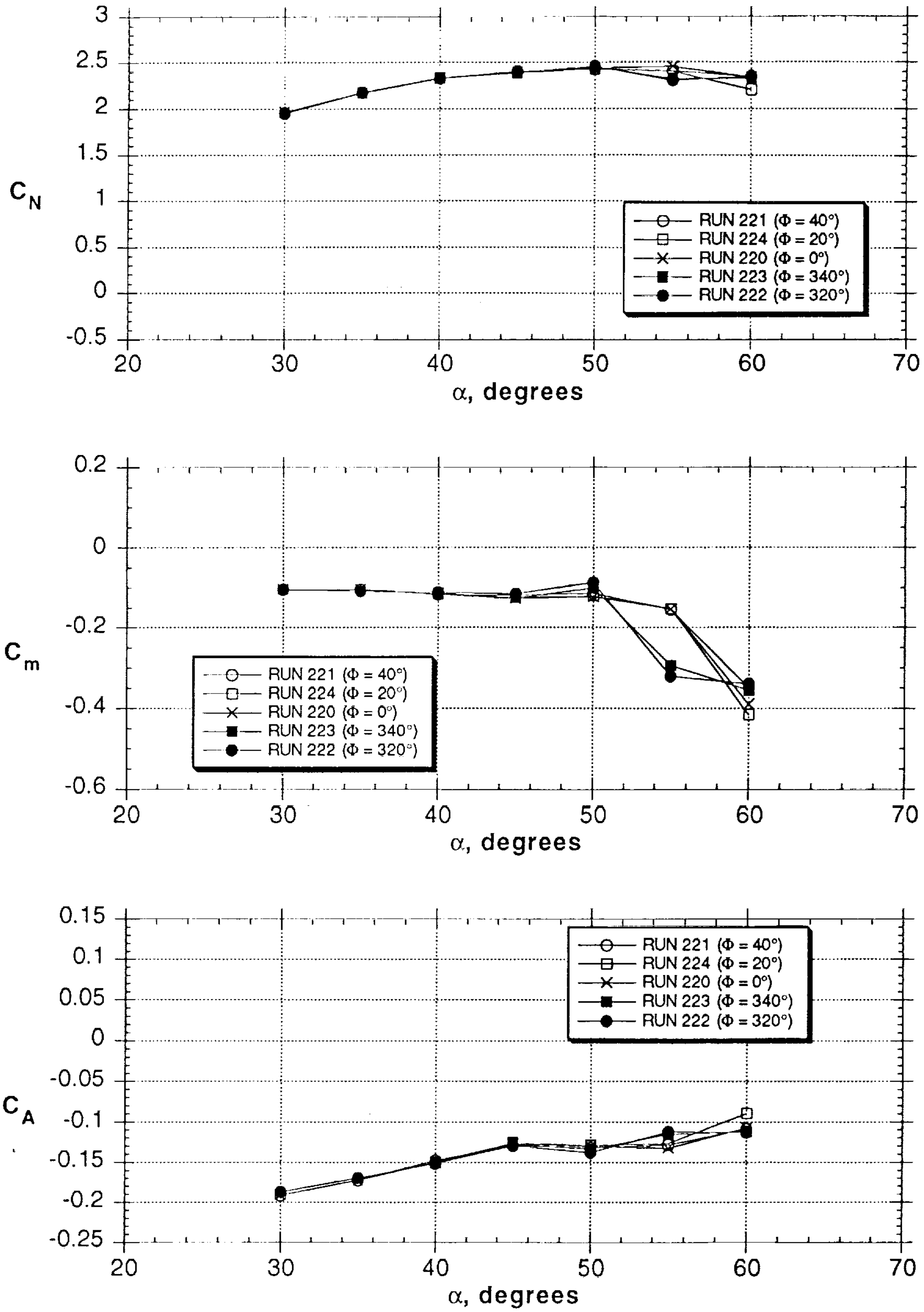

Figure 77 - Effect of dual strakes (ΔΦ = 120°) on forces and moments

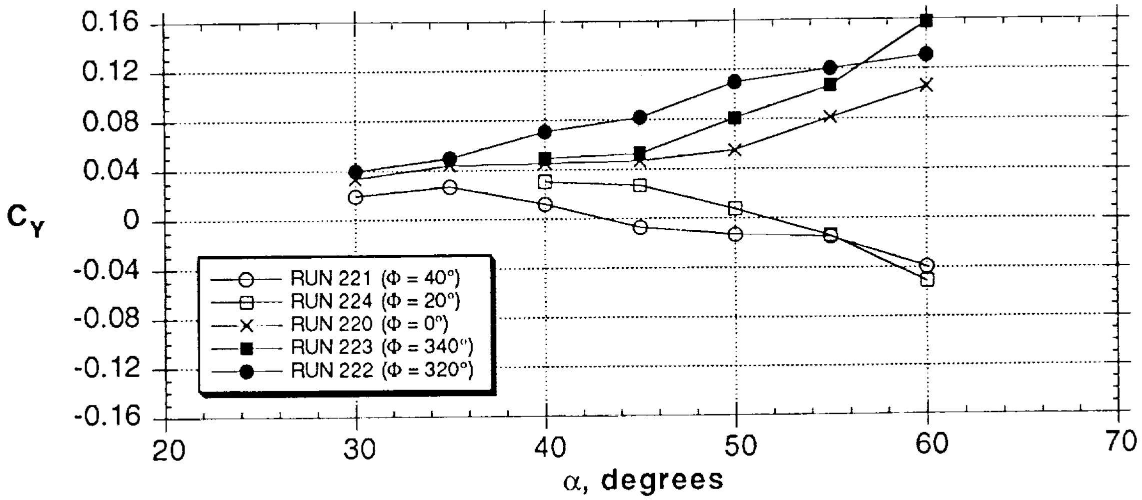

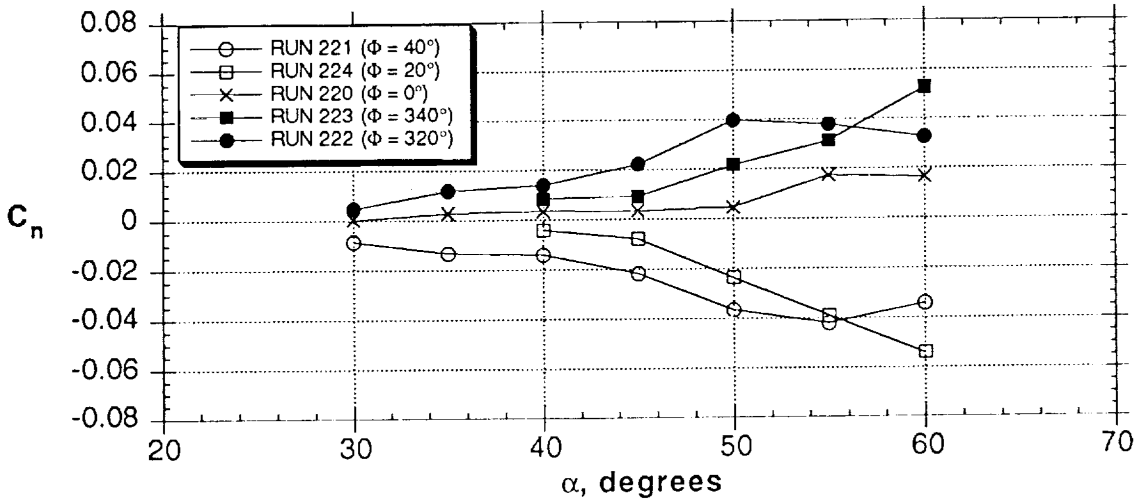

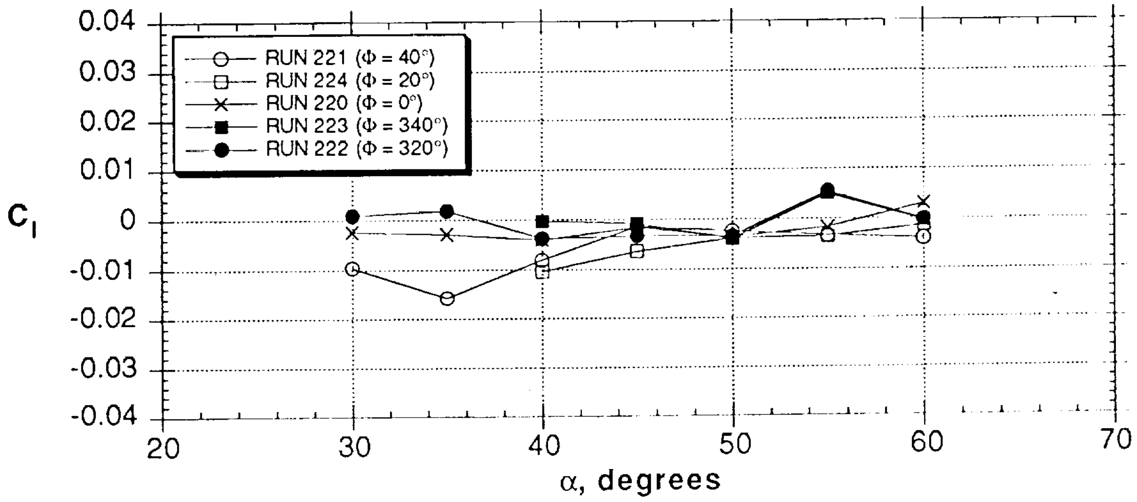

Figure 77 - Concluded

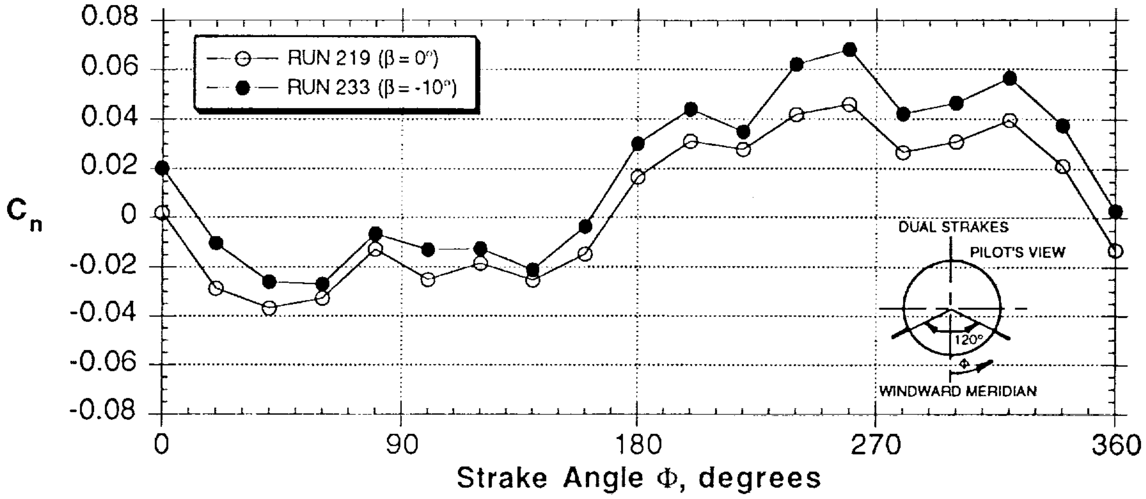

Figure 78 - Effect of sideslip on dual strakes effectiveness (ΔΦ = 120°, α = 50°)

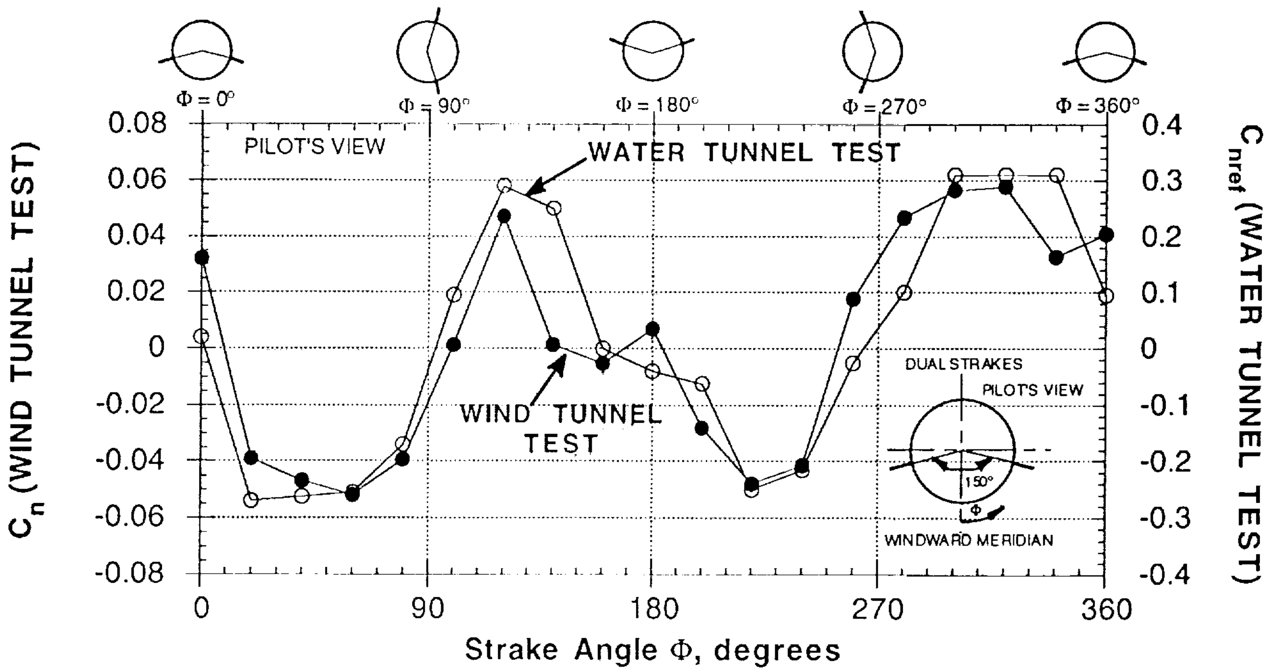

Figure 79 - Comparison of wind tunnel and water tunnel data from Ref. 29 (dual strakes, ΔΦ = 150°, α = 50°)

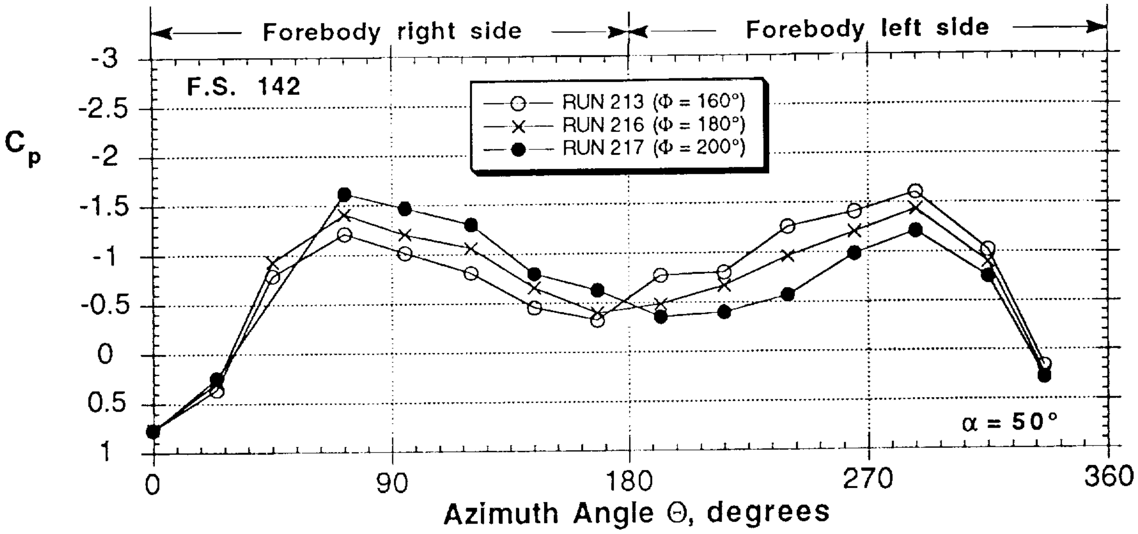

(a) α = 50°

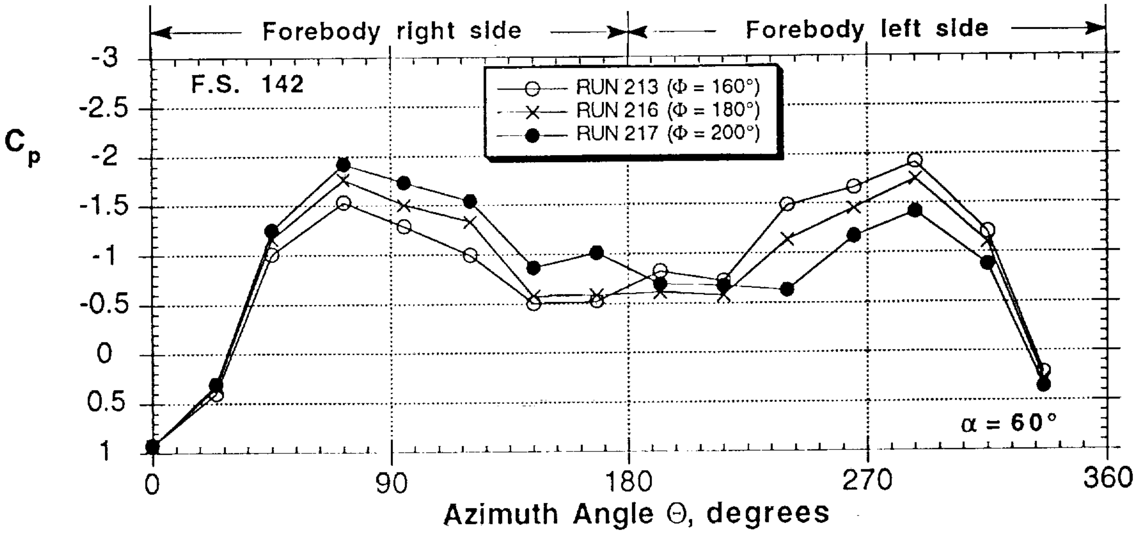

(b) α = 60°

Figure 80 - Effect of a single strake on pressure distributions

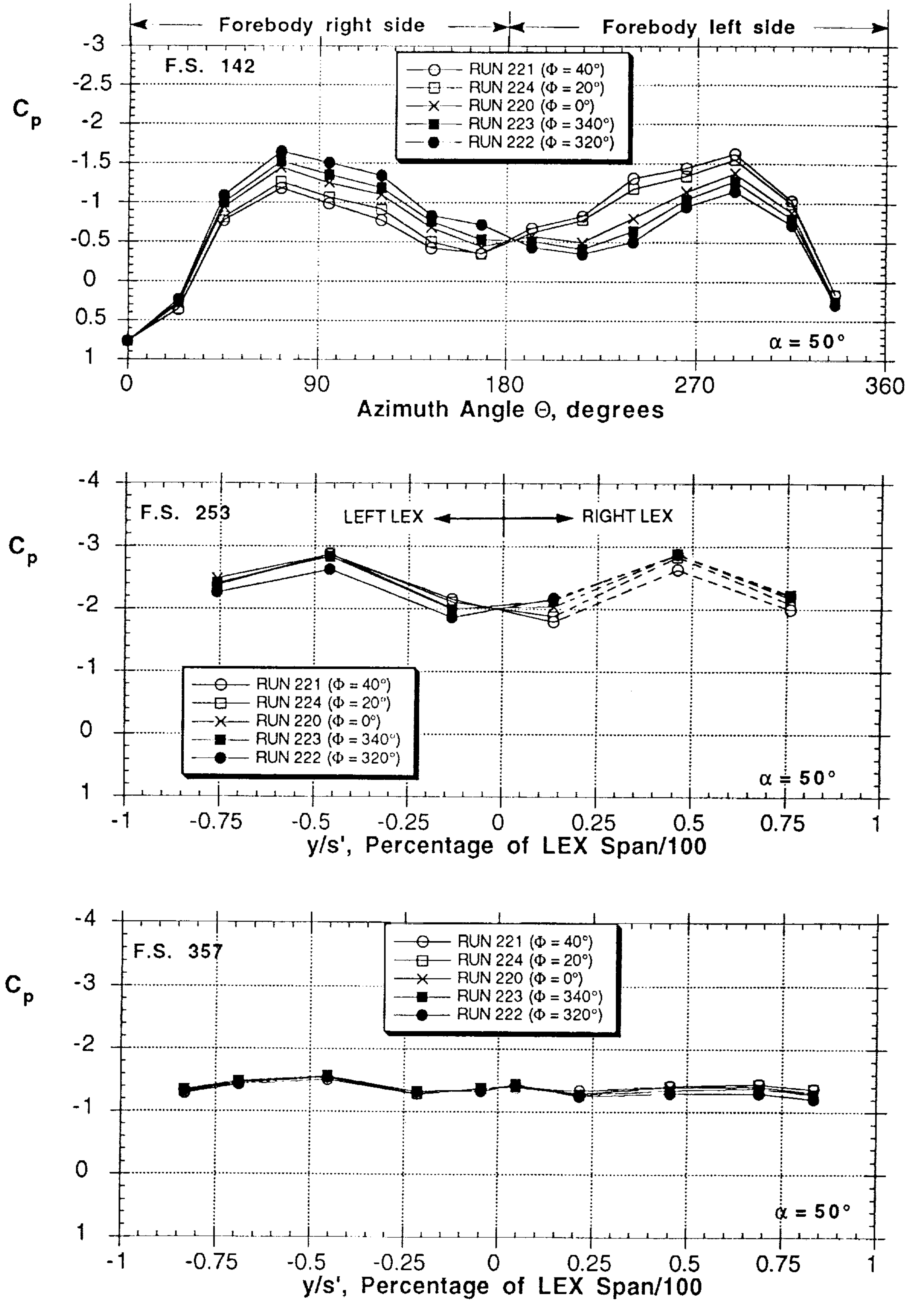

(a) α = 50°

Figure 81 - Effect of dual strakes on pressure distributions (ΔΦ = 120°)

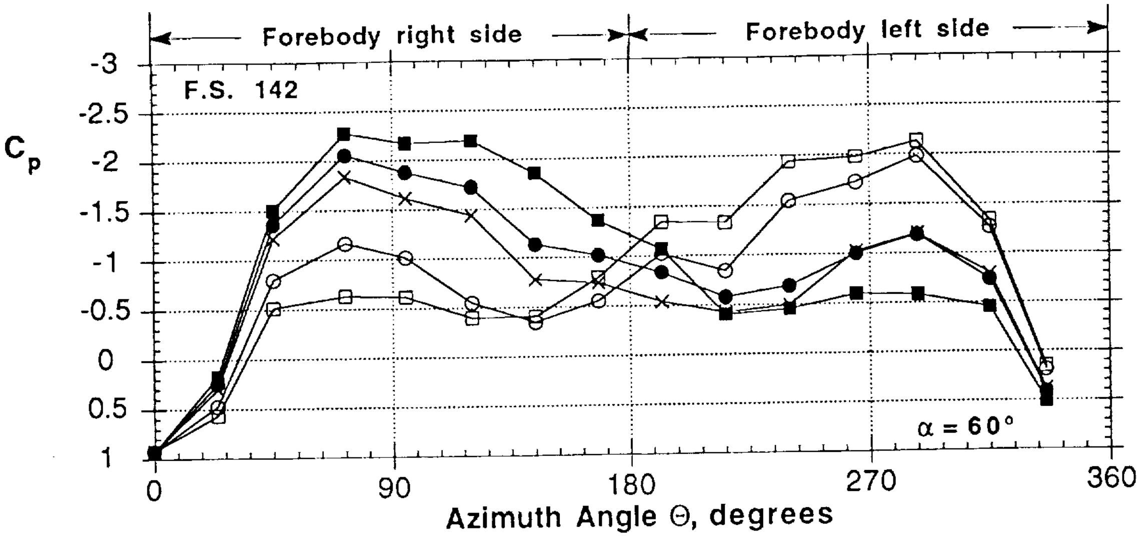

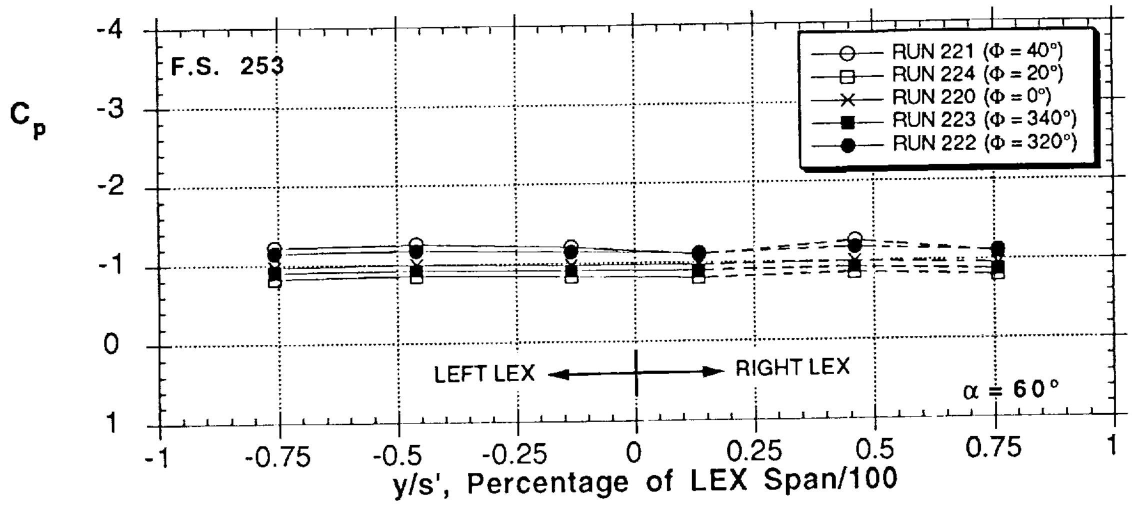

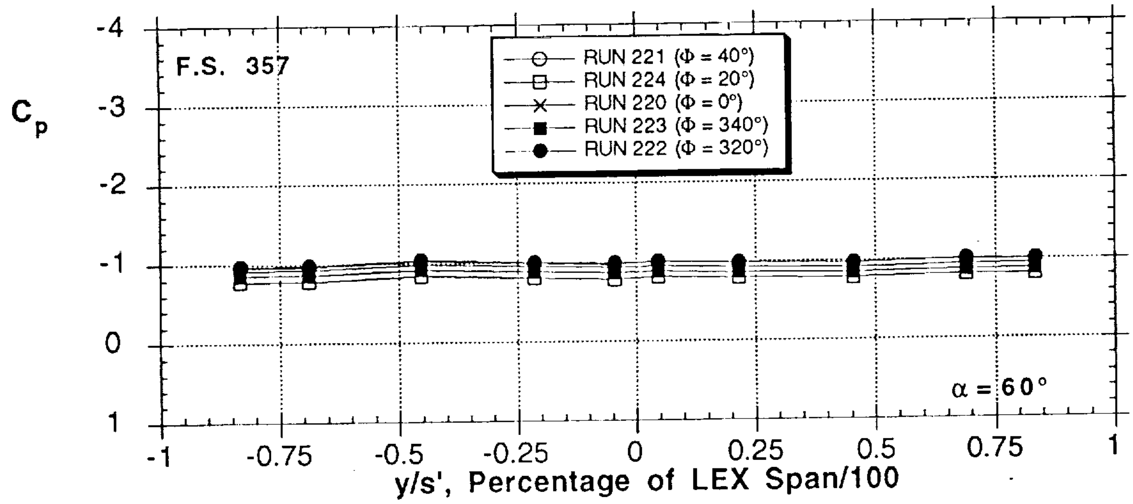

(b) α = 60°

Figure 81 - Concluded

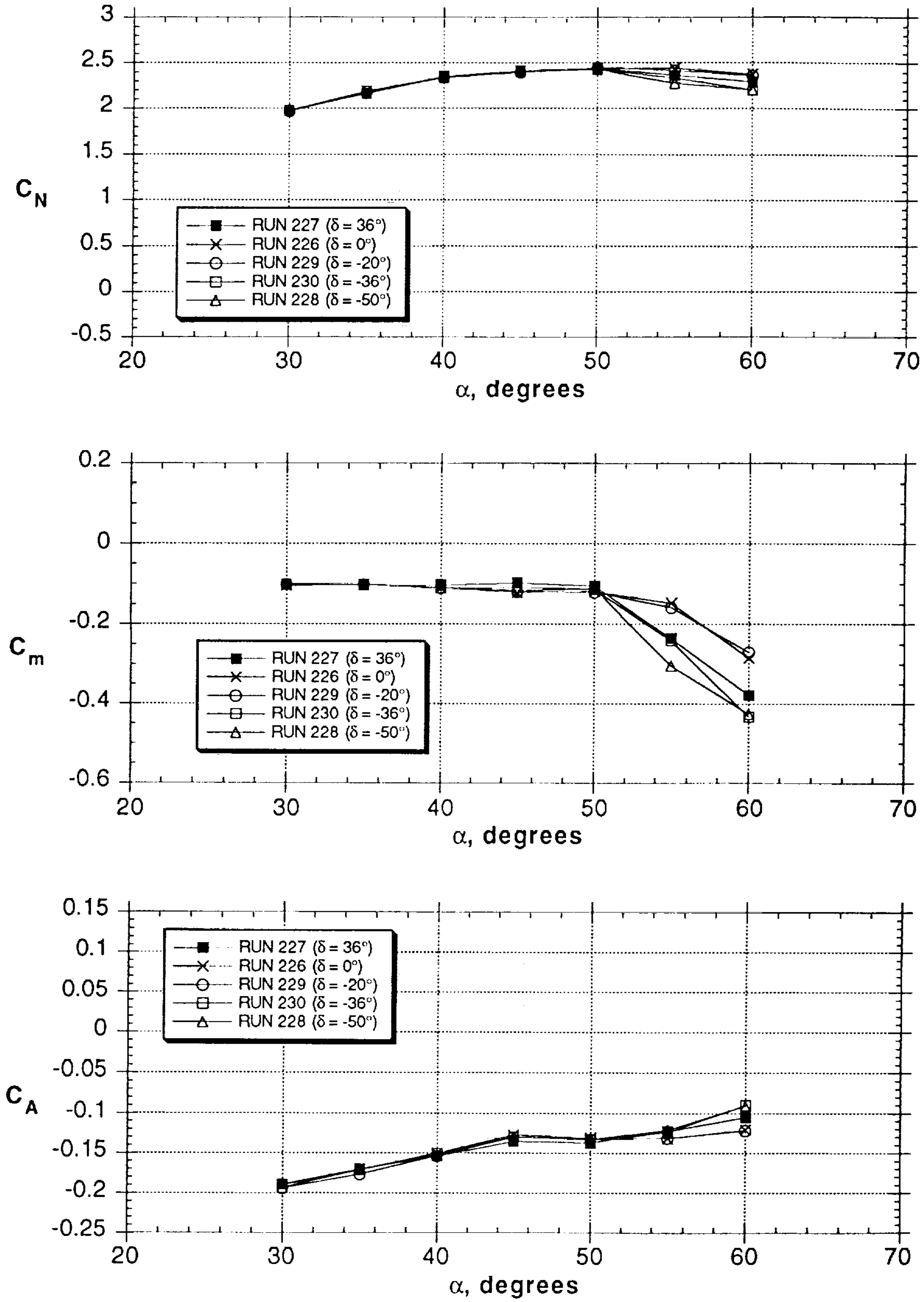

Figure 82 - Effect of vertical nose strake on forces and moments

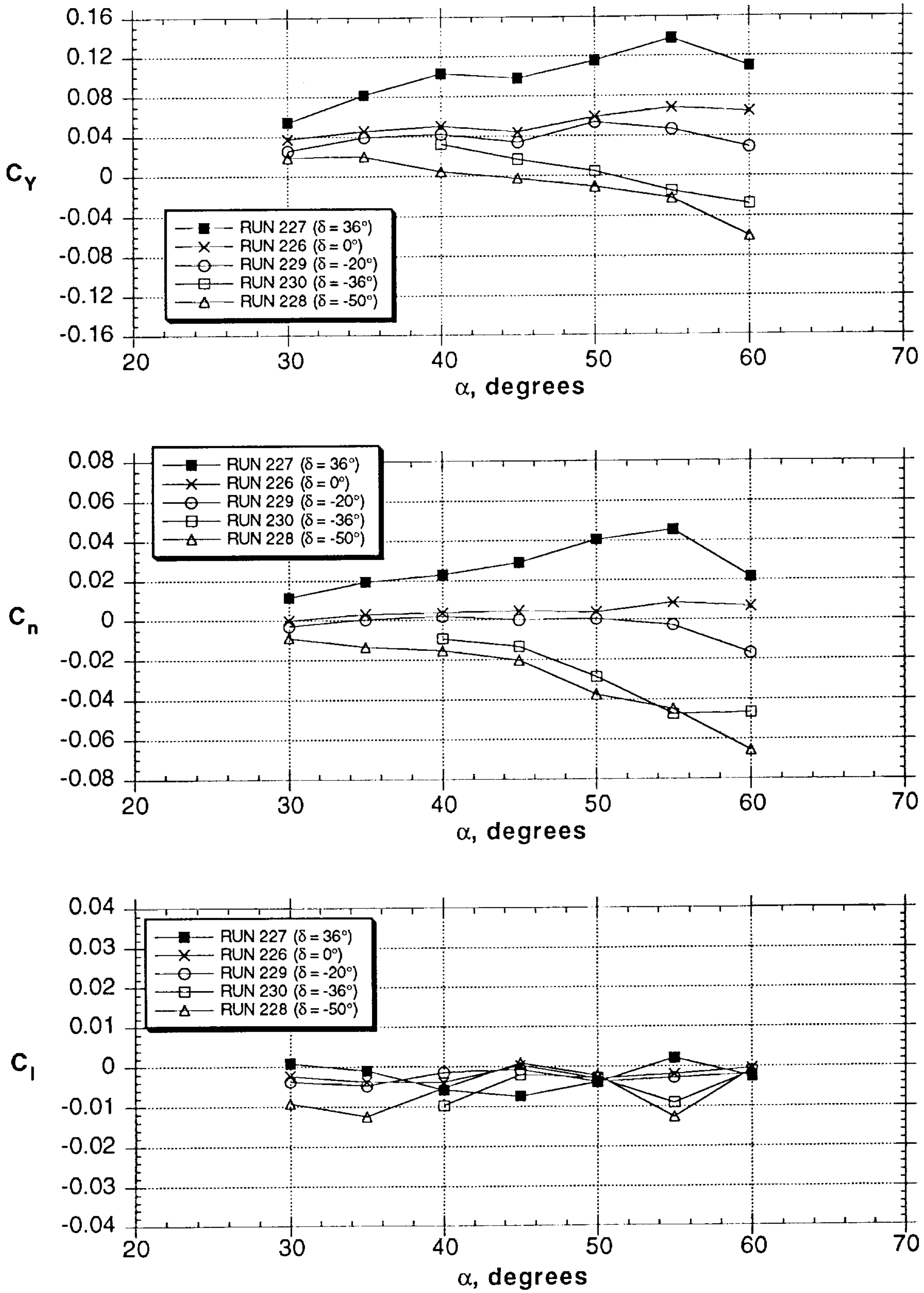

Figure 82 - Concluded

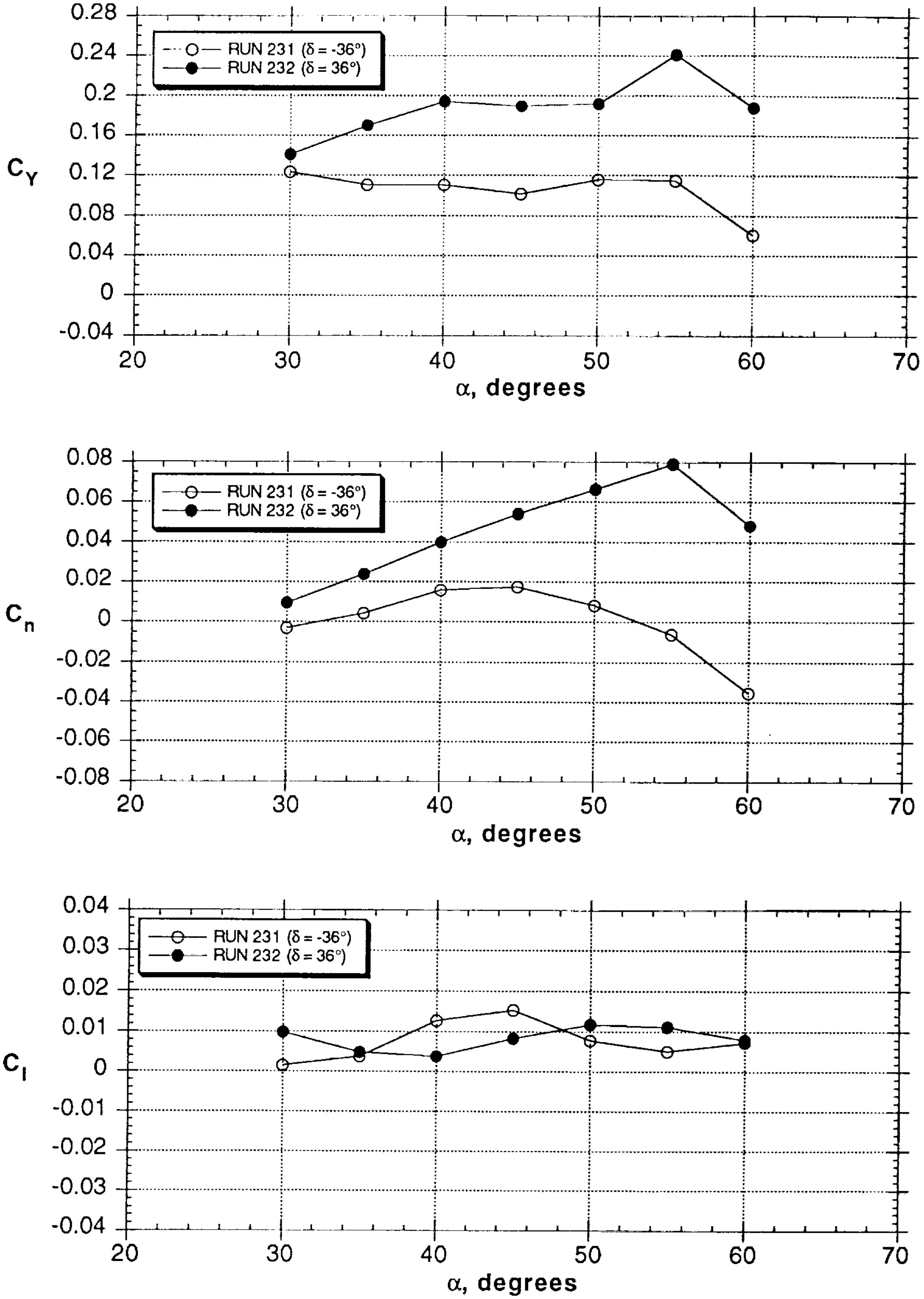

Figure 83 - Effect of sideslip on vertical nose strake effectiveness (β = -10°)

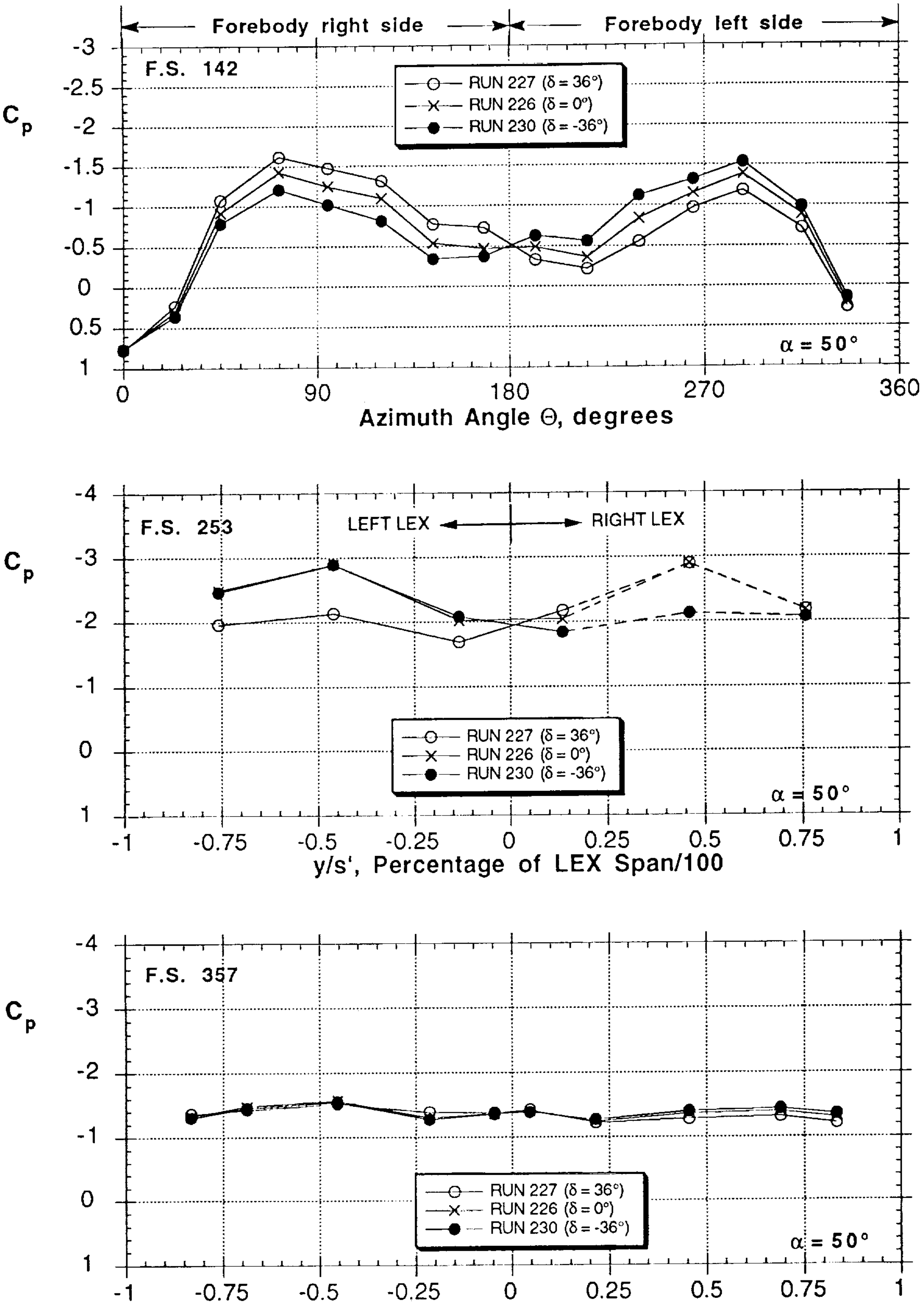

(a) α = 50°

Figure 84 - Effect of vertical nose strake on pressure distributions

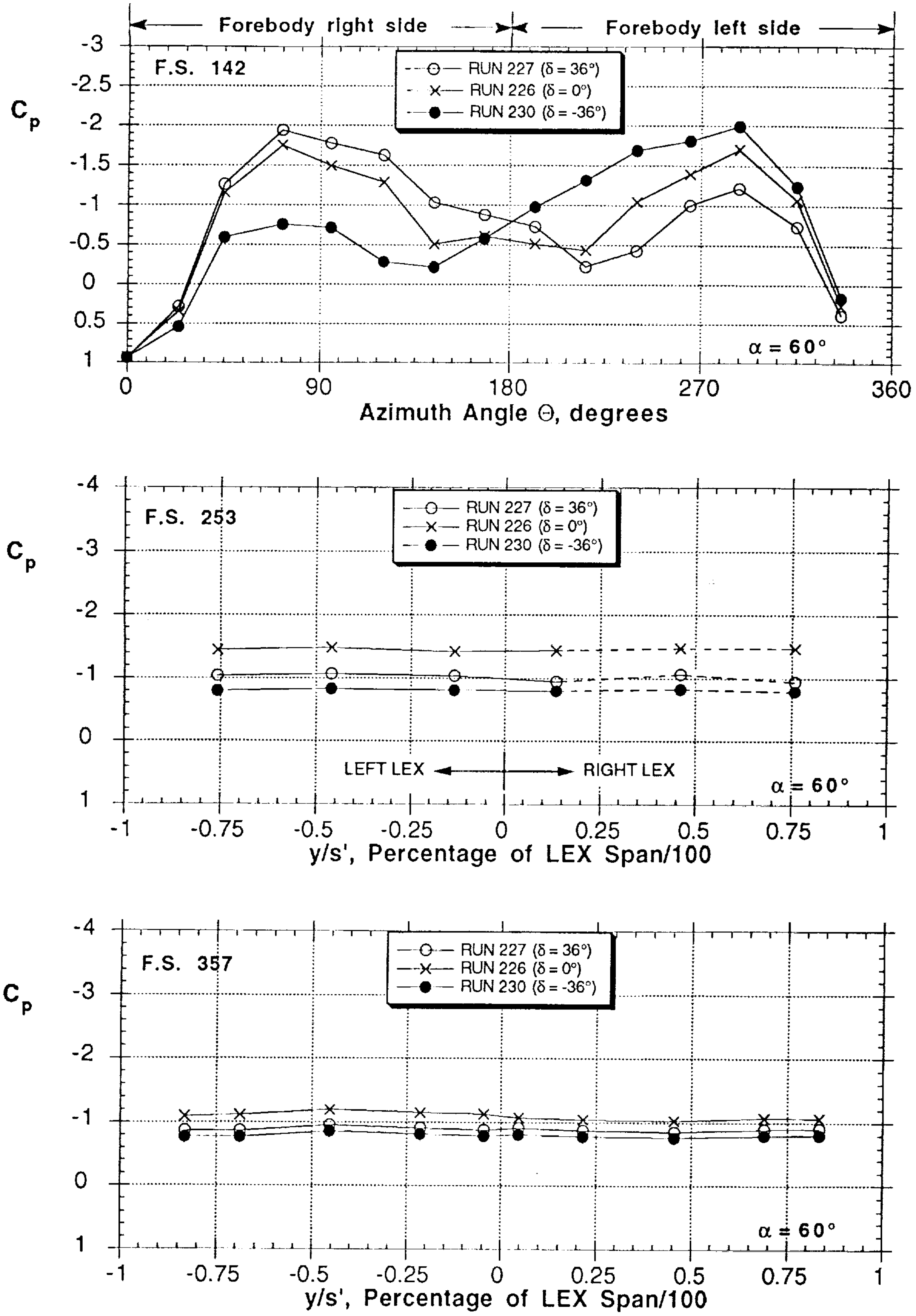

(b) α = 60°

Figure 84 - Concluded

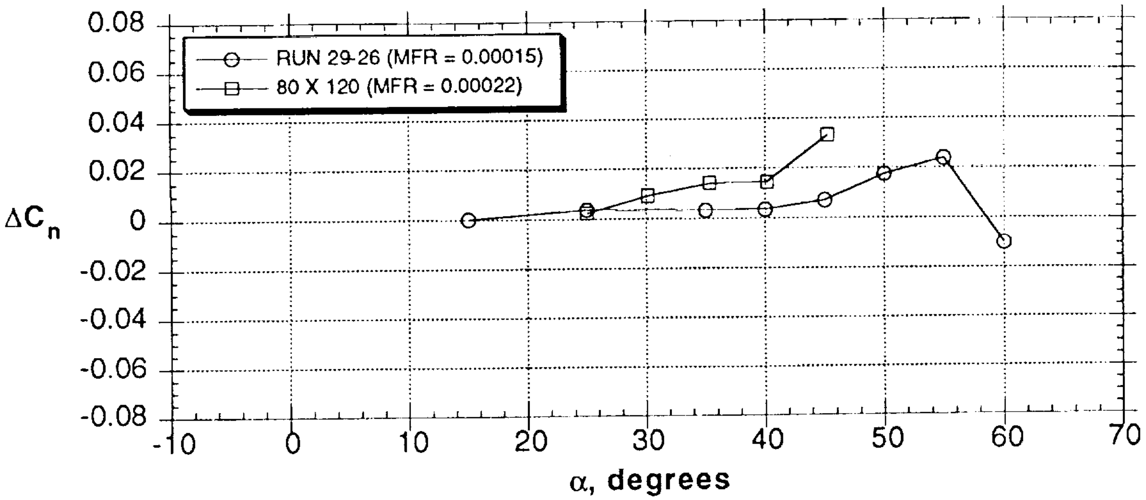

(a) Jet blowing (straight aft, nose 2)

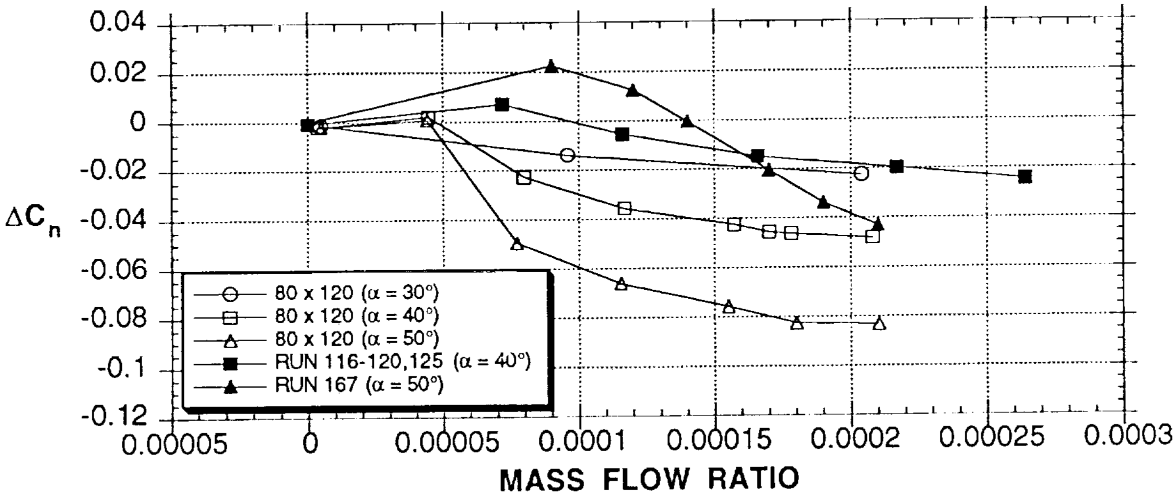

(b) Slot blowing (slot AB)

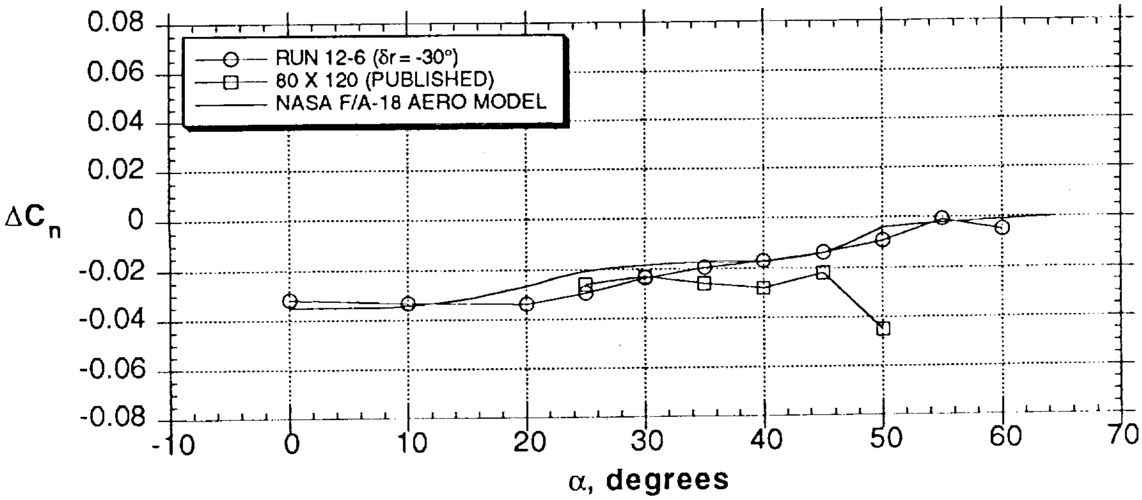

(c) 30° rudder deflection

Figure 85 - Comparison of data obtained in this test, and data from full-scale F/A-18 test in the 80 x 120' (Refs. 8 and 18)

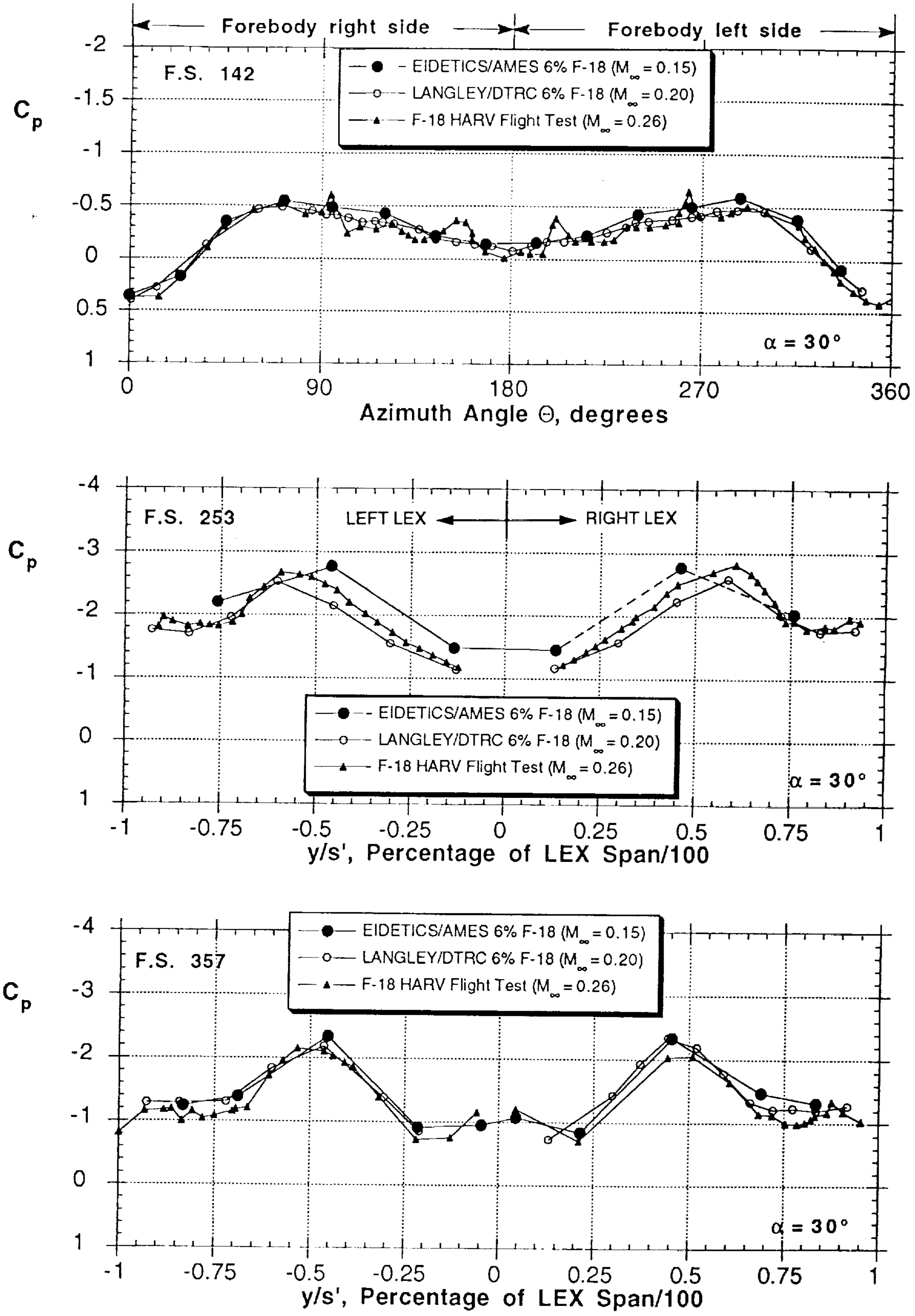

(a) α = 30°

Figure 86 - Comparison of pressure data obtained in this test, data from the 6% F/A-18 model tested in DTRC (Ref. 33), and flight test data from F/A-18 HARV (Refs. 35-37)

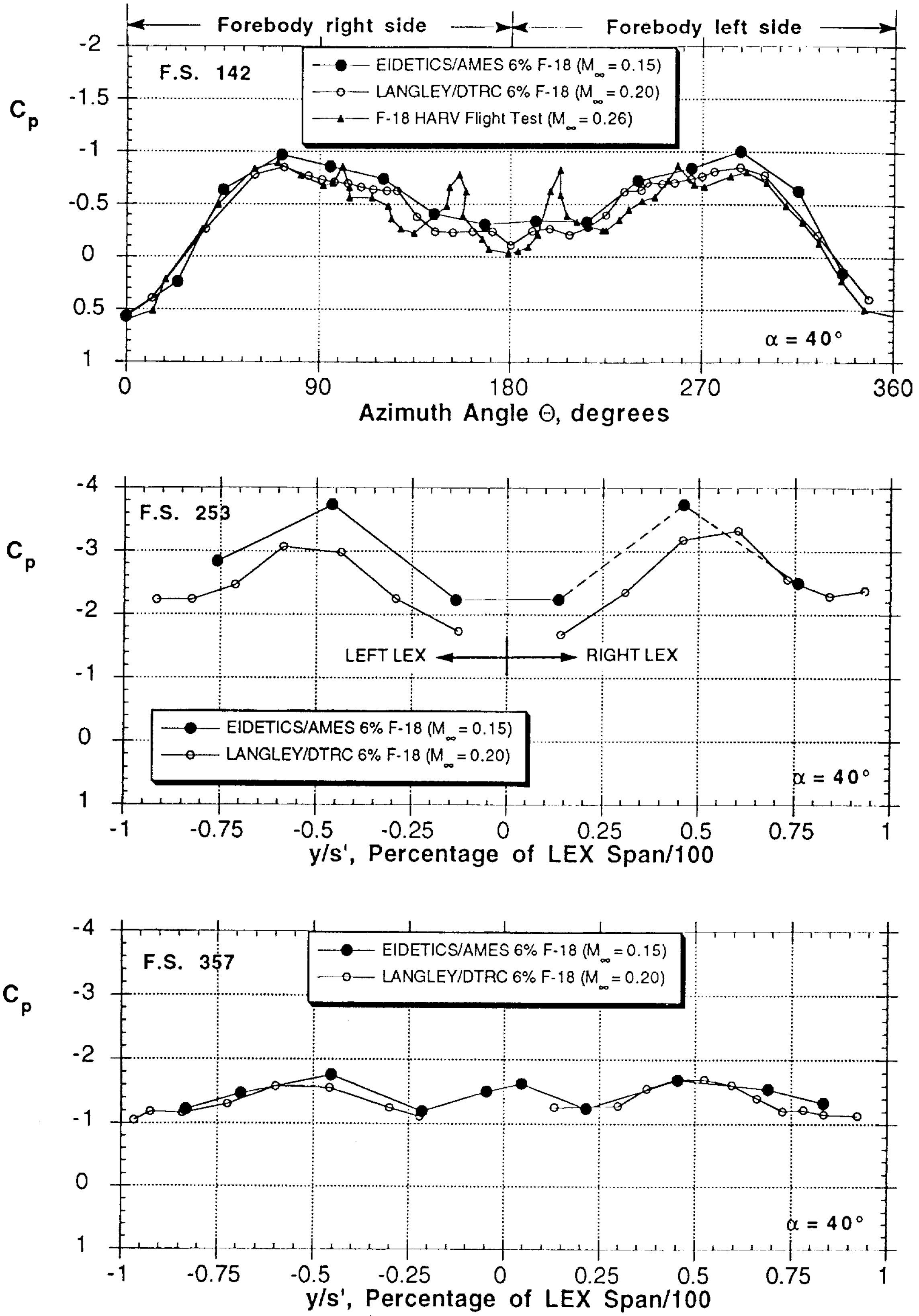

(b) α = 40°

Figure 86 - Continued

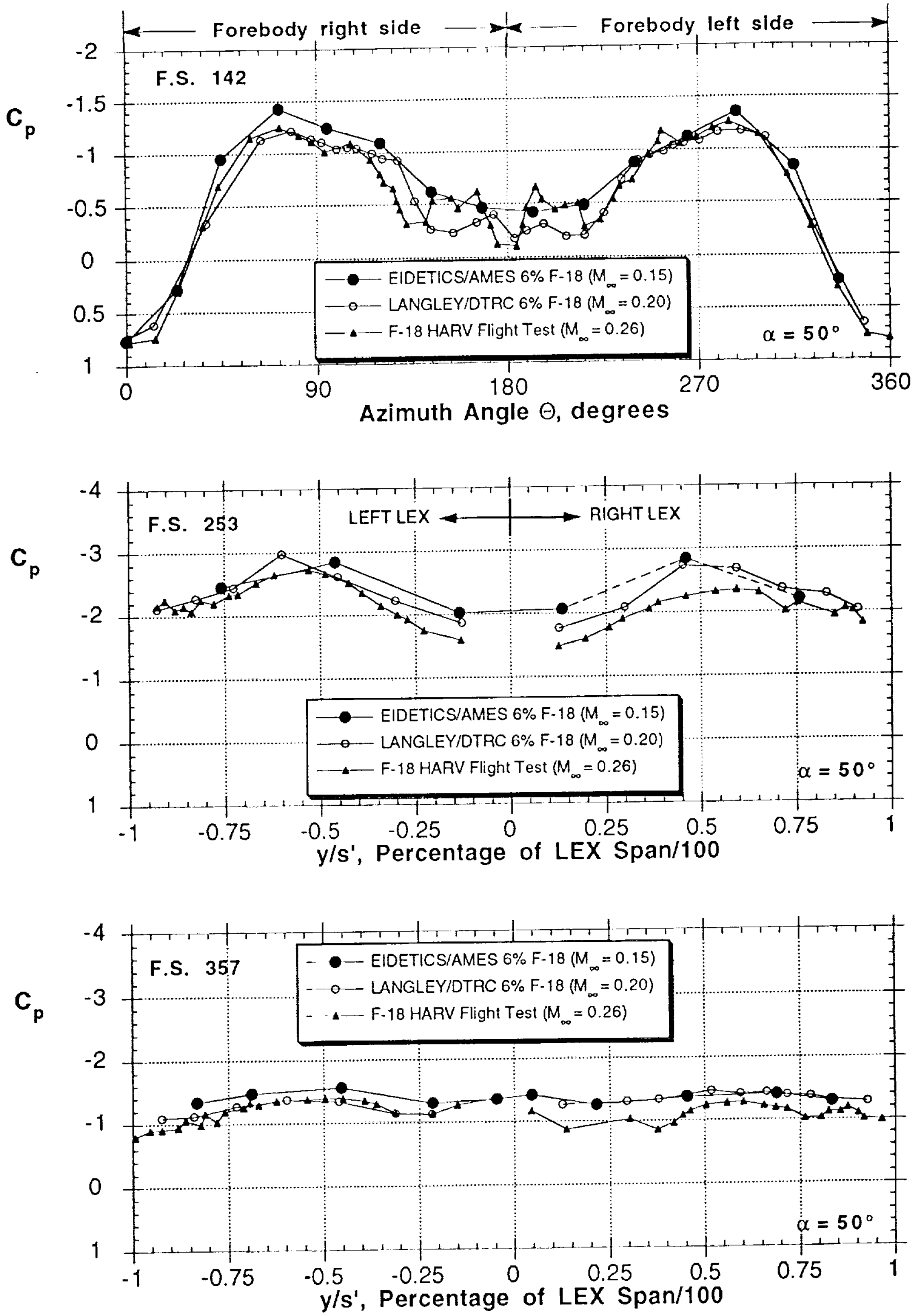

(c) α = 50°

Figure 86 - Concluded

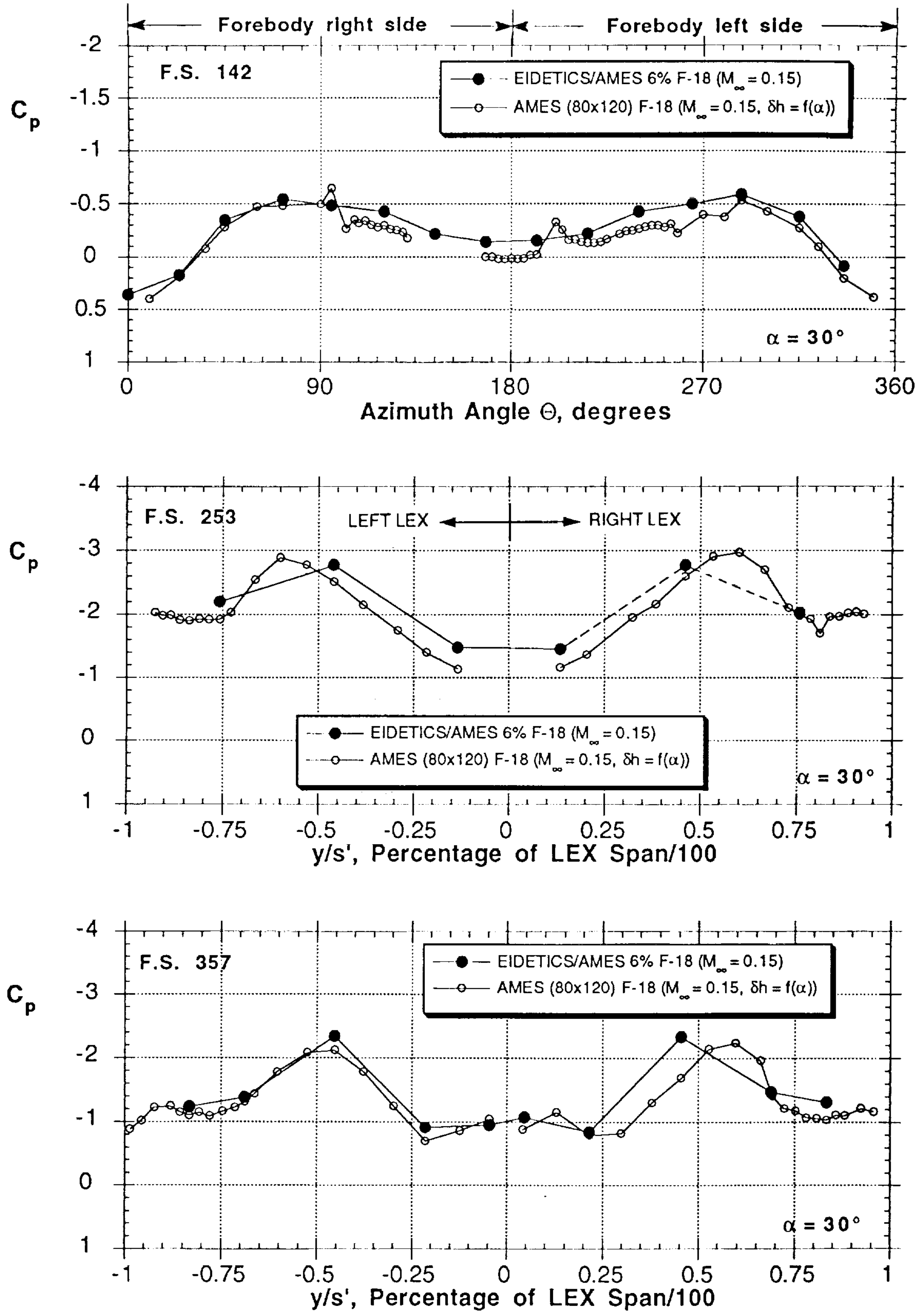

(a) α = 30°

Figure 87 - Comparison of pressure data obtained in this test, and data from full-scale F/A-18 test in the 80 x 120' (Refs. 8 and 18)

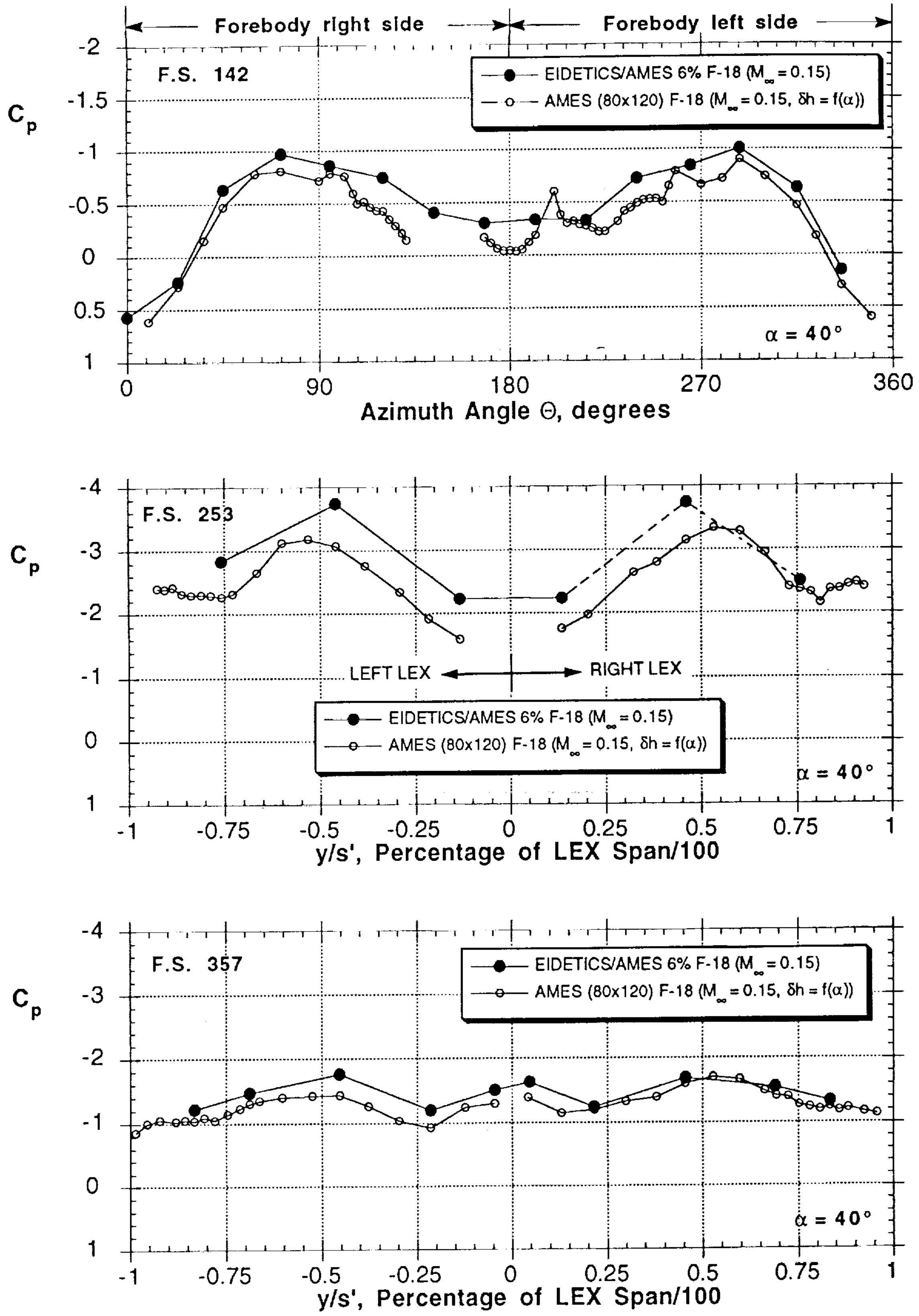

(b) α = 40°

Figure 87 - Continued

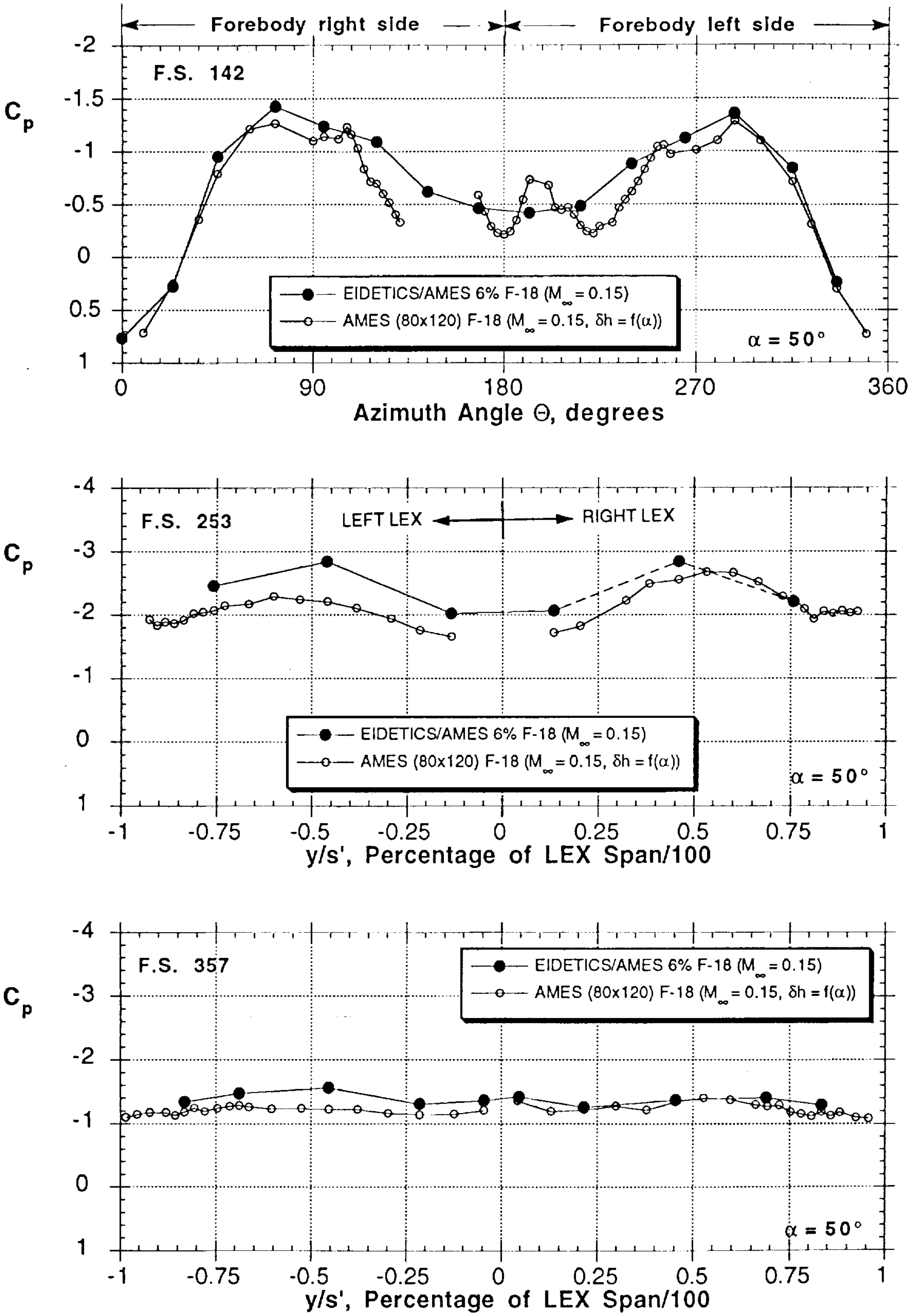

(c) α = 50°

Figure 87 - Concluded

REPORT DOCUMENTATION PAGE

Form Approved
OMB No. 0704-0188

1. AGENCY USE ONLY *(Leave blank)*

2. REPORT DATE
March 1994

3. REPORT TYPE AND DATES COVERED
Contractor Report

4. TITLE AND SUBTITLE
F/A-18 Forebody Vortex Control
Volume 1—Static Tests

5. FUNDING NUMBERS
NAS2-13383

6. AUTHOR(S)
Brian R. Kramer, Carlos J. Suárez, Gerald N. Malcolm, and Bert F. Ayers

7. PERFORMING ORGANIZATION NAME(S) AND ADDRESS(ES)
Eidetics International, Inc.
3415 Lomita Blvd.
Torrance, CA 90505

8. PERFORMING ORGANIZATION REPORT NUMBER
A-94056

9. SPONSORING/MONITORING AGENCY NAME(S) AND ADDRESS(ES)
National Aeronautics and Space Administration
Washington, DC 20546-0001

10. SPONSORING/MONITORING AGENCY REPORT NUMBER
NASA CR-4582 -Vol-1

11. SUPPLEMENTARY NOTES
Point of Contact: Lewis Schiff, Ames Research Center, MS 258-1, Moffett Field, CA 94035-1000;
(415) 604-4467

12a. DISTRIBUTION/AVAILABILITY STATEMENT
Unclassified — Unlimited
Subject Category 02

12b. DISTRIBUTION CODE

13. ABSTRACT *(Maximum 200 words)*

A wind tunnel test was conducted on a six percent model of the F/A-18 at the NASA Ames 7 X 10-Foot Low Speed Wind Tunnel. The primary objective of the test was to evaluate several forebody vortex control configurations at high angles of attack in order to determine the most effective method of obtaining well behaved yawing moments, in preparation for the rotary balance test (Volume 2). Both mechanical and pneumatic systems were tested. Single and dual rotating nose tip strakes and a vertical nose strake were tested at different sizes and deflections. A series of jet blowing configurations were located at various fuselage stations, azimuth angles, and pointing angles ranging from straight aft to 60° canted inboard. Slot blowing was investigated for several slot lengths and fuselage stations. The effect of blowing rate was tested for both of these pneumatic systems. The most effective configurations were then further tested with a variation of both sideslip angle and Reynolds number over a range of angles of attack from 0 to 60°. It was found that a very robust system can be developed that provides yawing moments at angles of attack up to 60° that significantly exceeds that available from 30° of rudder deflection (F/A-18 maximum) at 0° angle of attack.

14. SUBJECT TERMS
F/A-18, Forebody vortex control, Vortex, Wind tunnel test

15. NUMBER OF PAGES
183

16. PRICE CODE
A09

17. SECURITY CLASSIFICATION OF REPORT
Unclassified

18. SECURITY CLASSIFICATION OF THIS PAGE
Unclassified

19. SECURITY CLASSIFICATION OF ABSTRACT

20. LIMITATION OF ABSTRACT

NSN 7540-01-280-5500

Standard Form 298 (Rev. 2-89)
Prescribed by ANSI Std. Z39-18
298-102